Geometries, electronic structures and physico-chemical properties of astatine species: An application of relativistic quantum mechanics

Dumitru-Claudiu Sergentu

UNIVERSITE BRETAGNE LOIRE

UNIVERSITÉ DE NANTES

Thèse de Doctorat

Dumitru-Claudiu SERGENTU

Mémoire présenté en vue de l'obtention du
grade de Docteur de l'Université de Nantes
sous le sceau de l'Université Bretagne Loire

École doctorale : 3MPL

Discipline : Chimie
Spécialité : Chimie théorique
Unité de recherche : SUBATECH, UMR CNRS 6457, IN2P3/Mines Nantes/Université de Nantes
Soutenue le : 19 octobre 2016

Geometries, electronic structures and physico-chemical properties of astatine species: An application of relativistic quantum mechanics

JURY

Président du jury :	**Denis JACQUEMIN**, Professeur, Université de Nantes
Rapporteurs :	**Trond SAUE**, Directeur de Recherche, Université de Toulouse 3 **Boris LE GUENNIC**, Directeur de Recherche, Université de Rennes 1
Examinateurs :	**Ria BRAAM-BROER,** Professeur, Université de Groningue **Florent RÉAL**, Maître de Conférences HDR, Université de Lille 1 **Nicolas GALLAND**, Maître de Conférences HDR, Université de Nantes (directeur de thèse) **Rémi MAURICE**, Chargé de Recherche CNRS, IN2P3/Mines Nantes/Université de Nantes (co-encadrant)

Acknowledgements

A proper supervision is the key to success in obtaining a PhD degree. As arrived to this end of defending a PhD thesis, I would like to acknowledge at first my supervisors, Nicolas and Rémi. During this three-year period of my doctoral stage, they have both been very dynamic, enthusiast and complementary to each other with respect to my research activities. I would like to thank them very much for delivering me a strong scientific background and for preparing me for the forthcoming scientific journey. I would also like to thank them for the very close daily guidance and for all the interesting and constructive talks that we had all three together. I would like to advise the forthcoming student to avoid sitting on the middle chair during these meetings! I finally wish to address my thanks to Nicolas and Rémi as being my friends more than supervisors.

Without a warm welcoming and pleasant host, something can hardly be done. I wish to express my gratitude to Jean-Yves Le Questel and to Gilles Montavon for having me acquainted in their wonderful research teams. I will never forget their dynamism and joyful presence in the labs.

I wish to express my sincere gratitude to Trond Saue, Boris Le Guennic, Ria Braam-Broer, Denis Jacquemin and Florent Réal for accepting to be jury members and to evaluate this work. In particular, I thank Trond Saue and Boris Le Guennic for accepting to be the referees of this thesis.

I would like to express my thanks to several of my colleagues as well. I thank in particular David Mendive-Tapia and Agisilaos Chantzis (but also Rémi) for the fruitful never-ending and science-related discussions that we had in the office, bus, tram, or at the “tandoori”, “saucisson”, “my kebab” and “restaurant pakistanais” places. Also, I would like to thank David Mendive-Tapia, Daniel Escudero and Simon Budzak for helping me in solving various scientific problems. I finally thank to all the other colleagues that have been around me: Patrick, Bob, Zak, Katy, Clo, Titouan, Gabriel and Elena and with whom I had various “existential” debates.

Before ending this “summary” of acknowledgements, I would like to deliver my special thanks to the persons that prepared me for being able to pursue a doctoral stage. I thank firstly to

Ionel Humelnicu, who had led me toward the beautiful lands of theoretical chemistry during the late years of my bachelor studies at the “A. I. Cuza” University in Romania. Secondly, I acknowledge Ria Braam-Broer and Remco Havenith for their support and scientific guidance during my master studies at the University of Groningen in The Netherlands. Thirdly, I thank Daniel Roca Sanjuán for supervising my first ever research project in theoretical chemistry, during the period that I was hosted at University of Valencia in Spain.

I finally acknowledge my brother, Andrei, and my hopefully future wife, Flori, for their support all along my PhD studentship.

Résumé de la thèse

L'astate (At, Z=85) est l'un des éléments les plus rares que l'on trouve naturellement sur Terre. Il appartient à la famille des halogènes et se situe en dessous de l'iode dans le tableau périodique. L'astate est, par l'intermédiaire de son isotope 211 (^{211}At, $t_{1/2}$=7,2 heures), considéré comme l'un des radionucléides les plus prometteurs pour la thérapie alpha ciblée. L'idée est de lier cet isotope à des agents biologiques sélectifs des cellules cancéreuses à traiter, de telle sorte que les particules alpha émises lors de sa désintégration altèrent la cible. La chimie de l'astate étant particulièrement mal connue, l'utilisation de l'astate en médecine nucléaire demeure un réel défi. L'astate se comporte souvent *in vivo* de façon analogue à l'iode : il a par exemple tendance à s'accumuler au niveau de la thyroïde. D'un point de vue plus chimique, l'astate peut être considéré comme un métalloïde, bien qu'il ait un comportement souvent similaire à celui de l'iode. Le caractère « métallique » de l'astate est illustré, par exemple, par la présence de formes cationiques stables en solution, telles At^+ et AtO^+, ce qui n'est pas observé pour les autres halogènes. Les difficultés liées à la production de l'astate font que des quantités de matière extrêmement faibles sont obtenues, ce qui rend impossible en pratique l'étude des composés de l'astate à l'aide de méthodes spectroscopiques. Il est donc délicat d'identifier et de caractériser de nouvelles espèces de l'astate.

Actuellement, révéler la chimie de base de At constitue un objectif majeur pour différentes équipes de recherche nantaises, notamment du laboratoire SUBATECH (laboratoire de physique SUBAtomique et des TECHnologies associées, UMR 6457, IN2P3/Mines Nantes/Université de Nantes) et du laboratoire CEISAM (Chimie Et Interdisciplinarité, Synthèse, Analyse, Modélisation, UMR 6230, Université de Nantes). Des chercheurs du groupe de radiochimie de SUBATECH effectuent des travaux expérimentaux qui visent principalement à mesurer des constantes de d'équilibre pour des réactions qui impliquent des composés de l'astate, l'astate étant lui-même produit au cyclotron ARRONAX (Accélérateur pour la Recherche en Radiochimie et Oncologie à Nantes Atlantique). Les approches calculatoires de la mécanique quantique sont un atout incontestable pour identifier et caractériser les espèces chimiques impliquées dans les équilibres

étudiés (formules brutes, structures géométriques, stabilités relatives et propriétés physico-chimiques). Antérieurement, les calculs ont surtout été menés par des chercheurs de l'équipe de modélisation du laboratoire CEISAM, maintenant aidés par des chercheurs du laboratoire SUBATECH. Ces approches complémentaires (modélisation et expériences) constituent actuellement la voie privilégiée par les laboratoires SUBATECH et CEISAM pour étudier la chimie de base de l'astate. Cette thèse constitue une étude théorique de l'astate et de plusieurs de ses espèces à l'aide de méthodes issues de l'état de l'art de la mécanique quantique, afin d'identifier des espèces à base de l'astate qui sont stables en solution, de caractériser les liaisons chimiques à l'origine de ces espèces, et de définir des méthodes efficaces qui peuvent être sereinement utilisées pour prédire différentes propriétés d'espèces de l'astate.

Cette thèse s'articule en six chapitres. Les deux premiers chapitres constituent une introduction générale de ce travail. Dans le chapitre 1, une revue de la littérature est donnée, dans laquelle sont présentés les protocoles de radiomarquage avec ^{211}At actuellement envisagés, et la nécessité d'investigations théoriques est également soulignée. Les méthodes théoriques non relativistes et relativistes qui sont utilisées dans le cadre de ce travail sont présentées dans le chapitre 2. Les résultats sont présentés dans les quatre chapitres suivants. Leurs objectifs et les conclusions principales associées sont brièvement repris ci-après.

Le chapitre 3 vise à établir des protocoles théoriques efficaces, basés sur la théorie de la fonctionnelle de la densité (« Density Functional Theory », DFT), qui peuvent être utilisés pour évaluer avec précision les structures et les propriétés physico-chimiques d'espèces de l'astate de moyenne et grandes taille. Plus précisément, l'objectif est d'identifier des fonctionnelles d'échange et de corrélation qui sont pertinentes pour étudier la chimie de base de l'astate, dans un formalisme quasi-relativiste. Un ensemble de 36 fonctionnelles non relativistes a été examiné dans le but de prédire aux mieux les géométries, les énergies de transition électroniques et les propriétés thermodynamiques de 19 espèces. Nous avons trouvé que la fonctionnelle hybride méta-GGA (« GGA » pour approximation des gradients généralisée) PW6B95, développée par le groupe du professeur Truhlar en 2005, représente globalement le meilleur choix. Cette fonctionnelle a permis le calcul (i) de géométries avec une erreur (en valeur absolue) moyenne de 1,1%, (ii) d'énergies de transition électronique avec une erreur (en valeur absolue) moyenne de 0,13 eV, et (iii) de constantes d'équilibre avec une erreur (en valeur absolue) moyenne de 0,9 unité logarithmique. En outre, nous avons établi que les fonctionnelles hybrides GGA généralistes telles que PBE0 et B3LYP sont aussi pertinentes, en particulier pour le calcul de géométries d'équilibre (PBE0) ou encore pour le calcul de constantes d'équilibre (B3LYP).

Le chapitre 4 se focalise sur une géométrie atypique du système AtF_3, qui fait l'objet de controverses dans la littérature en raison d'interférences entre les effets relativistes et l'effet pseudo Jahn-Teller. En particulier, nous avons analysé la topologie de la surface d'énergie potentielle (SEP) de l'état fondamental du système AtF_3. Cette étude a été réalisée en utilisant différentes approches relativistes, basées sur la DFT ou sur la fonction d'onde, ces dernières prenant en compte l'effet de couplage spin-orbite a posteriori. Premièrement, nous avons montré que cette approche en deux étapes est appropriée pour étudier le potentiel caractère multiconfigurationnel de la fonction d'onde de l'état fondamental du système AtF_3, et nous avons constaté qu'il est essentiellement mono-configurationnelle et à couches fermées. Deuxièmement, nous avons trouvé que la topologie de la SEP de l'état fondamental de AtF_3 est différente de celles de ses analogues plus légers, et donc de celle de IF_3. Même dans des systèmes relativement simples, l'astate peut se comporter différemment de l'iode contrairement à ce qui est (trop souvent ?) considéré. Deux types de minimum ont été identifiés sur la SEP de l'état fondamental de AtF_3, avec trois minima globaux équivalents ayant une structure de symétrie C_{2v} en forme de T, et un minimum local ayant une structure trigonale plane de symétrie D_{3h}, dans lesquelles l'astate est lié chimiquement aux atomes de fluor par des liaisons essentiellement ioniques. Après avoir pris en compte les corrections liées aux effets de température, nous avons établi que la géométrie D_{3h} devrait être la géométrie apparente observable dans les expériences, si elles étaient possibles. En utilisant l'approche en deux étapes basée sur la fonction d'onde, nous avons constaté que la géométrie D_{3h} résulte de la somme et de la synergie entre les effets relativistes scalaires et la corrélation électronique.

Le chapitre 5 vise à élucider le changement d'état fondamental d'AtO^+ induit par la solvatation de ce dernier en solution aqueuse. Ce phénomène peut expliquer la réactivité de ce cation en solution aqueuse avec des ligands à couches électroniques fermées, c'est à dire singulets de spin. En phase gaz, AtO^+ a un état fondamental $^3\Sigma^-$. Lorsque le couplage spin-orbite est pris en compte, la composante M_S=0 de cet état constitue la contribution majeure à l'état spin-orbite fondamental $X\ 0^+$ (~68%), qui a donc un caractère dominant triplet de spin. Néanmoins, l'état spin-orbite $X\ 0^+$ a également un caractère singulet à couches fermées marqué (~26%, provenant de l'état relativiste scalaire $^1\Sigma^+$). En l'absence de couplage spin-orbite et en présence de molécules d'eau, nous avons montré qu'AtO^+ adopte un état fondamental essentiellement à couches fermées (donc essentiellement singulet de spin), ce qui est en accord avec de précédentes études. Nous avons montré pour la première fois que cet état est corrélé avec la composante à couches fermées de l'état $^1\Delta$. Lorsque le couplage spin-orbite est pris en compte, nous avons constaté que les systèmes $AtO^+(H_2O)_n$ les plus stables ($n\geq5$) ont des états fondamentaux spin-orbite qui sont essentiellement

singulets de spin. Ensuite, nous avons démontré que leurs contributions majeures corrèlent à la composante à couches fermées de l'état $^1\Delta$ d'AtO^+, donc que les états fondamentaux spin-orbite corrèlent avec une des deux composantes de l'état **a** 2 (celle essentiellement à couches fermées). Enfin, des calculs d'ordres de liaison effectifs portant sur la liaison chimique dans AtO^+ ont fait apparaitre des similitudes entre phase gazeuse et solution aqueuse, même si la solvatation diminue le caractère σ liant de la liaison tout en augmentant le caractère π liant.

Enfin, nous abordons dans le chapitre 6 l'établissement du diagramme de Pourbaix de l'astate en solution aqueuse et en milieu non complexant, c'est à dire le diagramme de spéciation de l'astate en fonction du potentiel de la solution (*E*) et du pH. Plus précisément, nous avons cherché à identifier l'espèce prédominante de l'astate en milieu basique et oxydant en combinant résultats d'expériences de radiochimie et de calculs quantiques relativistes. Les mesures expérimentales montrent que cette espèce de l'astate porte une seule charge négative et qu'avec l'abaissement du pH de 11 à 5,5, cette espèce se transforme en AtO(OH). En outre, la constante d'équilibre correspondante a été déterminée. Concernant la réaction chimique impliquée, deux hypothèses ont été formulées : soit elle correspond à la réaction de déprotonation de l'espèce AtO(OH), c'est à dire à la formation de l'espèce anionique $AtOO^-$, soit elle correspond à la réaction d'hydrolyse de AtO(OH), c'est à dire à la formation de l'espèce anionique $AtO(OH)_2^-$. Les calculs quantiques avaient pour objet d'identifier l'hypothèse pertinente, par la confrontation des données calculées selon chaque hypothèse à la valeur mesurée de la constante d'équilibre (Log K=−6,9±0,2). Dans une première étape, nous avons exclu la possibilité que l'espèce $AtOO^-$ puisse être formée à partir de pH=6. Ensuite, nous avons constaté que la constante d'équilibre calculée (Log K=−7,1) pour la formation de l'espèce anionique $AtO(OH)_2^-$, est en très bon accord avec celle déterminée expérimentalement. Ceci à permit d'établir que c'est l'espèce $AtO(OH)_2^-$ qui prédomine en milieu aqueux, non complexant, basique, et oxydant. Ce résultat est important pour la communauté scientifique impliquée dans la radiomarquage avec ^{211}At, notamment si l'on compte que l'espèce At^- soit utilisée dans le protocole de marquage.

Pour conclure, nous pouvons dire que cette thèse essentiellement théorique a permis d'identifier des niveaux de calcul fiables pour prédire les structures et propriétés physico-chimiques de composés de l'astate, tout en amenant des informations cruciales pour comprendre et interpréter les expériences. Sans nul doute, ce travail devra être prolongé par d'autres études théoriques ou collaborations théorie/expérience afin de mieux appréhender la chimie de l'astate et de ses

composés, ce qui permettra peut-être d'envisager à moyen terme de nouvelles voies de marquage avec ^{211}At.

List of Abbreviations

2*c*	Two components
4*c*	Four components
AO	Atomic Orbital
BFC	Bifunctional Chelating Agent
BNCT	Boron Neutron Capture Therapy
(SOF-/SOC-)(E)BO	(Spin-Orbit Free/Spin-Orbit Coupled) (Effective) Bond Order
CAS(SCF/PT2)	Complete Active Space (Self-Consistent Field/Perturbation Theory at second order)
(NR/SR/2*c*/4*c*-) CC(SD/SDT/SD(T))	(Nonrelativistic/Scalar Relativistic/Two-component/Four-component/) Coupled-Cluster (with Single and Double excitations/with Single, Double and Triple excitations/with Single, Double and non-iterative Triple excitations)
(FS/IHFS)CC	(Fock Space/Intermediate Hamiltonian Fock Space) Coupled-Cluster
CI(S/SD)	Configuration Interaction (with Single excited determinants/with Single and Double excited determinants)
CSF	Configuration State Function
(KS/TD/SR/2*c*-)DFT	(Kohn-Sham/Time-Dependent/Scalar Relativistic/two-component) Density Functional Theory
DK(H)	Douglas-Kroll (-Hess)
EA	Electron Affinity
EAS	Electrophilic Aromatic Substitution
ELF	Electron Localization Function
ESC	Elimination of the Small Component
FCI	Full Configuration Interaction
GGA	Generalized Gradient Approximation

(R/U)HF	(Restricted/Unrestricted) Hartree-Fock
HPIEC	High-Pressure Ion-Exchange Chromatography
(R/L)HS	(Right/Left) Hand Side
HSAB	Hard and Soft Acids and Bases theory
IP	Ionization Potential
IRC	Intrinsic Reaction Coordinate
KS	Kohn-Sham
LDA	Local Density Approximation
LLC	Liquid-Liquid Competition
MaxD	Maximum Deviation
MO	Molecular Orbital
MP(2)	Møller–Plesset (perturbation theory at second order)
MRCI(-SD)	Multireference Configuration Interaction (with Single and Double excitations)
MRPT	Multireference Perturbation Theory
MSE	Mean-Signed Error
MUE	Mean-Unsigned Error
NAS	Nucleophilic Aromatic Substitution
(UC/PC/SC/QD-) NEVPT2	(Uncontracted/Partially Contracted/Strongly Contracted/Quasi-Degenerate) N-electron valence state perturbation theory at second order
(C)PCM	(Conductor-like) Polarizable Continuum Model
PES	Potential Energy Surface
PJTE	*Pseudo* Jahn-Teller Effect
PP	Pseudopotential
QTAIM	Quantum Theory of Atoms in Molecules
RECP	Relativistic Effective Core Potential
RMSD	Root-Mean-Square Deviation
SA	State-Average
SA-CASSCF	State-Averaged Complete Active Space Self-Consistent Field

SCF	Self-Consistent-Field
SI	State Interaction
SLC	Solid-Liquid Competition
SO(C/F)	Spin-Orbit (Coupling/Free)
(uc/c-)SOCI	(uncontracted/contracted) Spin-Orbit Configuration Interaction
TF(D)	Thomas-Fermi (-Dirac)
TS	Transition State
UA	United Atom topological model
UAHF	United-Atom Hartree-Fock
UAKS	United-Atom Kohn-Sham
UEG	Uniform Electron Gas
UFF	Universal Force Field
VSEPR	Valence Shell Electron Pair Repulsion
XC	Exchange-Correlation
ZORA	Zero-Order Regular Approximation

List of Publications

1. D.-C. Sergentu, M. Amaouch, J. Pilmé, N. Galland and R. Maurice, "Electronic structures and geometries of the XF3 (X = Cl, Br, I, At) fluorides", *J. Chem. Phys.*, 2015, 143, 114306.

2. D.-C. Sergentu, D. Teze, A. Sabatié-Gogova, C. Alliot, N. Guo, F. Bassal, I. Da Silva, D. Deniaud, R. Maurice, J. Champion, N. Galland and G. Montavon, "Advances on the determination of the astatine Pourbaix diagram: predomination of $AtO(OH)_2^-$ over At^- in basic conditions", *Chem. Eur. J.*, 2016, 22, 2964.

3. D.-C. Sergentu, G. David, G. Montavon, R. Maurice and N. Galland, "Scrutinizing "invisible" astatine: a challenge for modern density functionals", *J. Comput. Chem.*, 2016, 37, 1345.

4. D.-C. Sergentu, F. Réal, G. Montavon, N. Galland and R. Maurice, "Unraveling the hydration-induced ground-state change of AtO^+ with relativistic and multiconfigurational wave-function-based methods", *Phys. Chem. Chem. Phys.*, 2016, 18, 32703.

Contents

Introduction

In 1940, a research team, hosted by the University of California and formed by D. R. Corson, K. R. MacKenzie and E. Segrè, reported the identification of a new highly-radioactive element with the atomic number 85.[1] Although the earlier claim of Hulubei and Cachois[2] was not directly refuted at that time,[3] Corson, MacKenzie and Ségre were credited with the discovery of element 85 after the publication of an editorial in Nature by Paneth.[4] The retained name for this element, astatine (At), was derived from the greek astatos (αστατοσ), which means "unstable".[5] At that time, At was the last known element in the halogen's group (XVII) of the periodic table, placed right below iodine and having polonium and radon as its left and right neighbors. Recently, element 117 (eka-astatine) has been added as the lower neighbor of At.[6] So far, around 39 At-isotopes have been identified and characterized. However, all of them are unstable and span a short range of half-life times, between nanoseconds (*e.g.* ^{213}At) and 8.1 hours (^{210}At). The natural occurrence of the At radioelement in Earth's crust is a result of radioactive decay of several heavier radionuclides, *e.g.* ^{232}Th or ^{238}U , and does not amount for more than ~30 grams at a given time. Actually, researches involving At require its artificial production in ultra-trace quantities, typically through alpha-particles bombardment of ^{209}Bi targets, with the help of cyclotron facilities.[7]

The low availability of At combined with its high radioactivity and instability has had a significant impact on the process of unraveling its basic chemistry, and finally in identifying eventual economical or societal applications. Nevertheless, 12 years after the discovery of At, Robert Shaffer proposes to use irradiation therapy for the treatment of a human eye epithelial cyst.[8] The need of irradiation with sufficient energy, capable to destroy the thin wounded area close to the iris, as well as with short penetration (to reduce healthy-tissue damage), brought Shaffer's attention to alpha-particle irradiation and so to the newly discovered At element by Corson *et al*. Schaffer also suggested that ^{211}At could be a candidate to remove localized tumors, *e.g.* at the thyroid gland. It was the beginning of the slow, and yet not achieved, industrialization process of At, through the potentially valuable application of its ^{211}At isotope in nuclear medicine.[9]

In France, several research units, namely, the National Institute for Health and Medical Research (INSERM), the National Center for Scientific Research (CNRS), and University Hospital Centers (CHUs), among others, perform collaborative and fundamental researches aiming at developing efficient drugs for cancer diagnosis and treatment. In the scientific context of life sciences and health, the ARRONAX PLUS "Translational Nuclear Medicine" and IRON "Innovative Radiopharmaceuticals in Oncology and Neurology" programs have been recently founded by the "Investissements d'Avenir" financing program. The research programs notably aim at cancer diagnosis and treatment through irradiation, using drugs that encapsulate specific radioactive isotopes. The ARRONAX PLUS and IRON programs are mainly developed in the French region "Pays de la Loire" and gather research laboratories as SUBATECH (UMR 6457 IN2P3/Ecole des Mines de Nantes/Université de Nantes), the "Centre de Recherche sur le Cancer de Nantes-Angers" (CRCNA, UMR 892 INSERM - 6299 CNRS), CEISAM (UMR 6230 CNRS/Université de Nantes), "l'École Nationale Vétérinaire, Agroalimentaire et de l'Alimentation Nantes-Atlantique" (ONIRIS). Note that the ARRONAX cyclotron, built specifically for general research in radiochemistry and oncology in the region of Nantes, play a crucial role in these collaborative projects. In particular, research teams in nuclear oncology have begun, in 2004, to explore the potential of alpha-emitter isotopes in destroying tumoral cells, by starting to design radiotherapeutic agents based on the ^{211}At isotope. In short, the procedure of designing such agents imply firstly the production of the ^{211}At isotope at the ARRONAX cyclotron facility and, secondly, the development of suitable carrier molecules capable of binding, in a first step, and delivering, in a second step, ^{211}At to the cancer site (*i.e.* targeting the cancer).

The process of radiolabeling, *i.e.* of binding ^{211}At to a carrier agent, is a difficult process in itself since so little is known on the chemistry of this element. Scott Wilbur has recently pointed out in Nature Chemistry, "the difficulty in studying the transient element astatine, and the need to understand its basic chemical nature to help in the development of targeted radiotherapy agents."[10] This translates to the straightforward question: how can we design edge radiotherapeutic agents based on At since the physico-chemical properties of At itself are unknown? Physiologically speaking, At may be regarded as behaving similarly to iodine, since, for instance, it was found to accumulate selectively at the thyroid gland.[11] From a more chemistry oriented viewpoint, it is still highly debated in the literature whether At shows halogenic behavior, as iodine, or that of a standard post-transitional metal. The idea of At being a metalloid element notably emerged from the striking identification of a predominant cationic form, At^+, in acidic solutions,[12,13] which bears no other halogen analogue. The difficulties in synthesizing At in decent amounts, which is required for

structural analysis with standard analytical chemistry tools, or as Wilbur stated,[10] "the invisibility" of this element, has been always detrimental to the process of unraveling its basic chemical properties.

Presently, unraveling the basic chemistry of At constitutes an important milestone for research teams in Nantes, from the SUBATECH and CEISAM laboratories. The radiochemistry team at SUBATECH performs experimental investigations that mainly aim at measuring the equilibrium constants of reactions involving At species and therefore relies on the production of At coming from the ARRONAX cyclotron facility. It is indisputable that computational approaches, based on quantum mechanical principles, are required for identifying the reaction products (natures, structures, stabilities, and physico-chemical properties). For almost a decade, the computational tasks were devoted to the modeling team at CEISAM; more recently researchers from SUBATECH are also involved in this. The combination of such approaches, modeling and experiments, constitutes currently the "golden" strategy employed by the SUBATECH and CEISAM laboratories to study the basic chemistry of At. The present thesis is focused at performing a theoretical study of At and several of its species, using "state-of-the-art" methods of quantum mechanics, in order to:

1. identify stable At species in aqueous solutions with potential use for the radiolabeling;
2. characterize the bonding patterns in these species;
3. establish efficient methodologies which can be used to predict various properties of At compounds.

This monograph is organized in six chapters. Chapter 1 concludes a literature survey in which the radiolabeling protocols used in targeted alpha-therapy with At will be discussed, while the need for theoretical investigations will also be pointed out. Chapter 2 consists in a general presentation of the theoretical methodologies that are used in this work. Chapter 3 aims at establishing efficient theoretical protocols, based on density functional theory (DFT), which can be used to accurately assess the structures and properties of medium to large At-containing systems. Chapter 4 focuses on the unexpected bonding pattern in the AtF_3 system, which is subject of controversies in the literature due to a rich mysterious interplay between the signatures of At as a heavy element, *i.e.* relativistic effects, and the *pseudo* Jahn-Teller effect (PJTE). Chapter 5 presents a "state-of-the-art" theoretical study of the bonding in the gas-phase and hydrated AtO^+ cation and further rationalizes its observed reactivity in aqueous solution. Chapter 6 tackles the completion of the Pourbaix diagram of At, *i.e.* the speciation diagram of At in solution as a function of both the

potential (*E*) and pH, which is certainly a “vital” information for radiolabeling. Finally, conclusions and perspectives will be highlighted.

Bibliography:

1. D. R. Corson, K. R. MacKenzie, E. Segrè, *Phys. Rev.* Artificially radioactive element 85, **1940**, 58, 672.
2. H. Hulubei, Y. Cauchois, *C. R. Séances Acad. Sci. Ser. C.* Spectres de l'émission propre ondulatorie du radon et de ses dérivés. Raies attribuables à l'élément 85, **1939**, 209, 39.
3. B. F. Thornton, S. C. Burdette, *Bull. Hist. Chem.* Finding eka-iodine: Discovery priority in modern times, **2010**, 35, 86.
4. F. A. Paneth, *Nature.* The making of the missing chemical elements, **1947**, 159, 8.
5. D. R. Corson, K. R. MacKenzie, E. Segre, *Nature.* Astatine-the element of atomic number-85, **1947**, 159, 24.
6. Y. T. Oganessian, F. S. Abdullin, P. D. Bailey, D. E. Benker, M. E. Bennett, S. N. Dmitriev, J. G. Ezold, J. H. Hamilton, R. A. Henderson, M. G. Itkis, Y. V. Lobanov, A. N. Mezentsev, K. J. Moody, S. L. Nelson, A. N. Polyakov, C. E. Porter, A. V. Ramayya, F. D. Riley, J. B. Roberto, M. A. Ryabinin, K. P. Rykaczewski, R. N. Sagaidak, D. A. Shaughnessy, I. V. Shirokovsky, M. A. Stoyer, V. G. Subbotin, R. Sudowe, A. M. Sukhov, Y. S. Tsyganov, V. K. Utyonkov, A. A. Voinov, G. K. Vostokin, P. A. Wilk, *Phys. Rev. Lett.* Synthesis of a new element with atomic number Z=117, **2010**, 104, 142502.
7. M. R. Zalutsky, M. Pruszynski, *Curr. Radiopharm.* Astatine-211: production and availability, **2011**, 4, 177.
8. R. N. Shaffer, *Trans. Am. Ophthalmol. Soc.* Alpha irradiation: effect of astatine on the anterior segment and on an epithelial cyst, **1952**, 50, 607.
9. I. Brown, *Int. J. Rad. Appl. Instrum. Part A. Appl. Radiat. Isot.* Astatine-211: its possible applications in cancer therapy, **1986**, 37, 789.
10. D. S. Wilbur, *Nat. Chem.* Enigmatic astatine, **2013**, 5, 246.
11. J. G. Hamilton, M. H. Soley, *Proc. Natl. Acad. Sci. U. S. A.* A comparison of the metabolism of iodine and of element 85 (eka-iodine), **1940**, 26, 483.
12. A. Cavallero, K. Roessler, *Radiochim. Acta.* Chromatography at fixed redox potential of inorganic forms of astatine (^{211}At), **1989**, 47, 113.
13. J. Champion, C. Alliot, S. Huclier, D. Deniaud, Z. Asfari, G. Montavon, *Inorg. Chim. Acta.* Determination of stability constants between complexing agents and At(I) and At(III) species present at ultra-trace concentrations, **2009**, 362, 2654.

Chapter 1

Literature Survey: The Intriguing Properties of Astatine Compounds

The goal of this chapter is to illustrate how computational studies can actually help in advancing with the current applications envisaged for At and its compounds. Firstly, we will see that there is a strong interest for At in nuclear medicine and, in this context, some recent developments will be highlighted. It will be shown that the release of At for medicinal applications is still problematic and that the actual challenges are related to the unknown basic chemistry of this element. Thus, we will also highlight some recent advances regarding this aspect. Finally, the interest in performing quantum mechanical calculations within the present context will be justified.

1.1 The medicinal perspective

The ^{211}At radionuclide is currently considered to be one of the most suitable sources of radioactivity (α-particle emission) in targeted radiotherapy. In the following, a short introduction of radiation therapies is firstly given in order to continue with the principles of targeted radiotherapy and the characteristics that make ^{211}At a good candidate for this. Finally, trials to label targeting agents with ^{211}At will be presented.

1.1.1 Radiation for cancer therapy

The recent advances in fundamental researches in chemistry, physics and related areas have brought, within the context of medicine, the battle against cancers to a new era. While classical methods as surgery and standard chemotherapies are still broadly used to treat them, the interest for radiotherapies and targeted-radiotherapies has recently grown. These two alternatives

explore the potential of radiation in damaging the genes responsible for cancerous cell division in order to cease the uncontrolled growth of the tumor and ultimately to remove it. The radiation can be delivered to cancer cells in two different ways:

a) One way, and is what generally radiotherapies imply, is to apply, essentially to the cancer site, external ionizing radiation.

In this case, the ionization radiation consists either in photon beams, X-rays or γ-rays, coming from radioactive sources such as ^{60}Co, ^{137}Cs, ^{192}Ir, or ^{169}Yb, or particle beams most commonly under the form of (i) electron beams generated through Auger emission, internal conversion, β-decay etc., (ii) proton beams generated from radioactive sources such as ^{53}Co, ^{151}Lu, ^{147}Tm, and (iii) neutron beams, generated from radioactive sources as ^{252}Cf, for instance.

Figure 1.1 Device used to apply an external radiation beam to a specific area that contains a tumor.

Choosing among these types of radiations is strongly based on the amount of energy needed to kill the tumor which is dealt with and its location in the body. For instance, electron beam radiation has low energy disposal and short penetration depth, therefore, it is well suited for the treatment of skin cancers.[1] Nevertheless, there are many issues *vis-à-vis* the use of such external beams to destroy cancer cells in the human body. They are mainly related with the difficulties in focusing them precisely on the cancer locus and their potential of destroying healthy tissues on the penetration pathway and around the targeted cells. The quest of targeting selectively tumoral cells with radiation has brought to a novel way of delivering *in situ* the radiation.

b) Another way, which is what generally targeted radiotherapies imply, is the use pharmaceuticals encapsulating specific radioisotopes, *i.e.* α-particle, β-particle or Auger-electron emitters, to target and destroy specific cells known to be vital for the tumor development.

Since nowadays the differences between cancer cells and normal ones are well understood, scientists can design radiopharmaceuticals that are selective of the affected cells and therefore avoid

the bottlenecks of the use of external ionizing radiation. Therefore, concerning the radiation delivery, targeted radiotherapies are usually considered to be precise techniques. Nevertheless, they do also present a few limitations which will be succinctly discussed in the followings, in the context of a particular targeted radiotherapy, namely the targeted radioimmunotherapy, which is of the widest interest for the ^{211}At radionuclide.

1.1.2 Targeted radioimmunotherapy

The targeted radioimmunotherapy explores the characteristics of both the immune system and radiation to "fight" against cancer cells. In this framework, antibodies are the best candidates as radioisotope carriers to the tumor. They are known to be used by the immune system to target and inhibit specific antigens located either at the tumor surface or inside it. Several issues regarding the choice of the antibodies must be addressed, (i) their selectivity for the targeted antigens, (ii) the possibility of redirection to healthy organs, (iii) the sparse distribution of the antigens on the tumor, and (iv) the capability of the antibodies to penetrate into the tumor. These issues may not be easy to tackle, and, as such, they bring together chemist researchers whose main tasks are to bring proper chemical modifications to the antibodies in order that they fulfill any particular conditions.

The choice of the radionuclide to be linked to the antibody is very important. There are mainly four criteria on which radionuclides are picked-up, three of which emerging from the above paragraphs:

a) emission type

b) energy transfer

c) penetration range

The fourth point that comes into play now is in connection with the radioactive decay rate, *i.e.* the half-life time ($t_{1/2}$) of the radionuclide. As it is actually inherent to the radionuclide, it must be chosen as not too long since it would pose serious safety problems otherwise, as well as not too short since it should allow enough time for the synthesis and delivery. With respect to the emission type, the labeling with α- and β-emitting radionuclides has received a wide attention.[2] A comparison between the two types of particle emitters in light of the aforementioned four criteria is illustrated in Table 1.1, and advantages and disadvantages of using one over the other are pointed out thereafter.

Table 1.1 α- and β-emitting radionuclides for targeted radiotherapies and their general characteristics.

	α-particle emission	β-particle emission
Typical radionuclides	^{213}Bi, ^{212}Bi, ^{211}At, ^{225}Ac, etc.	^{90}Y, ^{131}I, ^{177}Lu, ^{186}Re, ^{212}Pb, etc.
Penetration depth	Short, ~40-100 μm	Long, up to ~600 μm
Energy transfer	High linear energy transfer, ~4.0-8.0 MeV	Sparse energy transfer, ~0.1-2.2 MeV
Energy deposition	Starting at the decay event site	Starting away from the initial event site[2,3]
Half-life times	Usually short, from several minutes to several hours	Usually long, from several hours to several days

The radionuclides decaying through α-emission are not readily used in targeted radioimmunotherapies since most of them require artificial synthesis using cyclotron facilities, unlike the β-emission ones, which are more likely be collected from natural sources. It is possibly the reason why the latter ones show more popularity in the present context.[2,4] The long-range penetration and sparse scattering of the β-particles could be advantageous as well as disadvantageous. It is advantageous whenever the targeted tumor is large enough to capture the sparse emission or whenever the distribution of the antigen receptors at its surface is deficient. It is disadvantageous in the sense that it can be as problematic as using for instance external radiation beams, *i.e.* the difficulty to avoid healthy-tissue damage beyond the targeted cells. Switching to α-particle emitting radionuclides may be promising given their shorter penetration range, and their high linear energy transfer. Also, the energy deposition starting right at the decay event[3] is considered an asset since it makes possible cell destruction starting at the immediate cancerous cell that is connected to the targeted antigen. The $t_{1/2}$ of the currently available α-emitting radionuclides is a factor that hinders the development of efficient targeted alpha immunotherapies over the targeted beta immunotherapies. From this perspective, the promising β-emitter ^{90}Y and the α-emitters ^{212}Bi or ^{213}Bi can be compared, just for the sake of exemplifying. While ^{90}Y has a $t_{1/2}$ of 64.1 hours which is therefore sufficient for synthesis and delivery, ^{212}Bi and ^{213}Bi have $t_{1/2}$ of only 60.0 and 45.7 minutes, respectively.

Considering that the best couples of antibodies and radionuclides have been chosen, the important point yet to be addressed is the linkage between them, *i.e.* the radiolabeling. This step is strongly dependent on the basic chemistry of the desired radionuclide, and it is of extreme

importance since the goal is to achieve an antibody-radionuclide complex with adequate *in vivo* stability. Current radiolabeling protocols usually employ one of the following two strategies:

1. Direct radiolabeling mechanism, *i.e.* direct linkage of the radionuclide to the antibody. A good example is the straightforward iodination with the ^{131}I isotope. Using chemical species as for instance iodine monochloride, ^{131}I can be linked to phenyl rings corresponding to terminal tyrosine groups[5] of antibodies.[2]

2. Radiolabeling *via* a two-step mechanism, *i.e.* typically by involving an *a priori* linkage of the radionuclide to a so called bifunctional chelating agent (BFC).

The second mechanism is usually used to label antibodies with radionuclides exhibiting "metallic" character.[2,4] As the name is suggesting, the BFC has a double functionality, (i) through one functional group it retains the metallic radionuclide and (ii) through the other one, it binds to the antibody. It is worth to underline that there is no universal BFC but rather they do have to be designed accordingly to the chemistry of the radionuclide, *i.e.* its typical coordination number(s), metal-binding character, etc.[2] A good example could be the thiol-containing BFCs that are widely employed for the labeling of antibodies with the almost pure ^{99m}Tc γ-emitter.[4]

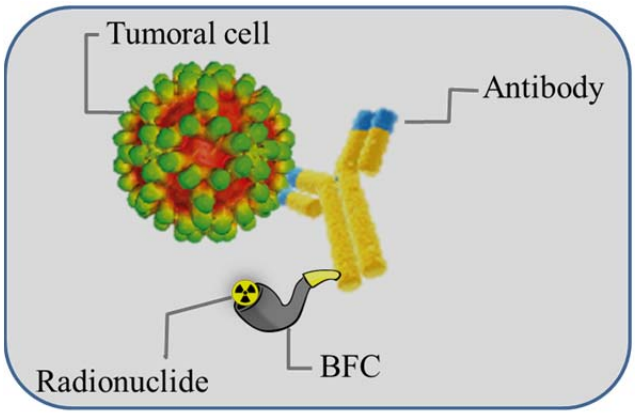

Figure 1.2 General representation of an antibody, linked to a radionuclide through a BFC, and binding to a tumoral cell as expected in targeted radioimmunotherapy.

Admittedly, radiolabeling involving α-emitters are preferential today and govern targeted radioimmunotherapies for small cancer loads or cases where healthy tissues span close proximities. Dealing with small tumors is actually more frequent today, and it will be even more in the near future due to the development of efficient approaches for cancer identification in its early stages. The list of the promising α-emitters is rather short and includes, among the most studied ones ^{212}Bi, ^{213}Bi, ^{223}Ra, ^{211}At and ^{225}Ac.[6] Among these radionuclides, ^{211}At is considered to be the candidate

with the best characteristics for application in targeted alpha-immunotherapy and it has been so far the subject of numerous studies.[7-14]

1.1.3 Production and characteristics of the ^{211}At radionuclide

^{211}At is characterized by a $t_{1/2}$ of 7.2 hours and it is the second longest-living isotope of At, hierarchically between ^{209}At and ^{210}At which have decay times of 5.4 and 8.1 hours, respectively. Among ^{209}At, ^{210}At and ^{211}At, the latter is the only one envisaged for targeted radioimmunotherapies due to its two favorable decay branches, briefly sketched in Fig. 1.3.

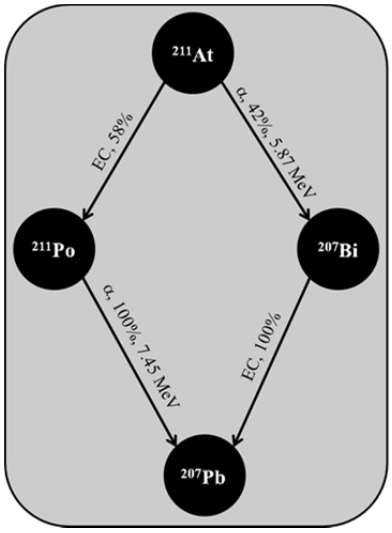

Figure 1.3 Illustration of the two decay branches of ^{211}At. EC stands for electron capture.

On one side, it decays (42%) through α-particle emission (5.87 MeV, tissue penetration range: 50 μm) to ^{207}Bi ($t_{1/2}$ = 31.6 years) which in turn decays (100%) through electron capture to stable ^{207}Pb. Note that through electron capture, a proton-rich nucleus usually absorbs a K-band electron and leads to either X-ray or Auger emissions. On the other side, ^{211}At decays (58%) through electron capture to its ^{211}Po ($t_{1/2}$ = 0.5 seconds) daughter which in turn decays almost instantaneously (100%) through α-particle emission (7.45 MeV, tissue penetration range: 70 μm) to stable ^{207}Pb. As a consequence of the electron capture decay on this second branch, Po K-band X-rays are emitted and offers the great opportunity to detect ^{211}At *via* imaging techniques.[15,16] The ^{211}At isotope can be produced accordingly to the following nuclear reaction:

$$^{209}\text{Bi}(\alpha,2n)^{211}\text{At:} \qquad ^{4}\text{He}^{2+} + ^{209}\text{Bi} \rightarrow ^{211}\text{At} + 2n$$

In practice, using cyclotron facilities, a metallic ^{209}Bi surface, usually deposited on an Al backing plate,[9] is bombarded with an incident α-particle beam with tuned energy, depending on the desired isotope to be produced. In order to achieve the most and purest quantity of ^{211}At, it would be

desirable to tune the incident beam energy between 20 and 29.5 MeV.[9] ^{211}At can then be isolated in two different ways, *i.e.* either solvent extraction[17-19] or dry distillation.[20,21] The latter is in particular performed by ARRONAX scientists and the procedure consists in the distillation of the ^{211}At-^{209}Bi-Al system above 650 °C plus capture of ^{211}At in methanol. Reported ^{211}At extraction yields obtained with this procedure reach about 80%.

In summary, the characteristics that make ^{211}At a promising candidate for targeted alpha-immunotherapy are:

1. Adequate $t_{1/2}$ value of 7.2 hours allowing for synthesis and any other required chemical treatments of the radionuclide, as well as being compatible with the kinetics of various biomolecular systems with potential involvement in the radiolabeling.[9,11]
2. Pure α-particle emission without competing decay mechanisms, with decay branches to suitable daughters. ^{212}Bi, for instance, is known to decay to ^{208}Tl (more than 30%) which in turn yields undesirable high-energy γ-rays.[11]
3. Sufficient α-particle emission energies, 6.8 MeV in average.
4. High and linear-energy transfer averaging 97 keV·μm^{-1}.
5. Short tissue penetration range up to maximum 70 μm.[9,11]
6. "Sufficient" X-rays emission, up to 92 keV, allowing for detection using imaging techniques.[11]
7. Yet reasonable production cost and straightforward production protocols.[9]
8. Diverse chemistry; current radiolabeling protocols involving ^{211}At explore its both metallic and halogenic characters.[9]

Medicinal chemists and oncologists have started to make profit of these good characteristics of ^{211}At to destroy cancer cells in humans for decades. The current obstacle to overcome in order to reach this goal consists in designing either standalone tumor-selective chelating agents capable of binding ^{211}At, or BFCs capable of safely binding ^{211}At. So far, three main strategies have been envisaged for retaining ^{211}At in compounds of medicinal interest; binding it (i) to a C atom, (ii) to a B atom or (iii) to a metal cation.

1.1.4 ^{211}At-labeling *via* At-C bonds

Direct astatination of protein carriers.

Since such an approach has been used for successful attachments of radioiodine to the aryl C atoms of terminal tyrosine residues in antibodies,[2,5] direct electrophilic aromatic substitution

(EAS) with $^{211}At^{+}$ has received wide interest.[22-27] However, retaining the ^{211}At-labeling using this protocol has proven to be problematic: the formed complexes have notably been demonstrated to be highly unstable *in vivo*, presumably due to the rather weak bond formed between At and C/S atoms.[25] It is actually unclear whether ^{211}At is attached to C atoms in tyrosine residues (as sketched in Fig. 1.4a) or not, and several studies suggest that it is actually fixed to S atoms of the cysteine residues. Deastatination may proceed *via* hydrolysis of the formed ^{211}At-S bond.[27] It became clear that ^{211}At must rather be attached to antibodies through BFCs.

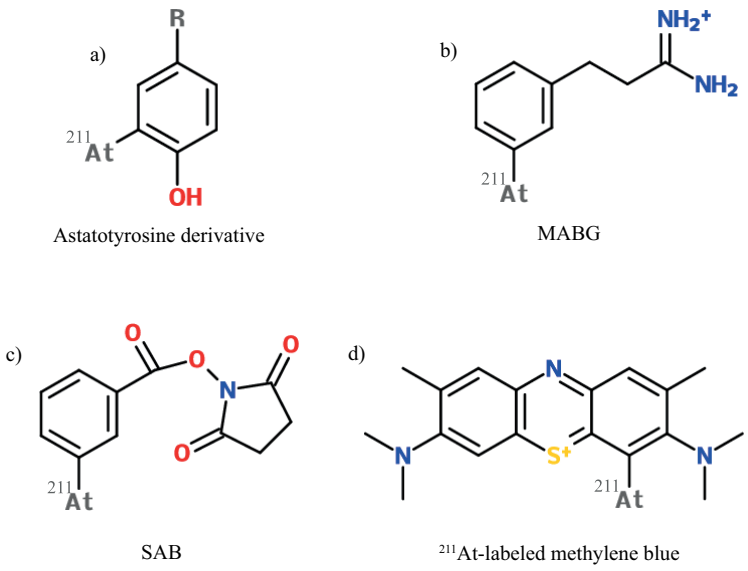

Figure 1.4 Examples of ^{211}At-targeting agents and ^{211}At-BFCs synthesized through EAS using $^{211}At^{+}$ or NAS using $^{211}At^{-}$.

Development of ^{211}At-targeting agents and ^{211}At-BFC bonds.

In order to achieve complexes with adequate stability, plenty of targeting agents and BFCs, retaining the radionuclide *via* an At-C bond have started to be developed. Prior studies[28] focused on measuring bond strengths between halogens and various C atoms have established that At forms stronger bonds with arylic sp^2 ones than with alkylic sp^3 ones. The insertion of ^{211}At on aryl C atoms has been achieved following either EAS using $^{211}At^{+}$ or nucleophilic aromatic substitution (NAS) using $^{211}At^{-}$, following classical protocols that were successfully applied for radioiodine labelings.[10,11,22,29]

The synthesis of complexes through EAS with $^{211}At^{+}$ has been successfully achieved *via* demetallation reactions involving for instance organotin precursors.[30-32] Interesting compounds obtained likewise include astaobenzylguanidine[32] (MABG, Fig. 1.4b) − a targeting agent that binds selectively to neuroblastoma tumors, and succinimidyl astatobenzoate[31] (SAB, Fig. 1.4c) − a ^{211}At-

BFC that has been successfully linked to specific antibodies through the succinimidyl anchor. The labeling of antibodies using SAB is generally achieved through a two-step protocol; in a first step ^{211}At is linked to the BFC, and in the second step the ^{211}At-BFC complex is anchored to the antibodies. The synthesis complexes through NAS with $^{211}At^-$ has been achieved via halogen exchange[33,34] or dediazoniation reactions.[35,36] Interesting compounds obtained through the former procedure include ^{211}At-labeled methylene blue[33] (Fig. 1.4d) − a targeting agent that binds almost exclusively to melanoma tumors.[37]

1.1.5 ^{211}At-labeling *via* At-B bonds

Boron compounds have been successfully used for cancer treatment within the boron neutron capture therapy (BNCT). They generally consist of anionic boron clusters like *closo*-$B_{12}H_{12}^{2-}$, *closo*-$B_{10}H_{10}^{2-}$ or similar clusters where one or two B atoms are substituted by C ones (*closo*-carboran or *nido*-carboran clusters). These compounds can be easily conjugated to targeting agents as antibodies, if they are properly functionalized. Thus, boron clusters are suitable for targeted radioimmunotherapy. Hawthorne and coworkers[38] have started to explore them as potential BFCs for labeling antibodies with radioiodine. Moreover, since the I-B bonds were known to be significantly stronger that the I-C ones, it led to the idea that radioastatinated boron clusters would bring enhanced stability over astato-aryl compounds regarding *in vivo* dehalogenation. Wilbur and coworkers have started to explore the potential of using boron clusters as BFCs for labeling antibodies with ^{211}At.[29,39-42] As such, they have synthesized plenty of ^{211}At-BFCs including among them [^{211}At]*nido*-carboranes (Fig. 1.5a), [^{211}At]bis-*nido*-carboranes (Fig. 1.5b) and [^{211}At][*closo*-decaborates]$^{2-}$ (Fig. 1.5c), functionalized with various groups to strengthen the antibody conjugation.

The antibody conjugation using ^{211}At-BFCs based on boron cluster derivatives as the ones shown in Fig. 1.5, turned out to be much more advantageous over the classic ^{211}At-BFCs retaining the radionuclide through an At-C bond (as for instance SAB, Fig. 1.4c). Due to the high affinity of ^{211}At for B atoms, the reaction with electrophilic ^{211}At leads unequivocally to a B atom labeling in the electron rich boron cage. This makes this radiolabeling approach a one-step approach as the boron cages can be conjugated to antibodies beforehand.

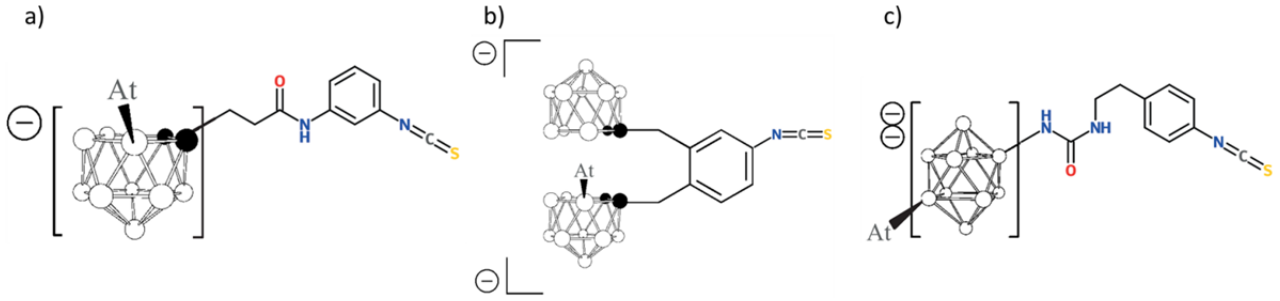

Figure 1.5 Examples of astatinated and functionalized boron clusters, a) a *nido*-carborane derivative, b) a bis-*nido*-carborane derivative and c) a *closo*-decaborate derivative. Filled circles stand for C atoms while empty ones stand for B atoms.

1.1.6 ^{211}At-labeling *via* At-metal cation bonds

More recently, and in parallel with the work of D. S. Wilbur and coworkers on boron clusters, a novel strategy to retain ^{211}At in stable complexes started to be pursued by M. Pruszyński *et al.*[43-45] The original idea is to attach an astatide anion to metal cations, which are themselves chelated by BFCs, assuming, as usually done in this field, that At bears similar properties as I. That is, extrapolating from I^-, it was hypothesized that At^- would have as well soft anion properties and the strongest interactions accordingly to the hard and soft acids and bases (HSAB) theory of Pearson[46,47] would be with soft metal cations. M. Pruszyński has notably reported[43,44] the complexation of $^{211}At^-$ with soft d^6 low-spin Rh^{III} and Ir^{III} metal cations retained on a thioether chelating agent, which could form the basis for a BFC (see Fig. 1.6).

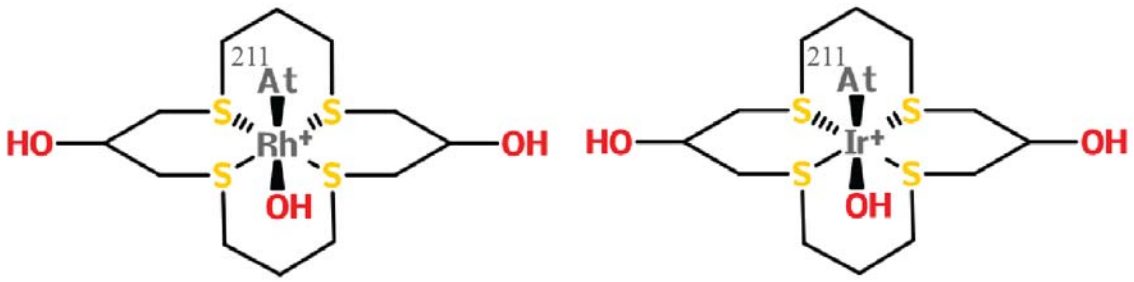

Figure 1.6 Examples of stable complexes with $^{211}At^-$ attached to Rh^{III} and Ir^{III} soft metal cations.

1.1.7 *In vivo* stability of ^{211}At-labeled complexes

The synthesis of ^{211}At-based complexes with adequate *in vivo* stability is a very important step for targeted radiotherapy. Yet, most of the ^{211}At complexes obtained through one of the aforementioned methods, which are nevertheless stable *in vitro*, are either unstable or showing limited *in vivo* stability.[8,10,22,40] As a consequence, undesired detection of free ^{211}At has been reported in healthy spleen, lungs, thyroid, liver, stomach, kidneys, etc., when studies are performed for instance on mice or monkeys. Even though it is not properly confirmed, in most cases it is

considered that the released form is astatide, $^{211}At^-$, while deastatination causes are either unknown or vary from one labeled agent to another. Some authors consider that deastatination possibly occurs due to the, yet not fully clear, halogenic-metallic dual behavior of At.[48] For instance, $^{211}At^-$ undergoes *in vivo* oxidation to $^{211}At^+$ and the latter is complexed and distributed to unspecific targets. More generally, the cause of deastatination is considered to be the rather weak character of the bond through which ^{211}At is retained. Binding it to aryl C atoms of the tyrosine residues in antibodies, through direct electrophilic substitution, leads to quite unstable complexes. The synthesis of *in vivo* stable ^{211}At-labeled antibodies by using BFCs retaining the radionuclide *via* a bond with an aryl C atom has culminated with the synthesis of SAB (Fig. 1.4c). While it had shown *a priori* efficient *in vitro* and *in vivo* stability, clinical trials with SAB have been attempted.[49] However the outcomes were unsatisfactory since, to some extent, deastatination had occurred. The fast metabolization may cause the deastatination for small-weight ^{211}At-labeled biomolecules,[50] and the weak character of the At-C(aryl) bonds can be invoked otherwise.[51] The assumption of D. S. Wilbur and coworkers that retaining ^{211}At *via* an At-B bond would lead to more stable complexes toward *in vivo* deastatination turned out in practice to be valid.[39-41] The synthesis of astatinated *closo*-decaborate derivatives (Fig. 1.5c) currently corresponds to the milestone of this strategy.[42] Lastly, labeling antibodies with ^{211}At via BFCs which bind the radionuclide *via* a soft metal cation is the subject of currently ongoing studies. Nevertheless, initial studies of M. Pruszyński on the stability of the complexes displayed on Fig. 1.6, have shown that *in vivo* deastatination can still occur to some extent.[44]

1.1.8 Outlook

Unfortunately, targeted radiotherapies involving the various ^{211}At-agents that were synthesized so far resume to significant *in vivo* deastatination. Certainly, retaining the radionuclide on the targeting agent through the strongest possible bond may turn out to be a good strategy but probably not a requirement. To succeed in this quest one must understand as much as possible the physico-chemical behavior of At in various molecular contexts and environmental conditions. As explained previously, all the radiolabeling protocols with ^{211}At are derived from the ones with radioiodine under the assumption that these heavier halogens have similar properties. Given the current failures, this assumption is perhaps unreliable. On the other side, developing ^{211}At-agents based on the standalone properties of At is currently not possible since, as concluded by D. S. Wilbur in Nature Chemistry,[7] "in the quest to produce targeted therapeutics for treatment of cancer and other diseases, many of the basic chemical studies with ^{211}At have unfortunately been set aside." The time has come to carefully pursue investigating basic chemistry of astatine, which may

contribute to identify alternative approaches for the development of original ^{211}At-labeled agents with suitable *in vivo* stability and pharmacokinetics.

1.2 The chemical perspective

At is undoubtedly a member of the halogen group that features both the halogenic and kind of a metallic behavior. From a chemist point of view, the difficulties encountered with the current application envisaged for At may be solved by focusing on the following points:

1. identifying the chemical forms of At that can exist in the experimental conditions used for the labeling,
2. studying as many reactions as possible involving identified species of At, including potential candidates for the labeling,
3. and/or rationalizing reactivity trends by exploring the nature of bonds in which At is involved.

1.2.1 Identifying At chemical forms

Identifying At chemical forms has proven to be a difficult task over the years and gave rise to several antithetic studies.[19,52,53] It deals in particular with establishing the oxidation degrees of At in different environmental conditions, *i.e.* pH and redox conditions, so that one can proceed in a more straightforward way with the assessment of its reactivity toward other chemical species. Mapping the predominant At species as a function of both the pH and the redox potential (E) of a given media, carries out the name of the Pourbaix diagram, or speciation diagram, of At. The knowledge of this diagram is of particular importance for the development of targeted radioimmunotherapies based on ^{211}At, since it determines the type of chemistry to be applied for the synthesis of targeting agents, and for controlling their *in vivo* behavior. The research teams at SUBATECH and CEISAM laboratories have been focusing in the last decade to rigorously establish the Pourbaix diagram of At. That is, to identify (i) what species of At actually exist, and (ii) what is their E-pH domain of predominance. For this, analytical chemistry methods able to deliver information on samples containing ultra-trace atomic concentrations of At (10^{-8} to 10^{-13} mol·L^{-1}), are necessary. Competition and high pressure ion exchange chromatography (HPIEC) have been the methods of choice for this over the years.[18,19,54-56]

Through competition experiments, the distribution of given sets of At species is studied in a biphasic system. If the latter consists of two liquids, then the method is classified as liquid-liquid

competition (LLC), while if it consists of a solid and a liquid, then the method is classified as solid-liquid competition (SLC). If a change in the experimental conditions causes a change in the At speciation, then the distribution coefficient between the two phases may change. However, if a change in the distribution coefficient is observed, it must indicate a speciation change. In a typical LLC-based experiment[19] aiming at studying the At speciation, a liquid and an organic phase (usually toluene) are initially brought to equilibrium. Then, after the astatine sample is added and the equilibrium partition between the two phases is achieved, the distribution coefficient (D) is calculated as:

$$D = \frac{V_{aq} \times A_{org}}{V_{org} \times A_{aq}} \quad (1.1)$$

where V_{aq} and V_{org} stand for the volumes of the aqueous and organic phases while A_{aq} and A_{org}, for the measured radioactivities in the respective phases.

In a typical HPIEC-based experiment, a buffer (eluent) which contains the desired media and the At sample is injected through a column consisting in a cationic or anionic exchange resin.[54,56] The column is coupled with two types of detectors: (i) an UV detector which produces chromatogram signals due to the elution of the organic or inorganic species present in the eluent, and (ii) a γ-detector which produces radiochromatogram signals due to the elution of the species that contain only ^{211}At. Depending on the buffer flow rate and the affinity of the At species formed (let say, species A) in the prepared media, for the exchange resin in the column, the radiochromatogram signal appears after a certain time. This time is defined as the retention time (t_R) of the species A. The data are usually presented in terms of the retention factor (k), which is calculated according to the following relation:

$$k = \frac{t_R - t_D}{t_D} \quad (1.2)$$

where t_D corresponds to the dead time, and is defined as the initial time needed for a species to pass through the column while not interacting with it. If changing the conditions during an HPIEC experiment causes changes in the radiochromatogram signal, *i.e.* in the retention time, then a change in the speciation of At may have occurred. Usually, a plot showing the correlation between the retention factor of the At species and, let say, the concentration of the media in the eluent,[54] is compared with a similar one of a model species (or etalon), *e.g.* if At^- is under study then it can be compared with the one of I^- or, if AtO^+ is under study, then it can be compared with the one of Tl^+

etc. This strategy can help in determining for instance the charge of the At species under study, which is of crucial importance for species identification.

Competition and HPIEC experiments are complementary and both can be performed in order to retrieve information on the At species charges or on the number of exchanged protons that may occur upon changing the experimental conditions. In most cases, there is a need to perform quantum mechanical calculations in order to help in analyzing the experimental outcomes. Combining these three methodologies, Champion and coworkers have successfully determined[19,54] parts of the Pourbaix diagram of At in non-complexing aqueous media (see Fig. 1.7).

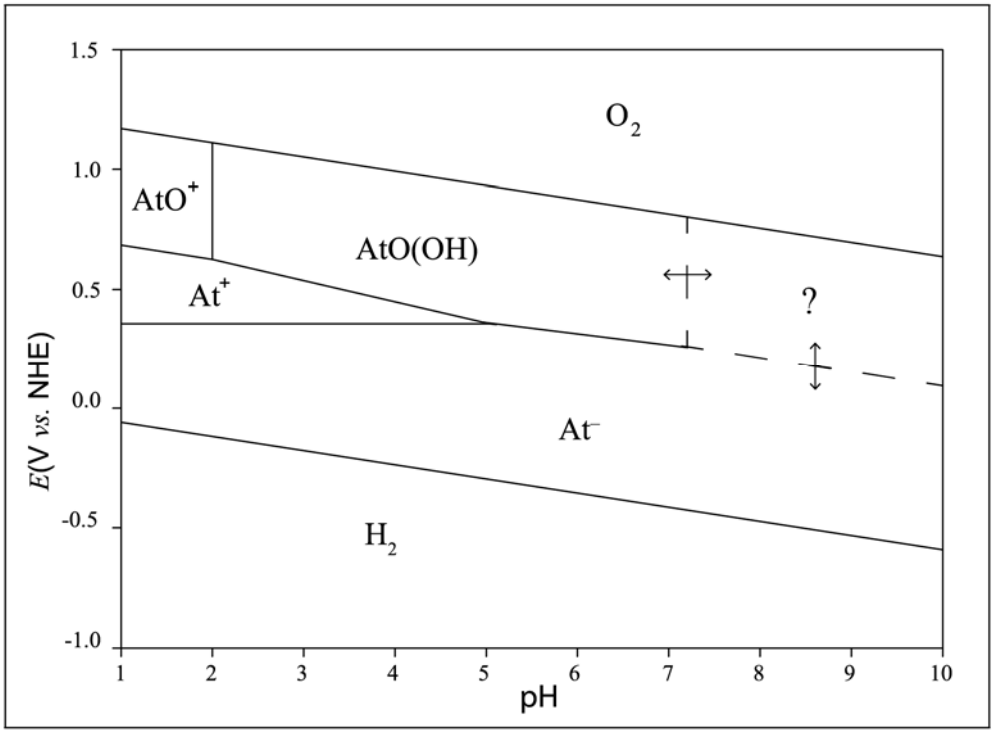

Figure 1.7 Pourbaix diagram of At in aqueous and non-complexing media built from the information that was available at the beginning of this project.

This diagram reveals the "chameleonic" character of At, which bears similarities with lighter halogens as well as having predominant cationic forms, as metals. In strong acidic conditions and in the range of potentials where the water is stable, Champion *et. al* confirmed[19] that At can have three oxidation states. At first, in reducing conditions, At was found to exist in the oxidation state of −I as At^-, in line with the trend shown by other halogens. When the redox potential is increased, two cationic species were thereafter identified and rigorously confirmed to be At^+ and AtO^+, *i.e.* in which At has the oxidation states of +I and +III, respectively. Toward weak acidic pH domain and while maintaining oxidizing conditions, Champion *et al.* have identified[54] the presence of a neutral species, starting at pH~2 and spanning the area supposedly up to neutral pH. This species has been

consistently proven to be the first hydrolysis product of AtO^+, AtO(OH), through the help of quantum mechanical calculations.[54] Increasing the pH toward basic conditions, the At^- species is assumed to exist while reducing conditions are maintained. This assumption is made from the analogy with I^-, combined with some electromobility experiments[57] that support a negatively charged At species. At^- may indeed be this species, but however, it is not yet known if it spans the whole potential range of water stability, in both reducing and oxidizing conditions. Discerning this information is rather important for the current radiolabeling protocols. Indeed, concentrated NaOH solutions are currently the preferred media for the extraction of cyclotron-produced ^{211}At *via* "wet chemistry" processes.[42,58-60] But it would not be sufficient to simply consider a basic medium if At^- is meant to react *via* nucleophilic substitution.

1.2.2 Studying reactions involving At species

Assessing the reactivity of At chemical forms toward different chemical species and identifying the reaction products has proven to be a difficult task over the past and recent years. In 1966, E. H. Appleman has reported the first and so far the last study concerning a direct identification of At species through time-of-flight mass spectrometry.[61] Among a few organic compounds, he successfully identified the interhalogen diatomics AtCl, AtBr and AtI, and offered a first solid argument for the existence of At in the oxidation state of +I and its reactivity toward other halogens. More generally, chemists have explored different experimental methodologies in order to obtain indirect proofs of At species participating to chemical reactions.[18,54,55]

In the context of the collaboration between the SUBATECH and CEISAM laboratories, identifying if a given At species participates to a chemical reaction is done through the measurement of the reaction equilibrium constant. The identification of the reaction product(s), if there are any uncertainties, is achieved through the comparison of quantum mechanical calculations and experiment outcomes. Champion and coworkers have employed competition experiments to study the distribution of a given At species in a biphasic system, this time as a function of the concentration of a complexing ligand.[55] The reactivity of the cationic forms At^+ and AtO^+ has been in particular studied. Briefly, the reactions involving these species would have the form:

$$At(x)^+ + mX^- \overset{\beta_m}{\rightleftharpoons} At(x)X_m^{1-m} \qquad (1.3)$$

where $At(x)^+$ stands for At^+ or AtO^+, X stands for the ligand and $At(x)X_m^{1-m}$ for the formed product. Naturally, the corresponding equilibrium constant, β_m, is written as:

$$\beta_m = \frac{A_{\mathrm{At(x)X}_m^{1-m}}}{A_{\mathrm{At(x)}^+}(A_{\mathrm{X}^-})^m} \quad (1.4)$$

The distribution coefficient in a biphasic system, let say *D* in the case of an LLC-based experiment, as a function of the ligand concentration [X^-], can be expressed as:

$$D = \frac{D_0}{1 + \sum_m \beta_m [\mathrm{X}^-]^m} \quad (1.5)$$

where D_0 is the distribution coefficient in the absence of any complexing ligand.

Following this strategy, Champion *et al.* have studied reactions in aqueous solutions between the $At(x)^+$ species and some inorganic ligands as Cl^-, Br^- and SCN^-, with different 1:1 and 1:2 stoichiometries.[55] The results pointed out that, in the framework of HSAB, metallic At appears to have a soft character. That is, the equilibrium constants were found higher with the Br^- and SCN^- soft bases than the ones with the Cl^- hard base. On the other hand, as the measured β_m values have proven to be in good agreement with existing data reported in the literature and with outcomes from quantum mechanical calculations, the possibility of using such competition experiments to study the reactivity of At was established in this work.

In the framework of a previous PhD thesis[62] centered on the further exploration of the "metallic" character of At, F. Bassal has studied the reactivity of AtO^+ with several model species based on S, O and N heteroatoms. The motivation was quite obvious since (i) the AtO^+ species may be regarded as a possible candidate for the radiolabeling, and (ii) most of the chelating agents are functionalized using S, O and N heteroatoms. A goal of the study was to identify possible ligands toward which AtO^+ is reactive and to classify the stability of the formed products. The study has been carried out mainly by means of quantum mechanical calculations, following previously established procedures. Nevertheless, when available, the comparison with the experimental data has shown a very good agreement. It was identified that AtO^+ reacts as an electrophile and binds in the most stable complexes (i) through its At atom with acyclic O- or N-based species, (ii) through its O atom with acyclic S-based species, and (iii) through its O atom with S, O and N aromatic heterocycles. Notably, weak interactions have been obtained for neutral O-based ligands, pointing out the least interest of using them as potential targeting agents or BFCs in eventual labelings with AtO^+. On the other side, the greater stability constants were obtained notably for the reactions between AtO^+ and N-based aromatic heterocycles. In such cases, the charge delocalization seems to play an important role and enhance the stability of the species formed with AtO^+. These findings

show that AtO^+ follows the trend of At^+ which forms as well much more stable At-C(aryl) bonds than At-C(alkyl) ones.[63,64]

Given the interest of D. S. Wilbur and coworkers in attaching At to B atoms, F. Bassal has studied as well the reactivity of AtO^+ toward various boron clusters, assuming that the reaction proceeds through electrophilic addition, *i.e.* without the elimination of a proton. Studying a series of *closo*-carborates and *closo*-borates, he has reported that AtO^+ binds covalently, through the O atom, to the most nucleophilic B atoms of the clusters, leading *a priori* to very stable complexes. Some calculated addition equilibrium constants related to such kind of reactions, *i.e.* between AtO^+ and boron clusters, were reported to reach even 10^{20}. This may seem to be in line with the assumption of Wilbur and coworkers that At or At species may have a greater affinity for B than for C atoms.[40,63] F. Bassal suggests that the less aromatic *closo*-borate derivatives are the ones that tend to form the most stable complexes, and they could be explored as potential targeting agents or BFCs in eventual labelings involving AtO^+.

1.2.3 Outlook: studying bonding schemes involving the At atom?

Clearly, to help the development of innovative ^{211}At-agents with suitable *in vivo* stability, there is an interest in acquiring knowledge on the At reactivity. Studying reactions of At or At species with as many chemical species as possible and quantifying the stability of the eventually formed complexes could lead to the derivation of useful trends and rationales. Nevertheless there are constraints in proceeding in this way. On one side, the direct identification of reaction products containing At, using standard spectroscopic tools, as nuclear magnetic resonance, or spectrometry tools, as mass spectrometry, is definitely not possible (experimental samples contain only ultra-trace concentrations of At, usually about 10^{-10} mol·L^{-1}). On the other side, there are only a few cyclotrons in the world having the beam capacities for producing At, *i.e.* accelerating incident α-beams up to ~30 MeV. In a study made by M. R. Zalutsky and M. Pruszynski,[9] the number of such cyclotrons is meant to be about 36, out of which about 10 of them produce At on a routine basis. Competition and HPIEC experiments can be used to retrieve useful indirect information concerning the formation of At species and their stabilities. However, in some cases the outcomes can suffer from large uncertainties and sometimes the information complies with more than a single hypothesis making the analysis somehow ambiguous if not impossible.

Alternatively, predicting reactivity trends may be possible by understanding the nature of the chemical bonds formed by At in various molecular contexts. However, based only on the currently available experimental data, not only that the bonding schemes in which At is involved

cannot be rationalized, but it seems that we also do not have a reasonable chemical intuition. Clearly, there is a need for predictive calculations, not only for the identification of adducts of reactions between ligands and stable chemical forms of At. It is possible to distinguish the different contributions that rule the formation of bonds involving At by means of quantum mechanical studies, which definitely play an important role in the field of At chemistry.

1.3 The quantum chemical perspective

Theoretical calculations based on quantum mechanical principles are nowadays performed almost routinely by computational chemists to understand, rationalize and even predict various properties concerning atoms, molecules and chemical reactions. From a quantum mechanical perspective, At is regarded as a heavy main-group element and its computational treatment requires the inclusion of relativistic effects, in particular the scalar relativistic ones and the so-called spin-orbit coupling (SOC). The former ones essentially cause corrections to the one-electron energies due to the mass-velocity dependence of electrons spinning close to heavy nuclei. They typically lead to the contraction and the stabilization of the *s* and *p* atomic orbitals and the expansion and destabilization of the *d* and *f* ones. The latter one, SOC, causes of course further energy corrections and also changes in the ground-state wave function due to the effective interaction between the spin of the electrons and the magnetic field induced by their motion around the nuclei. Many computational methodologies have been developed in order to deal with relativistic effects through one way or another, and they will be discussed in details in the next chapter.

In the context of At research computational studies are particularly attractive as they may help in interpreting experimental data and also lead to reasonable predictions. Performing such studies on At species is certainly not routine owing (i) to peculiarities in their electronic structures arising from relativistic effects, (ii) to bottlenecks in the current computational strategies that can deal efficiently with the various electronic and environmental effects, *i.e.* relativistic effects, electron correlation, solvation etc., and (iii) to some extent, the lack of experimental data and reference high-level theoretical results to validate the choice of an employed computational strategy. A computational chemist must understand *a priori* the basic signatures of At species electronic structures in order to select appropriate levels of theory to study bonding schemes in which the At atom is involved, or to predict relevant observables in the context of experimental investigations.

1.3.1 Electronic structure signatures of At compounds

The electronic structure of atomic At spans 85 electrons up to the 6*p* shell, $[Xe]4f^{14}5d^{10}6s^{2}6p^{5}$, and corresponds to a spin-doublet ground-state multiplicity, ^{2}P, in the spin-orbit free (SOF) formalism. Relativistic effects are known to cause significant changes. Regarding the valence shells, the scalar relativistic ones over-stabilize and contract the 6*s* orbital of At, making it kind of semi-core orbital. For some neighboring elements of At, *e.g.* Hg, Tl or Pb, the 6*s* stabilization is so strong that it becomes inert, causing in this way unexpected chemistries.[65,66] Due to SOC, the valence 6*p* shell of At splits into two spinors, denoted accordingly to the total angular momentum as $6p_{1/2}$ and $6p_{3/2}$. Accordingly, the fine electronic structure of the 6*p* shell reads the non-degenerate $^{2}P_{3/2}$ and the $^{2}P_{1/2}$ terms, the former one actually corresponding to the SOC ground-state of At. The $^{2}P_{1/2}\leftarrow{}^{2}P_{3/2}$ zero-field splitting has yet not been determined through experiment while theoretical calculations predict large values between 2.45 and 2.89 eV, depending on the level of theory that is employed (2.89 eV being considered as a "reference" value).[67] The first ionization potential of At (IP_1) is 9.32 eV, as recently measured by Rothe and coworkers.[68] On the other side, the electron affinity of At (EA) has yet not been measured through experiment while computational studies predict values between 2.20 and 3.21 eV.[69-72] This unknown variable hinders the proper definition of the electronegativity (χ) of this element, which currently is assumed to be similar (or even smaller than) the one of H, *i.e.* 2.2 on the revised Pauling scale.[73]

1.3.2 Characteristics of the chemical bond involving the At atom

Not much is known on the bonding schemes involving At. Over the years, only a few of its species have been deeply studied so far, *e.g.* HAt and At_2. The interest of computational chemists for them was mainly to study the influence of relativistic effects in heavy-atom systems, or to test new developments in various relativistic codes. While these two systems put forth the proclivity of At for certain bonding types, they deserve being quoted here in some detail. In both systems, relativistic effects have proven to tremendously affect the bonding pictures. While bond contractions occur in many heavy-atom systems (due to the relativistic contraction of the *s* and $p_{1/2}$ valence shells),[66] bond expansions occur in both the HAt and At_2 systems, meaning that relativistic effects weaken the chemical bond. Admittedly, a dominant contribution to this behavior is brought by SOC, which turns out to be as much as important as the electron correlation, or even more.[55,67,74] Pioneering works of Gomes *et al.*[75] and Saue *et al.*[76] on HAt, have proven that the equilibrium bond length (r_e) is shortened by about 0.022 Å under scalar relativistic effects, while it lengthens by about 0.029 Å under the effect of SOC. The trend in these numbers is understood as (i) the 6*p* and

the 6*s* atomic orbitals of At contract under the scalar relativistic effects, and allow the 1*s* orbital of H to approach much closer, and (ii) the σ^* antibonding orbital mixes under the effect of SOC with the nonbonding π orbitals of At which causes a bond lengthening. The case of At_2 is much more spectacular than the one of HAt. Pioneering work on this system has been reported by Visscher and Dyall in the 90's. They have analyzed the influence of relativistic effects in the halogen diatomics,[77] and found that they manifest by strongly destabilizing the chemical bond in At_2. Surprisingly, in this system they cause an r_e lengthening of about 5%, reduction of the ω_e by about 40% and reduction of the D_e by about 200%, which is actually more than the value of the D_e itself. The role of relativistic effects on the bond destabilization in At_2 has been well rationalized from complementary viewpoints over the years. The latest explanation has been built around the concept of the effective bond-order (EBO), arising from spin-orbit coupled multiconfigurational wave-functions.[67] In the scalar relativistic limit, it was found that the ground-state wave-function of At_2 is essentially described by the $\sigma_g^2\pi_u^4\pi_g^{*4}\sigma_u^{*0}$ configuration, the bond order (BO) of such configuration being 1. Under the effect of SOC, it turned out that this ground-state configuration is mixed with excited ones having less σ bonding character, in particular the $\sigma_g^2\pi_u^3\pi_g^{*4}\sigma_u^{*1}$ ones (BO = 0). This mixing leads in At_2 to a SOC ground-state that is less bonding (EBO ~ 0.7) than in the single reference, scalar relativistic limit.

The bond in HAt has been described by Saue *et al.* as having covalent character based on the nearly zero calculated dipole moment (0.06 D), with a slightly negatively charged H atom.[76] More recently, the covalent character of the bond in HAt has been confirmed by Pilmé and coworkers using the quantum theory of atoms in molecules (QTAIM) and the topological analysis of the electronic localization function (ELF).[74] They have questioned as well the covalent character of the chemical bond in At_2.[74,78] The authors have identified that the electron occupancy of the bonding basin is nearly one electron in the absence of SOC. Under the effect of SOC, its occupancy drops to about half an electron putting forth again the tremendous impact of this relativistic effect on the chemical bonding in At_2. In fact, while the occupancy of the bonding basin is decreased by SOC, the authors have identified that the π population of the non-bonding basins of the two At atoms is increased. That is, accordingly to their results, SOC weakens the chemical bond in At_2 by withdrawing electronic population from the bonding basin and redistributing it among the valence π system in lone pair regions. Based on the trend shown by the inferior homonuclear dihalogens and some computed properties at the bond critical point (depleted density, small and positive density Laplacian), Pilmé and coworkers argued for the charge-shift (CS) bonding type in At_2. That is, the

bond energy in At_2 is governed by the fluctuation of the electron pair density between the two limit ionic forms.

While investigating several other types of bonds involving At, Pilmé and coworkers found that the same CS type of bonding appears in the AtX (X = Cl, Br, and I) species and to some extent in the At–CH_3 one, but not for instance in the aforementioned AtH species or the At–BH_2 one which were found to be characterized by covalent bonding.[74] Studying the bonding schemes involving At and C- or B-containing molecules is actually important for the labeling process. But the sole study of the At–BH_2 and At–CH_3 systems does not allow drawing general conclusions.[63,64] Definitely, there is a need for further theoretical investigations in this context.

Describing the bonding schemes involving At certainly requires theoretical methods beyond Hartree-Fock (HF). Perhaps, most desirable is to use (approximate) relativistic DFT due to its computational expediency and implicit inclusion of electron correlation. This methodology has been so far successfully applied to investigate At species and actually favored "ground-breaking" advancements on the research of the basic chemistry of At.[19,55,74,78] However, its application is limited to At species that feature essentially single configurational ground-states. Using two-step multiconfigurational methods to study bonding schemes involving At shows some conveniences. Beside that they can obviously deal with the eventual multiconfigurational character of the studied electronic states, while including adjustable amounts of electron correlation, they provide a picture of the bonding scheme in terms of a set of SOF states. These states can be coupled *a posteriori* in a cost-effective fashion *via* a SOC operator to account for the effects of SOC. This obviously supplies the computational chemist with a SOC bonding scheme which can be easily expressed in terms of the SOF one, by just interpreting the SOC-perturbed wave functions. Moreover, distinguishing between the influence of electron correlation and SOC on the chemical bond becomes easy since these effects are treated in two different steps. The bonding scheme in At_2 has been investigated using such a methodology.[67] The SOC has been shown to reduce the covalent character of the chemical bond to a significantly much more extent than electron correlation, putting forth the fact that this effect can indeed play a much more important role on the chemical bonding involving At. It is therefore of an extreme importance to treat both electron correlation and relativistic effects at adequate levels of theory in order to address correctly the bonding schemes and other properties of At systems.

1.3.3 Outlook: quantum mechanical calculations for research on At compounds

Trials to destroy cancer cells with currently synthesized ^{211}At-agents are not yet fully satisfactory, on one hand due to the weak character of the bond through which At is retained and on the other hand due to the limited knowledge of the basic chemistry of At and the reactivity of its species. Undoubtedly, with quantum mechanical calculations we are able to unravel bonding patterns that involve the At atom in different molecular contexts. This would certainly help medicinal chemist to design new and ground-breaking ^{211}At-agents that retain the radionuclide through a bond having adequate stability. Moreover, the knowledge on the bonding schemes involving At or At-species that can exist in given conditions would certainly help. In the above paragraphs it has been shown that computational studies can provide insights in both aspects.

Bibliography:

1. R. Morrison, *Proc. R. Soc. Med.* Electron beam therapy, **1965**, 58, 160.
2. D. E. Milenic, E. D. Brady, M. W. Brechbiel, *Nat. Rev. Drug. Discov.* Antibody-targeted radiation cancer therapy, **2004**, 3, 488.
3. J. L. Humm, *J. Nucl. Med.* Dosimetric aspects of radiolabeled antibodies for tumor therapy, **1986**, 27, 1490.
4. S. Liu, *Adv. Drug. Deliv. Rev.* Bifunctional coupling agents for radiolabeling of biomolecules and target-specific delivery of metallic radionuclides, **2008**, 60, 1347.
5. E. Hallaba, H. El-Asrag, Y. Abou Zeid, *Int. J. Appl. Radiat. Isot.* ^{131}I-labelling of tyrosine by iodine monochloride, **1970**, 21, 107.
6. R. M. McDevitt, G. Sgouros, D. R. Finn, L. J. Humm, G. J. Jurcic, M. S. Larson, A. D. Scheinberg, *Eur. J. Nucl. Med.* Radioimmunotherapy with alpha-emitting nuclides, **1998**, 25, 1341.
7. D. S. Wilbur, *Nat. Chem.* Enigmatic astatine, **2013**, 5, 246.
8. D. S. Wilbur, *Curr. Radiopharm.* [^{211}At] astatine-labeled compound stability: issues with released [^{211}At] astatide and development of labeling reagents to increase stability, **2008**, 1, 144.
9. M. R. Zalutsky, M. Pruszynski, *Curr. Radiopharm.* Astatine-211: production and availability, **2011**, 4, 177.
10. G. Vaidyanathan, M. R. Zalutsky, *Curr. Radiopharm.* Astatine radiopharmaceuticals: prospects and problems, **2008**, 1, 177.
11. M. R. Zalutsky, G. Vaidyanathan, *Curr. Radiopharm. Des.* Astatine-211-labeled radiotherapeutics an emerging approach to targeted alpha-particle radiotherapy, **2000**, 6, 1433.
12. G. Vaidyanathan, M. R. Zalutsky, *Phys. Med. Biol.* Targeted therapy using alpha emitters, **1996**, 41, 1915.
13. R. H. Larsen, B. W. Wieland, M. R. Zalutsky, *Appl. Radiat. Isot.* Evaluation of an internal cyclotron target for the production of ^{211}At via the ^{209}Bi (α, 2n) ^{211}At reaction, **1996**, 47, 135.
14. O. Lebeda, R. Jiran, J. Ráliš, J. Štursa, *Appl. Radiat. Isot.* A new internal target system for production of ^{211}At on the cyclotron U-120M, **2005**, 63, 49.
15. T. G. Turkington, M. R. Zalutsky, R. J. Jaszczak, P. K. Garg, G. Vaidyanathan, R. E. Coleman, *Phys. Med. Biol.* Measuring astatine-211 distributions with SPECT, **1993**, 38, 1121.
16. E. L. Johnson, T. G. Turkington, R. J. Jaszczak, D. R. Gilland, G. Vaidyanathan, K. L. Greer, R. E. Coleman, M. R. Zalutsky, *Nucl. Med. Biol.* Quantitation of ^{211}At in small volumes for evaluation of targeted radiotherapy in animal models, **1995**, 22, 45.
17. A. T. Yordanov, O. Pozzi, S. Carlin, G. Akabani, B. Wieland, M. R. Zalutsky, *J. Radioanal. Nucl. Chem.* Wet harvesting of no-carrier-added ^{211}At from an irradiated ^{209}Bi target for radiopharmaceutical applications, **2004**, 262, 593.
18. J. Champion, C. Alliot, S. Huclier, D. Deniaud, Z. Asfari, G. Montavon, *Inorg. Chim. Acta.* Determination of stability constants between complexing agents and At(I) and At(III) species present at ultra-trace concentrations, **2009**, 362, 2654.
19. J. Champion, C. Alliot, E. Renault, B. M. Mokili, M. Chérel, N. Galland, G. Montavon, *J. Phys. Chem. A.* Astatine standard redox potentials and speciation in acidic medium, **2010**, 114, 576.
20. S. Lindegren, T. Bäck, H. J. Jensen, *Appl. Radiat. Isot.* Dry-distillation of astatine-211 from irradiated bismuth targets: a time-saving procedure with high recovery yields, **2001**, 55, 157.

21. M. R. Zalutsky, X.-G. Zhao, K. L. Alston, D. Bigner, *J. Nucl. Med.* High-level production of α-particle–emitting ^{211}At and preparation of ^{211}At-labeled antibodies for clinical use, **2001**, 42, 1508.
22. F. Guérard, J.-F. Gestin, M. W. Brechbiel, *Cancer Biother. Radiopharm.* Production of [^{211}At]-Astatinated radiopharmaceuticals and applications in targeted α-particle therapy, **2013**, 28, 1.
23. Y. V. Norseyev, D. D. Nhan, V. A. Khalkin, N. Q. Huan, L. Vasaros, *J. Radioanal. Nucl. Chem.* The preparation of astatine labelled tyrosine using an electrophilic reaction, **1985**, 94, 185.
24. C. Aaij, W. R. J. M. Tschroots, L. Lindner, T. E. W. Feltkamp, *Int. J. Appl. Radiat. Isot.* The preparation of astatine labelled proteins, **1975**, 26, 25.
25. A. T. M. Vaughan, J. H. Fremlin, *Int. J. Nucl. Med. Biol.* The preparation of astatine labelled proteins using an electrophilic reaction, **1978**, 5, 229.
26. A. T. M. Vaughan, J. H. Fremlin, *Int. J. Appl. Radiat. Isot.* The preparation of astatotyrosine, **1977**, 28, 595.
27. G. W. M. Visser, E. L. Diemer, F. M. Kaspersen, *Int. J. Appl. Radiat. Isot.* The nature of the astatine-protein bond, **1981**, 32, 905.
28. H. H. Coenen, S. M. Moerlein, G. Stöcklin, *Radiochim. Acta.* No-carrier-added radiohalogenation methods with heavy halogens, **1983**, 34, 47.
29. D. S. Wilbur, *Bioconjugate Chem.* Radiohalogenation of proteins: An overview of radionuclides, labeling methods and reagents for conjugate labeling, **1992**, 3, 433.
30. P. K. Garg, C. S. John, M. R. Zalutsky, *Nucl. Med. Biol.* Preparation and preliminary evaluation of 4-[^{211}At]astato-N-piperidinoethyl benzamide, **1995**, 22, 467.
31. A. S. Narula, M. R. Zalutsky, *Radiochim. Acta.* No-carrier-added astatination of N-succinimidyl-3-(tri-n-butylstannyl) benzoate (ATE) via electrophilic destannylation, **1989**, 47, 131.
32. G. Vaidyanathan, D. J. Affleck, K. L. Alston, X.-G. Zhao, M. Hens, D. H. Hunter, J. Babich, M. R. Zalutsky, *Bioorg. Med. Chem.* A kit method for the high level synthesis of [^{211}At]MABG, **2007**, 15, 3430.
33. Y. Norseev, *J. Radioanal. Nucl. Chem.* Synthesis of astatine-tagged methylene blue, a compound for fighting micrometastases and individual cells of melanoma, **1998**, 237, 155.
34. G. J. Meyer, A. Walte, S. R. Sriyapureddy, M. Grote, D. Krull, Z. Korkmaz, W. H. Knapp, *Appl. Radiat. Isot.* Synthesis and analysis of 2-[^{211}At]-L-phenylalanine and 4-[^{211}At]-L-phenylalanine and their uptake in human glioma cell cultures in-vitro, **2010**, 68, 1060.
35. G. W. M. Visser, E. L. Diemer, *Radiochem. Radioanal. Lett.* The reaction of astatine with aromatic diazonium compounds, **1982**, 51, 135.
36. G. Wunderlich, S. Fischer, R. Dreyer, W. G. Franke, *J. Radioanal. Nucl. Chem.* A simple method for labelling proteins with ^{211}At via diazotized aromatic diamine, **1987**, 117, 197.
37. E. M. Link, R. N. Carpenter, *Cancer Res.* ^{211}At-Methylene blue for targeted radiotherapy of human melanoma xenografts: Treatment of micrometastases, **1990**, 50, 2963.
38. M. F. Hawthorne, A. Maderna, *Chem. Rev.* Applications of radiolabeled boron clusters to the diagnosis and treatment of cancer, **1999**, 99, 3421.
39. D. S. Wilbur, M.-K. Chyan, D. K. Hamlin, R. L. Vessella, T. J. Wedge, M. F. Hawthorne, *Bioconjugate Chem.* Reagents for astatination of biomolecules. 2. Conjugation of anionic boron cage pendant groups to a protein provides a method for direct labeling that is stable to *in vivo* deastatination, **2007**, 18, 1226.

40. D. S. Wilbur, M.-K. Chyan, D. K. Hamlin, B. B. Kegley, R. Risler, P. M. Pathare, J. Quinn, R. L. Vessella, C. Foulon, M. Zalutsky, *Bioconjugate Chem.* Reagents for astatination of biomolecules: Comparison of the *in vivo* distribution and stability of some radioiodinated/astatinated benzamidyl and nido-carboranyl compounds, **2004**, 15, 203.
41. D. S. Wilbur, D. K. Hamlin, M.-K. Chyan, B. B. Kegley, J. Quinn, R. L. Vessella, *Bioconjugate Chem.* Biotin reagents in antibody pretargeting. 6. Synthesis and *in vivo* evaluation of astatinated and radioiodinated aryl-and nido-carboranyl-biotin derivatives, **2004**, 15, 601.
42. D. S. Wilbur, M.-K. Chyan, H. Nakamae, Y. Chen, D. K. Hamlin, E. B. Santos, B. T. Kornblit, B. M. Sandmaier, *Bioconjugate Chem.* Reagents for astatination of biomolecules. 6. An intact antibody conjugated with a maleimido-closo-decaborate (2-) reagent via sulfhydryl groups had considerably higher kidney concentrations than the same antibody conjugated with an isothiocyanato-closo-decaborate (2-) reagent via lysine amines, **2012**, 23, 409.
43. M. Pruszyński, A. Bilewicz, M. R. Zalutsky, *Bioconjugate Chem.* Preparation of Rh[16aneS4-diol] ^{211}At and Ir[16aneS4-diol]^{211}At complexes as potential precursors for astatine radiopharmaceuticals. Part I: Synthesis, **2008**, 19, 958.
44. M. Pruszyński, M. Łyczko, A. Bilewicz, M. R. Zalutsky, *Nucl. Med. Biol.* Stability and in vivo behavior of Rh[16aneS4-diol]^{211}At complex: A potential precursor for astatine radiopharmaceuticals, **2015**, 42, 439.
45. M. Pruszyński, A. Bilewicz, B. Wąs, B. Petelenz, *J. Radioanal. Nucl. Chem.* Formation and stability of astatide-mercury complexes, **2006**, 268, 91.
46. R. G. Pearson, *J. Chem. Educ.* Hard and soft acids and bases, HSAB, part 1: Fundamental principles, **1968**, 45, 581.
47. R. G. Pearson, *J. Chem. Educ.* Hard and soft acids and bases, HSAB, part II: underlying theories, **1968**, 45, 643.
48. R. H. Larsen, S. Slade, M. R. Zalutsky, *Nucl. Med. Biol.* Blocking [^{211}At]astatide accumulation in normal tissues: Preliminary evaluation of seven potential compounds, **1998**, 25, 351.
49. M. R. Zalutsky, D. A. Reardon, G. Akabani, R. E. Coleman, A. H. Friedman, H. S. Friedman, R. E. McLendon, T. Z. Wong, D. D. Bigner, *J. Nucl. Med.* Clinical experience with α-particle–emitting ^{211}At: treatment of recurrent brain tumor patients with ^{211}At-labeled chimeric antitenascin monoclonal antibody 81C6, **2008**, 49, 30.
50. S. W. Hadley, D. S. Wilbur, M. A. Gray, R. W. Atcher, *Bioconjugate Chem.* Astatine-211 labeling of an antimelanoma antibody and its Fab fragment using N-succinimidyl p-[^{211}At]astatobenzoate: comparisons in vivo with the p-[^{125}I]iodobenzoyl conjugate, **1991**, 2, 171.
51. L. Vasaros, Y. Norseyev, D. Nhan, V. Khalkin, N. Huan, *J. Radioanal. Nucl. Chem.* Determination of the dissociation energy of the C-At bond in substituted astatobenzenes, **1984**, 87, 31.
52. E. H. Appelman, *J. Am. Chem. Soc.* The oxidation states of astatine in aqueous solution, **1961**, 83, 805.
53. G. W. M. Visser, *Radiochim. Acta.* Inorganic astatine chemistry 2. The chameleon behavior and electrophilicity of At-species, **1989**, 47, 97.
54. J. Champion, A. a. Sabatié-Gogova, F. Bassal, T. Ayed, C. Alliot, N. Galland, G. Montavon, *J. Phys. Chem. A.* Investigation of astatine (III) hydrolyzed species: Experiments and relativistic calculations, **2013**, 117, 1983.

55. J. Champion, M. Seydou, A. Sabatié-Gogova, E. Renault, G. Montavon, N. Galland, *Phys. Chem. Chem. Phys.* Assessment of an effective quasirelativistic methodology designed to study astatine chemistry in aqueous solution, **2011**, 13, 14984.
56. A. Sabatié-Gogova, J. Champion, S. Huclier, N. Michel, F. Pottier, N. Galland, Z. Asfari, M. Chérel, G. Montavon, *Anal. Chim. Acta.* Characterization of At^- species in simple and biological media by high performance anion exchange chromatography coupled to gamma detector, **2012**, 721, 182.
57. I. Dreyer, R. Dreyer, V. A. Chalkin, *Radiochem. Radioanal. Lett.* Studies of the migration rates of astatine compounds in an electric field, **1978**, 35, 257.
58. C. Alliot, M. Chérel, J. Barbet, T. Sauvage, G. Montavon, *Radiochim. Acta.* Extraction of astatine-211 in diisopropylether (DIPE), **2009**, 97, 161.
59. E. R. Balkin, D. K. Hamlin, K. Gagnon, M.-K. Chyan, S. Pal, S. Watanabe, D. S. Wilbur, *Appl. Sci.* Evaluation of a wet chemistry method for isolation of cyclotron produced [^{211}At] astatine, **2013**, 3, 636.
60. D. J. Green, M. Shadman, J. C. Jones, S. L. Frayo, A. L. Kenoyer, M. D. Hylarides, D. K. Hamlin, D. S. Wilbur, E. R. Balkan, Y. Lin, *Blood.* Astatine-211 conjugated to an anti-CD20 monoclonal antibody eradicates disseminated B-cell lymphoma in a mouse model, **2015**, 125, 2111.
61. E. H. Appelman, E. N. Sloth, M. H. Studier, *Inorg. Chem.* Observation of astatine compounds by time-of-flight mass spectrometry, **1966**, 5, 766.
62. F. Bassal, PhD dissertation: Exploration des propriétés métalliques de At(+III): Approche théorique, Université de Nantes, **2013**.
63. T. Ayed, J. Pilmé, D. Tézé, F. Bassal, J. Barbet, M. Chérel, J. Champion, R. Maurice, G. Montavon, N. Galland, *Eur. J. Med. Chem.* ^{211}At-labeled agents for alpha-immunotherapy: On the in vivo stability of astatine-agent bonds, **2016**, 116, 156.
64. M. Amaouch, G. Montavon, N. Galland, J. Pilmé, *Mol. Phys.* What can tell the quantum chemical topology on carbon–astatine bonds?, **2016**, 114, 1326.
65. J. Autschbach, *J. Chem. Phys.* Perspective: Relativistic effects, **2012**, 136, 150902.
66. P. Pyykko, *Chem. Rev.* Relativistic effects in structural chemistry, **1988**, 88, 563.
67. R. Maurice, F. Réal, A. S. P. Gomes, V. Vallet, G. Montavon, N. Galland, *J. Chem. Phys.* Effective bond orders from two-step spin–orbit coupling approaches: The I_2, At_2, IO^+, and AtO^+ case studies, **2015**, 142, 094305.
68. S. Rothe, A. N. Andreyev, S. Antalic, A. Borschevsky, L. Capponi, T. E. Cocolios, H. de Witte, E. Eliav, D. V. Fedorov, V. N. Fedosseev, D. A. Fink, S. Fritzsche, L. Ghys, M. Huyse, N. Imai, U. Kaldor, Y. Kudryavtsev, U. Köster, J. F. W. Lane, J. Lassen, V. Liberati, K. M. Lynch, B. A. Marsh, K. Nishio, D. Pauwels, V. Pershina, L. Popescu, T. J. Procter, D. Radulov, S. Raeder, M. M. Rajabali, E. Rapisarda, R. E. Rossel, K. Sandhu, M. D. Seliverstov, A. M. Sjödin, P. van den Bergh, P. van Duppen, M. Venhart, Y. Wakabayashi, K. D. A. Wendt, *Nat. Commun.* Measurement of the first ionization potential of astatine by laser ionization spectroscopy, **2013**, 4, 1835.
69. A. V. Mitin, C. van Wüllen, *J. Chem. Phys.* Two-component relativistic density-functional calculations of the dimers of the halogens from bromine through element 117 using effective core potential and all-electron methods, **2006**, 124, 064305.

70. L. Junqin, Z. Zilong, A. Martin, Z. Xuemei, C. Chongyang, *J. Phys. Chem. B.* Theoretical study for the electron affinities of negative ions with the MCDHF method, **2012**, 45, 165004.

71. K. A. Peterson, D. Figgen, E. Goll, H. Stoll, M. Dolg, *J. Chem. Phys.* Systematically convergent basis sets with relativistic pseudopotentials. II. Small-core pseudopotentials and correlation consistent basis sets for the post-d group 16–18 elements, **2003**, 119, 11113.

72. B. O. Roos, R. Lindh, P.-Å. Malmqvist, V. Veryazov, P.-O. Widmark, *J. Phys. Chem. A.* Main group atoms and dimers studied with a new relativistic ANO basis set, **2004**, 108, 2851.

73. R. E. Vernon, *J. Chem. Educ.* Which elements are metalloids?, **2013**, 90, 1703.

74. J. Pilmé, E. Renault, F. Bassal, M. Amaouch, G. Montavon, N. Galland, *J. Chem. Theory Comput.* QTAIM analysis in the context of quasirelativistic quantum calculations, **2014**, 10, 4830.

75. A. S. P. Gomes, L. Visscher, *Chem. Phys. Lett.* The influence of core correlation on the spectroscopic constants of HAt, **2004**, 399, 1.

76. T. Saue, K. Faegri, O. Gropen, *Chem.Phys. Lett.* Relativistic effects on the bonding of heavy and superheavy hydrogen halides, **1996**, 263, 360.

77. L. Visscher, K. G. Dyall, *J. Chem. Phys.* Relativistic and correlation effects on molecular properties. I. The dihalogens F_2, Cl_2, Br_2, I_2, and At_2, **1996**, 104, 9040.

78. J. Pilmé, E. Renault, T. Ayed, G. Montavon, N. Galland, *J. Chem. Theory Comput.* Introducing the ELF topological analysis in the field of quasirelativistic quantum calculations, **2012**, 8, 2985.

Chapter 2

Theory and Methods

In molecular quantum mechanics, the derivation of the electronic energy and molecular properties for a chemical system requires the knowledge of the wave function or, at least, of the electron density associated with a particular quantum state. Depending on which quantity is sought, a quantum mechanical calculation classifies as wave-function-based or electron-density-based calculation. Building exact wave functions or electron densities is highly desirable, but it is limited in practice to only one-electron systems. While "real life" chemistry goes far beyond that, several models that allow the construction of approximate wave functions and electron densities have been developed over the years. These models gather several approximations in a hierarchy of levels of theories of increasing sophistication and accuracy. In practice, there is no better model than another for all purposes, and the successful application of a particular one strongly depends on the physics of the studied system. Since assuredly we live in a relativistic world, the models should be in principle relativistic. That is, they must somehow comply with both Schrodinger's nonrelativistic quantum mechanics and Einstein's special relativity. Depending mostly on the studied system and property, relativity may play a trifling role and it can be neglected in a branch of approximated nonrelativistic models. If it does not, a relativistic model must be used. If differences appear in a quantity calculated with a relativistic and a nonrelativistic model, given that the two models differ only in the treatment of relativity, these differences are then qualified as relativistic effects. Such effects can be differentiated only in the abstract world of relativistic quantum mechanics, while in reality no such distinction can be made and even less measured.

In the present chapter, an introduction to the quantum mechanical approaches used throughout the present manuscript is given. When necessary, additional methods are also discussed in order to give an overview of alternative methods that could be employed to solve a given problem. Since compact mathematical description of the various nonrelativistic and relativistic

models can be found elsewhere,[1-4] only a few representative equations will be here reported for the sake of clarity.

2.1 Electronic structure wave-function-based methods

The simplest approximation to a "true" wave function is a single Slater determinant while more complex ones consist of variationally optimized spin- and symmetry-adapted linear combinations of them:

$$\Psi = \sum_i C_i \left| i \right\rangle \tag{2.1}$$

A Slater determinant itself is an antisymmetric product of one-electron orbitals. Desirable is that the Slater determinants are constructed from orbitals that form a complete one-electron basis and that the expansion in Eq. 2.1 includes all determinants that arise from this basis in the N-electron Fock space. Since these spaces should be in principle of infinite size, in practice both the one-electron basis and the determinant expansion must be truncated in a decent way. Wave functions expressed in terms of Slater determinants are sought as eigenfunctions of the nonrelativistic molecular electronic Hamiltonian which, in the light of the Born-Oppenheimer approximation, can shortly be expressed as:

$$\hat{H} = \hat{h} + \hat{g} + h_{\mathrm{nn}} = \sum_{pq} h_{pq} E_{pq} + \frac{1}{2} \sum_{pqrs} g_{pqrs} e_{pqrs} + h_{\mathrm{nn}} \tag{2.2}$$

where $\hat{h}$ and $\hat{g}$ are monoelectronic and bielectronic operators, E_{pq} and e_{pqrs} are the corresponding one ($a_p^\dagger a_q$) and two-electron ($a_p^\dagger a_q^\dagger a_r a_s$) shift operators, and h_{nn} is a scalar quantity corresponding to the nuclear-repulsion energy.[1] Assuming that the bielectronic contributions are negligible, an approximate wave function and associated eigenvalue for the Hamiltonian shown in Eq. 2.2 can be simply obtained by diagonalizing its monoelectronic part in a given one-electron basis. It is of course far from being sufficient but this may actually be used as a trial wave function. The HF model is one of the simplest models than can provide a wave function while dealing with the bielectronic interactions in an elegant and effective fashion.

2.1.1 Hartree-Fock

The HF wave function is fundamental in *ab initio* electronic structure theory and constitutes the zero-order wave function for a wide range of more accurate quantum mechanical models. It can be constructed by constraining it to be an eigenfunction of the total and projected

spin – the basis of spin-restricted HF (RHF) theory, or not – the basis of spin-unrestricted HF (UHF) theory. In RHF theory, the spin adaption is obtained *ad hoc* by forcing the α and β spinorbitals to have the same spatial parts and one-electron energies two-by-two while the wave function is constructed as a fixed linear expansion of Slater determinants (only one for closed-shell species). Additionally, the symmetry adaption of the RHF wave function is obtained by enforcing the spatial parts to transform accordingly to the appropriate irreducible representations of the molecular point group. Note that anyway, even if the symmetry is not imposed, the obtained solutions essentially fulfill symmetry requirements (up to numerical accuracy at least). All these requirements may be lifted in the UHF theory and operating with such wave functions is usually less "comfortable" than with the RHF ones. Generally speaking, the UHF wave function is always chosen to be a single Slater determinant while, the RHF one, usually a single (spin- and symmetry-adapted) configuration state function (CSF) which is expressed as a fixed expansion of Slater determinants which usually belong to the same orbital configuration. Considering a closed-shell system, such a RHF-like wave function can be written as:

$$\left|\mathrm{CSF}\right\rangle = \left(\prod_i a_{i\alpha}^\dagger a_{i\beta}^\dagger\right)\left|\mathrm{vac}\right\rangle \tag{2.3}$$

where the product in the parenthesis corresponds to the core creation operator that doubly-occupies a set of *i* orbitals from the vacuum state, with α and β electrons. Starting from Eq. 2.3, a HF-like wave function for a triplet-symmetry state with two singly-occupied active orbitals (v and w) may be simply obtained by operating on it with triplet two-body creation operators, *i.e.* $a_{v\alpha}^\dagger a_{w\alpha}^\dagger$, $1/\sqrt{2}\left(a_{v\alpha}^\dagger a_{w\beta}^\dagger + a_{v\beta}^\dagger a_{w\alpha}^\dagger\right)$ and $a_{v\beta}^\dagger a_{w\beta}^\dagger$.[1] The true HF wave function corresponds to a state where the HF energy is stationary with respect to unitary transformations within the spinorbital basis. That is, one needs to optimize the individual spinorbitals spanning the Slater determinant such that the energy of the determinant itself is the lowest possible stationary one. Conveniently, an exponential *ansatz* is used to parameterize the HF wave function:

$$\left|\Psi^{\mathrm{HF}}\right\rangle = \exp(-\hat{\kappa})\left|\mathrm{CSF}\right\rangle \tag{2.4}$$

where $\hat{\kappa}$ is an anti-hermitian one-electron operator that carries out orbital unitary transformations. Then, the HF state is obtained by minimizing the expectation value of the energy with respect to the non-redundant orbital rotation parameters of $\hat{\kappa}$:

$$E^{\mathrm{HF}} = \min_{\kappa} \left\langle \Psi^{\mathrm{HF}} \middle| H \middle| \Psi^{\mathrm{HF}} \right\rangle \tag{2.5}$$

Since a Slater determinant does characterize a state in which the electrons are formally moving under the influence of only Fermi correlation, a set of Schrödinger-like equations can be independently solved for each electron. These are the so-called canonical HF equations. Their solutions are the individual spinorbitals and their associated energies. The antisymetrized product of the spinorbitals defines then the N-electron HF wave function while the summation of the spinorbital energies contribute to the HF total energy. The effective one-electron Hamiltonian for which the spinorbitals are sought to be eigenfunctions, is called the Fock operator. It is a hermitian operator that retains the monoelectronic part of the Hamiltonian shown in Eq. 2.2, and replaces the bielectronic part by a one-electron effective potential ($\hat{V}$). The latter is generated by the average charge distribution of the remaining N−1 electrons (mean-field approximation). The form of the Fock operator is:

$$\hat{f} = \sum_{pq} f_{pq} E_{pq} \tag{2.6}$$

where f_{pq} are Fock matrix elements:

$$f_{pq} = h_{pq} + \sum_{i} \left(2g_{pqii} - g_{piiq} \right) \tag{2.7}$$

In Eq. 2.7, h_{pq} are matrix elements related to the monoelectronic part of the Hamiltonian (Eq. 2.2) and the two terms in the summation correspond to the Coulomb and exchange interactions.[1] The diagonalization of the Fock matrix yields the canonical orbitals and their energies. In practice, the HF equations are solved self-consistently, *i.e.* in an iterative process: a set of trial orthogonal orbitals are used to construct a Fock matrix whose diagonalization would yield a new set of orbitals. This process is repeated until the old and new orbitals produced by the diagonalization are similar and/or the total HF energy is converged. In practice, one wants to avoid this procedure since it requires an expensive transformation step of the bielectronic integrals in the orbital basis. The Roothan-Hall procedure overcomes this step.[5,6] In a molecular context, the orbitals (MOs) are expanded in a linear combination of usually nuclear centered Gaussian atomic orbitals (AOs), whose coefficients are used as variational parameters. The Fock matrix is built from its elements expressed in such an AO basis, and used to solve iteratively the Roothan-Hall equations:

$$f^{\mathrm{AO}}\mathrm{C} = \mathrm{SC}\varepsilon \tag{2.8}$$

where C is a vector of AO coefficients, ε is a diagonal matrix containing the orbital energies on the diagonal, and S is the AO overlap matrix. Solving Eq. 2.8 is routinely done even for quite large chemical systems, and yields the HF wave function and energy.

The HF model is currently mostly used for qualitative studies rather than quantitative, and sometimes not even for this, depending on the property and system under study. The reasons rely strongly on the single determinental/configurational approximation to the "true" wave function, and to the mean-field approximation. The HF model is inappropriate to study (i) chemical processes that involve the formation or dissociation of chemical bonds, (ii) diradicals, (iii) chemical systems with degenerate or nearly-degenerate electronic configurations/states, etc. That is because the motions of the electrons are strongly coupled (correlated). In order to properly describe this kind of correlated motions with Slater determinants, a wave function consisting of a variationally optimized linear combination of them is required, *i.e* like the one in Eq. 2.1. The electron correlation shares generally two categories. While a single determinant may be a good approximation of the true wave function, quantitatively it yields poor energies since it neglects the instantaneous Coulomb repulsions between the electrons. This type of correlation is called dynamic correlation. In cases where two or more determinants may happen to interact, *i.e.* as for instance when (near-) degeneracies between electronic configurations/states occur, the stabilization energy results from the so-called static electron correlation. Since the HF wave function only spans a single determinant, the static electron correlation is by construction neglected. In theory, one cannot distinguish between static and dynamic correlation in "real" situations. In practice, quite often static electron correlation is seen as arising from limited Slater determinant expansions, while the dynamic electron correlation is seen as occurring beyond that. Generally, the electron correlation is introduced starting from the HF solution, with post-HF methods as Møller-Plesset (MP) perturbation theory,[7] coupled-cluster (CC)[1,8] or configuration-interaction (CI).[9]

2.1.2 Møller-Plesset perturbation theory

Starting from a HF solution, (single reference) MP perturbation theory can be used to account for dynamic correlation. In cases where static correlation does not manifest strongly, the derived approximate methods can give a reasonable estimation of the true total energy. In MP perturbation theory, the Fock operator (Eq. 2.6), which is diagonal in the canonical HF orbital basis, is considered as the zeroth-order Hamiltonian. The orthonormal set of states which are eigenfunctions of the Fock operator, *i.e.* the HF determinant and all singly, doubly etc. excited determinants with respect to the HF one are taken as the zeroth-order states. The perturbation is

constituted by the so-called fluctuation potential (Φ), which is defined as the difference between the Coulomb bielectronic term ($\hat{g}$) of the true Hamiltonian (see Eq. 2.2) and its approximated version within the Fock operator, *i.e.* the one-electron mean-field Fock potential:

$$\Phi = \hat{g} - \hat{V} = \hat{H} - \hat{f} - h_{nn} \tag{2.9}$$

It is easily seen that the physical interpretation of Φ is the degree of electron fluctuation aside from the mean-field picture (assumed within the HF formalism). By applying perturbation theory to zeroth-order in Φ, one obtains the zeroth-order MP energy which is the sum of the occupied HF spinorbital energies. Further proceeding to first order in Φ leads to the first order MP energy correction, which is in practice a necessary ingredient to calculate the HF energy. Electron correlation is introduced when perturbation theory is applied to second and higher orders in Φ. Applying perturbation theory only to second-order in Φ is often sufficient, and may recover up to 99% of the correlation energy in cases where the HF state is a good zeroth-order approximation of the true wave function. This is the basis of the so-called MP2 method: Møller-Plesset perturbation theory at second order. The MP2 energy is then the summation of the HF energy and the second order MP correction. Of course, this simplistic approach may prove to be insufficient in many cases and more sophisticated approaches are required.

2.1.3 Configuration interaction

If static electron correlation manifests strongly then MP perturbation theory is not suitable since it mainly accounts for part of the dynamic correlation. CI can in principle account for both types of correlations. In CI, electron correlation is accounted for by generating a wave function that is a linear combination of Slater determinants/configurations. A rigorous description of electron correlation would be obtained if all the determinants that can arise from a given one-electron basis are included in the CI wave function. This type of wave function corresponds to Eq. 2.1. If a full configuration interaction (FCI) is performed in conjunction with an infinite one-electron basis, the exact eigenfunction of the true nonrelativistic Hamiltonian is obtained. The determinants in the FCI expansion can be obtained from the HF reference by applying a set of annihilation and creation operators:

$$\left|\Psi^{\mathrm{FCI}}\right\rangle = \left|\Psi^{\mathrm{HF}}\right\rangle + \underbrace{\left(\sum_{A,I} C_I^A a_A^\dagger a_I\right)\left|\Psi^{\mathrm{HF}}\right\rangle}_{\text{singly excited (S)}} + \underbrace{\left(\sum_{A>B,I>J} C_{IJ}^{AB} a_A^\dagger a_B^\dagger a_I a_J\right)\left|\Psi^{\mathrm{HF}}\right\rangle}_{\text{doubly excited (D)}} + \ldots \tag{2.10}$$

where *A*, *B*, etc., are virtual orbitals, *I*, *J*, etc., are occupied orbitals, and C_I^A, C_{IJ}^{AB}, etc., are the expansion coefficients. $\left|\Psi^{\mathrm{FCI}}\right\rangle$ is obtained variationally as the expectation value of the energy, the expansion coefficients being the variational parameters:

$$E^{\mathrm{FCI}} = \min_{C} \frac{\left\langle \Psi^{\mathrm{FCI}} \middle| H \middle| \Psi^{\mathrm{FCI}} \right\rangle}{\left\langle \Psi^{\mathrm{FCI}} \middle| \Psi^{\mathrm{FCI}} \right\rangle} \tag{2.11}$$

One should note that in CI, the orbitals spanning the Slater determinants are not re-optimized but taken as it is from a previous HF calculation. Nevertheless, any orbital rotations would be redundant since all determinants in the N-electron Fock space are retained. The FCI energy cannot vary with respect to any rotation of the reference orbitals. The correlation energy is simply the difference between the FCI energy and the HF one, both being calculated in the same one-electron basis. Since in practice the one-electron basis is finite, what is generally calculated is the electron correlation for this given basis set, or the electron correlation is extrapolated at the basis set limit.

Although FCI yields the exact eigenfunctions and eigenvalues of the true nonrelativistic Hamiltonian, it can rarely be applied to systems that bear more than few atoms. The reasoning is based on the intractable expansion of determinants in Eq. 2.10, than can easily reach beyond billions with the increasing number of electrons and orbitals. While certainly not all determinants play an important role for the property of the system under study, it may be wise to truncate the CI expansion (with respect to FCI). This leads to truncated CI, and, depending on the truncation threshold, it can bear the name of CIS (only up to the singly excited determinants are retained in the wave function), CISD (up to the doubly excited determinants are retained in the wave function) and so on. Increasing the truncation threshold, the convergence to the FCI result will slowly be achieved. Furthermore, such truncated CI wave functions lack size-extensivity and size-consistency, and the resulting energies may not make much sense, although they can be corrected.[10,11] Such a behavior of truncated CI results from the linear parameterization of the CI wave function (Eq. 2.10). Also, any truncated CI suffers from the dependence with respect to the reference orbitals. Alternatively, CC is based on a different type of wave function parameterization which ensures both size-consistency and size-extensivity, while improving in principle the description of the correlation energy.

2.1.4 Coupled Cluster

While the HF wave function can be considered as a good zeroth-order approximation to the FCI one, it is also the case for CC in many cases. CC is often thought as the golden standard to compute correlation energies. The CC correlated wave function reads a product of configurations, nonetheless similar to the linear FCI expansion, and is written usually using an exponential *ansatz*:

$$\left|\Psi^{\mathrm{CC}}\right\rangle = \exp\left(\underbrace{\sum_{AI} t_I^A a_A^\dagger a_I}_{\hat{\mathrm{T}}_1} + \frac{1}{4}\underbrace{\sum_{ABIJ} t_{IJ}^{AB} a_A^\dagger a_B^\dagger a_I a_J}_{\hat{\mathrm{T}}_2} + \ldots\right)\left|\Psi^{\mathrm{HF}}\right\rangle \tag{2.12}$$

where *A*, *B* etc. are occupied orbitals in the HF state, *I*, *J*, etc. are virtual ones, and t_I^A, t_{IJ}^{AB}, etc. are known as the CC amplitudes for the respective singly, doubly, etc. excited configurations that are generated from the HF state. As a whole, the term in the parenthesis in Eq. 2.12 is known as the cluster operator ($\hat{\mathrm{T}}$) while its individual terms, $\hat{\mathrm{T}}_1$, $\hat{\mathrm{T}}_2$, etc., are the single, double, etc., excitation operators. A particular excited configuration with respect to the HF state can be generated with certain amplitudes in various ways. For instance, a doubly-excited configuration can be produced either by operating directly with $\hat{\mathrm{T}}_2$, or twice with $\hat{\mathrm{T}}_1$ on the HF state. However, in the expansion of the final CC wave function, all amplitudes leading to the same configuration are gathered such as having a single weight. Usually, $\hat{\mathrm{T}}$ is safely truncated at a given excitation level leading to a family of CC methods: CC with single and double excitations (CCSD) when $\hat{\mathrm{T}}$ is truncated at the level of $\hat{\mathrm{T}}_2$, CC with single, double and triple electronic excitations (CCSDT) when $\hat{\mathrm{T}}$ is truncated at the level of $\hat{\mathrm{T}}_3$, etc. The CCSDT method has been proven in many case to be a sufficient level of truncation, and is currently considered for essentially single-reference states as the "golden standard" method of quantum mechanics. Note that more popular is the CCSD(T) method which is a slight approximation to CCSDT but which leads quite often to more accurate results based on error cancelations. In this case, the parenthesis T means that the contributions of some triple excitations are accounted for by means of perturbation theory.

The CC equations resume at solving a set of non-linear equations for the CC amplitudes. Proceeding with the variational principle, *i.e.* solving self-consistently a set of CC equations under the form of Eq. 2.11 turned out to be impractical and the CC theory is thus regarded as a non-variational method.[1] In turn, the CC wave function and energy are obtained by a series of

projections of a Schrödinger-like equation, where the wave function is in the CC form, onto the HF state and onto the set of states spanned by the excited configurations generated by $\hat{T}$.[1]

So far, only single-reference approaches have been mentioned. Naturally, perturbation theory, CI and CC can be formulated for multiconfigurational states, and such extensions will be discussed in forthcoming subsections.

2.1.5 Multiconfigurational self-consistent-field

The multiconfigurational self-consistent-field (MCSCF) theory can be seen as an elegant solution to the bottlenecks of FCI and truncated CI. That is, it can deal with the multiconfigurational character of electronic states, it limits the CI expansion, and it can be considered as size-extensive and size-consistent. The idea of MCSCF consists in wisely selecting a set of determinants/CSFs to be included meanwhile both the CI coefficients and MCSCF orbitals are variationally optimized. In practice, several schemes have been developed on the past decades to limit the user intervention for selecting the CI space. Most of the schemes rely on selecting an orbital window, comprising both occupied and virtual orbitals, in which the CI is performed. This orbital window is called the active space (of electrons and orbitals). The later should be defined such that the distribution of the active electrons within the active orbitals gives rise to determinants/CSFs in the MCSCF wave function that dominate the FCI one. The MCSCF wave function can be written as:

$$\left|\Psi^{\mathrm{MCSCF}}\right\rangle = \exp(-\hat{\kappa})\sum_i C_i \left|i\right\rangle \tag{2.13}$$

It is variationally optimized by minimizing the expectation value of the energy with respect to two sets of variational parameters: the C_i expansion coefficients and the non-redundant orbital rotation parameters of $\hat{\kappa}$:

$$E^{\mathrm{MCSCF}} = \min_{\kappa,C} \frac{\left\langle \Psi^{\mathrm{MCSCF}} \middle| H \middle| \Psi^{\mathrm{MCSCF}} \right\rangle}{\left\langle \Psi^{\mathrm{MCSCF}} \middle| \Psi^{\mathrm{MCSCF}} \right\rangle} \tag{2.14}$$

In contrast to truncated CI, both the expansion coefficients and the orbitals are hence optimized in the MCSCF theory, which, provided that the active space is properly chosen, means that at least a good zeroth-order wave function is obtained for any subsequent treatment. A particular and very popular MCSCF method is the complete active space self-consistent-field (CASSCF) one.[12,13] In CASSCF, the orbitals are split in three categories, (i) the inactive orbitals, which are always doubly occupied in all determinants/CSFs, (ii) the active orbitals which can have all possible occupations

(the active or CAS space), and (iii) the virtual orbitals (or secondary orbitals) that are always unoccupied in all determinants/CSFs. Since a FCI calculation is performed within the CAS space, the latter must be limited in size for practical reasons. The dimensions of the CAS space is usually defined through the notation CASSCF(*m*, *n*), where *m* represents the number of active electrons that are distributed among the *n* active orbitals. To account properly for the electron correlation, the CAS space should be as large as possible; desirable is the full valence space. Nevertheless, even for small systems, the full valence space can be quite large and hence it must be restricted. Using reasonable one-electron basis, routine CASSCF calculations can today be carried out with CAS spaces comprising up to about 16 electrons in 16 orbitals. Only a limited CI expansion can arise from such a CAS space, the electron correlation which is accounted for in CASSCF is then mostly static electron correlation, although a clear distinction between static and dynamic correlation is problematic at this level. Nevertheless, multireference post-CASSCF methods as multireference perturbation theory (MRPT) or multireference configuration interaction (MRCI) can be used in order to recover an important part of the missed dynamic electron correlation.

2.1.6 Post-MCSCF perturbation theory

MRPT can be seen as an extension to single-reference MP perturbation theory, which is applicable to multiconfigurational zeroth-order wave functions. Various MRPT methods are available, among which the complete active space perturbation theory at second order (CASPT2)[14] and the N-electron valence state perturbation theory at second order (NEVPT2),[15] are worth mentioning. Both of them are applicable to CASSCF wave functions and account for the effect of perturber functions, defined as CSFs "external" to the CAS space, to the CASSCF energy and wave function. While CASPT2 and NEVPT2 implementations may differ in the choice and treatment of such perturber functions, the essential difference between them is actually the zeroth-order Hamiltonian. Like in single reference MP theory, the zeroth-order Hamiltonian in CASPT2 is of monoelectronic Fock type, modified in such a way that the CASSCF wave function becomes its eigenfunction, and that in the limit of a vanishing CAS space in CASSCF, it reduces to the standard Fock operator used in MP theory. However, such a choice leads frequently to "intruder states", and procedures are often invoked in practice to avoid this behavior.[16] The Dyall's Hamiltonian was proven to be an alternative to the "faulty" monoelectronic Fock-type Hamiltonian used in CASPT2, and it is used as the zeroth-order one in NEVPT2.[17] According to the partition of the orbitals in CASSCF, the Dyall's Hamiltonian is a summation of a monoelectronic part, diagonal in the canonical inactive and virtual orbital spaces, and a bielectronic part operating only in the CAS space, that accounts for bielectronic interactions between the active electrons. The use of such a

zeroth-order Hamiltonian generally prevents the occurrence of intruder states, but it renders the NEVPT2 energy to be more dependent on the choice of the CAS space than the CASPT2 one(s).[18] So far, three types of NEVPT2 approaches have been formulated, classified accordingly to the contraction pattern of the perturber functions: uncontracted (UC), partially contracted (PC) and strongly contracted (SC). The SC-NEVTP2 approach[19] is the default one in most quantum-mechanical codes, and the one here retained. In this approach, the contraction scheme considers a single perturber function from each of the eight possible categories: singly- and doubly-excited CSFs with up to 2 electrons promoted to/withdrawn from the active space. One should note that using such post-CASSCF perturbation theory schemes is perhaps the most comfortable way of accounting for the dynamic electron correlation, provided that the reference space is large enough. Nevertheless, post-CASSCF variational schemes as MRCI can also be used for this purpose, and are particularly recommended for specific applications.

2.1.7 Multireference configuration interaction

MRCI is a post-CASSCF variational method that accounts for dynamic electron correlation by extending the CAS-CI expansion with additional classes of CSFs. These CSFs are produced by applying different classes of electron excitation (S, D, T, …), to each individual CSF from the CASSCF reference configurational space. Hence, with the dimension of this reference space and with the level of excitations, the complexity of MRCI quickly rises. A current approximation is to extend the CAS-CI expansion only with up to doubly excited CSFs. This leads to the very popular MRCI-SD method. The MRCI-SD wave function can be written as:[20]

$$\left|\Psi^{\text{MRCI-SD}}\right\rangle = \sum_{I} C^{I}\Psi_{I} + \sum_{S}\sum_{a} C_{a}^{S}\Psi_{S}^{a} + \sum_{P}\sum_{ab} C_{ab}^{P}\Psi_{P}^{ab} \qquad (2.15)$$

where *a* and *b* are called external orbitals from the virtual CASSCF orbital space, *I*, *S* and *P* are called internal states and correspond to CASSCF configurations with 0, 1 or 2 electron-holes in the active orbitals as well as in the inactive ones which are meant to be correlated in MRCI (*i.e.* the internal orbital space of MRCI), Ψ_I, Ψ_S^a and Ψ_P^{ab} are the internal, singly- and doubly-external excited CSFs. From the CASSCF reference configurational space, the set of *P* states are obtained by applying two electron annihilation operators to the internal orbital space, the set of *S* states are obtained from *P* by applying an electron creation operator and the set of *I* states are obtained from *S* by applying again an electron creation operator. From *S* and *P*, the Ψ_S^a and Ψ_P^{ab} excited CSFs are obtained by applying, respectively, one and two electron creation operators to the external orbital

space. In order to manage the number of Ψ_S^a and Ψ_P^{ab}, two different contraction schemes have been designed: they can be externally contracted, with the contraction pattern handled with perturbation theory,[21,22] or internally contracted,[20] where they are expanded in term of the internal states. Of course, MRCI suffers from the same pitfalls as truncated CI. Therefore, such methods must be handled with care. Size-consistency corrections exist,[11] and some MRCI schemes are considered as the state-of-the-art to compute magnetic coupling constants.[23]

2.1.8 Multireference coupled cluster

CC theory in its standard formulation works on a single-configurational reference state, while extensions to multiconfigurational ones have been made available but are yet hardly applicable.[24-26] We wish not to detail on the formalism of such approaches, but notice that multireference CC methods that grow in popularity nowadays are the so called Fock space coupled cluster method (FSCC), and the intermediate Hamiltonian FSCC (IHFSCC) one.[25-27] Notably, a relativistic formulation of IHFSCC has been used to accurately determine various spectroscopic parameters of At and At species.[28,29]

2.2 Density functional theory methods

2.2.1 The electron density and the Hohenberg-Kohn theorems

DFT is in itself an *ab intio* complex theory, and a machinery to address the complicated electronic structure of atoms and molecules. It arose as a necessity to maintain in practice the simplicity of the HF theory, while attempting to deliver a correct picture of many-electron problems. DFT does not rely on the knowledge of the wave function, which is a complicated function of the electron spatial and spin coordinates, but rather on the total one-electron density, $\rho(\mathbf{r})$, which resumes to a function of only three spatial coordinates:

$$\rho(\mathbf{r}) = N\int\ldots\int\left|\Psi\left(\mathbf{x}_1,\mathbf{x}_2,\ldots,\mathbf{x}_N\right)\right|^2 \mathrm{d}\sigma\mathrm{d}\mathbf{x}_2\ldots\mathrm{d}\mathbf{x}_N \qquad (2.16)$$

In Eq. 2.16, N corresponds to the total number of electrons, σ denotes the arbitrary spin of electron one, and the $\mathbf{x}_i$ map the spin and spatial coordinates of the remaining $N-1$ electrons. From Eq. 2.16 one can deduce the total number of electrons, N, by simply integrating out $\rho(\mathbf{r})$ over the whole space. The total (ground-state) energy is sought as the eigenvalue of a Hamiltonian characterizing the motion of the electrons in an external potential (v) exerted by the clamped nuclei:

$$E[v] = \left\langle \Psi_\rho \middle| T + W \middle| \Psi_\rho \right\rangle + (v \mid \rho) \tag{2.17}$$

where T and W are the kinetic energy and the electron-electron repulsion energy, respectively, Ψ_ρ corresponds to the wave function issued by the ground-state density ($\rho \geq 0$ and integrates out to the total number of electron), and the last term is an integral corresponding to the interaction between the electron density and the external potential. The biunivocal relationship between ρ and v is fundamental in DFT, and has been exposed by Hohenberg and Kohn in 1964.[30] Through reduction to absurd, they have shown that the exact electron density of a ground-state determines the external potential up to a constant ($\rho \leftrightarrow v_\rho + c$). Hence, this density uniquely determines the Hamiltonian and its knowledge is a freeway to any property of interest. In a subsequent theorem,[30] Hohenberg and Kohn have shown that the ground-state energy of a system can be obtained variationally by minimizing the expression in Eq. 2.17 over all valid densities:

$$E[v] = \min_\rho \left(F_{\mathrm{HK}}[\rho] + (\rho \mid v) \right) \tag{2.18}$$

where $F_{\mathrm{HK}}[\rho]$ is known as the Hohenberg-Kohn functional, and corresponds to the first term of the right hand side (RHS) of Eq. 2.17. The form of this "exact" functional is unknown and many approximations have been developed on the last decades.

2.2.2 The Thomas-Fermi model, the local-density approximation and the density gradient

In 1927, well before Hohenberg and Kohn's work, Thomas and Fermi (TF) have proposed a density functional derived from a non-interacting uniform electron gas (UEG).[31,32] This functional takes into account the kinetic energy for such a system, obtained by applying locally the UEG expression for the kinetic energy (which is referred to as a local density approximation, LDA), while the electron-electron interaction has been accounted for in a HF-like fashion by ignoring the exchange-correlation hole (self-interacting density):

$$F_{\mathrm{TF}}[\rho] = T_{\mathrm{TF}}[\rho] + J[\rho] = 2.87 \int \rho^{5/3}(\mathbf{r}) \mathrm{d}(\mathbf{r}) + \frac{1}{2} \iint \frac{\rho(\mathbf{r}_1)\rho(\mathbf{r}_2)}{r_{12}} d\mathbf{r}_1 \mathrm{d}\mathbf{r}_2 \tag{2.19}$$

In 1930, Dirac has revised this functional by accounting for the exchange Fermi-hole.[33] Dirac has added to the expression in Eq. 2.19 a term, $K_D = 0.74 \int \rho^{4/3}(\mathbf{r}) \mathrm{d}\mathbf{r}$, leading to the TFD functional:

$$F_{\mathrm{TFD}}[\rho] = T_{\mathrm{TF}}[\rho] + J[\rho] - K_{\mathrm{D}}[\rho] \tag{2.20}$$

Both the TF and TFD models were unsuccessful since they are not able to predict atomic-shell structure and bonding in molecules.[34] This faulty behavior comes from the poor description of the kinetic energy, associated with the LDA. In order to improve the description, the gradient of the density can be used, which has led to various gradient-expansion approximations. A popular one has been proposed by von Weizsäcker, known as von Weizsäcker kinetic energy,[35] which was able to predict bonding in molecules when added to the TFD model.

2.2.3 From non-interacting to interacting systems

Considering a fully interacting system, the exact functional is given by $F_{\mathrm{HK}}[\rho]$, which retains the true kinetic energy and electron-electron interactions. The presence of the latter is, as we have seen as well in the wave-function-based methods, a difficult problem in quantum mechanics. Assuming that the system consists of non-interacting electrons, simplifies the form of $F_{\mathrm{HK}}[\rho]$, leaving only a non-interacting kinetic energy functional which, employing orbitals (ϕ_l), can be written as:

$$T_{\mathrm{s}}[\rho] = \min_{\rho} \sum_{l} \langle \phi_l | -\frac{1}{2}\nabla^2 | \phi_l \rangle \text{ where } \rho(\mathbf{r}) = \sum_{l} |\phi_l(\mathbf{r})|^2 \tag{2.21}$$

Proceeding this way, one may indeed tend to the exact kinetic energy functional, which is however a lower bound to the one of the interacting system. One may define some terms needed to be added to $F_{\mathrm{HK}}[\rho]$, alongside the approximated $T_{\mathrm{s}}[\rho]$, such that $F_{\mathrm{HK}}[\rho]$ incorporates the additional effects of an interacting system. Those terms would be the kinetic-energy correlation correction, $T[\rho] - T_{\mathrm{s}}[\rho]$, and the bielectronic exchange-correlation (XC) correction, $W[\rho] - J[\rho]$. The sum of these two terms defines the well-known exchange-correlation functional, $E_{\mathrm{XC}}[\rho]$. The exact universal density functional is then written as:

$$F[\rho] = T_{\mathrm{s}}[\rho] + J[\rho] + E_{\mathrm{XC}}[\rho] \tag{2.22}$$

Eq. 2.22 lies at the core of what is known today as the Kohn-Sham DFT (KS-DFT).[36]

2.2.4 Kohn-Sham density functional theory

KS-DFT, proposed in 1965 by the future Nobel prize winner Walter Kohn, and Lu Jeu Sham, is the DFT flavor that is mostly applied nowadays.[37] Kohn and Sham have further explored the simplistic TF model, and put forth the idea of constructing a “rigorous” Hamiltonian

characterizing a fictitious non-interacting system that has the same electron density as the physical one. The KS total energy is then calculated by minimizing the universal functional in Eq. 2.22 over all valid densities:

$$E[v] = \min_{\rho}\left(T_s[\rho] + J[\rho] + E_{XC}[\rho] + (v \mid \rho)\right) \tag{2.23}$$

Solving Eq. 2.23 resumes in practice to solving a system of one-electron equations for the orbitals (KS orbitals) known as the canonical KS equations:

$$\left[-\frac{1}{2}\nabla^2 + v_{KS}(\mathbf{r})\right]\phi_l(\mathbf{r}) = \varepsilon_l\phi_l(\mathbf{r}) \tag{2.24}$$

where ε_l are KS orbital energies, and v_{KS} is the KS effective potential which contains an exchange correlation potential (v_{XC}) defined as the functional derivative of $E_{XC}[\rho]$ with respect to the density. The KS wave function is then a Slater determinant built from the ϕ_l KS orbitals, determined self-consistently as solutions to Eq. 2.24. In practice, the exactness of the KS approach is hindered by the $E_{XC}[\rho]$ term for which no analytical expression is yet known. The accuracy of the KS wave function is therefore strongly dependent on approximations to the two terms, $E_X[\rho]$ and $E_C[\rho]$, that build up $E_{XC}[\rho]$. These approximations carry out the name of exchange-correlation density functional approximations.

2.2.5 Exchange-correlation density functional approximations

A straightforward solution for expressing the XC term is known as the S (Slater)-VWN (Vosko-Wilkes-Nusair) density functional.[38] This functional falls in the category of local (spin) density approximations, and it is built from the Dirac exchange functional (last term in Eq. 2.20) and the VWN correlation functional, which was achieved from an analytic fit from Monte-Carlo numerical simulations. Such LDA approximations are often over-binding due to overestimation of both exchange and correlation terms. For correcting this behavior, the density gradient has been introduced which led to a set of gradient expansion approximations, giving rise to the generalized gradient approximations (GGAs). Similarly to LDA, GGAs are local functionals that contain a set of parameters adjusted either to some exact relationships or to experimental data. A popular GGA functional is BLYP,[39,40] which is composed of the B88 exchange,[40] an exchange functional introduced by Becke in 1988 that contains one empirical parameter, and the LYP correlation functional,[39] introduced by Lee, Yang and Parr in 1988 that contains four empirical parameters. One

may go beyond the density gradient expansions and retain into a functional form also the second derivative of the density. Functionals obtained in this way carry out the name of meta-GGAs. GGAs and meta-GGAs may perform better than LDAs, however they (as well as LDAs) are far from the concept of an exact XC functional. The reason for this is their locality while exchange and correlation have no reason to be only formally local. Indeed, since the self-interacting density errors introduced by $J[\rho]$ in the KS energy expression are nonlocal, the XC corrections should also be nonlocal. Replacing part of the local exchange with HF-like exchange (nonlocal in essence), in an empirically determined mixture of exchange and correlation functionals, led to new classes of functionals denoted as hybrid density functionals: hybrid GGAs and hybrid meta-GGAs. B3LYP[39,41,42] is a popular hybrid GGA functional and it is nowadays the mostly used one in chemistry. Its expression reads:

$$E_{\mathrm{XC}}^{\mathrm{B3LYP}} = (1-a)E_{\mathrm{Dirac}} + aE_{\mathrm{X}}^{\mathrm{HF}} + bE_{\mathrm{X}}^{\mathrm{B88}} + (1-c)E_{\mathrm{C}}^{\mathrm{VWN}} + cE_{\mathrm{C}}^{\mathrm{LYP}} \qquad (2.25)$$

where the percentage of "exact" HF exchange is *a*=20%, of B88 exchange is *b*=71% and of LYP correlation is *c*=81%. Perhaps, one of the most popular hybrid meta-GGAs nowadays is the M06-2X one developed in 2008 by Zhao and Truhlar.[43] This functional retains 54% of exact HF exchange while it contains a "pool" of empirical parameters fitted with a broad range of chemical data. Another class of hybrid functionals that has emerged is the range-separated one. These hybrid functionals retain different percentages of exact HF exchange within the short- and long-range parts of the Coulomb operator. Long-range corrected functionals usually employ up to 100% exact HF exchange in the long-range part while they retain less than 50% in the short-range part. For instance, the CAM-B3LYP functional[44] has 65% and 19% of exact exchange in the long-range and short-range part, respectively. In contrast, short-range corrected hybrid functionals retain exact exchange only in the short-range part building up the family of screened-exchange hybrid functionals. A popular functional of this type is the HSE06[45,46] one worked out by Heyd, Scuseria and Erzenhorf in 2003. HSE06 retains 20% exact exchange in the short-range part.

2.3 Relativistic quantum mechanical approaches

So far we have introduced common computational approaches that are used nowadays to deal with the complex electronic structures of atoms and molecules. These models are all based on the Schrödinger equation, and potentially lead to accurate predictions as soon as relativistic effects are negligible. Relativity manifests broadly across the periodic table, admittedly with a much less influence on the chemistry of "light" atoms. In principle, there is no such a strict separation but it is

rather acknowledged that relativistic contributions to the electronic structure increase according to Z^2/c^2, where *c* is the constant speed of light.[47,48] Typical outcomes that have relativity at the origin are the yellow doublet emission of the Na atom, the drastic color change from Ag to Au, the inhibition of the $Pb^{2+} \rightarrow Pb^{4+}$ oxidation process that allows the lead-acid battery to work as it should, the change in oxidation numbers toward the end of groups XIII and XIV of the periodic table, the nearly 100% phosphorescent emission of benzophenone, the liquid state of Hg in normal conditions, etc.

Sometimes, relativistic effects can be accounted for by simply adding perturbative relativistic corrections to the nonrelativistic Hamiltonian. Proceeding in such a way may still lead to quantitatively and, perhaps, qualitatively inconsistent results. Thus, one may need to use a relativistic quantum theory from the outset. In such a theory, two important aspects are acquainted, namely a finite light speed (c ~ 137 a.u.) and the clamped nuclei approximation, the latter aspect being used also in nonrelativistic theories. It remains then to solve the electronic structure problem within a model developed from a relativistic Hamiltonian. Starting from the Hamiltonian form in Eq. 2.2, then one can at first ignore electron-electron interactions and replace the monoelectronic part with the Dirac monoelectronic Hamiltonian.

2.3.1 The Dirac Hamiltonian

The struggle to introduce relativity in the Schrödinger equation has formally been started by Klein and Gordon in 1926. Using the relativistic formulation of the kinetic energy, they have derived a relativistic Schrödinger-like wave equation that actually corresponds to a spinless quantum field.[2] Hence, the Klein-Gordon equation does not include spin degrees of freedom and it cannot be considered as a workhorse to develop a fully relativistic quantum theory. A solution for this came two years later from the British physicist Paul Dirac, nowadays considered as the father of the relativistic quantum mechanics. The Dirac equation for an electron moving in a potential *V* exerted by the clamped nuclei, and in the absence of any other perturbation, is written in a matrix form as:

$$\begin{pmatrix} V & c\boldsymbol{\sigma}\cdot\mathbf{p} \\ c\boldsymbol{\sigma}\cdot\mathbf{p} & V-2mc^2 \end{pmatrix}\begin{pmatrix} \Psi^{\mathrm{L}} \\ \Psi^{\mathrm{S}} \end{pmatrix} = E\begin{pmatrix} \Psi^{\mathrm{L}} \\ \Psi^{\mathrm{S}} \end{pmatrix} \tag{2.26}$$

where $\boldsymbol{\sigma}$ are Pauli spin matrices, $\mathbf{p}$ is the momentum operator and *m* is the electron mass. The matrix on the left hand side (LHS) of Eq. 2.26 corresponds to the one-electron Dirac Hamiltonian, sometimes more compactly written as: $h^{D;V} = \beta' mc^2 + c(\boldsymbol{\alpha}\cdot\mathbf{p}) + \hat{V}$ with β' and $\boldsymbol{\alpha}$ being the 4x4

Dirac matrices. The eigenfunctions of this Hamiltonian are four-component (4*c*) spinors composed of two bispinors (or two, two-component (2*c*) spinors), a large one (Ψ^{L}) for the α and β electrons ($\Psi^{L\alpha}, \Psi^{L\beta}$) and a small one (Ψ^{S}) for the α and β positrons ($\Psi^{S\alpha}, \Psi^{S\beta}$). Accordingly, the eigenvalues of this Hamiltonian are both positive and negative energy solutions, discretized by mc^2, corresponding to both electrons and positrons, respectively.

2.3.2 The Dirac-Coulomb-Breit Hamiltonian

Naturally, one wants to perform relativistic calculations on "real-life" molecular systems of interacting electrons. Beside the monoelectronic Dirac terms, one needs to incorporate into the relativistic Hamiltonian bielectronic terms corresponding to the electron-electron interactions. Using the non-relativistic Coulomb operator sounds appealing, and it has been justified from the principles of quantum electrodynamics. Such operator corresponds to the first and most important term from an expansion describing the full electron-electron interaction in the relativistic formalism. Breit has also proposed to retain from the full expansion, beside the non-relativistic Coulomb term, the further important one leading to the Coulomb-Breit operator for the electron-electron interaction in the relativistic framework:[2,48,49]

$$g_{ij}^{\mathrm{CB}} = \frac{1}{r_{ij}} - \frac{1}{2}\left(\frac{\left(\alpha_i \cdot \alpha_j\right)}{r_{ij}} + \frac{\left(\alpha_i \cdot r_{ij}\right)\left(\alpha_j \cdot r_{ij}\right)}{r_{ij}^3} \right) \tag{2.27}$$

where the first term in the parenthesis is known as the Gaunt term, characterizing the magnetic interaction between electron spins, and the second term is a gauge-dependent term characterizing the relativistic nature of the bielectronic interaction. One can thus write a full relativistic molecular Hamiltonian as:

$$\hat{H}^{\mathrm{DCB}} = \sum_{pq} h_{pq}^{D;V} E_{pq} + \sum_{pqrs} g_{pqrs}^{\mathrm{CB}} e_{pqrs} + h_{nn} \tag{2.28}$$

where the summations now run over spinors, the first term on the r.h.s. retains the sum of the monoelectronic Dirac Hamiltonians, the second term is the sum of the bielectronic Coulomb-Breit interaction terms, and the last one corresponds to the nuclear-repulsion energy. The Hamiltonian in Eq. 2.28 is known as the Dirac-Coulomb-Breit Hamiltonian and can be used within standard variational or perturbative wave-function based calculations, or even "adapted" to the framework of DFT. While there are only advantages in using such a Hamiltonian over the nonrelativistic one, owing of course to the treatment of relativity, its use come with some limitations. On one hand, the

spinors used to build the 4*c* wave function have both a real and a complex part, becoming less straightforward to interpret as compared to the molecular orbitals in the nonrelativistic formalism. On the other hand, calculations based on the full Dirac-Coulomb-Breit Hamiltonian turn out to be time consuming, and even impractical beyond few atoms. The complexity arises notably from the 4*c* formalism of the Dirac equation, researchers have therefore developed various 2*c* alternatives.

2.3.3 Approximations to the Dirac Hamiltonian

Chemists are generally interested only in the large components – the fermionic solutions – and hence, some separation schemes to discard the small components have been designed. Such schemes are usually based either on the elimination of the small component (ESC) or on decouplings *via* a series of unitary transformations. The ESC starts from the matrix formulation of the Dirac equation (Eq. 2.26) by expressing at first the small component in terms of the large one:

$$\Psi^{S} = \frac{1}{2mc}\left[1+\frac{E-V}{2mc^2}\right]^{-1}\boldsymbol{\sigma}\cdot\mathbf{p}\Psi^{L} = \frac{1}{2mc}k(E)\Psi^{L} \tag{2.29}$$

and then using it to express the Dirac equation only in terms of the large component:

$$\hat{H}^{ESC}\Psi^{L} = \left[\frac{1}{2m}\boldsymbol{\sigma}\cdot\mathbf{p}\,k(E)+V\right]\Psi^{L} = E\Psi^{L} \tag{2.30}$$

Finally, one needs to renormalize Ψ^{L} from Eq. 2.30 in order to obtain the full decoupling. This is achieved by operating with $\hat{O}\hat{H}^{ESC}\hat{O}^{-1}$, where $\hat{O} = \sqrt{1+k^{\dagger}k}$ is the renormalization energy-dependent operator:

$$\hat{H}^{eff} = \hat{O}\hat{H}^{ESC}\hat{O}^{-1} = \sqrt{1+k^{\dagger}k}\left[\frac{1}{2m}\boldsymbol{\sigma}\cdot\mathbf{p}\,k(E)+V\right]\frac{1}{\sqrt{1+k^{\dagger}k}} \tag{2.31}$$

Eq. 2.31 is the final 2*c* form of the Dirac Hamiltonian.[2,50]

Furthermore, three approximate Hamiltonians can be obtained, by employing different expansions of the *k*(*E*) term. Expanding it in powers series of $(E-V)/2mc^2$ to first order, then the Pauli Hamiltonian is recovered:[2,50]

$$\hat{H}^{P} = \frac{p^2}{2m}+V-\frac{p^4}{8m^3c^2}-\frac{e}{8m^2c^2}(\nabla\cdot\mathbf{E})+\frac{ie\boldsymbol{\sigma}}{4m^2c^2}\cdot(\mathbf{E}\times\nabla) \tag{2.32}$$

where the first two terms correspond to the nonrelativistic Hamiltonian, the third one is the mass-velocity term characterizing the relativistic increase of the electron masses, the forth one is the Darwin term which is a correction due to the rapid oscillations of the electrons, and the fifth term corresponds to the spin-orbit operator describing the effective coupling between the electron spin and the magnetic field generated by nuclei and other electrons in relative motion. If one rewrites the expression of $k(E)$ under a slightly different form:

$$k(E) = \frac{2mc^2}{2mc^2 - V}\left(1 + \frac{E}{2mc^2 - V}\right)^{-1} \tag{2.33}$$

an expansion to zeroth-order in terms of $E/\left(2mc^2 - V\right)$ leads then to the ZORA (zero-order regular approximation) Hamiltonian:[2,51,52]

$$\hat{H}^{\text{ZORA}} = \hat{V} + (\boldsymbol{\sigma}\cdot\mathbf{p})\frac{c^2}{2mc^2 - V}(\boldsymbol{\sigma}\cdot\mathbf{p}) \tag{2.34}$$

The ZORA Hamiltonian is widely used nowadays for routine molecular electronic structure calculations since it is implemented in many quantum mechanical codes. Also popular, is the Douglas-Kroll-Hess (DKH)[53-55] Hamiltonian which follows a different philosophy. As specified above, the reduction of the full Dirac Hamiltonian to the 2*c* form can also be attained *via* decoupling through a series of unitary transformations. Such a decoupling is performed with a unitary operator (U) by operating with $\mathrm{U}h^{D;V}\mathrm{U}^{\dagger}$. Douglas and Kroll have proposed to perform sequential decouplings by applying unitary transformations with the operator U decomposed as $(\ldots)\mathrm{U}_2\mathrm{U}_1\mathrm{U}_0$. The resulting DK Hamiltonian is then expanded in terms of the external potential V leading to various DKn Hamiltonians, n corresponding to the order in V.[56] At second order, the DK2 Hamiltonian is commonly known as DKH. Note that at infinite order, the exact Dirac splitting is recovered. A convenient feature of the ZORA and DK Hamiltonians is that they can further be separated in a spin-orbit and a scalar relativistic part, which can be employed separately in molecular electronic structure calculations according to particular needs.

One should mention a peculiarity that appears when a DFT calculation includes the spin-orbit coupling *a priori*.[57] One is concerned in this context with the spin since the non-relativistic XC functionals are spin-dependent. Their use in a relativistic framework requires a proper definition of the spin density in order to obtain the correct energy. One simple way to do this consists in defining it *via* the projection of the spin-magnetization vector onto a chosen axis (commonly the z-axis).[57] This is the basis of the collinear approach and it is formally inconsistent with the spin-orbit

interaction, leading the XC energy to depend on the coordinate frame that is used in the calculation. In contrast to open-shell systems, the consequences of this approach are actually rather limited on the calculated properties of essentially-closed-shell systems. Alternatively, one can define the spin density using the non-collinear approach which promotes the length of the spin-magnetization vector.[57] The success of this approach is related to the fact that this quantity is invariant to any rotation in the coordinate frame.

2.3.4 Two-step approaches

Relativistic effects can be treated following several strategies, including in two-step ways. Of course, one consistent way is to perform one-step calculations where relativistic effects and electron correlation are treated on an equal footing in the self-consistent-field (SCF) treatment. An alternative strategy consists in treating the SOC *a posteriori*, as a perturbation to the spin-orbit free Hamiltonian. In such approaches, scalar relativistic DKH or ZORA Hamiltonians can be used to retain scalar relativistic effects within MCSCF-based electron correlation methods in a first step. In a second step, an effective spin-orbit Hamiltonian (*e.g.* the Breit-Pauli one) is used. A state-interaction (SI) matrix is then constructed from the M_S components of the SOF states and its diagonal is usually dressed with correlated energies obtained with post-MCSCF perturbative or variational schemes. The spin-orbit corrected eigenvalues and eigenvectors are obtained by diagonalizing this SI matrix, *i.e.* diagonalizing $H^{\mathrm{SI}} = E_{el} + \hat{H}^{\mathrm{SO}}$. A typical example of a two-step approach is the contracted spin-orbit configuration interaction (c-SOCI). In the c-SOCI flavor here retained, the set of SOF states are generated through scalar relativistic state-averaged CASSCF (SA-CASSCF) calculations. The correlated energies to dress the diagonal of the SI matrix are obtained using subsequent NEVTP2 calculations. We note that uncontracted schemes (*i.e.* uc-SOCI) also exist,[58] and may be required in some cases to reach spectroscopy accuracy.[28,58]

2.3.5 Relativistic effective core potentials

Relativistic effective core potentials (RECPs) can be used to treat implicitly relativistic effects within non-relativistic or relativistic schemes.[26] Their use can bring many advantages. On the one hand, it reduces the computational effort by "replacing" core electrons and their effects with properly parameterized potentials. Consequently, it reduces the number of electrons and basis functions to be treated, and orients the computational effort on the chemically-relevant valence electrons. On the other hand, it allows the implicit or explicit inclusion of the major relativistic effects (scalar relativistic effects and SOC) in a valence-only calculation. An extraordinary asset of RECPs is that they can be employed in almost all kinds of wave function or DFT-based

calculations, delivering highly accurate geometries, energies or relativistic contributions fairly comparable to all-electron fully-relativistic calculations. For example, the NWChem and TURBOMOLE program packages[59,60] implement 2*c*-DFT methods which make use of scalar relativistic and spin-orbit parameterized RECPs, thus allowing the simultaneous treatment of relativistic effects and electron correlation in an elegant fashion. When a RECP is employed, one needs to formulate a valence-only model Hamiltonian to describe the interactions (i) among the valence electrons and (ii) among the valence electrons and the atomic/molecular core(s). The general form of this model Hamiltonian reads:[26]

$$\hat{H}^{\mathrm{V}} = \sum_{i}^{n_v} -\frac{1}{2}\Delta_i + \sum_{i<j}^{n_v} \frac{1}{r_{ij}} + \sum_{i}^{n_v}\sum_{I}^{N} V_{cv}^{I}(i) + \sum_{I>J}^{N} \frac{Q_I Q_J}{R_{IJ}} + \hat{V}_{\mathrm{CPP}} \tag{2.35}$$

where the first term sums up the valence one-electron kinetic energies, the second term sums up the valence electron-electron repulsions, the third term sums up the interactions between valence electron and the nuclei/cores present in the system, the forth term sums up the repulsions between cores and nuclei, and the last term is a core polarization potential. Scalar relativistic effects and SOC are then incorporated through proper parameterizations of the V_{cv}^{I} term. A general classification of ECPs proceeds with model potentials, designed to reproduce valence orbitals with the correct number of radial nodes, and pseudopotentials (PPs), designed to produce pseudo valence orbitals with a reduced number of radial nodes that usually display a qualitatively correct shape in the valence region. PPs can be energy or shape-consistent, depending on the way they are generated. The former ones are for instance heavily developed by the Stuttgart/Cologne groups in Germany, and are parameterized to reproduce accurately atomic spectra.[61] Their general notation reads ECP*n*XY where *n* specifies the number of core electrons to be replaced by the ECP, X can be either S or M corresponding to single- or multi-electron fits, and Y stands for the theoretical method used to produce the reference data against which the ECP is parameterized. DF can be a choice for Y, meaning in this case that the reference data is obtained in multiconfigurational Dirac-Hartree-Fock calculations based on the Dirac-Coulomb(-Breit) Hamiltonian.[62] The shape-consistent PPs are parameterized to reproduce the shape of the valence orbitals in the valence region.

2.4 Quantum mechanical calculations including solvent effects

When experimental measurements are carried out in solutions, the measured properties then include solvation effects. In most cases, such effects are not negligible and can manifest to such an extent that they can even completely change the gas-phase picture. Dealing with solvation processes

may not necessarily be straightforward in computational studies. One way to proceed is to use an explicit solvation model, *i.e.* to add to the system under study a consistent number of surrounding explicit solvent molecules in a dynamic or static fashion. However, this approach has the obvious disadvantage to add up a tremendous computational effort when the quantum mechanical treatment of the individual solvent molecules is attempted. A more convenient way is to employ an implicit solvation model, *i.e.* to model the solvent as a continuum characterized by a dielectric constant. In this spirit, one can use for instance the polarizable continuum model (PCM).[63,64] In this approach, the solute molecule is placed in a cavity surrounded by a dielectric continuum, whose polarization induces point charges at the cavity surface. The accuracy of such a model may then depend on several factors as the boundary conditions for the dielectric constant, the shape of the solute cavity or the balanced treatment of the various factors contributing to solvation. The main quantity which is sought in a PCM calculation, is the free energy of solvation:

$$\Delta G_s = \Delta G_{\text{es}} + \Delta G_{\text{disp-rep}} + \Delta G_{\text{cav}} \tag{2.36}$$

Where ΔG_{es} is the electrostatic contribution, $\Delta G_{\text{disp-rep}}$ is the dispersion and repulsion contributions, and ΔG_{cav} is known as the cavitation energy necessary to create the cavity which hosts the solute within the dielectric continuum. From this partitioning, the electrostatic component is the dominant one that drives the solvation free energy and is sought to be calculated with high accuracy. Moreover, this term is the only one entering the quantum mechanical formulation of PCM, the dispersion-repulsion and the cavitation energies being calculated in a semi-classical fashion. The general form of ΔG_{es} reads:[63]

$$\Delta G_{\text{es}} = \frac{1}{2}\int_{\Gamma} \sigma(\vec{s}) \left[\int_{V} \frac{\rho_{\text{M}}(\vec{r})}{|\vec{r}-\vec{s}|} d^3 r \right] d^2 s \tag{2.37}$$

where $\sigma(\vec{s})$ is the surface charge distribution and $\rho_{\text{M}}(\vec{r})$ is the solute charge distribution inside the cavity. Several PCM flavors have emerged depending on the formulation of the $\sigma(\vec{s})$ term, a widely used one being the conductor-like PCM model (CPCM).[65] Its main characteristic is that it models the solvent as a conductor, *i.e.* with a large dielectric constant, while employing some scaled boundary conditions for the dielectric constant in order to reproduce the results for a case where the dielectric constant is finite. CPCM is hence very successful for highly polar solvents, such as water, while less accurate results are expected for solvents with low polarity. In some cases, PCM cannot reproduce quantitatively the free energies of solvation. It is in particular true in cases when specific

interactions between the solute and the solvent occur, *e.g.* hydrogen bonds. To retain such effects, the implicit model can be combined with the explicit one: several solvent molecules from the first hydration sphere of the solute are treated explicitly while the bulk solvent is treated with a continuum.

The cavity in which the solute is placed plays a very important role in PCM as it dramatically influences the free energy of solvation. It is usually built from a set of interlocking spheres centered on the solute atoms.[66] The dimension of the individual spheres building up the cavity, and hence the topology of the cavity itself, depends on the radius assigned to each atom of the solute. There are several cavity models widely used today including among the most popular ones, the universal force-field (UFF) model and the united atom (UA) topological models. The UA models can build cavities according to radii optimized at the HF/6-31G(d) level of theory, leading to the UAHF cavity model,[67] or from radii optimized at the PBE0/6-31G(d) level of theory, leading to the UAKS cavity model. An asset of the UA models, that is not present in the UFF one, is that they offer flexible radii that can adjust according to chemical considerations as hybridization state of the atom, formal charge and first-neighbor inductive effects.

Note that in the Gaussian 09 program package,[68] the $\Delta G_{\text{disp-rep}}$ and ΔG_{cav} terms are no longer computed by default while they essentially cancel each other (they are of opposite signs).[69] Furthermore, the dispersion and repulsion contributions are even unknown for At species due to the lack of specific parameters for At. Hence, only the dominant electrostatic parts of the free energies of solvation are retained in the free energies of solvation that will be presented in this thesis.

2.4.1 Computational studies of At species in aqueous solution

As pointed out previously, experiments involving At and/or At species are carried out in aqueous solution. Similarly, medicinal trials with ^{211}At-agents are also carried out in aqueous media. Whenever the context requires it, solvation effects on At species must be accounted for in the theoretical predictions. However, treating them on a same footing as SOC is yet a bottleneck for a computational study, and a compromising strategy needs to be established. Champion *et al.* have proposed a strategy and applied it successfully in predicting reaction equilibrium constants, for instance, for reactions similar to the ones shown in Eq. 1.3.[70] This strategy proposes the derivation of the stability constant from the free energy change in aqueous solution (ΔG_s^*), which in turn is calculated using a thermodynamic cycle, similar to the one shown in Scheme 2.1.

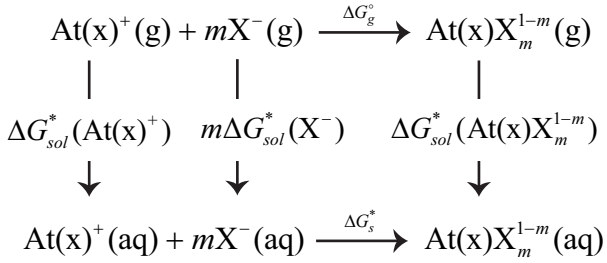

Scheme 2.1 Thermodynamic cycle used to compute free energy changes in aqueous solution for reactions similar to the ones shown in Eq. 1.3.

According to this cycle, ΔG_s^* is written as:

$$\Delta G_s^* = \Delta G_g^\circ + \Delta G_{sol}^*(\mathrm{At(x)X}_m^{1-m}) - \Delta G_{sol}^*(\mathrm{At(x)}^+) - m\Delta G_{sol}^*(\mathrm{X}^-) \qquad (2.38)$$

where ΔG_g° is the free energy change in the gas-phase and the remaining terms are the free energies of solvation of the respective species in water. SOC can be included routinely in the gas phase calculations (hence in the ΔG_g° term), while the free energies of solvation are calculated in the absence of SOC but in the presence of scalar relativistic effects. It turns out that the calculated ΔG_s^*, from which the reaction equilibrium constant is derived, somehow includes both the effect of SOC and solvation. With proper choices of the thermodynamic cycles *(e.g.* choosing, for instance, thermodynamic cycles corresponding to ligand-exchange reactions, as it will be exemplified later), equilibrium constants of reactions involving At species can accurately be predicted.[70,71]

Bibliography:

1. T. Helgaker, P. Jørgensen, J. Olsen, Molecular electronic-structure theory. John Wiley & Sons, **2014**.
2. T. Saue, PhD dissertation: Principles and applications of relativistic molecular calculations, University of Oslo, **1995**.
3. W. Koch, M. C. Holthausen, A chemist's guide to density functional theory. John Wiley & Sons, **2015**.
4. K. G. Dyall, J. K. Faegri, Introduction to relativistic quantum chemistry. Oxford University Press, **2007**.
5. C. C. J. Roothaan, *Rev. Mod. Phys.* New developments in molecular orbital theory, **1951**, 23, 69.
6. G. G. Hall, *Proc. Roy. Soc. Lond.* The molecular orbital theory of chemical valency. VIII. A method of calculationg ionization potentials, **1951**, 205, 441.
7. C. Møller, M. S. Plesset, *Phys. Rev.* Note on an approximation treatment for many-electron systems, **1934**, 46, 618.
8. J. Paldus, Theory and applications of computational chemistry. Elsevier, **2005**.
9. D. Sherrill, H. F. Schaefer, *Adv. Quantum Chem.* The configuration interaction method: Advances in highly correlated approaches, **1999**, 34, 143.
10. S. R. Langhoff, E. R. Davidson, *Int. J. Quantum Chem.* Configuration interaction calculations on the nitrogen molecule, **1974**, 8, 61.
11. E. R. Davidson, K. B. Lipkowitz, D. B. Boyd, Perspectives on *ab initio* calculations. VCH, **1990**.
12. B. O. Roos, P. T. Taylor, P. E. M. Siegbahn, *Chem. Phys.* A complete active space SCF method (CASSCF) using a density matrix formulated super-CI approach, **1980**, 48, 157.
13. C. Dykstra, G. Frenking, K. Kim, G. Scuseria, Theory and Applications of Computational Chemistry: the first forty years. Elsevier, **2011**.
14. K. Andersson, P.-Å. Malmqvist, B. O. Roos, *J. Chem. Phys.* Second-order perturbation theory with a complete active space self-consistent field reference function, **1992**, 96, 1218.
15. C. Angeli, R. Cimiraglia, S. Evangelisti, T. Leininger, J. P. Malrieu, *J. Chem. Phys.* Introduction of n-electron valence states for multireference perturbation theory, **2001**, 114, 10252.
16. N. Forsberg, P.-Å. Malmqvist, *Chem. Phys. Lett.* Multiconfiguration perturbation theory with imaginary level shift, **1997**, 274, 196.
17. K. G. Dyall, *J. Chem. Phys.* The choice of a zeroth-order Hamiltonian for second-order perturbation theory with a complete active space self-consistent-field reference function, **1995**, 102, 4909.
18. R. W. A. Havenith, P. R. Taylor, C. Angeli, R. Cimiraglia, K. Ruud, *J. Chem. Phys.* Calibration of the n-electron valence state perturbation theory approach, **2004**, 120, 4619.
19. C. Angeli, R. Cimiraglia, J.-P. Malrieu, *Chem. Phys. Lett.* N-electron valence state perturbation theory: a fast implementation of the strongly contracted variant, **2001**, 350, 297.
20. H. J. Werner, P. J. Knowles, *J. Chem. Phys.* An efficient internally contracted multiconfiguration–reference configuration interaction method, **1988**, 89, 5803.
21. P. E. M. Siegbahn, *Chem. Phys.* The direct configuration interaction method with a contracted configuration expansion, **1977**, 25, 197.
22. P. E. M. Siegbahn, *Int. J. Quantum Chem.* The externally contracted CI method applied to N_2, **1983**, 23, 1869.
23. J. P. Malrieu, *Chem. Rev.* Magnetic interactions in molecules and highly interacting correlated materials: physical content, analytical derivation, and rigurous extraction of magnetic Hamiltonians, **2014**, 114, 429.

24. A. Banerjee, J. Simons, *Int. J. Quantum Chem.* The couppled-cluster method with a multiconfiguration reference state, **1981**, 19, 207.
25. U. Kaldor, *Theor. Chim. Acta.* The Fock space coupled cluster method: Theory and application, **1991**, 80, 427.
26. M. Dolg, Computational methods in lanthanide and actinide chemistry. John Wiley & Sons, **2015**.
27. A. Landau, E. Eliav, Y. Ishikawa, U. Kaldor, *J. Chem. Phys.* Intermediate Hamiltonian Fock-space coupled-cluster method: Excitation energies of barium and radium, **2000**, 113, 9905.
28. R. Maurice, F. Réal, A. S. P. Gomes, V. Vallet, G. Montavon, N. Galland, *J. Chem. Phys.* Effective bond orders from two-step spin–orbit coupling approaches: The I_2, At_2, IO^+, and AtO^+ case studies, **2015**, 142, 094305.
29. A. S. P. Gomes, F. Réal, N. Galland, C. Angeli, R. Cimiraglia, V. Vallet, *Phys. Chem. Chem. Phys.* Electronic structure investigation of the evanescent AtO^+ ion, **2014**, 16, 9238.
30. P. Hohenberg, W. Kohn, *Phys. Rev. B.* Inhomogeneous electron gas, **1964**, 136, 864.
31. L. H. Thomas, *Proc. Cambridge Philos. Soc.* The calculation of atomic fields, **1927**, 23, 542.
32. E. Fermi, *Rend. Accad. Naz. Lincei.* Statistical method to determine some properties of atoms, **1927**, 6, 602.
33. P. A. M. Dirac, *Proc. Cambridge Philos. Soc.* Note on exchange phenomena in the Thomas atom, **1930**, 26, 376.
34. E. Teller, *Rev. Mod. Phys.* On the stability of molecules in the Thomas-Fermi theory, **1962**, 34, 627.
35. C. F. Weizsäcker, *Z. Phys.* Zur theorie der kernmassen, **1935**, 96, 431.
36. W. Kohn, L. J. Sham, *Phys. Rev. A.* Self-consistent equations including exchange and correlation effects, **1965**, 140, 1133.
37. A. D. Becke, *J. Chem. Phys.* Perspective: Fifty years of density-functional theory in chemical physics, **2014**, 140, 18A301.
38. S. H. Vosko, L. Wilk, M. Nusair, *Can. J. Phys.* Accurate spin-dependent electron liquid correlation energies for local spin density calculations: a critical analysis, **1980**, 58, 1200.
39. C. Lee, W. Yang, R. G. Parr, *Phys. Rev. B.* Development of the Colle-Salvetti correlation-energy formula into a functional of the electron density, **1988**, 37, 785.
40. A. D. Becke, *Phys. Rev. A.* Density-functional exchange-energy approximation with correct asymptotic behavior, **1988**, 38, 3098.
41. A. D. Becke, *J. Chem. Phys.* Density-functional thermochemistry. III. The role of exact exchange, **1993**, 98, 5648.
42. P. J. Stephens, F. J. Devlin, C. Chabalowski, M. J. Frisch, *J. Phys. Chem. Ab initio* calculation of vibrational absorption and circular dichroism spectra using density functional force fields, **1994**, 98, 11623.
43. Y. Zhao, D. G. Truhlar, *Theor. Chem. Acc.* The M06 suite of density functionals for main group thermochemistry, thermochemical kinetics, noncovalent interactions, excited states, and transition elements: two new functionals and systematic testing of four M06-class functionals and 12 other functionals, **2008**, 120, 215.
44. T. Yanai, D. P. Tew, N. C. Handy, *Chem. Phys. Lett.* A new hybrid exchange–correlation functional using the Coulomb-attenuating method (CAM-B3LYP), **2004**, 393, 51.
45. J. Heyd, G. E. Scuseria, M. Ernzerhof, *J. Chem. Phys.* Erratum: "Hybrid functionals based on a screened Coulomb potential" [J. Chem. Phys. 118, 8207 (2003)], **2006**, 124, 219906.

46. J. Heyd, G. E. Scuseria, M. Ernzerhof, *J. Chem. Phys.* Hybrid functionals based on a screened Coulomb potential, **2003**, 118, 8207.
47. P. Pyykko, *Chem. Rev.* Relativistic effects in structural chemistry, **1988**, 88, 563.
48. J. Autschbach, *J. Chem. Phys.* Perspective: Relativistic effects, **2012**, 136, 150902.
49. W. A. Jong, PhD dissertation: Relativistic quantum chemistry applied, University of Groningen, **1998**.
50. T. Saue, *ChemPhysChem.* Relativistic Hamiltonians for chemistry: A primer, **2011**, 12, 3077.
51. E. V. Lenthe, E. J. Baerends, J. G. Snijders, *J. Chem. Phys.* Relativistic regular two-component Hamiltonians, **1993**, 99, 4597.
52. C. Chang, M. Pelissier, P. Durand, *Phys. Scr.* Regular two-component Pauli-like effective Hamiltonians in Dirac theory, **1986**, 34, 394.
53. M. Douglas, N. M. Kroll, *Ann. Phys.* Quantum electrodynamical corrections to the fine structure of helium, **1974**, 82, 89.
54. G. Jansen, B. A. Heß, *Phys. Rev. A.* Revision of the Douglas-Kroll transformation, **1989**, 39, 6016.
55. B. A. Hesß, *Phys. Rev. A.* Relativistic electronic-structure calculations employing a two-component no-pair formalism with external-field projection operators, **1986**, 33, 3742.
56. T. Nakajima, K. Hirao, *Chem. Rev.* The Douglas–Kroll–Hess approach, **2012**, 112, 385.
57. C. V. Wüllen, *J. Comput. Chem.* Spin densities in two-component relativistic density functional calculations: Noncollinear versus collinear approach, **2002**, 23, 779.
58. V. Vallet, L. Maron, C. Teichteil, J.-P. Flament, *J. Chem. Phys.* A two-step uncontracted determinental effective Hamiltonian-based SO-CI method, **2000**, 113, 1391.
59. M. Valiev, E. J. Bylaska, N. Govind, K. Kowalski, T. P. Straatsma, H. J. J. V. Dam, D. Wang, J. Nieplocha, E. Apra, T. L. Windus, *Comput. Phys. Commun.* NWChem: a comprehensive and scalable open-source solution for large scale molecular simulations, **2010**, 181, 1477.
60. R. Ahlrichs, M. K. Armbruster, R. A. Bachorz, M. Bär, H.-P. Baron, R. Bauernschmitt, F. A. Bischoff, S. Böcker, N. Crawford, P. Deglmann, Fabio Della Sala, M. Diedenhofen, M. Ehrig, K. Eichkorn, S. Elliott, D. Friese, F. Furche, A. Glöß, F. Haase, M. Häser, C. Hättig, A. Hellweg, S. Höfener, H. Horn, C. Huber, U. Huniar, M. Kattannek, W. Klopper, A. Köhn, C. Kölmel, M. Kollwitz, K. May, P. Nava, C. Ochsenfeld, H. Öhm, M. Pabst, H. Patzelt, D. Rappoport, O. Rubner, A. Schäfer, U. Schneider, M. Sierka, D. P. Tew, O. Treutler, B. Unterreiner, M. von Arnim, F. Weigend, P. Weis, H. Weiss, N. Winter, TURBOMOLE version 6.6, a development of University of Karlsruhe and Forschungszentrum Karlsruhe GmbH, TURBOMOLE GmbH, **2014**.
61. Available at the following link: http://www.tc.uni-koeln.de/PP/clickpse.en.html.
62. M. Dolg, H. Stoll, H. Preuss, R. M. Pitzer, *J. Phys. Chem.* Relativistic and correlation effects for element 105 (Hahnium, Ha): a comparative study of M and MO (M = Nb, Ta, Ha) using energy-adjusted *ab initio* pseudopotentials, **1993**, 97, 5852.
63. B. Mennucci, *Wires Comput. Mol. Sci.* Polarizable continuum model, **2012**, 2, 386.
64. J. Tomasi, M. Persico, *Chem. Rev.* Molecular interactions in solution: an overview of methods based on continuous distributions of the solvent, **1994**, 94, 2027.
65. M. Cossi, N. Rega, G. Scalmani, V. Barone, *J. Comput. Chem.* Energies, structures, and electronic properties of molecules in solution with the C-PCM solvation model, **2003**, 24, 669.

66. J.-L. Pascual-Ahuir, E. Silla, I. Tunon, *J. Comput. Chem.* GEPOL: An improved description of molecular surfaces. III. A new algorithm for the computation of a solvent-excluding surface, **1994**, 15, 1127.

67. V. Barone, M. Cossi, J. Tomasi, *J. Chem. Phys.* A new definition of cavities for the computation of solvation free energies by the polarizable continuum model, **1997**, 107, 3210.

68. M. J. Frisch, G. W. Trucks, H. B. Schlegel, G. E. Scuseria, M. A. Robb, J. R. Cheeseman, G. Scalmani, V. Barone, B. Mennucci, G. A. Petersson, H. Nakatsuji, M. Caricato, X. Li, H. P. Hratchian, A. F. Izmaylov, J. Bloino, G. Zheng, J. L. Sonnenberg, M. Hada, M. Ehara, K. Toyota, R. Fukuda, J. Hasegawa, M. Ishida, T. Nakajima, Y. Honda, O. Kitao, H. Nakai, T. Vreven, J. A. Montgomery, J. E. Peralta, F. Ogliaro, M. Bearpark, J. J. Heyd, E. Brothers, K. N. Kudin, V. N. Staroverov, R. Kobayashi, J. Normand, K. Raghavachari, A. Rendell, J. C. Burant, S. S. Iyengar, J. Tomasi, M. Cossi, N. Rega, J. M. Millam, M. Klene, J. E. Knox, J. B. Cross, V. Bakken, C. Adamo, J. Jaramillo, R. Gomperts, R. E. Stratmann, O. Yazyev, A. J. Austin, R. Cammi, C. Pomelli, J. W. Ochterski, R. L. Martin, K. Morokuma, V. G. Zakrzewski, G. A. Voth, P. Salvador, J. J. Dannenberg, S. Dapprich, A. D. Daniels, Ö. Farkas, J. B. Foresman, J. V. Ortiz, J. Cioslowski, D. J. Fox, Gaussian 09; Gaussian Inc.: Wallingford, CT, **2009**.

69. C. J. Cramer, Essentials of computational chemistry: theories and models. John Wiley & Sons, **2004**.

70. J. Champion, M. Seydou, A. Sabatié-Gogova, E. Renault, G. Montavon, N. Galland, *Phys. Chem. Chem. Phys.* Assessment of an effective quasirelativistic methodology designed to study astatine chemistry in aqueous solution, **2011**, 13, 14984.

71. J. Champion, A. a. Sabatié-Gogova, F. Bassal, T. Ayed, C. Alliot, N. Galland, G. Montavon, *J. Phys. Chem. A.* Investigation of astatine (III) hydrolyzed species: Experiments and relativistic calculations, **2013**, 117, 1983.

Chapter 3

Identifying Adequate DFT Functionals to Investigate the Properties of At Species

DFT-based approaches are highly desirable to investigate properties of medium to large At species. However, in order to reach relevant results, a density functional approximation must be properly chosen at first and then adequate basis sets and strategies to account for environmental effects. These aspects are tackled in the present chapter, and we note that the data has been published in *J. Comput. Chem.*,[1] and it is presented here in a slightly different way.

3.1 Introduction

Due to its simple formulation, DFT is undoubtedly an attractive method to pursue quantum mechanical investigations of medium to large At-containing systems. One then has to choose an appropriate DFT setup in order to approach targeted accuracies when computing various properties concerning such species. While we pointed out in Chapter 1 that the computational study of At species requires the treatment of relativity, one has to perform relativistic DFT computations based on the Dirac-Coulomb Hamiltonian. Fully relativistic (4*c*) formulations of DFT have been reported and all-electron calculations based on such a framework have been successfully performed for instance on various diatomics involving some halogens or some transitional metals.[2,3] Conveniently, (2*c*) quasi-relativistic formulations of DFT have been developed.[4,5] Such methods (2*c*-DFT or SO-DFT) may use 2*c* RECPs to treat relativistic effects and electron correlation on an equal footing, at cost-effective levels. If a proper XC functional is used in a 2*c*-DFT calculation, one can in principle retrieve results comparable to experiment or all-electron, let say 4*c*-CCSD(T) calculations. As such, 2*c*-DFT is appealing for geometry optimizations and calculations of vibrational frequencies for medium to large At species, which can be very tedious if not impossible for relativistic wave-

function-based methods. The major degree of freedom that remains at play is the choice of a proper XC functional to study At chemistry (not to mention the choice of RECP-basis set couples). So far, and strictly in basic At-chemistry oriented applications, *e.g.* in the calculation of reaction equilibrium constants,[6] or in the investigation of the AtO^+ behavior in aqueous solution,[7,8] the B3LYP and M06-2X hybrid functionals have been used. While B3LYP appears to be a good choice as it allowed for instance the computation of reaction equilibrium constants in very good agreement with experiment,[6] the choice of the M06-2X functional has recently been questioned in the literature.[9] Some other quasi-relativistic DFT studies have been carried out by Lee and coworkers or Mitin and coworkers.[10-12] These studies concerned monoatomic At or some At diatomics (*e.g.* AtH, AtTl, At_2), and were oriented on the calibration of the quasi-relativistic DFT methodology and/or on the magnitude of SOC on spectroscopic constants. Nevertheless, while these studies confirm the reliability of using such a methodology for At species, they report different accuracies for different XC functionals when compared to reference 2*c*- or 4*c*-CCSD(T) calculations. Given our motivation to further use quasi-relativistic DFT calculations to explore the chemistry of medium to large At species, we now present the objectives of the current chapter.

A first objective consists in identifying XC functionals that are, within the quasi-relativistic DFT framework, adequate to investigate medium to large At-containing systems in order to (i) obtain accurate geometries which may be thereafter used for instance in more accurate relativistic wave-function-based single-point calculations and, (ii) obtain accurate vibrational frequencies in view of thermodynamic analyses. A second objective consists in establishing a computational strategy, based on quasi-relativistic DFT, which can be safely used for predicting At-chemistry in aqueous solution. Hence, this second objective concerns both the choice of a proper XC functional and of the solvation scheme/model. Nonetheless, both objectives concern as well the choice of reasonably-sized basis sets. As such, a panel of nonrelativistic XC density functionals spanning several categories (LDA, GGA, meta-GGA, hybrid GGA, hybrid meta-GGA and range-separated), three basis sets of increasing size, and different solvation approaches, are employed to compute geometries, transition energies and thermodynamic properties for the At species for which reference experimental or high-level theoretical data is available.

3.2 Computational details

In this chapter, 2*c*-DFT calculations on most essentially closed-shell At species are performed with the NWChem program package[13] while the TURBOMOLE program package[14] was generally used for calculations on open-shell At species. In contrast with the former, the latter

package implements the 2*c*-DFT method with the non-collinear approach,[15] which is a consistent way to define the spin density when a spin-orbit Hamiltonian is involved in calculations on open-shell species (see Chapter 2). 2*c*-DFT calculations are performed in order to get insights of geometries, transition energies and/or vibrational frequencies on the following systems: $At/At^+/At^-$, $I/I^+/I^-$, At_2, HAt, AtF_3, AtO^+, AtCl, $AtCl_2^-$, AtBr, $AtBr_2^-$, AtSCN, $AtSCN_2^-$, AtOCl, $AtOCl_2^-$, AtOOH and AtOSCN. A set of 36 XC density functionals comprising the SVWN[16] LSDA functional, the BLYP,[17,18] BP86,[18,19] PW91,[20,21] PBE,[22] revPBE,[23] HCTH[24] and OLYP[17,25] GGA functionals, the PKZB,[26] TPSS,[27] VS98,[28] M06-L[29] and M11-L[30] meta-GGA functionals, the B3LYP,[17,31,32] X3LYP,[33] B3PW91,[21,31] BH&HLYP,[31] PBE0,[34] B97-2[35] and B98[36,37] hybrid GGA functionals, the TPSSh,[38] MPW1B95,[39] PW6B95,[40] MPWB1K,[39] PWB6K,[40] M05,[41] M06,[42] M05-2X,[43] M06-2X,[42] M08-HX[44] and M08-SO[44] hybrid meta-GGA functionals, and the CAM-B3LYP,[45] LC-ωPBE,[46] HSE06,[47,48] BNL[49,50] and M11[51] range-separated functionals, is benchmarked. For the Br, I and At centers, energy-consistent ECP*n*MDF PPs are used to mimic the role of the n = 10, 28 and 60 core electrons, respectively, while implicitly accounting for relativistic effects.[52,53] The remaining 25 valence electrons are dealt with the aug-cc-pV*X*Z-PP basis sets of double-, triple- or quadruple-zeta quality (*i.e.* X = D, T, Q).[52,53] The 2*c* extensions for these basis sets, generated by Armbruster *et al.*, are retained.[54] For the aug-cc-pVDZ-PP basis set of At, the retained 2*c* extension is the one proposed by Champion *et at.*,[6] which improves the one of Armbruster *et al*. The conventional aug-cc-pV*X*Z basis sets are used for all the other atoms.[55-57] Depending on the X cardinal number, the basis set will be denoted as AV*X*Z hereafter, for the sake of simplicity. For comparison purposes, 2*c*-HF and 2*c*-MP2 calculations are also performed. These calculations make use of the resolution of the identity (RI) technique as implemented in the TURBOMOLE program package. According to the construction of the aug-cc-pV*X*Z-PP basis sets, note that the semi-core 3*s*3*p*3*d*, 4*s*4*p*4*d* and 5*s*5*p*5*d* pseudo-spinors of Br, I and At are kept frozen in the 2*c*-MP2 calculations.

The Gaussian 09 program package[58] has been used to calculate free energies of solvation. The CPCM solvation approach is retained and used in conjunction with the UFF, UAHF and the UAKS cavity models. Originally, the UA cavities do not include parameters for At. Hence, a basic radius of 2.41 Å is used, and a charge factor of −0.87 for a positively charged At atom, which have been proposed recently by Champion and coworkers.[6,59] An electrostatic scaling factor of 1.2 is used for multiplying the individual sphere radii, which is not the default one in Gaussian 09. Note that this factor has been used in the original formulation of the UA cavity models.[60]. Solvation free energies are then computed following four different schemes, (i) geometries and energies are

optimized in the gas-phase and then in the presence of the implicit solvent using the UAKS cavities, at the scalar relativistic B3LYP/AVDZ level of theory (denoted hereafter as CPCM-UAKS), (ii) geometries and energies are optimized in the gas-phase and then in the presence of the implicit solvent using the UAHF cavities, at the scalar relativistic HF/AVDZ level of theory (denoted hereafter as CPCM-UAHF), (iii) geometries and energies are optimized in the gas-phase and then in the presence of the implicit solvent using the UFF cavities, at the scalar relativistic HF/AVDZ level of theory (denoted hereafter as CPCM-UFF), and (iv) starting from the CPCM-UAKS optimized geometries, single-point energy calculations are performed in gas-phase and then in the presence of the implicit solvent using the UAHF cavities, at the scalar relativistic HF/AVDZ level of theory (denoted hereafter as CPCM-UAHF//UAKS). Finally, the free energies of solvation of At species that exhibit several conformers are calculated according to a Boltzmann distribution:[61]

$$G_{\{\mathrm{Y}\}} = -\mathrm{R}T \ln \sum_{i \in \{\mathrm{Y}\}} \exp\left(-\frac{G_i}{\mathrm{R}T}\right) \tag{3.1}$$

where the summation runs over the conformers of the Y species and T is 298 K.

3.3 Molecular geometries

3.3.1 Reference data set

At first, the 36 XC functional panel and the AVXZ basis sets have been used to compute geometrical parameters. According to the reasons pointed out in Chapter 1, structural information for At species cannot be currently retrieved from any spectroscopy experiment. Therefore, we have selected from the literature At systems for which the geometries have been calculated within a robust relativistic framework, *i.e.* 2*c* or 4*c*, and at a level of theory involving the CCSD(T) "golden standard" method in conjunction with large basis sets, *i.e.* at least polarized triple-zeta bases augmented with diffuse functions. Accordingly, we have retained At species with ground states that are known to exhibit essentially single-configurational and closed-shell characters, namely At_2, HAt and AtF_3, and one with marked open-shell character, *i.e.* AtO^+. Among those, the structures of At_2 and AtF_3 have been calculated with a 2*c*-CCSD(T) method[62,63] while that of HAt and AtO^+, with a 4*c*-CCSD(T) one.[9,64] For the AtF_3 system, the reference 2*c*-CCSD(T) calculations have proven that it can exhibit two stable structures, one with a D_{3h} geometry whose energy is about 7 kJ·mol^{-1} higher than the one of three equivalent bent T-shaped C_{2v} structures corresponding to the global minima on the potential energy surface (PES). Hence, both the D_{3h} and C_{2v} AtF_3 structures are retained in the present study. The equilibrium bond lengths define our reference data set.

3.3.2 Assessment of 36 XC functionals

In Table 3.1, bond lengths and associated relative mean-signed errors (MSEs), mean-unsigned errors (MUEs), root-mean-square deviations (RMSDs) and maximum absolute deviations (MaxDs), calculated at the 2*c*-DFT/AVTZ level of theory, are shown. Values obtained at the 2*c*-DFT/AVDZ level are placed for convenience in Table A1.1 (see Appendix 1). Concerning each error/deviation criterion, the five best values are evidenced in red and the best of them is also displayed in bold. Focusing on the results shown in Table 3.1, we identified first that the D_{3h} structure of AtF_3 does not correspond to a minimum in HF calculations. Also, several density functionals do not predict a stable C_{2v} structure for AtF_3. It is in particular true for the pure functionals LSDA, GGAs and the PKZB and TPSS meta-GGAs. It is worth noting that this trend is already present when the AVDZ basis sets are used (see Table A1.1). Moreover, we noticed that Yang *et al.* reported similar findings in their 2*c*-DFT calculations employing some of the aforementioned functionals and def2-QZVPP basis sets.[63] Therefore, in the case where the C_{2v} or the D_{3h} structure of AtF_3 was not identified to correspond to a minimum, we have removed it from the calculation of the errors/deviations. Nevertheless, we conclude that these functionals are inadequate for studying geometries of systems containing an At atom. From the meta-GGA block, the functionals that do not pose such an issue, *i.e.* VS98, M06-L and M11-L, yield the largest errors/deviations among all other functionals (*e.g.* MaxDs $\geq$ 3.0%), and therefore, are also not recommended for this purpose.

Focusing on the hybrid GGA block of functionals, we identified that all of them predict accurate geometries with MaxDs of at most ~3% and MUEs and RMSDs always smaller than ~2%. PBE0 appears to be the best-performing hybrid GGA functional. It delivers the lowest MaxD (1.5%) among all other density functionals, and a MSE and a RMSD which are among the five lowest values. It is worth noting that alongside B97-2 and B3PW91, PBE0 predicts lower or similar errors/deviations than MP2. At a first glance, BH&HLYP appears attractive too. That is, since compared to PBE0, it delivers as well a MSE and a RMSD which are within the evidenced lowest five values, while it delivers this time the lowest MUE among all the other relevant functionals (0.7%). Nonetheless, one can note that the D_{3h} structure for AtF_3 is no longer a minimum when the BH&HLYP functional is used in conjunction with the AVDZ basis sets (see Table A1.1).

Table 3.1 Calculated bond lengths (in Å) using several XC functionals and AVTZ basis sets, and associated MSEs, MUEs, RMSDs and MaxDs (in %).

Functional	At_2	HAt	AtF_3^{C2v}		AtF_3^{D3h}	AtO^+	MSE	MUE	RMSD	MaxD
LSDA										
SVWN[a]	2.972	1.742	-	-	2.072	1.918	0.2	1.1	1.1	1.4
GGAs										
BLYP[a]	3.116	1.759	-	-	2.124	1.959	2.8	2.8	3.0	3.8
BP86[a]	3.048	1.750	-	-	2.106	1.942	1.7	1.7	1.9	2.9
PW91[a]	3.068	1.744	-	-	2.157	1.929	1.5	1.5	1.7	2.8
PBE[a]	3.036	1.749	-	-	2.104	1.953	1.7	1.7	1.9	2.8
revPBE[a]	3.057	1.751	-	-	2.114	1.946	1.9	1.9	2.1	3.3
HCTH[a]	3.036	1.748	-	-	2.103	1.940	2.3	2.3	3.0	5.4
OLYP[a]	3.052	1.742	-	-	2.103	1.932	1.5	1.5	1.7	2.8
Meta-GGAs										
PKZB[a]	3.032	1.747	-	-	2.108	1.940	1.5	1.5	1.8	3.0
TPSS[a]	3.023	1.742	-	-	2.095	1.935	1.1	1.1	1.4	2.4
VS98	3.095	1.738	2.097	2.047	2.100	1.932	2.1	2.1	2.3	3.0
M06-L	3.097	1.742	2.095	2.050	2.094	1.920	2.0	2.1	2.3	3.2
M11-L	2.983	1.716	1.984	1.917	1.995	1.856	−2.3	2.3	2.7	3.8
Hybrid GGAs										
B3LYP	3.048	1.741	2.091	2.044	2.089	1.922	1.6	1.7	1.9	2.9
X3LYP	3.043	1.740	2.088	2.038	2.086	1.919	1.4	1.6	1.7	2.6
B3PW91	2.982	1.732	2.073	2.020	2.072	1.907	0.5	1.2	1.2	1.6
BH&HLYP	2.988	1.722	2.054	1.990	2.056	1.883	−0.3	**0.7**	1.1	2.4
PBE0	2.978	1.730	2.068	2.012	2.068	1.902	0.3	1.1	1.1	**1.5**
B97-2	3.004	1.731	2.075	2.022	2.074	1.905	0.7	1.1	1.2	1.8
B98	3.014	1.734	2.081	2.029	2.079	1.911	0.9	1.3	1.4	2.1
Hybrid meta-GGAs										
TPSSh	3.001	1.735	2.082	2.031	2.081	1.919	1.0	1.2	1.4	2.2
MPW1B95	2.975	1.728	2.062	2.005	2.063	1.895	0.0	1.0	**1.1**	1.8
PW6B95	2.995	1.730	2.070	2.016	2.070	1.903	0.5	1.1	1.1	1.5
MPWB1K	2.949	1.719	2.046	1.983	2.048	1.878	−0.8	0.8	1.3	2.7
PWB6K	2.953	1.718	2.046	1.983	2.048	1.877	−0.8	0.8	1.3	2.7
M05[a]	3.078	1.756	-	-	2.083	1.899	1.2	2.0	2.0	2.4
M06	3.067	1.750	2.080	2.035	2.080	1.901	1.3	1.9	1.9	2.4
M05-2X	2.919	1.718	2.052	1.985	2.053	1.891	−0.7	1.0	1.5	2.9
M06-2X	2.940	1.721	2.058	1.993	2.059	1.891	−0.4	1.0	1.3	2.2
M08-HX	2.923	1.723	2.062	1.993	2.063	1.894	−0.4	1.1	1.4	2.8
M08-SO	3.038	1.748	2.084	2.031	2.085	1.906	1.3	1.7	1.7	2.2
Range-separated										
CAM-B3LYP	2.988	1.729	2.070	2.015	2.070	1.896	0.3	1.1	1.2	1.8
LC-ωPBE	2.935	1.724	2.071	2.017	2.071	1.891	**0.0**	1.5	1.6	2.4
HSE06	2.994	1.732	2.074	2.019	2.073	1.905	0.6	1.1	1.2	1.6
BNL	2.979	1.758	2.092	2.039	2.092	1.914	1.3	1.9	2.0	2.6
M11	2.946	1.729	2.079	2.017	2.080	1.901	0.3	1.5	1.5	2.0
Ab initio										
HF[b]	2.968	1.715	2.033	1.953	-	1.849	−1.6	1.6	2.1	4.2
MP2	2.978	1.722	2.075	2.020	2.075	1.948	0.9	1.1	1.2	1.7
Reference										
	3.006[62]	1.718[64]	2.046[63]	1.987[63]	2.046[63]	1.930[9]				

[a]The C_{2v} structure of AtF_3 is not a minimum and hence it is removed from the calculation of the different errors/deviations.

[b]The D_{3h} structure of AtF_3 is not a minimum and hence it is removed from the calculation of the different errors/deviations.

In view of calculating accurate geometries for medium to large At systems, then BH&HLYP could be problematic since in such cases one would rather use a "small" basis set such as the AVDZ one.

Accordingly, in general, we do not consider the BH&HLYP functional appropriate for studying geometries of At species.

Several functionals from the hybrid meta-GGA block, developed mainly by the Minnesota group, were found problematic. Among them, only the M05 functional could not locate a minimum C_{2v} structure for AtF_3 when the AVTZ basis set is used. In change, five functionals, MPWB1K, PWB6K and the M06-2X, M08-HX and M08-SO ones from the "M" family, were unable to locate a D_{3h} minimum for AtF_3 when used in conjunction with the AVDZ basis sets (see Table A1.1). Invoking the argument that was given for the BH&HLYP case, we do not consider the aforementioned hybrid meta-GGA functionals as generally adequate to compute geometries for At species. It is worth highlighting that these functionals have a common point. That is, they all share a high fraction of "exact" exchange: 44% for MPWB1K, 46% for PWB6K, 54% for M06-2X, 52% for M08-HX, and 57% for M08-SO. We classify the MPW1B95 and the PW6B95 the best-performing hybrid meta-GGA functionals for predicting geometries of At species. Both these functionals belong to the Minnesota set of functionals and predict accurate geometries with MaxD not exceeding 1.8%, and MUEs and RMSDs lower than ~1%. In view of the selected criteria shown in Table 3.1, MPW1B95 and PW6B95 perform on average better than MP2 but quite similar to the best-performing functionals from the hybrid GGA block (PBE0, B3PW91 and B97-2). In particular, it is worth noting that MPW1B95 delivers among all the functionals the lowest RMSD (1.1%). Finally, we rank as robust the M05-2X and M06 hybrid meta-GGA functionals from the Minnesota "M" family, in view of their behavior when used in conjunction with both the AVDZ and AVTZ basis sets. However, when compared to the meta-GGA "M" functionals, they bring only slight improvements. Apparently, M05-2X is the best-performing functional among all the studied functionals when used in conjunction with the AVDZ basis sets, scoring the best values for all the four criteria (see Table A1.1).

We finally turn our attention to the functionals from the range-separated block. The CAM-B3LYP, LC-ωPBE, BNL and M11 ones were found inadequate to calculate geometries for medium to large At species since, when used in conjunction with the AVDZ basis set, they failed to localize a minimum D_{3h} structure for AtF_3 (see Table A1.1). Note that these functionals share a high percentage of exact exchange in the long-range limit; CAM-B3LYP has 65% while LC-ωPBE, BNL and M11 have 100%. In contrast, the HSE06 range-separated functional has 0% exact exchange in the long-range limit and actually is the only range-separated functional which we classify as robust for computing geometries in the field of At chemistry. In conjunction with the AVTZ basis set, and in view of the four error/deviation criteria, HSE06 performs generally better

than MP2 and similar to the best-performing functionals from the hybrid GGA block (*e.g.* PBE0, B3PW91 and B97-2) or from the hybrid meta-GGA one (*i.e.* MPW1B95 and PW6B95). It is worth pointing out that even though HSE06 appears satisfactorily for calculating geometries of At species, its choice becomes less and less attractive with the increasing system size. That is, because the computational cost associated with range-separated functionals increases tremendously with the system size, even when they are used in conjunction with small basis sets.

Summarizing relatively the above paragraphs, we can draw a ranking of some top functionals that can generally predict accurate geometries for At species. Among the investigated 36 XC functionals, we found that 21 of them, comprising in general pure and range-separated functionals, are not adequate for the present purpose. Among the 15 remaining ones, we classify the PBE0, MPW1B95 and PW6B95 as the top-three best-performing functionals. For at least two of the selected statistical criteria, they score values that are among the highlighted five best ones. This holds true for both the AVDZ basis sets (see Table A1.1) and for the AVTZ one (see Table 3.1). It is worth pointing out that good candidates are also the B3PW91 and HSE06 functionals, and that the popular B3LYP one performs quite satisfactorily.

3.3.3 Basis set convergence

Ultimately, focusing on the concluded top-five best-performing functionals, *i.e.* PBE0, MPW1B95, PW6B95, B3PW91 and HSE06, we would like to draw some conclusions *vis à vis* the basis set convergence. In this sense, we plot in Fig. 3.1 the evolution of the RMSDs and MSEs with increasing AV*X*Z basis set sizes. From Fig. 3.1, it is evident that going from AVDZ to the AVTZ basis set, MSEs are generally reduced by half while the reductions in RMSDs vary between 0.1 up to at most 0.5 percent units. Switching from AVTZ to AVQZ, MSEs are overall changed by 0.4 percent units, while RMSDs are changed by 0.2 percent units. We thus draw the conclusion that the AVTZ basis set lies close enough to the convergence regime.

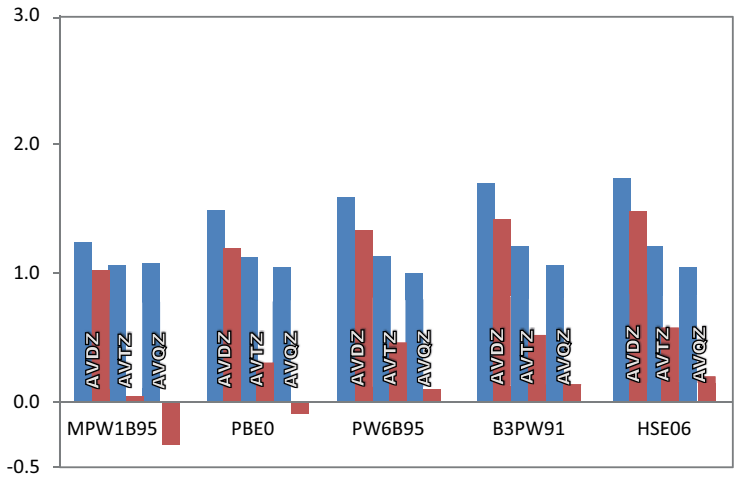

Figure 3.1 RMSDs (blue bars) and MSEs (red bars), in percentage, for computed bond lengths using selected DFT functionals and the different AV*X*Z basis sets.

3.4 Electronic transition energies

3.4.1 Reference data set and methodologies

In the present section we assess the performance of XC functionals in predicting electronic transition energies of At species. Note that only a subset of the abovementioned 36 XC functionals is used for the present purpose, and in particular those which are currently implemented in the TURBOMOLE program package. That is, since most of the calculations performed in this section involve open-shell At species. We have selected in the training set some At species for which transition energies are known either from experiment or have been calculated at a reference level of theory. We noted that the only available experimental data (in the present context) is the first ionization potential of At (IP_1 = 9.32 eV).[65] Furthermore, Borschevsky and coworkers undertook 4*c*-CCSD(T) calculations and provided reference values for the second ionization potential (IP_2 = 17.75 eV) and for the EA (2.41 eV) of At.[66] Other reference data reported in the literature exist for the AtO^+ cation. Gomes *et al.* reported the excitation energies to the first two spin-orbit coupled excited states, $X\ 0^+ \rightarrow$ **a** 1 and $X\ 0^+ \rightarrow$ **a** 2, using multireference 4*c*-CCSD calculations.[9] Note that both studies made use of large basis sets. We hence establish our reference dataset as comprising the IP_1, IP_2, and the EA of At and the first three spin-orbit coupled states of AtO^+, $X\ 0^+$, **a** 1 and **a** 2.

The classical and straightforward procedure to obtain the IPs and the EA of At would be to relax in 2*c*-DFT calculations the neutral atom and ions, and to subtract the obtained electronic energies. However, by proceeding this way we expect to sum several errors, rooted from the electron correlation and relativistic contributions, in the final computed values. For instance, the error on the correlation energy of the open-shell neutral atom would differ from the one of the

closed-shell anion, due to some kind of spin-contamination in the former case. Likewise, the error on relativistic contributions is expected to be larger for the neutral atom than for the anion since much stronger SOC is expected for the former case. The two errors may add up in the computed value of the EA. Hence, we propose to calculate the IPs and the EA of At starting from balanced reactions preserving the number of charged and neutral species, in order to take profit from error cancellations. As such, we consider the following electron-transfer reactions between At and I:

$$\begin{aligned} &\mathrm{At} + \mathrm{I}^{+} \xleftrightarrow{\Delta \mathrm{IP}_1} \mathrm{At}^{+} + \mathrm{I}; \qquad \mathrm{IP}_1\left(\mathrm{At}\right) = \mathrm{IP}_1\left(\mathrm{I}\right) + \Delta \mathrm{IP}_1 \\ &\mathrm{At}^{+} + \mathrm{I}^{2+} \xleftrightarrow{\Delta \mathrm{IP}_2} \mathrm{At}^{2+} + \mathrm{I}^{+}; \ \mathrm{IP}_2\left(\mathrm{At}\right) = \mathrm{IP}_2\left(\mathrm{I}\right) + \Delta \mathrm{IP}_2 \\ &\mathrm{At} + \mathrm{I}^{-} \xleftrightarrow{\Delta \mathrm{EA}} \mathrm{At}^{-} + \mathrm{I}; \qquad \mathrm{EA}\left(\mathrm{At}\right) = \mathrm{EA}\left(\mathrm{I}\right) + \Delta \mathrm{EA} \end{aligned} \tag{3.1}$$

Using the experimental values for the iodine IP_1 (10.45 eV), IP_2 (19.13 eV) and EA (3.06 eV),[67] and by computing the ΔIP_1, ΔIP_2 and ΔEA quantities, one may expect to estimate accurately the IP_1, IP_2 and EA of At.

Concerning the spin-orbit coupled electronic states of AtO^+, we approach them through single-point 2*c*-DFT calculations and the presented transition energies are ΔSCF values. The interatomic distance in AtO^+ was fixed to 1.916 Å and we note that this value corresponds to the distance for which the reference data was reported.[9]

3.4.2 Results

In Table 3.2 we report the calculated vertical transition energies to the **a** 1 and **a** 2 spin-orbit coupled states of AtO^+, the IP_1, IP_2 and EA of At, and the associated errors/deviations obtained at 2*c*-DFT/AV*X*Z levels of theory. Regarding each of the selected statistical criteria, and for a given AV*X*Z basis set, the best three values are evidenced in red while the best of them in bold as well. At start, we found that calculating the IP_1, IP_2 and EA of At according to the proposed balanced reactions is appealing. That is, we found that all the investigated functionals provide accurate values, generally within 0.1 eV from the reference ones, independently of the used basis set. In particular, using the AVTZ one, we found TPSSh to provide exceptional deviations on the IP_1 and IP_2 values, 0.09 eV and 0.14 eV, respectively, while BLYP is found to deliver the largest deviation on the EA, 0.05 eV. Concerning the spin-orbit coupled energy levels of AtO^+, we found that the different classes of functionals deliver notable large errors. The pure functionals tend to overstabilize the **a** 2 states (amounting ~0.33 eV with the AVDZ basis sets and ~0.27 eV with the AVTZ and AVQZ ones), while the opposite is valid for the **a** 1 ones with the hybrid functionals (**a** 1 is overstabilized by ~0.42 eV with the AVDZ basis sets and ~0.41 eV with the AVTZ and AVQZ

ones). Notably large errors are delivered by the BH&HLYP hybrid GGA functional, which underestimates the excitation energies to both **a** 1 and **a** 2 states by more than 0.5 eV. Given the accuracy of the calculated IP_1, IP_2 and EA of At, we observe that the MSE, MUE, RMSD, and MaxD criteria reflect mainly the errors on the excitation energies in AtO^+. This fact is clearly seen by inspecting for instance the MaxD values. In each case, they mirror the large deviation on the excitation energy to the **a** 2 (the case of pure functionals) or to the **a** 1 (the case of hybrids) state. Concerning the MSEs, MUEs and RMSDs, all functionals provide uniform values rising to at most 0.18 eV, excepting the particular case of BH&HLYP. In view of the four criteria, all the investigated functionals perform better than both HF and MP2.

Ranking three best-performing functionals for the present scope, we put forth the SVWN LSDA one, which delivers generally the best MSE, MUE, RMSD, and MaxD values irrespective of the used basis set, and the BP86 and PBE GGA ones, which provide errors/deviations among the best three ones for at least two of the four criteria, also irrespective of the basis set.

Intrigued by the large errors obtained on the first transition energies of AtO^+, we have observed that the errors can be even larger when they are computed at a quasi-relativistic level within the time-dependent DFT (TD-DFT) formalism. Employing the Minnesota M06-2X XC functional, Gomes *et al.* found both **a** 1 and **a** 2 states occurring below the true $X\ 0^+$ ground state.[9] Moreover, they concluded that both states are tremendously overstabilized with the increasing fraction of exact exchange, when comparing the results obtain with the M06-L, M06 and M06-2X functionals. Inspecting our ΔSCF values obtained with the PBE and PBE0 functionals for instance (irrespective of the basis set), a similar trend is unraveled for the excitation energy to the **a** 1 state but a fraction of exact exchange appears necessary to be accurate on the excitation energy to the **a** 2 state. For some pure functionals, we report in Table 3.2 some complementary TD-DFT results (in the framework of *2c*-DFT calculations). While in general we obtain similar values for the **a** 2 state as in ΔSCF calculations, we found the **a** 1 state occurring below the true $X\ 0^+$ ground-state. In agreement with the conclusion of Gomes *et al.*,[9] we advocate for the unreliability of the TD-DFT approach for computing excited electronic states of AtO^+.

Table 3.2 Calculated vertical energies for AtO^+ (r_e = 1.916 Å), IPs and EA of At (in eV), and associated MSEs, RMSDs and MaxDs (all in eV), using several XC functionals and AV*X*Z basis sets.

		AtO^+		At						
Functional		$X\ 0^+ \rightarrow$ **a** 1	$X\ 0^+ \rightarrow$ **a** 2	IP_1	IP_2	EA	MSE	MUE	RMSD	MaxD
LSDA										
	AVDZ	0.47 (−0.01)[a]	0.73 (1.02)[a]	9.35	17.68	2.49	−0.08	**0.12**	**0.16**	**0.29**
SVWN	AVTZ	0.51 (−0.01)[a]	0.80 (1.01)[a]	9.31	17.65	2.45	**−0.08**	**0.10**	**0.12**	**0.22**
	AVQZ	0.51 (−0.01)[a]	0.80 (1.01)[a]	9.30	17.64	2.47	−0.08	**0.11**	**0.13**	**0.22**
GGAs										
	AVDZ	0.43 (−0.02)[a]	0.69 (0.77)[a]	9.36	17.69	2.49	−0.09	0.14	0.18	0.33
BLYP	AVTZ	0.46 (−0.02)[a]	0.76 (0.74)[a]	9.31	17.66	2.46	−0.10	0.11	0.15	0.26
	AVQZ	0.46 (−0.02)[a]	0.76 (0.74)[a]	9.30	17.66	2.48	−0.09	0.12	0.15	0.26
	AVDZ	0.40 (−0.02)[a]	0.67 (0.77)[a]	9.36	17.82	2.48	**−0.08**	0.15	0.19	0.35
BP86	AVTZ	0.43 (−0.02)[a]	0.74 (0.73)[a]	9.31	17.79	2.44	−0.08	0.11	0.16	0.28
	AVQZ	0.43 (−0.02)[a]	0.74 (0.72)[a]	9.29	17.79	2.47	**−0.08**	0.12	0.16	0.28
	AVDZ	0.41 (−0.02)[a]	0.67 (0.81)[a]	9.35	17.83	2.46	−0.08	0.15	0.19	0.35
PBE	AVTZ	0.44 (−0.02)[a]	0.73 (0.77)[a]	9.30	17.79	2.43	−0.09	0.11	0.16	0.29
	AVQZ	0.44 (−0.02)[a]	0.74 (0.76)[a]	9.28	17.79	2.46	−0.08	0.12	0.15	0.28
Meta-GGAs										
	AVDZ	0.38	0.67	9.32	17.87	2.44	−0.09	0.15	0.20	0.35
TPSS	AVTZ	0.40	0.73	9.24	17.88	2.40	−0.10	0.15	0.18	0.29
	AVQZ	0.40	0.73	9.20	17.88	2.46	−0.09	0.18	0.18	0.29
Hybrid GGAs										
	AVDZ	0.28	0.75	9.34	17.72	2.44	−0.12	0.14	0.20	0.35
B3LYP	AVTZ	0.30	0.83	9.29	17.69	2.41	−0.12	0.12	0.17	0.33
	AVQZ	0.30	0.82	9.30	17.68	2.42	−0.12	0.13	0.18	0.33
	AVDZ	0.02	0.28	9.33	17.77	2.43	−0.26	0.28	0.43	0.74
BH&HLYP	AVTZ	0.04	0.29	9.26	17.76	2.41	−0.27	0.28	0.42	0.73
	AVQZ	0.04	0.29	9.27	17.76	2.42	−0.27	0.28	0.42	0.73
	AVDZ	0.21	0.78	9.33	17.87	2.42	−0.10	0.16	0.22	0.42
PBE0	AVTZ	0.22	0.85	9.28	17.84	2.39	−0.11	0.15	0.20	0.41
	AVQZ	0.22	0.84	9.28	17.84	2.40	−0.11	0.15	0.20	0.41
Hybrid meta-GGAs										
	AVDZ	0.31	0.70	9.31	17.88	2.41	−0.10	0.16	0.21	0.32
TPSSh	AVTZ	0.33	0.77	9.23	17.89	2.38	−0.11	0.16	0.19	0.30
	AVQZ	0.33	0.76	9.24	17.89	2.39	−0.11	0.16	0.19	0.30
	AVDZ	0.22	0.82	9.32	17.70	2.43	−0.13	0.14	0.21	0.41
PW6B95	AVTZ	0.23	0.88	9.29	17.66	2.40	−0.13	0.13	0.19	0.40
	AVQZ	0.23	0.87	9.29	17.66	2.41	−0.13	0.14	0.20	0.40
Ab initio										
	AVDZ	−0.03	0.11	9.34	18.16	2.45	−0.22	0.41	0.53	0.91
HF	AVTZ	0.02	0.11	9.26	18.19	2.44	−0.22	0.41	0.53	0.91
	AVQZ	0.02	0.11	9.27	18.19	2.44	−0.22	0.41	0.53	0.91
	AVDZ	−0.16	0.08	9.39	18.04	2.40	−0.27	0.42	0.57	0.94
MP2	AVTZ	−0.15	0.07	9.28	18.03	2.37	−0.30	0.42	0.56	0.95
	AVQZ	−0.15	0.07	9.27	18.01	2.36	−0.31	0.42	0.56	0.95
Reference										
		0.63[9]	1.02[9]	9.32[65]	17.75[66]	2.41[66]				

[a]TD-DFT results are given in parenthesis.

Inspecting the four statistical criteria shown in Table 3.2 obtained with the different AV*X*Z basis sets, it is clear that the AVTZ basis set lie in the convergence regime irrespective of the used functional. Nonetheless, it is true that improvements brought over the smaller AVDZ basis set are only moderate. They amount for at most 0.04 eV on MSEs, MUEs and RMSDs, and at most 0.07 eV on MaxDs. Comparing the AVTZ and AVQZ results, the criteria are either similar or changed by at most 0.01 eV, irrespective of the used XC functional.

3.5 Thermodynamic properties

3.5.1 Reference data set and methodological aspects

The aim in this section is to assess the performance of the 36 DFT functionals in predicting thermodynamic properties of At species, and more specifically, in predicting reaction equilibrium constants. As explained in Chapter 1, Champion and coworkers have measured in aqueous solution a set of equilibrium constants for several reactions involving the $At(x)^+$ cationic forms of At, *i.e.* At^+ and AtO^+.[6,68] Hence, the equilibrium constants made available, associated with the reactions involving $At(x)^+$ species and the Cl^-, Br^-, OH^- and SCN^- ligands in stoichiometric rapports of 1:1 and/or 1:2, define our reference data set.

From a computational viewpoint, the aforementioned reaction equilibrium constants could be calculated according to thermodynamic cycles as sketched in Scheme 2.1. Nevertheless, Champion and coworkers have shown that more accurate results can be obtained when the thermodynamic cycle involves not direct complexation reactions, but rather ligand-exchange reactions.[6,68] The basic reasoning justifying this relies on error cancellations. We hence proceed accordingly, and, in our calculations, we employ ligand-exchange reactions involving the $At(x)Br_m^{1-m}$ species as shown in Scheme 3.1.

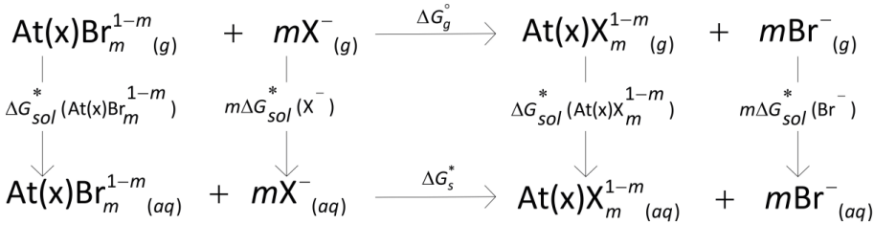

Scheme 3.1 Thermodynamic cycle used to compute free energy changes in aqueous solution.

The ligand-exchange equilibrium constant, $K_{m,\mathrm{exc}}$, is then calculated from the free energy change in aqueous solution, ΔG_s^*, which can be expressed as:

$$\Delta G_s^* = \Delta G_g^\circ + \Delta G_{\mathrm{sol}}^*\left(\mathrm{At(x)X}_m^{1-m}\right) + m\Delta G_{\mathrm{sol}}^*\left(\mathrm{Br}^-\right) - \Delta G_{\mathrm{sol}}^*\left(\mathrm{At(x)Br}_m^{1-m}\right) - m\Delta G_{\mathrm{sol}}^*\left(\mathrm{X}^-\right) \qquad (3.2)$$

where ΔG_g° is the free energy change in gas phase and $\Delta G_{\mathrm{sol}}^*\left(\mathrm{At(x)X}_m^{1-m}\right)$, $\Delta G_{\mathrm{sol}}^*\left(\mathrm{Br}^-\right)$, $\Delta G_{\mathrm{sol}}^*\left(\mathrm{At(x)Br}_m^{1-m}\right)$ and $\Delta G_{\mathrm{sol}}^*\left(\mathrm{X}^-\right)$ are the free energies of solvation of the respective species (in water). Making use of the experimental values of the equilibrium constants associated with the formation of the $\mathrm{At(x)Br}_m^{1-m}$ species,[6] we can obtain the equilibrium constant characterizing the formation of the $\mathrm{At(x)X}_m^{1-m}$ ones, according to the following relation:

$$\mathrm{Log}\ K_{m\mathrm{X}^-} = \mathrm{Log}\ K_{m\mathrm{Br}^-} + \mathrm{Log}\ K_{m,\mathrm{exc}} \qquad (3.3)$$

Hence, we are left to bring a computational estimate for the $\mathrm{Log}\ K_{m,\mathrm{exc}}$ term.

3.5.2 Assessment of 36 XC functionals

In their studies, Champion and coworkers showed that when the B3LYP hybrid GGA functional is used in conjunction with the AVDZ basis set, accurate equilibrium constants can be obtained by employing the CPCM-UAHF//UAKS scheme to compute solvation free energies for the different species involved in Scheme 3.1. We comment at first the results obtained within this framework, with the remarks that (i) the solvation free energies are kept to the CPCM-UAHF//UAKS(B3LYP) values, and (ii) the gas phase free energies (ΔG_g°) are computed with the panel of 36 XC functionals. To avoid a lengthy table, we present in Table 3.3 only the MSEs, MUEs, RMSDs and MaxDs (in units of Log) while the computed equilibrium constants and the reference values are placed in Table A1.2 (see Appendix 1). The best five values for each statistical criterion are evidenced in red while the best of them is as well shown in bold. We stress again that the errors/deviations shown in Table 3.3 correspond to the equilibrium constants associated with the formation of AtCl, AtSCN, AtOCl, AtOSCN, AtOOH, AtCl_2^-, AtSCN_2^- and AtOCl_2^-.

Table 3.3 MSEs, MUEs, RMSDs and MaxDs (in Log units) for the calculated equilibrium constants using several DFT functionals in conjunction with the AVDZ basis set and the CPCM-UAHF//UAKS(B3LYP) solvation scheme.

Functional	MSE	MUE	RMSD	MaxD
LSDA				
SVWN	0.1	0.9	1.1	2.3
GGAs				
BLYP	−0.3	1.2	1.6	3.6
BP86	−0.2	0.9	1.2	2.2
PW91	−0.3	0.9	1.2	2.1
PBE	−0.2	0.9	1.2	2.2
revPBE	−0.2	1.1	1.5	3.0
HCTH	−0.3	1.0	1.2	2.2
OLYP	−0.1	1.1	1.4	3.0
Meta-GGAs				
PKZB	−0.1	0.7	0.8	1.3
TPSS	0.1	0.7	0.9	1.6
VS98	−0.3	0.9	1.0	1.7
M06-L	−0.7	1.6	1.9	3.2
M11-L	3.9	3.9	4.9	11.2
Hybrid GGAs				
B3LYP	−0.2	0.6	0.7	1.2
X3LYP	−0.1	**0.5**	**0.7**	1.3
B3PW91	0.0	0.7	0.8	1.5
BH&HLYP	1.2	1.5	1.9	3.2
PBE0	0.1	0.7	0.9	1.7
B97-2	0.2	0.7	0.8	1.3
B98	0.1	0.6	0.8	1.4
Hybrid meta-GGAs				
TPSSh	0.1	0.6	0.8	1.4
MPW1B95	**0.0**	0.8	0.9	1.3
PW6B95	−0.1	0.6	0.7	**1.1**
MPWB1K	0.5	1.0	1.3	2.7
PWB6K	0.6	1.1	1.4	2.7
M05	−0.3	1.1	1.4	2.3
M06	−0.6	1.2	1.6	3.1
M05-2X	2.6	2.6	3.3	7.2
M06-2X	2.1	2.1	2.7	5.7
M08-HX	2.6	2.7	3.5	7.9
M08-SO	−0.1	1.0	1.2	2.3
Range-separated				
CAM-B3LYP	0.6	0.9	1.1	2.1
LC-ωPBE	0.4	1.1	1.3	2.4
HSE06	0.0	0.6	0.7	1.4
BNL	1.1	1.2	1.5	2.6
M11	1.1	1.7	2.4	5.9
Ab initio				
HF	3.8	3.8	5.6	11.7
MP2[a]	0.4	0.8	1.0	2.0

[a]These values are based on single point MP2/AVTZ energies obtained on previously optimized B3LYP/AVDZ geometries.

We start by discussing at first the results obtained with the hybrid functionals. From Table 3.3 it can be observed that the B3LYP, X3LYP, TPSSh, MPW1B95, PW6B95 and HSE06 functionals allow the computation of very accurate equilibrium constants with MaxDs smaller than 1.5 Log units and MUEs generally lower than 0.6 units. On a free energy scale, this error

corresponds to only 3.5 kJ·mol^{-1}. It is worth noting that these functionals were also found particularly accurate in predicting geometries of At species. On the other side, we found that the hybrid functionals that have a large fraction of exact exchange (at least 44% for the global hybrids and 65% in the long-range limit for the range-separated ones) provide from poor to catastrophic equilibrium constants (in some cases, the MaxDs rise above 5 units of Log). We refer to the BH&HLYP hybrid GGA functional, to the range-separated ones excepting HSE06, and notably to hybrid meta-GGA functionals from the Minnesota "M" family, in particular to M05-2X, M06-2X, M08-HX and M08-SO. Note that these functionals were also found problematic in computing geometries for At species.

Based on the four criteria displayed in Table 3.3, we classify the pure functionals as unreliable for computing thermodynamic properties of At species. For instance, they lead to unreasonable MaxDs of at least 2.1 units of Log. On the free energy scale, these errors/deviations reach above 12 kJ·mol^{-1}. Browsing for reasoning, we identified that this issue appears mainly associated with the computed equilibrium constant for the formation of the AtOSCN species (see Table A1.2). In this particular case, we observed that pure functionals predict equilibrium geometries for the most stable AtOSCN conformers that deviate significantly from the ones obtained with the best-performing hybrids. We show one example in Fig. 3.2.

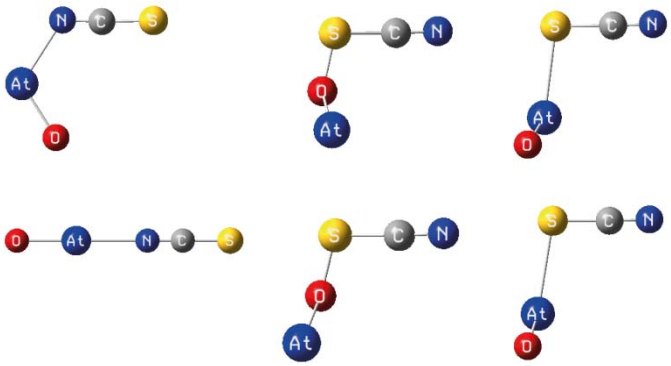

Figure 3.2 Equilibrium geometries for the most stable conformers of the AtOSCN species calculated at the 2*c*-PBE0/AVDZ (top) and 2*c*-BP86/AVDZ (bottom) levels of theory.

Notably, pure functionals predict a very stable AtOSCN conformer with linear equilibrium geometry pertaining to the $C_{\infty v}$ point group symmetry. We noted that such geometry does not correspond to a minimum when a hybrid functional, that we concluded relevant for calculating geometries for At species, is involved. For instance, at the 2*c*-PBE0/AVDZ level, a linear AtOSCN geometry corresponds to a second order saddle point. It is worth pointing out once more that pure functionals were previously found unreliable for computing geometries of At species. We noted that among all the pure functionals, the PKZB meta-GGA one appears to be a noticeable exception. It is

the only one that predicts accurate equilibrium constants with a MaxD of at most 1.3 units of Log while all the other errors/deviations are below 0.8 units.

In short, we state that the best five functionals that deliver accurate equilibrium constants for At species are the hybrid GGA B3LYP and X3LYP ones, the hybrid meta-GGA TPSSh and PW6B95 ones, and the range-separated HSE06 one.

3.5.3 Accounting for dispersion corrections

We have then investigated the possibility that dispersion corrections have a significant impact on the computed equilibrium constants. This issue may perhaps very well alter our ranking of functionals. Hence, considering the Grimme's DFT-D3 dispersion correction[69] in the gas-phase 2*c*-DFT calculations, we have re-calculated the equilibrium constants for some DFT functionals. The values themselves are placed in Table A1.2 while the errors/deviations, in Table 3.4. Generally, we found that the calculated values for the different equilibrium constants hardly modify upon accounting for a dispersion correction. A specific trend is actually not that obvious when one inspects the errors/deviations shown in Table 3.4.

Table 3.4 MSEs, MUEs, RMSDs and MaxDs (in units of Log) corresponding to equilibrium constants calculated using several DFT functionals, the AVDZ basis set, the CPCM-UAHF//UAKS(B3LYP) solvation scheme, and the Grimmes's DFT-D3 dispersion correction. Values calculated without any dispersion correction are recalled from Table 3.3 and are given within parenthesis.

Functional	MSE	MUE	RMSD	MaxD
GGA				
BLYP	0.0 (−0.3)	1.5 (1.2)	1.8 (1.6)	3.5 (3.6)
Meta-GGA				
TPSS	0.3 (0.1)	0.7 (0.7)	0.9 (0.9)	2.1 (1.6)
Hybrid GGAs				
B3LYP	0.2 (−0.2)	0.7 (0.6)	0.7 (0.7)	1.1 (1.2)
PBE0	0.3 (0.1)	0.6 (0.7)	0.8 (0.9)	1.6 (1.7)
Hybrid meta-GGAs				
TPSSh	0.4 (0.1)	0.6 (0.6)	0.7 (0.8)	1.3 (1.4)
MPWB1K	0.7 (0.5)	1.0 (1.0)	1.3 (1.3)	2.7 (2.7)
M06	−0.6 (−0.6)	1.2 (1.2)	1.5 (1.6)	3.0 (3.1)

Bearing in mind that dispersion may become more important in larger complexes, we have looked more carefully at the equilibrium constants corresponding to the formation of the 1:2 complexes (*i.e.* $AtCl_2^-$, $AtSCN_2^-$, $AtOCl_2^-$). In these cases some improvements can indeed be seen, notably when hybrid functionals are used. Nonetheless they appear to be very small and actually they lead to ~0.1 units of Log reductions in the calculated errors/deviations shown in Table 3.4. In change, there is no net improvement on the description of the equilibrium constants corresponding to the 1:1 complexes. Notably, when the DFT-D3 correction is included in the calculations, all the tested DFT

functionals predict less accurate equilibrium constants corresponding to the formation of the AtSCN and AtOSCN species (see Table A1.2). Overall, we note that the considered dispersion correction hardly changes the calculated errors/deviations by trifling 0.1 units of Log and do not alter in any way our "ranking" of reliable DFT functionals.

3.5.4 Basis set convergence

Assessing the basis set convergence in the present context appears particularly important since some functionals are, when used in conjunction with the AVDZ basis set, prone to fail in predicting correct geometries, which should translate in principle to large errors in the calculated equilibrium constants. For few selected functionals, we show in Fig. 3.3 the evolution of the RMSDs, as calculated with the AVDZ and AVTZ basis sets in conjunction with the CPCM-UAHF//UAKS(B3LYP) solvation scheme. We place the equilibrium constants and statistical criteria obtained with the AVTZ basis set in Tables A1.3 and A1.4, respectively.

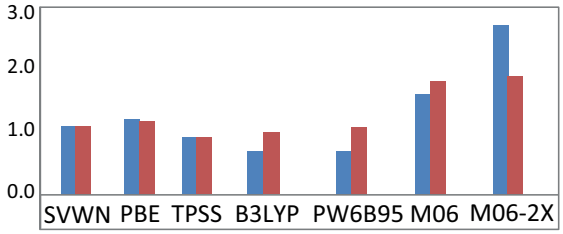

Figure 3.3 Evolution of RMSDs (in Log units) for computed equilibrium constants using selected DFT functionals, AVDZ (blue bars) and AVTZ (red bars) basis sets and the CPCM-UAHF//UAKS(B3LYP) solvation scheme.

While increasing the basis set size from AVDZ to AVTZ, the computed equilibrium constants may slightly improve for the cases of pure functionals. In contrast, we found that for some hybrid functionals, the results do not necessarily improve. The AVTZ basis set seems to be a better compromise for the M06-2X functional as there is an improvement not only on RMSD, but for instance of ~2.5 units on the MaxD. However, the latter is still above 3.0 units, for both the M06 and M06-2X Minnesota functionals.

3.5.5 Influence of the solvation scheme

As stated in Chapter 2, the choice of the cavity model in PCM computations may have a critical impact on calculated solvation free energies and hence on the calculated equilibrium constants. So far, we have shown that the CPCM-UAHF//UAKS solvation scheme, *i.e.* a hybrid scheme that makes use of both UAKS and UAHF cavities, may allow the computation of equilibrium constants for At species within an expected accuracy of ~1 Log unit. Hereafter, we seek

for any improvements on these thermodynamic properties upon changing the solvation scheme, and in particular, of the cavity model. In Fig. 3.4, we show the evolution of the MUEs associated with calculated equilibrium constants with selected functionals, AVDZ basis sets, and the CPCM-UAHF//UAKS, CPCM-UAHF, CPCM-UAKS and CPCM-UFF solvation schemes. The Log *K* values and the retained statistical criteria are placed in Tables A1.5 and A1.6, respectively.

At first, we noticed that the default cavity model available in Gaussian 09 program, namely UFF, delivers catastrophic equilibrium constants with MaxDs above 10 units, independently of the used XC functional. Note that similar results are obtained when the 1.1 default electrostatic factor (in Gaussian 09 program) is used together with UFF radii (see Table A1.6). As briefly pointed out in Chapter 2, the poor performance of the UFF model in the present case relates with its "faulty" formalism. That is, within UFF, each nucleus is placed in a similar sphere irrespective of the environmental context (*e.g.* change in the atom hybridization, first neighbor inductive effects, etc.). In Fig. 3.4, it is displayed that the CPCM-UAHF solvation scheme slightly improves (w.r.t. CPCM-UAHF//UAKS) the equilibrium constants with the top-five best performing functionals (B3LYP, X3LYP, TPSSh, PW6B95 and HSE06). Nevertheless, this trend is reversed when CPCM-UAHF is used with the pure or Minnesota "M" hybrid functionals. Switching to the CPCM-UAKS solvation scheme seems to be unworthy. For all the investigated functionals, it leads to errors/deviations that can rise up to more than twice the ones obtained with the previous solvation schemes (see evolution of MUEs in Fig. 3.4 and values in Table A1.6). Finally, we state that the CPCM-UFF and the CPCM-UAKS solvation schemes are unreliable to investigate thermodynamic properties of At species in aqueous solution, as for instance are the equilibrium constants. For this task we promote both the CPCM-UAHF/UAKS(B3LYP) and CPCM-UAHF schemes. Note that the use of functional-specific geometries within the CPCM-UAHF//UAKS scheme was not investigated since no important improvement is expected and since it would further complicate the analogies of the results. For the simplest scheme, we recommend the use of CPCM-UAHF, which, overall, performs as similar to the CPCM-UAHF//UAKS one.

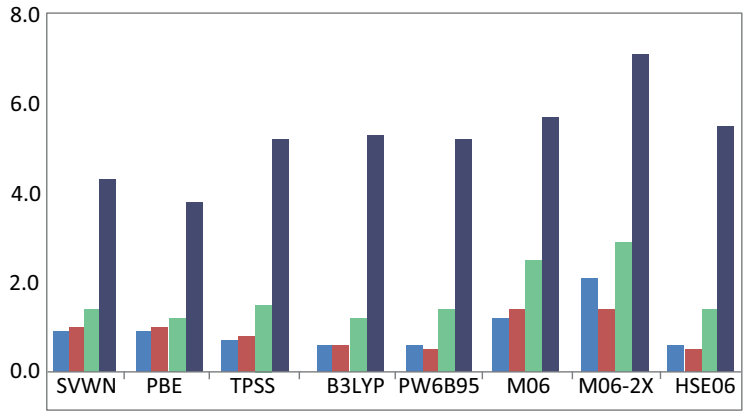

Figure 3.4 Evolution of the MUEs (in Log units) for calculated equilibrium constants using selected DFT functionals, the AVDZ basis set and the four proposed solvation schemes. Colour code: CPCM-UAHF//UAKS in blue, CPCM-UAHF in red, CPCM-UAKS in green and CPCM-UFF in purple.

3.6 Application: At reactivity indicators

The reactivity of At is hardly predictable from arguments that were acquired so far. In Chapter 1 we have detailed particular cases where the reactivity of At is either thought similar to the one of I or predicted using general concepts as the HSAB theory of Pearson. Nonetheless, it appears that At reacts either non-specifically (*e.g.* with direct addition on S atoms of protein-residues) or with the formation of At-therapeutic agents which are unstable *in vivo*. In the present section we propose to study the unintuitive effect of relativity, and in particular in the one of SOC, on basic reactivity indicators of At. In this perspective, we investigate the effect of SOC on the electronegativity (χ) of At and on some other reactivity descriptors arising from conceptual DFT,[70] in particular the hardness (η) and the electrophilicity (ω). The usefulness of these descriptors for explaining various chemical phenomena, including the reactivity of atoms and molecules, is well established. However, it is worth noting that the latest reported values of χ and η for At do not include SOC contributions.[71] In this study, the electronegativity, $\chi = 1/2(IP_1 + EA)$, the hardness, $\eta = 1/2(IP_1 - EA)$, and the electrophilicity, $\omega = \chi^2/2\eta$, are calculated with scalar relativistic DFT and with 2*c*-DFT using AVTZ basis sets and some of our best-performing XC functionals. Since the targeted quantities are expressed in terms of the IP_1 and the EA of At, we choose specifically three functionals, B3LYP, PBE0 and PW6B95 that were notably found accurate in predicting this kind of transition energies. The results are shown in Table 3.5. At first, we found that SOC has a strong impact on the electronegativity and on the electrophilicity values. The former is reduced under the effect of SOC by ~10% down to ~5.85 eV on the Mulliken scale (value which translates to ~1.82 in the Pauling scale). This value is consistent with current considerations in the literature that it should be close or lower than the one of H. The latter (*i.e.* the electrophilicity) is reduced under the effect

of SOC by 15%. Hence, one can state that SOC renders At less reactive for electrophilic approaches to attach ^{211}At to carrier molecules. It appears that SOC has only a moderate impact on the At hardness (~2%). In light of the HSAB principle, the calculated value of ~3.45 eV is consistent with the observed affinity toward soft S atoms (η(S) = 4.14 eV) during the direct labeling of proteins.

Table 3.5 Calculated electronegativity (χ), hardness (η) and electrophilicity (ω) using selected XC functionals and the AVTZ basis set. The IP_1 and the EA values of At, calculated with 2*c*-DFT, are recalled for convenience from Table 3.2.

Functional	IP_1	EA	χ (eV)[b]	η (eV)	ω (eV)
B3LYP	9.29	2.41	5.85 (1.82)	3.44	2.49
ΔSO[c]	−0.61	−0.48	−0.54 (−0.15)	−0.07	−0.43
PBE0	9.28	2.39	5.84 (−1.81)	3.45	2.47
ΔSO[c]	−0.60	−0.48	−0.54 (−0.14)	−0.06	−0.43
PW6B95	9.29	2.40	5.85 (1.82)	3.45	2.48
ΔSO[c]	−0.60	−0.47	−0.54 (−0.14)	−0.07	−0.42

[b]The values in parenthesis are expressed in Pauling units, using a half-power formula: $\chi_P = 1.934\sqrt{\chi_M + 7.02} - 5.012$.[72]

[c]ΔSO is defined as the difference between the results obtained from 2*c*-DFT and scalar relativistic DFT calculations.

3.7 Conclusion

The overall goal of this chapter was to identify XC functionals that are suitable to investigate the basic chemistry of At within a (2*c*) quasi-relativistic DFT framework. A set of 36 nonrelativistic functionals (or a subset of it), was assessed for predicting geometries, electronic transition energies and thermodynamic properties for a set of 19 At species. While some functionals were found to perform very well for particular tasks, *e.g.* M05 in conjunction with the AVDZ basis sets to predict geometries, we put forth as the overall best choice the PW6B95 hybrid meta-GGA functional. We note that the old and very popular PBE0 and B3LYP hybrid GGAs are overall safe choices. For instance, B3LYP delivered MUEs of 1.7% on bond lengths, 0.12 eV on electronic transition energies and 0.8 logarithmic units for equilibrium constants, when used in conjunction with the AVTZ basis sets. We note that these functionals are found sufficiently accurate also when used in conjunction with the AVDZ basis sets, especially for computing geometries and thermodynamic properties. This aspect is particularly important for computational purposes since it allows geometry optimizations/frequency calculations of medium to large At species at a reasonable cost. As a general trend we obtained large errors/deviations with XC functionals that have a high percentage of exact exchange. This includes for instance very popular Minnesota functionals from the "M" family, *e.g.* M06-2X. Ultimately, we have clearly established/confirmed a computational strategy to safely predict the chemistry of At in solution. This strategy proposes the use of the CPCM-UAHF//UAKS scheme or the CPCM-UAHF one to calculate solvation free energies of At species.

Bibliography:

1. D.-C. Sergentu, G. David, G. Montavon, R. Maurice, N. Galland, *J. Comput. Chem.* Scrutinizing "invisible" astatine: A challenge for modern density functionals, **2016**, 37, 1345.
2. O. Fossgaard, O. Gropen, M. C. Valero, T. Saue, *J. Chem. Phys.* On the performance of four-component relativistic density functional theory: Spectroscopic constants and dipole moments of the diatomics HX and XY (X, Y= F, Cl, Br, and I), **2003**, 118, 10418.
3. T. Saue, T. Helgaker, *J. Comput. Chem.* Four-component relativistic Kohn–Sham theory, **2002**, 23, 814.
4. M. K. Armbruster, F. Weigend, C. van Wüllen, W. Klopper, *Phys. Chem. Chem. Phys.* Self-consistent treatment of spin–orbit interactions with efficient Hartree–Fock and density functional methods, **2008**, 10, 1748.
5. M. Valiev, E. J. Bylaska, N. Govind, K. Kowalski, T. P. Straatsma, H. J. J. van Dam, D. Wang, J. Nieplocha, E. Apra, T. L. Windus, *Comput. Phys. Commun.* NWChem: a comprehensive and scalable open-source solution for large scale molecular simulations, **2010**, 181, 1477.
6. J. Champion, M. Seydou, A. Sabatié-Gogova, E. Renault, G. Montavon, N. Galland, *Phys. Chem. Chem. Phys.* Assessment of an effective quasirelativistic methodology designed to study astatine chemistry in aqueous solution, **2011**, 13, 14984.
7. T. Ayed, M. Seydou, F. Réal, G. Montavon, N. Galland, *J. Phys. Chem. B.* How does the solvation unveil AtO^+ reactivity?, **2013**, 117, 5206.
8. T. Ayed, F. Réal, G. Montavon, N. Galland, *J. Phys. Chem. B.* Rationalization of the solvation effects on the AtO^+ ground-state change, **2013**, 117, 10589.
9. A. S. P. Gomes, F. Réal, N. Galland, C. Angeli, R. Cimiraglia, V. Vallet, *Phys. Chem. Chem. Phys.* Electronic structure investigation of the evanescent AtO^+ ion, **2014**, 16, 9238.
10. Y. J. Choi, C. Bae, Y. S. Lee, S. Lee, *Bull. Korean. Chem. Soc.* Spin-orbit density functional theory calculations for TlAt with relativistic effective core potentials, **2003**, 24, 728.
11. Y. J. Choi, Y. S. Lee, *J. Chem. Phys.* Spin–orbit density functional theory calculations for heavy metal monohydrides, **2003**, 119, 2014.
12. A. V. Mitin, C. van Wüllen, *J. Chem. Phys.* Two-component relativistic density-functional calculations of the dimers of the halogens from bromine through element 117 using effective core potential and all-electron methods, **2006**, 124, 064305.
13. E. Apra, E. J. Bylaska, W. A. de Jong, N. Govind, K. Kowalski, T. P. Straatsma, M. Valiev, H. J. J. van Dam, D. Wang, T. L. Windus, J. Hammond, J. Autschbach, K. Bhaskaran-Nair, J. Brabec, K. Lopata, F. Aquino, S. Hirata, M. T. Hackler, J. Mullin, P. Nichols, R. Peverati, J. Pittner, Y. Zhao, P.-D. Fan, R. J. Harrison, M. Dupuis, D. Silverstein, D. M. A. Smith, J. Nieplocha, V. Tipparaju, M. Krishnan, B. E. van Kuiken, A. Vazquez-Mayagoitia, L. Jensen, M. Swart, Q. Wu, T. van Voorhis, A. A. Auer, M. Nooijen, L. D. Crosby, E. Brown, G. Cisneros, G. I. Fann, H. Fruchtl, J. Garza, K. Hirao, R. Kendall, J. A. Nichols, K. Tsemekhman, K. Wolinski, J. Anchell, D. Bernholdt, P. Borowski, T. Clark, D. Clerc, H. Dachsel, M. Deegan, K. Dyall, D. Elwood, E. Glendening, M. Gutowski, A. Hess, J. Jaffe, B. Johnson, J. Ju, R. Kobayashi, R. Kutteh, Z. Lin, R. Littlefield, X. Long, B. Meng, T. Nakajima, S. Niu, L. Pollack, M. Rosing, K. Glaesemann, G. Sandrone, M. Stave, H. Taylor, G. Thomas, J. H. van Lenthe, A. Wong, Z. Zhang, NWChem version 6.3: A comprehensive

and scalable open-source solution for large scale molecular simulations. Pacific Northwest National Laboratory: Richland, WA, **2013**.

14. R. Ahlrichs, M. K. Armbruster, R. A. Bachorz, M. Bär, H.-P. Baron, R. Bauernschmitt, F. A. Bischoff, S. Böcker, N. Crawford, P. Deglmann, F. D. Sala, M. Diedenhofen, M. Ehrig, K. Eichkorn, S. Elliott, D. Friese, F. Furche, A. Glöß, F. Haase, M. Häser, C. Hättig, A. Hellweg, S. Höfener, H. Horn, C. Huber, U. Huniar, M. Kattannek, W. Klopper, A. Köhn, C. Kölmel, M. Kollwitz, K. May, P. Nava, C. Ochsenfeld, H. Öhm, M. Pabst, H. Patzelt, D. Rappoport, O. Rubner, A. Schäfer, U. Schneider, M. Sierka, D. P. Tew, O. Treutler, B. Unterreiner, M. von Arnim, F. Weigend, P. Weis, H. Weiss, N. Winter, TURBOMOLE version 6.6, a development of University of Karlsruhe and Forschungszentrum Karlsruhe GmbH, TURBOMOLE GmbH, **2014**.
15. C. van Wüllen, *J. Comput. Chem.* Spin densities in two-component relativistic density functional calculations: Noncollinear versus collinear approach, **2002**, 23, 779.
16. S. H. Vosko, L. Wilk, M. Nusair, *Can. J. Phys.* Accurate spin-dependent electron liquid correlation energies for local spin density calculations: a critical analysis, **1980**, 58, 1200.
17. C. Lee, W. Yang, R. G. Parr, *Phys. Rev. B.* Development of the Colle-Salvetti correlation-energy formula into a functional of the electron density, **1988**, 37, 785.
18. A. D. Becke, *Phys. Rev. A.* Density-functional exchange-energy approximation with correct asymptotic behavior, **1988**, 38, 3098.
19. J. P. Perdew, *Phys. Rev. B.* Density-functional approximation for the correlation energy of the inhomogeneous electron gas, **1986**, 33, 8822.
20. J. P. Perdew, K. Burke, Y. Wang, *Phys. Rev. B.* Generalized gradient approximation for the exchange-correlation hole of a many-electron system, **1996**, 54, 16533.
21. K. Burke, J. P. Perdew, Y. Wang. Electronic density functional theory: Recent progress and new directions; Springer US, Boston, MA, 1998.
22. J. P. Perdew, K. Burke, M. Ernzerhof, *Phys. Rev. Lett.* Generalized gradient approximation made simple, **1996**, 77, 3865.
23. Y. Zhang, W. Yang, *Phys. Rev. Lett.* Comment on "Generalized gradient approximation made simple", **1998**, 80, 890.
24. F. A. Hamprecht, A. J. Cohen, D. J. Tozer, N. C. Handy, *J. Chem. Phys.* Development and assessment of new exchange-correlation functionals, **1998**, 109, 6264.
25. N. C. Handy, A. J. Cohen, *Mol. Phys.* Left-right correlation energy, **2001**, 99, 403.
26. J. P. Perdew, S. Kurth, A. Zupan, P. Blaha, *Phys. Rev. Lett.* Accurate density functional with correct formal properties: A step beyond the generalized gradient approximation, **1999**, 82, 2544.
27. J. Tao, J. P. Perdew, V. N. Staroverov, G. E. Scuseria, *Phys. Rev. Lett.* Climbing the density functional ladder: Nonempirical meta–generalized gradient approximation designed for molecules and solids, **2003**, 91, 146401.
28. T. van Voorhis, G. E. Scuseria, *J. Chem. Phys.* A novel form for the exchange-correlation energy functional, **1998**, 109, 400.
29. Y. Zhao, D. G. Truhlar, *J. Chem. Phys.* A new local density functional for main-group thermochemistry, transition metal bonding, thermochemical kinetics, and noncovalent interactions, **2006**, 125, 194101.

30. R. Peverati, D. G. Truhlar, *J. Phys. Chem. Lett.* M11-L: A local density functional that provides improved accuracy for electronic structure calculations in chemistry and physics, **2011**, 3, 117.
31. A. D. Becke, *J. Chem. Phys.* Density-functional thermochemistry. III. The role of exact exchange, **1993**, 98, 5648.
32. P. J. Stephens, F. J. Devlin, C. Chabalowski, M. J. Frisch, *J. Phys. Chem. Ab initio* calculation of vibrational absorption and circular dichroism spectra using density functional force fields, **1994**, 98, 11623.
33. X. Xu, W. A. Goddard, *Proc. Natl. Acad. Sci. USA.* The X3LYP extended density functional for accurate descriptions of nonbond interactions, spin states, and thermochemical properties, **2004**, 101, 2673.
34. C. Adamo, V. Barone, *J. Chem. Phys.* Toward reliable density functional methods without adjustable parameters: The PBE0 model, **1999**, 110, 6158.
35. P. J. Wilson, T. J. Bradley, D. J. Tozer, *J. Chem. Phys.* Hybrid exchange-correlation functional determined from thermochemical data and *ab initio* potentials, **2001**, 115, 9233.
36. H. L. Schmider, A. D. Becke, *J. Chem. Phys.* Optimized density functionals from the extended G2 test set, **1998**, 108, 9624.
37. M. Bienati, C. Adamo, V. Barone, *Chem. Phys. Lett.* Performance of a new hybrid Hartree–Fock/Kohn–Sham model (B98) in predicting vibrational frequencies, polarisabilities and NMR chemical shifts, **1999**, 311, 69.
38. V. N. Staroverov, G. E. Scuseria, J. Tao, J. P. Perdew, *J. Chem. Phys.* Comparative assessment of a new nonempirical density functional: Molecules and hydrogen-bonded complexes, **2003**, 119, 12129.
39. Y. Zhao, D. G. Truhlar, *J. Phys. Chem. A.* Hybrid meta density functional theory methods for thermochemistry, thermochemical kinetics, and noncovalent interactions: the MPW1B95 and MPWB1K models and comparative assessments for hydrogen bonding and Van der Waals interactions, **2004**, 108, 6908.
40. Y. Zhao, D. G. Truhlar, *J. Phys. Chem. A.* Design of density functionals that are broadly accurate for thermochemistry, thermochemical kinetics, and nonbonded interactions, **2005**, 109, 5656.
41. Y. Zhao, N. E. Schultz, D. G. Truhlar, *J. Chem. Phys.* Exchange-correlation functional with broad accuracy for metallic and nonmetallic compounds, kinetics, and noncovalent interactions, **2005**, 123, 161103.
42. Y. Zhao, D. G. Truhlar, *Theor. Chem. Acc.* The M06 suite of density functionals for main group thermochemistry, thermochemical kinetics, noncovalent interactions, excited states, and transition elements: two new functionals and systematic testing of four M06-class functionals and 12 other functionals, **2008**, 120, 215.
43. Y. Zhao, N. E. Schultz, D. G. Truhlar, *J. Chem. Theory Comput.* Design of density functionals by combining the method of constraint satisfaction with parametrization for thermochemistry, thermochemical kinetics, and noncovalent interactions, **2006**, 2, 364.
44. Y. Zhao, D. G. Truhlar, *J. Chem. Theory Comput.* Exploring the limit of accuracy of the global hybrid meta density functional for main-group thermochemistry, kinetics, and noncovalent interactions, **2008**, 4, 1849.
45. T. Yanai, D. P. Tew, N. C. Handy, *Chem. Phys. Lett.* A new hybrid exchange–correlation functional using the Coulomb-attenuating method (CAM-B3LYP), **2004**, 393, 51.
46. O. A. Vydrov, G. E. Scuseria, *J. Chem. Phys.* Assessment of a long-range corrected hybrid functional, **2006**, 125, 234109.
47. J. Heyd, G. E. Scuseria, M. Ernzerhof, *J. Chem. Phys.* Hybrid functionals based on a screened Coulomb potential, **2003**, 118, 8207.

48. J. Heyd, G. E. Scuseria, M. Ernzerhof, *J. Chem. Phys.* Erratum:"Hybrid functionals based on a screened Coulomb potential"[J. Chem. Phys. 118, 8207 (2003)], **2006**, 124, 219906.
49. R. Baer, D. Neuhauser, *Phys. Rev. Lett.* Density functional theory with correct long-range asymptotic behavior, **2005**, 94, 043002.
50. E. Livshits, R. Baer, *Phys. Chem. Chem. Phys.* A well-tempered density functional theory of electrons in molecules, **2007**, 9, 2932.
51. R. Peverati, D. G. Truhlar, *J. Phys. Chem. Lett.* Improving the accuracy of hybrid meta-GGA density functionals by range separation, **2011**, 2, 2810.
52. K. A. Peterson, D. Figgen, E. Goll, H. Stoll, M. Dolg, *J. Chem. Phys.* Systematically convergent basis sets with relativistic pseudopotentials. II. Small-core pseudopotentials and correlation consistent basis sets for the post-d group 16–18 elements, **2003**, 119, 11113.
53. K. A. Peterson, B. C. Shepler, D. Figgen, H. Stoll, *J. Phys. Chem. A.* On the spectroscopic and thermochemical properties of ClO, BrO, IO, and their anions, **2006**, 110, 13877.
54. M. K. Armbruster, W. Klopper, F. Weigend, *Phys. Chem. Chem. Phys.* Basis-set extensions for two-component spin–orbit treatments of heavy elements, **2006**, 8, 4862.
55. T. H. Dunning Jr, *J. Chem. Phys.* Gaussian basis sets for use in correlated molecular calculations. I. The atoms boron through neon and hydrogen, **1989**, 90, 1007.
56. R. A. Kendall, T. H. Dunning Jr, R. J. Harrison, *J. Chem. Phys.* Electron affinities of the first-row atoms revisited. Systematic basis sets and wave functions, **1992**, 96, 6796.
57. D. E. Woon, T. H. Dunning Jr, *J. Chem. Phys.* Gaussian basis sets for use in correlated molecular calculations. III. The atoms aluminum through argon, **1993**, 98, 1358.
58. M. J. Frisch, G. W. Trucks, H. B. Schlegel, G. E. Scuseria, M. A. Robb, J. R. Cheeseman, G. Scalmani, V. Barone, B. Mennucci, G. A. Petersson, H. Nakatsuji, M. Caricato, X. Li, H. P. Hratchian, A. F. Izmaylov, J. Bloino, G. Zheng, J. L. Sonnenberg, M. Hada, M. Ehara, K. Toyota, R. Fukuda, J. Hasegawa, M. Ishida, T. Nakajima, Y. Honda, O. Kitao, H. Nakai, T. Vreven, J. A. Montgomery, J. E. Peralta, F. Ogliaro, M. Bearpark, J. J. Heyd, E. Brothers, K. N. Kudin, V. N. Staroverov, R. Kobayashi, J. Normand, K. Raghavachari, A. Rendell, J. C. Burant, S. S. Iyengar, J. Tomasi, M. Cossi, N. Rega, J. M. Millam, M. Klene, J. E. Knox, J. B. Cross, V. Bakken, C. Adamo, J. Jaramillo, R. Gomperts, R. E. Stratmann, O. Yazyev, A. J. Austin, R. Cammi, C. Pomelli, J. W. Ochterski, R. L. Martin, K. Morokuma, V. G. Zakrzewski, G. A. Voth, P. Salvador, J. J. Dannenberg, S. Dapprich, A. D. Daniels, Ö. Farkas, J. B. Foresman, J. V. Ortiz, J. Cioslowski, D. J. Fox, Gaussian 09, revision A02; Gaussian Inc.: Wallingford, CT, **2009**.
59. J. Champion, C. Alliot, E. Renault, B. M. Mokili, M. Chérel, N. Galland, G. Montavon, *J. Phys. Chem. A.* Astatine standard redox potentials and speciation in acidic medium, **2010**, 114, 576.
60. V. Barone, M. Cossi, J. Tomasi, *J. Chem. Phys.* A new definition of cavities for the computation of solvation free energies by the polarizable continuum model, **1997**, 107, 3210.
61. C. J. Cramer, Essentials of computational chemistry: theories and models. John Wiley & Sons, **2004**.
62. S. Höfener, R. Ahlrichs, S. Knecht, L. Visscher, *ChemPhysChem.* Relativistic and non-relativistic electronic molecular-structure calculations for dimers of 4p-, 5p-, and 6p-block elements, **2012**, 13, 3952.
63. D.-D. Yang, F. Wang, *Phys. Chem. Chem. Phys.* Structures and stabilities of group 17 fluorides EF_3 (E= I, At, and element 117) with spin–orbit coupling, **2012**, 14, 15816.

64. A. S. P. Gomes, L. Visscher, *Chem. Phys. Lett.* The influence of core correlation on the spectroscopic constants of HAt, **2004**, 399, 1.

65. S. Rothe, A. N. Andreyev, S. Antalic, A. Borschevsky, L. Capponi, T. E. Cocolios, H. de Witte, E. Eliav, D. V. Fedorov, V. N. Fedosseev, D. A. Fink, S. Fritzsche, L. Ghys, M. Huyse, N. Imai, U. Kaldor, Y. Kudryavtsev, U. Köster, J. F. W. Lane, J. Lassen, V. Liberati, K. M. Lynch, B. A. Marsh, K. Nishio, D. Pauwels, V. Pershina, L. Popescu, T. J. Procter, D. Radulov, S. Raeder, M. M. Rajabali, E. Rapisarda, R. E. Rossel, K. Sandhu, M. D. Seliverstov, A. M. Sjödin, P. van den Bergh, P. van Duppen, M. Venhart, Y. Wakabayashi, K. D. A. Wendt, *Nat. Commun.* Measurement of the first ionization potential of astatine by laser ionization spectroscopy, **2013**, 4, 1835.

66. A. Borschevsky, L. F. Pašteka, V. Pershina, E. Eliav, U. Kaldor, *Phys. Rev. A.* Ionization potentials and electron affinities of the superheavy elements 115–117 and their sixth-row homologues Bi, Po, and At, **2015**, 91, 020501.

67. D. R. Lide. Handbook of chemistry and physics, 79th ed.; CRC Press LLC: New York, 1998.

68. J. Champion, A. a. Sabatié-Gogova, F. Bassal, T. Ayed, C. Alliot, N. Galland, G. Montavon, *J. Phys. Chem. A.* Investigation of astatine (III) hydrolyzed species: Experiments and relativistic calculations, **2013**, 117, 1983.

69. S. Grimme, J. Antony, S. Ehrlich, H. Krieg, *J. Chem. Phys.* A consistent and accurate *ab initio* parametrization of density functional dispersion correction (DFT-D) for the 94 elements H-Pu, **2010**, 132, 154104.

70. P. Geerlings, F. De Proft, W. Langenaeker, *Chem. Rev.* Conceptual density functional theory, **2003**, 103, 1793.

71. J. Furtado, F. De Proft, P. Geerlings, *J. Phys. Chem. A.* The noble gases: How their electronegativity and hardness determines their chemistry, **2015**, 119, 1339.

72. D. R. Herrick, *J. Chem. Theory Comput.* Connecting Pauling and Mulliken electronegativities, **2005**, 1, 255.

Chapter 4

Unexpected Structures of At Species: The Case of AtF_3

In this chapter, we focus on the PES of the AtF_3 system, which has been the subject of various theoretical studies in the last decades. This work has been the subject of a publication in *J. Chem. Phys.*,[1] and will be presented in a slightly different way in the present chapter.

4.1 Introduction

The fluorination of astatine has been attempted by Appleman *et al.* in their race for observing At species through time-of-flight mass spectrometry.[2] However when mixed with the fluorination agent, ClF_3, At adhered strongly to the glass and could not be transferred into the spectrometer. Up to nowadays no other attempts to synthesize At fluorides were made. AtF_3 is thus a hypothetical system studied by theoretical chemists as an analogue to the experimentally evidenced ClF_3, BrF_3 and IF_3 fluorides, in order to study some trends in group XVII. The gas phase geometries of ClF_3 and BrF_3 are well known to be planar and T-shaped pertaining to the C_{2v} symmetry point group (see Fig. 4.1, left panel), as derived from various spectroscopic evidences (*e.g.* microwave, rotational spectra, infrared spectra etc.).[3-7] IF_3 is a highly unstable molecule and its structure has been unraveled only in the condensed phase. Nonetheless, from the recording of its vibrational spectra[8] or from X-ray analysis,[9] it turned out to be alike the gas phase ones of ClF_3 and BrF_3, *i.e.* T-shaped C_{2v}. No experiments have yet been reported for the synthesis of the $(117)F_3$ species. One may assume that AtF_3 has T-shaped C_{2v} structure, and we shall see in the following how this assumption can be checked with various theories.

The valence shell electron pair repulsion (VSEPR) model[10-13] has been widely recalled, either for educational purposes or in scientific investigations, in order to establish molecular geometries. Due to its empirical foundation, the accuracy of the VSEPR model has been largely debated up to nowadays. While it has been proven to fail in predicting geometries for some systems involving transitional[14] or heavier elements,[15] one can state that VSEPR is overall able to predict qualitatively correct molecular architectures for systems involving most of the elements in the periodic table. Considering an AX_nE_m case (where A stands for the central atom, X for the ligands and E for the lone pairs of the central atom), the VSEPR geometry is ruled by the mutual repulsion between the n A–X bond pairs, between these bond pairs and the m E lone pairs, and more importantly between the m lone pairs, which is considered in this model as the dominant factor in determining the geometry. The XF_3 (X = Cl, Br, I, At and even element 117, *i.e.* eka-astatine) fluorides fall in the AX_3E_2 category and would adopt bent T-shaped C_{2v} structures, according to the VSEPR model. Considering the ClF_3, BrF_3 and IF_3 cases, the VSEPR geometries are in line with the observed experimental ones. It is hence conferring some note of strength to the assumption that AtF_3 would have as well a T-shaped C_{2v} structure. Note that in the AtF_3 case and even more in the $(117)F_3$ case, one lone pair of X may be considered as chemically inert, which may question the applicability of VSEPR to these cases.

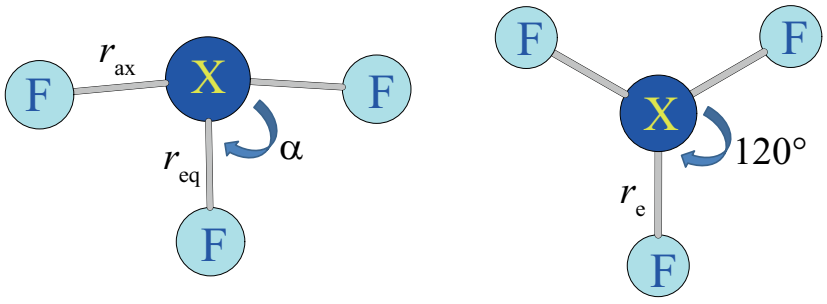

Figure 4.1 Ball and stick representations of T-shaped C_{2v} (left) and trigonal-planar D_{3h} (right) XF_3 (X = Cl, Br, I, At) geometries.

In the following, we discuss these geometries based on quantum mechanical considerations. For the XF_3 (X = Cl, Br and I) fluorides, trigonal-planar D_{3h} structures (see Fig. 4.1, right panel) are known to be second-order saddle points on the ground-state PESs.[16] The experimentally observed T-shaped C_{2v} structures are interpreted as resulting from the *pseudo* Jahn-Teller effect (PJTE) that is active at the D_{3h} geometries. Note that PJTE is the only source of instability in the case of non-linear polyatomic systems that exhibit non-degenerate electronic ground-states, at highly symmetric geometrical configurations.[17] In such situations, energy is gained

by following geometrical distortions due to vibronic coupling between states of same spin multiplicity, either between ground and excited states, or between excited states which leads to a ground-state change (case referred to as "hidden" PJTE). The spatial symmetry of the excited state that is involved must contain the symmetry of the nuclear displacement vector. At the D_{3h} structure of each XF_3 system (X = F, Cl, Br, I), the PJTE involves a *E*' degenerate excited state arising from an electron promotion from the a_1' HOMO orbital to the e' LUMO ones, and the doubly degenerate e' imaginary normal mode (*i.e.* often referred to the $E'_{a_{1,\mathrm{HOMO}}' \otimes e'_{\mathrm{LUMO}}} \times e'$ *pseudo* Jahn-Teller case).[16] Schwerdtfeger showed that the $a_{1,\mathrm{HOMO}}'$ orbital is relativistically stabilized down the group toward AtF_3, due to some mixing with the outermost *ns* occupied valence orbital of the central X atom, and hence diminishing the effectiveness of the PJTE.[16] Actually, in the AtF_3 case, the D_{3h} geometry was reported to be a "weak" local minimum, nearly isoenergetic with the T-shaped C_{2v} one, suggesting that the PJTE is not active anymore at the D_{3h} geometry.[15,16,18,19] Actually, AtF_3 is a borderline system as computational studies suggest its heavier analogue, the $(117)F_3$ species, to be only stable in a trigonal-planar D_{3h} structure.[15,18] Nonrelativistic, scalar relativistic and SOC calculations have so far been performed in order to determine critical points on the ground-state PES of AtF_3.[15,18,19] Significant effort was put in determining precisely the energy difference between the D_{3h} and the T-shaped C_{2v} structures, $\Delta E^{D_{3h}-C_{2v}}$. In a recent 2*c*-CCSD(T)/def2-QZVPP study,[15] Yang and Wang showed that the T-shaped C_{2v} structure is ~7 $kJ \cdot mol^{-1}$ more stable than the D_{3h} one, and stated that it is the candidate structure to be observed through experiments. This statement is obviously questionable and, moreover, the influence of the different electronic factors (electron correlation and relativistic effects) on the PJTE is not yet well understood, in particular for the case of AtF_3. Notably, there is no definite statement on the relationship between SOC and PJTE. One should not forget that numerous properties of At species are highly sensitive to SOC.[20-25] To our opinion, one needs to consider the impact of the different electronic factors not solely at the D_{3h} and T-shaped C_{2v} structures but also how they affect the PES in their close vicinities, in order to reach relevant conclusions.

Employing 2*c*-DFT and notably a two-step multiconfigurational wave-function-based approach (c-SOCI), the AtF_3 system is investigated in order to (i) check the potential multiconfigurational character of the ground-state wave functions at the D_{3h} and T-shaped C_{2v} structures, (ii) establish the topology of the ground-state PES of AtF_3, (iii) determine the role of different electronic factors, namely electron correlation, scalar relativistic effects and SOC, on this topology, (iv) identify and rationalize differences between AtF_3 and its lighter analogues, ClF_3, BrF_3

and IF_3, and (v) establish whether a computationally cost-effective approach like c-SOCI can be used in order to address the electronic structure of At species, which is more of fundamental interest.

4.2 The ground-state PES of AtF_3: a 2*c*-DFT study

In this section, we aim at identifying different critical points of the ground-state PES of AtF_3 and to establish the connectivities between them. Scalar relativistic DFT (SR-DFT) (using the Gaussian 09 program package[26]) and 2*c*-DFT (using the NWChem program package[27]) calculations are performed. The PBE0 hybrid GGA functional is employed as the density functional approximation. For the At center, the ECP60MDF energy-consistent PP[28] is used to mimic the role of the 60 core electrons and implicitly account for relativistic effects while the remaining electrons are treated with the aug-cc-pVTZ-PP-2*c* basis set.[28,29] For the F centers, the aug-cc-pVTZ basis set is used.[30] Note that this particular combination of functional and basis sets was found (see Chapter 3) to be a relevant compromise for retrieving accurate geometries for At species, including AtF_3. Different transition states (TSs) are initially located at the scalar relativistic level of theory and are afterwards refined by accounting for SOC. The connectivities between the identified TSs and minima are established at the scalar relativistic level through the computation of intrinsic reaction coordinate (IRC) pathways. Note that the nature of each critical point has been verified through the computation of harmonic vibrational frequencies.

4.2.1 Critical points on the ground-state PES of AtF_3

Geometrical parameters and relative energies between identified critical points on the ground-state PES of AtF_3 are gathered in Table 4.1. In line with the VSEPR qualitative prediction and with previous quantum mechanical calculations,[15,16,18,19] we have identified a T-shaped C_{2v} structure as the global minimum for the AtF_3 system. Note that there are three equivalent T-shaped C_{2v} structures on the ground-state PES. The D_{3h} structure is found to be a local minimum that is 2.4 $kJ \cdot mol^{-1}$ higher in energy than the T-shaped C_{2v} ones, according to our 2*c*-PBE0 calculations. Note that this energy difference is in reasonable agreement with the 2*c*-CCSD(T) value reported by Yang and Wang, 7.72 $kJ \cdot mol^{-1}$. For convenience, to evidence the effect of SOC on the individual geometries and $\Delta E^{D_{3h}-C_{2v}}$, we print scalar relativistic results in Table 4.1. It can be seen that in both structures, SOC lengthens the equilibrium bond lengths (by ~0.03 Å) while in the T-shaped C_{2v} one it also enlarges the α bond angle by ~5°. As well, SOC appears to reduce the relative energy between these minima (by 7.5 $kJ \cdot mol^{-1}$). One may thus deduce that SOC actually acts oppositely to

the PJTE and contributes to create a minimum D_{3h} structure in AtF_3. The conversion of the D_{3h} geometry to the T-shaped C_{2v} one would occur primarily *via* displacements along its doubly-degenerate $\nu_{e'}$ bending mode. In SR-PBE0 calculations we identify this vibrational normal mode to be 72 cm^{-1} while when SOC is accounted for, it is reduced to 47 cm^{-1}. Hence, this time one can deduce that SOC actually favors the PJTE, contributing to the destabilization of D_{3h} structure. The connection between SOC and PJTE will be clarified later on.

Table 4.1 Geometrical parameters for the identified minima and TSs (bond lengths in Å and angles in degrees) of the ground-state PES of AtF_3, relative energies (in $kJ \cdot mol^{-1}$) with respect to the T-shaped C_{2v} minima, and magnitude of the imaginary frequency (in cm^{-1}) for each TS. For the definition of the geometrical parameters, see Figs. 4.1 and 4.3.

Minima	D_{3h}	T-shaped C_{2v}			$\Delta E^{D_{3h}-C_{2v}}$
	r_e	r_{ax}	r_{eq}	α	
SR-PBE0	2.040	2.043	1.961	85.6	9.9
2*c*-PBE0	2.068	2.068	2.012	91.0	2.4
Transition states		Y-shaped C_{2v}			$\Delta E^{TS-C_{2v}}$
		r_{ax}	r_{eq}	α	ν_{a_1}	
SR-PBE0		2.053	2.001	107.4	66i	11.9
2*c*-PBE0		2.075	2.047	108.7	42i	3.1
		C_s				
		r_{in}	r_{out}		$\nu_{a''}$	
SR-PBE0		1.969	2.078		308i	242.8

We now question the nature of the Y-shaped C_{2v} TS identified by Yang and Wang.[15] Its geometrical parameters and the relative energy with respect to the global T-shaped C_{2v} minima, are presented in Table 4.1. Comparing its structure with the one of the D_{3h} local minimum, we noted that it displays a α bond angle smaller than 120°, a r_{ax} bond length larger than r_e and r_{eq} bond lengths smaller than r_e. This TS lies slightly above the D_{3h} minimum, by 0.7 $kJ \cdot mol^{-1}$ (in very good agreement with the 0.5 $kJ \cdot mol^{-1}$ value obtained in 2*c*-CCSD(T) calculations[15]), and it appears to connect this minimum with any of the three T-shaped C_{2v} global minima. The IRC energy profile shown in Fig. 4.2, calculated at the SR-PBE0 level, clearly demonstrates the abovementioned statement.

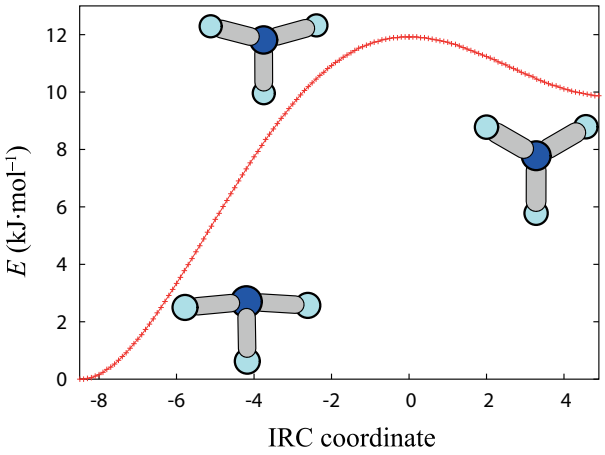

Figure 4.2 Energy along the IRC path starting from a Y-shaped C_{2v} TS of AtF_3, calculated at the SR-PBE0 level. The energy of the T-shaped C_{2v} structures energy is chosen as the zero of energy.

In the literature, the potential existence of a TS connecting the equivalent T-shaped C_{2v} global minima has not been considered. In SR-PBE0 calculations, we have identified that such TS has a distorted non-planar geometry pertaining to the C_s symmetry point group, as illustrated in Fig. 4.3. Its geometrical parameters are compiled in Table 4.1. Displacements along the in-plane $\nu_{a''}$ imaginary frequency mode, brings this C_s TS into the T-shaped C_{2v} global minima, as demonstrated by the IRC profile displayed in Fig. 4.3 (right panel). We have actually failed in converging on such a C_s TS structure in 2*c*-PBE0 calculations; all our trials led to a second-order saddle point C_{3v} structure that has a doubly degenerate normal mode with $\nu_e = 67\text{i}\ \text{cm}^{-1}$. One can thus state that either the C_s TS does not exist at the 2*c*-PBE0 level, or that the C_s and the C_{3v} structures are energetically near-degenerate, fact that leads to the practical impossibility of converging on a C_s stationary point. Scrutinizing the literature, we noted that in the limit of a doubly degenerate zero frequency normal mode, our identified C_{3v} structure would comply with the concept of a "monkey" saddle point associated with the trifurcation toward the three possible C_s TSs.[31,32]

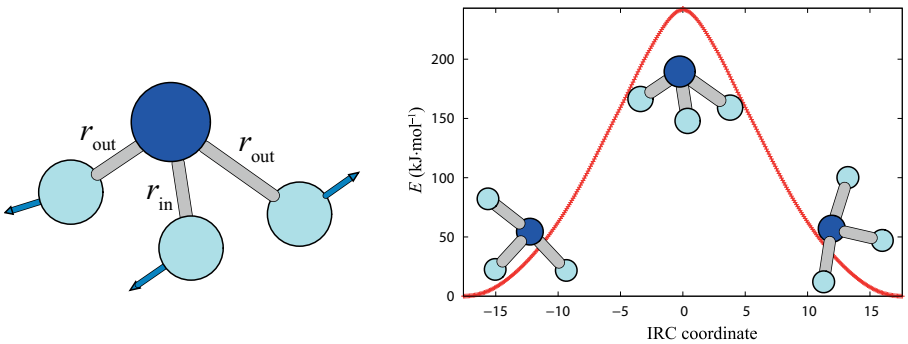

Figure 4.3 C_s TS structure of AtF_3 with displacement vectors traced for the imaginary frequency (see Table 4.1) and energy along the IRC path starting from this TS, computed at the SR-PBE0 level. The energy of the T-shaped C_{2v} structures is chosen as the zero of energy.

Furthermore, effective "monkey" saddle points are known to correspond to C_{3v} second-order saddle points that exhibit a doubly degenerate imaginary frequency, usually of the order of ~50i cm^{-1}. Such an effective "monkey" saddle has been suggested, for instance, in tetra-coordinated AX_4 systems.[33] Note that the near-degeneracy between the C_{3v} and the C_s structures is also a signature for the existence of an effective "monkey" saddle point. Presently, we cannot give a definite statement on the existence of an effective "monkey" saddle at the C_{3v} structure of AtF_3. Note that a classic pictorial view of a "monkey" saddle point, and a schematic representation of the PES around it for the AtF_3 case, is placed in Fig. A2.1 (see Appendix 2).

4.2.2 Topology of the AtF_3 ground-state PES

A schematic representation of the connectivity map between the different critical points of the ground-state PES of AtF_3 is shown in Fig. 4.4. It bears a local minimum having trigonal-planar D_{3h} structure surrounded by three equivalent T-shaped C_{2v} global minima. Between the D_{3h} and the T-shaped C_{2v} structures, there are slight energy barriers to be overcome that are associated with Y-shaped C_{2v} TSs. In the absence of SOC, undoubtedly, the *pseudo*-rotation energy barrier to go from one C_{2v} minimum to another one is associated with a C_s TS. Nevertheless such a barrier appears too high in energy and hence is not expected to be chemically relevant. When SOC is accounted for, instead of a C_s TS we identified a higher symmetry C_{3v} structure corresponding eventually to an effective "monkey" saddle point.

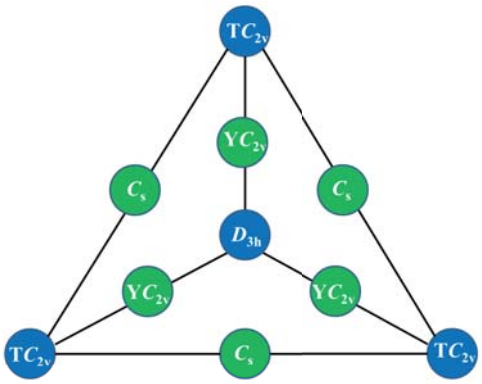

Figure 4.4 Scheme showing the connectivity map between the critical points of the ground-state PES of AtF_3. Color code: blue is used for minima, green for TSs.

Note that all the critical points reported in Fig. 4.4 are lower in energy than the lowest dissociation limit. To support this statement, the dissociation energies leading to AtF + F_2 or AtF_2 + F have been computed and reported in Table A2.1 (see Appendix 2).

Finally we would like to comment on the energy difference between the T-shaped C_{2v} and the D_{3h} minima of AtF_3. While the relative energy between them is already very small, we found that the inclusion of the thermal and entropic contributions reduces it furthermore. At T = 298 K and P = 1 atm, the free energy difference computed at the 2*c*-PBE0/AVTZ level of theory is less than 0.3 kJ·mol^{-1}. It is thus impossible to conclude on the nature of the most stable AtF_3 structure given the accuracy of the used approach. However, since the free energy difference between these structures and the associated energy barriers are so small, the thermal energy would lead to perpetual movement between the three equivalent T-shaped C_{2v} structures and the D_{3h} one. Hence, it would be impossible to experimentally distinguish between them and an average D_{3h} geometry would be seen in experiments, if they were possible.

4.3 Insights from wave-function-based methods

In this subsection, we study the PES of AtF_3 using a two-step multiconfigurational wave-function-based approach where SOC is introduced *a posteriori* (*i.e.* c-SOCI). Hence, we perform a series of SA-CASSCF (to retrieve 0th order wave functions), NEVPT2 (to retrieve more accurate correlated energies) and c-SOCI (to account for SOC) calculations, on the previously obtained 2*c*-PBE0 equilibrium structures of AtF_3. All these computations were performed with the ORCA program package.[34] Scalar relativistic effects are accounted through the use of the DKH Hamiltonian.[35-37] For the At and F centers, the segmented all-electron relativistically contracted SARC-TZVP-DKH basis sets were employed.[38,39] Two active spaces have been considered in the SA-CASSCF calculations, (i) 2 electrons and the 6*p* orbitals of the At center, *i.e.* SA-CASSCF(2/3), and (ii) 20 electrons and the 6*p* and 2*p* orbitals of At and F respectively, *i.e.* SA-CASSCF(20/12). In the SA-CASSCF(2/3) calculations, different SOF states are generated by performing an equally-weighted orbital average over 6 spin-singlet (6S) and 3 spin-triplet (3T) states. In the SA-CASSCF(20/12) calculations, the averaging is performed over 21S and 20T states. In this latter case, the choice of the averaging scheme was made in such a way that (i) it does not artificially break the D_{3h} symmetry, (ii) it includes all the essentially singly excited states which are of particular importance in view of SOC, and (iii) enlargement of the SA and of the SI spaces hardly affects the computed SOC ground-state energy stabilizations.

In the following, we start by assessing the dependence of the results on the specific degrees of freedom of the method. In Table 4.2 we print several energy parameters, $\Delta E^{D_{3h}-C_{2v}}$ (calculated with and without SOC), $E_{SOC}^{D_{3h}}$ and $E_{SOC}^{C_{2v}}$, which are the SOC energy stabilizations of the individual

D_{3h} and C_{2v} structures, and $\Delta E_{SOC}^{D_{3h}-C_{2v}}$, which shows the overall impact of SOC on $\Delta E^{D_{3h}-C_{2v}}$. Note that unless specified otherwise, we always refer to the T-shaped C_{2v} structure of AtF_3, as C_{2v} structure.

Table 4.2 Contributions (in kJ·mol^{-1}) to $\Delta E^{D_{3h}-C_{2v}}$ in AtF_3, computed at various levels of theory.

	NEVPT2	c-SOCI/NEVPT2[a]				2*c*-CCSD(T)
(CAS), SA	$\Delta E^{D_{3h}-C_{2v}}$	$E_{SOC}^{D_{3h}}$	$E_{SOC}^{C_{2v}}$	$\Delta E_{SOC}^{D_{3h}-C_{2v}}$	$\Delta E^{D_{3h}-C_{2v}}$	$\Delta E^{D_{3h}-C_{2v}}$
(2/3), 6S3T	5.5	−89.9	−83.8	−6.1	−0.5	7.7[15]
(20/12), 20S21T	7.4	−58.8	−58.1	−0.7	6.7	
	CASSCF	c-SOCI/CASSCF[b]				
(20/12), 20S21T	18.4	−51.7	−53.4	+2.3	20.1	

[a]c-SOCI calculations are performed using SA-CASSCF wave functions and NEVPT2 energies.
[b]c-SOCI calculations are performed using both SA-CASSCF wave functions and energies.

At first, the calculated $\Delta E^{D_{3h}-C_{2v}}$ value at the NEVPT2(2/3) level appears in good agreement with the reference 2*c*-CCSD(T) value, even though SOC has not been incorporated. Since the computed $\Delta E_{SOC}^{D_{3h}-C_{2v}}$ value is of the same order of magnitude as the $\Delta E^{D_{3h}-C_{2v}}$ one, the latter almost vanishes at the c-SOCI/NEVPT2(2/3) level (−0.5 kJ·mol^{-1}). Furthermore, similar energy parameters determined for the X = Cl, Br and I trifluorides using such a (2/3) active space were found unreliable, with respect to (2*c*-)CCSD(T) values, especially for ClF_3 which may notably feature some significant degree of covalence in the Cl−F bonds (see Table A2.2). We can better describe this covalence by enlarging the active space with the valence 2*p* orbitals of the F centers, leading to CAS(20/12) calculations. Note that the energy parameters obtained using this larger active space for the X = Cl, Br and I trifluorides will be later presented. For the present AtF_3 case, using such a large active space, one can observe that the calculated relative energy of 20.1 kJ·mol^{-1} at the c-SOCI/CASSCF(20/12) level is quite large compared to the reference 2*c*-CCSD(T) result (see Table 4.2). Accounting for the remaining part of the electron correlation appears to be essential for determining accurate energies in AtF_3, which is supported by the c-SOCI/NEVPT2(20/12) calculated value of $\Delta E^{D_{3h}-C_{2v}}$ (6.7 kJ·mol^{-1}). Moreover, it appears that the NEVPT2(20/12) $\Delta E^{D_{3h}-C_{2v}}$ value resemble well the c-SOCI/NEVPT2(20/12) one. That is, even though SOC induces large stabilizations of the individual D_{3h} and C_{2v} structures (~58 kJ·mol^{-1}, see the $E_{SOC}^{D_{3h}}$ and $E_{SOC}^{C_{2v}}$ values in Table 4.2), these stabilizations are rather similar rendering $\Delta E_{SOC}^{D_{3h}-C_{2v}}$ small. Nonetheless, the calculated $\Delta E_{SOC}^{D_{3h}-C_{2v}}$ of −0.7 kJ·mol^{-1} appears too small compared to the value obtained from 2*c*- and SR-PBE0 calculations (7.5 kJ·mol^{-1}). We speculate that this difference originates in the

neglect of the geometry relaxation in the calculated energies at the NEVPT2 and c-SOCI/NEVPT2 levels, which will be further commented.

4.3.1 On the ground-state PES of AtF_3

In the SA-CASSCF(20/12) calculations at both the C_{2v} and D_{3h} 2*c*-PBE0 equilibrium structures, we found that the ground-state wave function has ~91% weight on the ground-state spin-singlet HF configuration. In addition, when SOC is introduced at the c-SOCI/NEVPT2(20/12) level, we found that the ground-state spin-orbit coupled wave-function has ~83% weight on the ground SOF singlet-spin component. Other important contributions amount to ~16% and ~13% weights on the $|M_S|$=1 spin components of the first two excited-SOF-triplet states, at the D_{3h} and C_{2v} structures respectively. This actually means that both the SOF and SOC wave functions in AtF_3 are essentially single configurational, fact that justifies the use of single-configurational and single-reference methods, such as (2*c*-)DFT and (2*c*-)CCSD(T), to determine the lowest energy structures in AtF_3.

We next attempted to identify, using NEVPT2(20/12) and c-SOCI/NEVPT2(20/12) calculations, if there is indeed a TS between the C_{2v} and D_{3h} minima of the ground-state PES of AtF_3. We performed scans between the aforementioned structures by varying the α, r_{ax} and r_{eq} geometrical parameters of the T-shaped C_{2v} structure. Similar scans were reported in the literature but they were restricted to distortions involving only the α bending angle. Our scans thus seek to evidence a better approximate minimum energy pathway between the two minima of the PES. In Fig. 4.5, contour plots of the obtained surfaces at the NEVPT2(20/12) and c-SOCI/NEVPT2(20/12) levels of theory are shown. Note that a non-uniform grid has been defined by interpolations between the C_{2v} and D_{3h} minima, and each r_{eq} value in the contour plots corresponds to a different r_{ax} value.

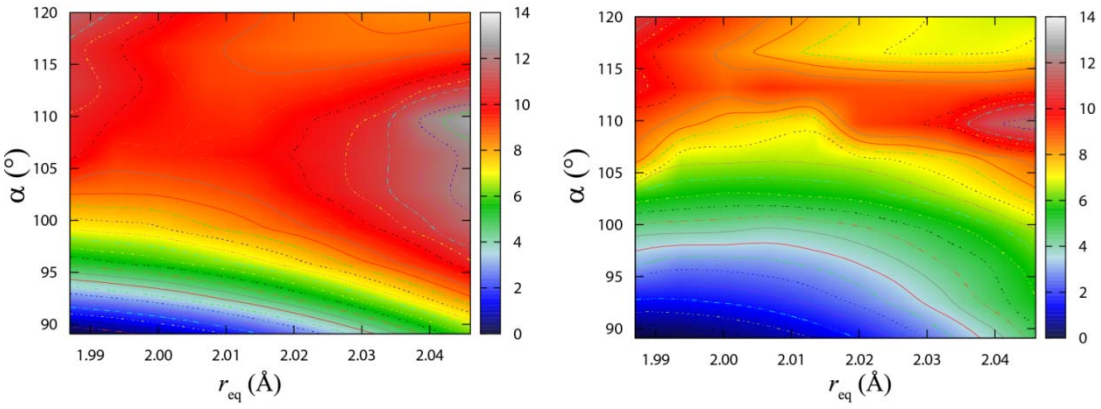

Figure 4.5 NEVPT2(20/12) (left) and c-SOCI/NEVPT2(20/12) (right) ground-state PES of AtF_3. The energy scale is expressed in kJ·mol^{-1} and the T-shaped C_{2v} structure energies are chosen as the zeroes of energy.

We observe that a TS is evidenced with and without SOC and that its approximate structure is similar to the one found at the (2*c*-)PBE0 level. That is, it has a α bond angle smaller than 120° and r_{ax} and r_{eq} are larger and smaller than r_e, respectively. The comparison between the two contour plots shows the effect of SOC on the ground-state PES of AtF_3. It is now clear that SOC "flattens" it, slightly decreasing the relative energy between the T-shaped C_{2v} and the trigonal-planar D_{3h} minima and, to a much lesser extent, between the T-shaped C_{2v} minimum and the Y-shaped C_{2v} TS. These findings agree also with 2*c*- and SR-CCSD(T) results that suggest an ~8 kJ·mol^{-1} reduction of $\Delta E^{D_{3h}-C_{2v}}$ upon the effect of SOC.

4.3.2 Electronic factor contributions to $\Delta E^{D_{3h}-C_{2v}}$ and $\Delta E^{TS-D_{3h}}$

As the relative energy between the T-shaped C_{2v} and the D_{3h} minima is to a less extent influenced by SOC, we seek to quantify the electronic factors that actually have the major impact. For this task, we perform a series of nonrelativistic and scalar relativistic HF and NEVPT2 single-point calculations at the 2*c*-PBE0 equilibrium geometries using uncontracted SARC-TZVP-DKH basis sets. As shown in Fig. 4.6, one can follow two ways to retrieve the contributions of the electron correlation and scalar relativistic effects.

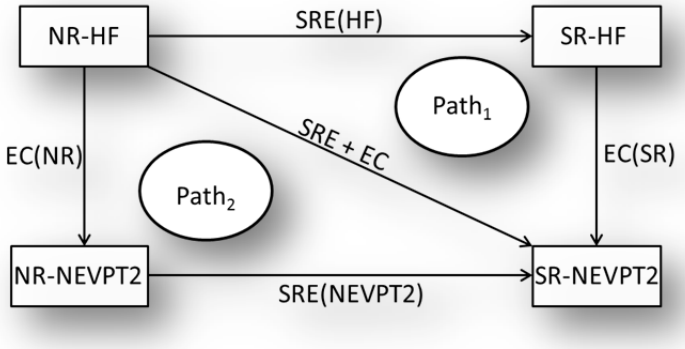

Figure 4.6 Different pathways used to define the contributions of scalar relativistic effects and electron correlation on $\Delta E^{D_{3h}-C_{2v}}$ [NR stands for nonrelativistic, SRE stands for scalar relativistic effects and EC stands for electron correlation].

According to $Path_1$, one obtains first the scalar relativistic contribution at the uncorrelated HF level and then the contribution of the electron correlation in the presence of scalar relativistic effects. According to $Path_2$, one obtains at first the contribution of electron correlation in the absence of scalar relativistic effects and then scalar relativistic contributions at the correlated NEVPT2 level. We present the different results in Table 4.3. It can be seen that the contributions of the electron correlation or scalar relativistic effects to $\Delta E^{D_{3h}-C_{2v}}$, as obtained following both pathways, are not

equal pointing out that these two effects are actually not additive, as expected. With both $Path_1$ and $Path_2$, scalar relativistic effects have a larger impact on the relative energy under study even though they largely interplay with electron correlation. One can see that the summation of SRE(HF) and EC(NR) is around 20 kJ·mol^{-1} over the one of EC(SR) and SRE(NEVPT2). We hypothesize that the aforementioned effects and their interplay are responsible for the large stabilization of the D_{3h} structure w.r.t. the T-shaped C_{2v} one.

Table 4.3 Contributions (in kJ·mol^{-1}) of electron correlation and scalar relativistic effects to $\Delta E^{D_{3h}-C_{2v}}$ as retrieved according to the two pathways depicted in Fig. 4.6.

NR-HF	$Path_1$		$Path_2$		SR-NEVPT2	
$\Delta E^{D_{3h}-C_{2v}}$	SRE(HF)	EC(SR)	EC(NR)	SRE(NEVPT2)	SRE + EC	$\Delta E^{D_{3h}-C_{2v}}$
80.5	−52.3	−22.1	−31.5	−42.9	−74.4	6.1

We have also investigated the different electronic factors that lead to the small energy barrier between the D_{3h} and T-shaped C_{2v} minima of AtF_3, *i.e.* affecting $\Delta E^{TS-D_{3h}}$ where by TS here we refer to the Y-shaped C_{2v} TS. Using as well uncontracted SARC-TZVP-DKH basis sets, we have performed nonrelativistic and scalar relativistic HF and NEVPT2(20/12) as well as c-SOCI/NEVPT2(20/12) single-point calculations at the 2*c*-PBE0 equilibrium geometries of the Y-shaped C_{2v} TS and of the D_{3h} local minimum of AtF_3. The results are presented in Table 4.4. It is now clear that the electron correlation and scalar relativistic effects are the main electronic factors which tend to raise the energy of the Y-shaped C_{2v} structure above the one of the D_{3h} minimum, and, meshed together, they both render the former structure as TS. SOC appears to play only a minor role on $\Delta E^{TS-D_{3h}}$, and a trifling 0.3 kJ·mol^{-1} energy increase is predicted. We note that this small influence of SOC is consistent with our (2*c*-)PBE0 findings or reference (2*c*-)CCSD(T) ones,[15] which show ~1 kj·mol^{-1} reduction in $\Delta E^{TS-D_{3h}}$. Hence, spin-dependent relativistic affects are definitely small and somewhat bland on the relative energy between the Y-shaped C_{2v} TS and the D_{3h} minimum.

Table 4.4 Energy difference (in kJ·mol^{-1}) between the Y-shaped C_{2v} TS and the D_{3h} minimum of AtF_3 ($\Delta E^{TS-D_{3h}}$) calculated at different levels of theory (2*c*-PBE0 geometries are used).

NR-HF	SR-HF	NR-NEVPT2	SR-NEVPT2	c-SOCI/NEVPT2
−12.0	−2.5	−6.2	1.8	2.2

4.4 A comparative study between AtF_3 and other XF_3 systems (X = Cl, Br, I)

In this section, we seek to perform a comparison between AtF_3 and its lighter trifluoride analogues. For this task, we have first carried out DFT calculations in the same fashion as described

previously for the AtF_3 case. Note that the ECP10MDF and ECP28MDF energy-consistent PPs have been used to avoid the treatment of the 10 and 28 core electrons of Br and I, respectively, while the remaining valence electrons have been treated with aug-cc-pVTZ-PP basis sets.[28,40] The 2*c* basis set extension has been retained for the I center.[29] For the Cl center, the aug-cc-pVTZ basis sets have been used.[30,41] In order to check the performance of the PBE0 functional for the current cases, we compare the geometrical parameters of the obtained T-shaped C_{2v} and D_{3h} equilibrium structures to experiment (when available) or to appropriate CCSD(T) results. For obtaining reference geometrical parameters for the D_{3h} structures, as well as reference $\Delta E^{D_{3h}-C_{2v}}$ values, for the ClF_3 and BrF_3 systems, we have performed geometry optimizations using the CCSD(T) method using the ORCA program package. For the ClF_3 case, relativistic effects have been neglected and all-electron TZVP basis sets have been used.[42] For the BrF_3 case, scalar relativistic effects have been introduced *via* the use of the DKH Hamiltonian and accordingly, segmented all-electron relativistic contracted SARC-TZVP-DKH basis sets[39] have been used.

The geometrical parameters of the obtained T-shaped C_{2v} and D_{3h} structures, as well as $\Delta E^{D_{3h}-C_{2v}}$ energies, along with available reference data, are presented in Table 4.5. One can observe at first that the CCSD(T) and PBE0 equilibrium geometries for the T-shaped C_{2v} structures of ClF_3 and BrF_3 are in exceptional agreement with the experimental ones. These findings allow us, in the cases where experimental data is not available, to use CCSD(T) results as reference for assessing the quality of the PBE0 ones. Nevertheless it is quite evident that PBE0 leads to very accurate T-shaped C_{2v} and D_{3h} geometries for all the studied XF_3 systems. Moreover, the PBE0 calculations reproduce well the trend on $\Delta E^{D_{3h}-C_{2v}}$ that arises from X = Cl to X = I, as predicted by CCSD(T) calculations.

A schematic representation of the connectivity maps between the different critical points of the ground-state PESs of the XF_3 (X = Cl, Br, I) fluorides is shown in Fig. 4.7. The reader can find the geometrical parameters of the different critical points, and relative energies, in Table 4.5. Alike the AtF_3 case, we have found that all the studied XF_3 systems (X = Cl, Br, I) exhibit T-shaped C_{2v} global minima. In contrast, the trigonal-planar D_{3h} structures are found to be second-order saddle points with one doubly degenerate imaginary frequency ($\nu_{e'} = 127i$ for ClF_3, $\nu_{e'} = 78i$ for BrF_3 and $\nu_{e'} = 54i$ for IF_3). The identified Y-shaped C_{2v} TSs for the present fluorides differs, in geometries and nature, from the Y-shaped C_{2v} TS found in the AtF_3 case. Comparing their geometries with the D_{3h} ones (see Table 4.5), one may notice that they exhibit r_{ax} bond lengths smaller than r_e, r_{eq} bond lengths larger than r_e, and α bond angles larger than 120°. For the ClF_3 and IF_3 systems, these Y-

shaped C_{2v} TSs have been hypothesized to be involved in the *pseudo*-rotation barriers between each two equivalent T-shaped C_{2v} minima.[15,43] Nonetheless, these hypotheses are valid, and moreover verified for all the XF_3 (X = Cl, Br, I) cases, as demonstrated by IRC profiles (see Fig. A2.2).

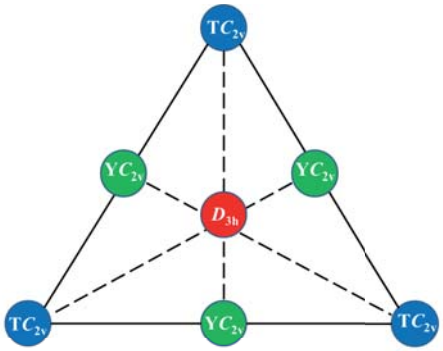

Figure 4.7 Scheme showing the connectivity map between the critical points of the ground-state PES of XF_3 (X = Cl, Br, I) [color code: blue is used for minima, green for TSs and red for second-order saddle points].

We remind that the analogue Y-shaped C_{2v} TS in the AtF_3 case was connecting the T-shaped C_{2v} and D_{3h} minima. Finally, we note again that all the critical points reported in Fig. 4.7 are lower in energy than the lowest dissociation limit for each XF_3 system (see Table A2.1).

Table 4.5 Geometrical parameters for the identified minima and TSs (bond lengths in Å and angles in degrees) of the ground-state PES of XF_3 (X = Cl, Br, I), relative energies (in kJ·mol^{-1}) with respect to the T-shaped C_{2v} minimum and the magnitude of the imaginary frequency (in cm^{-1}) for each TS.

Minima		D_{3h}	T-shaped C_{2v}			$\Delta E^{D_{3h}-C_{2v}}$
System		r_e	r_{ax}	r_{eq}	α	
	NR-PBE0	1.728[a]	1.706	1.603	87.4	91.5
ClF_3	NR-CCSD(T)	1.738[a]	1.703	1.605	87.1	96.7
	Expt.[4]	-	1.698	1.598	87.5	-
	2*c*-PBE0	1.825[a]	1.812	1.725	86.4	60.2
BrF_3	SR-CCSD(T)	1.828[a]	1.811	1.725	86.0	70.7
	Expt.[3]	-	1.810	1.721	86.2	-
	2*c*-PBE0	1.965[a]	1.950	1.878	83.8	55.0
IF_3	2*c*-CCSD(T)[15]	1.941[a]	1.926	1.853	83.3	67.8
Transition states			Y-shaped C_{2v}			$\Delta E^{TS-C_{2v}}$
System			r_{ax}	r_{eq}	α	ν_{b_2}	
ClF_3	NR-PBE0		1.703	1.762	128.7	207i	89.3
BrF_3	2*c*-PBE0		1.814	1.843	125.6	127i	59.9
IF_3	2*c*-PBE0		1.958	1.978	124.4	90i	54.9

[a]The D_{3h} structure corresponds to a second-order saddle point.

4.4.1 Electronic factor contributions to $\Delta E^{D_{3h}-C_{2v}}$

Similarly to what was done for AtF_3, we approached the ground-state PESs of the XF_3 systems (X = Cl, Br, I) with a two-step multiconfigurational wave-function-based approach where SOC is introduced *a posteriori*. We hence performed SA-CASSCF(20/12), NEVPT2(20/12) and c-

SOCI calculations. We made use of SARC-TZVP-DKH basis sets[39] and the scalar relativistic effects were accounted for through the use of the DKH Hamiltonian. The ground-state PESs of the XF_3 fluorides have notably been scanned between the D_{3h} and T-shaped C_{2v} structures at the c-SOCI/NEVPT2(20/12) level of theory. Contour plots of the resulted surface scans are shown in Figure 4.8.

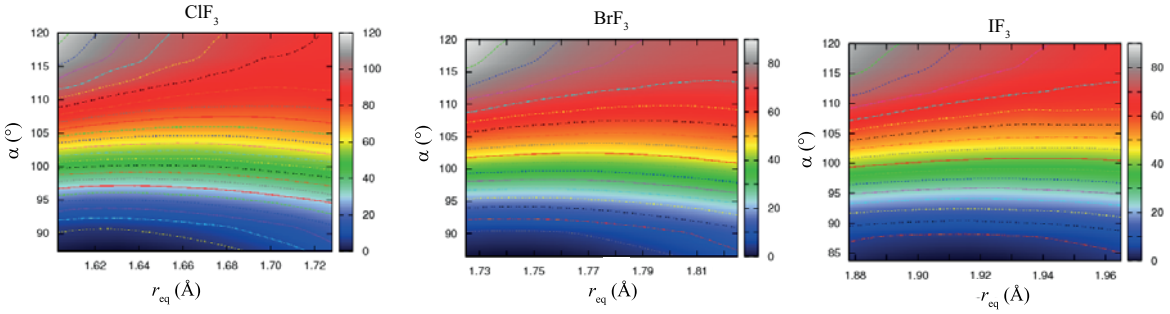

Figure 4.8 c-SOCI/NEVPT2(20/12) ground-state PESs of the XF_3 (X = Cl, Br, I) systems. The energy scales are expressed in kJ·mol^{-1} and the energy of the T-shaped C_{2v} structures is chosen as the zero of energy in each case.

This study allows us to spot, at the present level of theory and in contrast to the AtF_3 case, that the D_{3h} structures do not correspond to minima and that there are no energy barriers on the pathways down to the T-shaped C_{2v} global minima. On the previously determined (2*c*-)PBE0 equilibrium structures of the present fluorides (D_{3h} and C_{2v} structures), single point calculations were performed and the obtained $\Delta E^{D_{3h}-C_{2v}}$, $E_{SOC}^{D_{3h}}$, $E_{SOC}^{C_{2v}}$ and $\Delta E_{SOC}^{D_{3h}-C_{2v}}$ parameters are gathered in Table 4.6. Note that values obtained for AtF_3 are recalled for comparison. The role of the dynamic electron correlation is highlighted by the comparison between the CASSCF and NEVPT2 results. For the ClF_3 and BrF_3 cases, the dynamic electron correlation increases the relative energy between the T-shaped C_{2v} and D_{3h} structures, while the opposite trend is observed for the IF_3 and AtF_3 systems. Actually, the dynamic electron correlation appears to be crucial in establishing the expected trend: only the $\Delta E^{D_{3h}-C_{2v}}$ calculated at the NEVPT2(20/12) level of theory show the correct trend with individual values in good agreement with the CCSD(T) ones. As expected, the SOC energy stabilizations to the D_{3h} and C_{2v} structures are negligible for the X = Cl and Br case and only moderate for the X = I case (~5.5 kJ·mol^{-1}). This is of course largely contrasting the case of AtF_3 (SOC energy stabilizations are larger than 50 kJ·mol^{-1}). If $E_{SOC}^{D_{3h}}$ and $E_{SOC}^{C_{2v}}$ enlarge with the atomic number, the increase do not perfectly correlate with Z^4. This potentially indicates a decrease in the reduction factors within the Cl−At series, *i.e.* that the systems become more and more ionic, in agreement with the increase in the electronegativity difference between the F and X atoms.

Table 4.6 Contributions (in kJ·mol^{-1}) to the $\Delta E^{D_{3h}-C_{2v}}$ in XF_3 (X = Cl, Br, I and At) systems computed at various levels, using the (20/12) active space and the 21S20T state-everaging and state interaction spaces.

	NEVPT2	c-SOCI/NEVPT2				(2*c*-)CCSD(T)
System	$\Delta E^{D_{3h}-C_{2v}}$	$E_{SOC}^{D_{3h}}$	$E_{SOC}^{C_{2v}}$	$\Delta E_{SOC}^{D_{3h}-C_{2v}}$	$\Delta E^{D_{3h}-C_{2v}}$	$\Delta E^{D_{3h}-C_{2v}}$
ClF_3[a]	88.6 (64.5)	−0.1 (−0.1)	−0.1 (−0.1)	−0.0 (−0.0)	88.6 (64.5)	96.7
BrF_3[a]	72.0 (69.5)	−1.2 (−1.2)	−1.0 (−1.0)	−0.2 (−0.2)	71.8 (69.3)	70.7
IF_3[a]	66.2 (78.6)	−6.1 (−5.5)	−5.4 (−5.1)	−0.7 (−0.4)	65.5 (78.3)	67.8[15]
AtF_3[a]	7.4 (18.4)	−58.8 (−51.7)	−58.1 (−53.4)	−0.7 (+2.3)	6.7 (20.1)	7.7[15]

[a]CASSCF and c-SOCI/CASSCF results are reported in parentheses.

Lastly, we wish to highlight the contribution of the electron correlation and scalar relativistic effects to the reductions in the relative energies between the D_{3h} and T-shaped C_{2v} structures, along the XF_3 (X = Cl, Br, I) series. For the present fluorides, we have followed the previously presented approach (see Fig. 4.6). The associated results are gathered in Table 4.7. Similar as in the AtF_3 case, one can spot the non-additivity between the electron correlation and scalar relativistic effects, *i.e.* the considered two paths issue different values for electron correlation and scalar relativistic effects showing the fact that they interplay. This interplay appears to be more and more pronounced going down the group XVII, as expected based on the increase of the importance of scalar relativistic effects. In contrast to the case of AtF_3, the electron correlation is the dominant electronic factor that diminishes the relative energy between the D_{3h} and T-shaped C_{2v} structures in the XF_3 (X = Cl, Br, I) fluorides. Finally, it is worth noting that the trend in $\Delta E^{D_{3h}-C_{2v}}$ in the XF_3 (X = Cl, Br, I and At) fluorides is already present at the nonrelativistic HF level even though the individual values are considerably larger than the scalar relativistic counterparts. That is, the simultaneous treatment of the electron correlation and scalar relativistic effects impacts in a similar way the $\Delta E^{D_{3h}-C_{2v}}$ values.

Table 4.7 Contributions (in kJ·mol^{-1}) of electron correlation (EC) and scalar relativistic effects (SRE) to $\Delta E^{D_{3h}-C_{2v}}$ as retrieved according to the two pathways depicted in Fig. 4.6.

	NR-HF	$Path_1$		$Path_2$		SR-NEVPT2	
XF_3	$\Delta E^{D_{3h}-C_{2v}}$	SRE(HF)	EC(SR)	EC(NR)	SRE(NEVPT2)	SRE + EC	$\Delta E^{D_{3h}-C_{2v}}$
ClF_3	185.8	−4.1	−92.6	−93.6	−3.1	−96.7	89.1
BrF_3	149.7	−14.7	−63.1	−65.9	−11.9	−77.8	71.9
IF_3	142.5	−29.4	−46.3	−51.1	−24.5	−75.7	66.8
AtF_3[a]	80.5	−52.3	−22.1	−31.5	−42.9	−74.4	6.1

[a]Values are recalled from Table 4.3 for comparison.

4.5 Conclusions

In this chapter we have analyzed the topology of the ground-state PES of the AtF_3 system and furthermore, we have established a comparison with the ones of the ground-state PESs of the lighter analogues. Several conclusions arise from this work. First we have shown that the used two-step spin-orbit configuration interaction approach is suitable to address the electronic structure of systems containing a heavy 6*p* element such as At. We noted that sometimes such an approach is considered to be problematic for investigating systems involving a heavy element from the 6*p* family.[44] The present approach allowed us for instance to investigate the potential multiconfigurational character of the ground-state wave functions, particularly in the AtF_3 system. In this latter case, the ground-state wave function has been found to be essentially single-configurational and closed-shell, even though a slight open-shell character (~16%) is rendered by SOC. It is hence an indisputable support for previous studies on AtF_3 that made use of single-determinental and single reference approaches. However, one should also mention that the consistent tracking of electronic states w.r.t. geometrical displacement should always be done or checked up with multiconfigurational calculations.

The topology of the ground-state PES of AtF_3 has been found to be different from the ones of the considered analogues, and in particular from the one of IF_3. This shows that even in simple systems, At may behave differently than I, reinforcing the statements that, the basic chemical behavior of At does not necessarily follow the one of I, and that care must be taken when such an analogy is assumed. On the ground-state PES of AtF_3 we have unraveled three new C_s TSs connecting pairs of two equivalent T-shaped C_{2v} minima. However, we restrict this conclusion to the scalar relativistic formalism only. We have furthermore demonstrated that (three equivalent) Y-shaped C_{2v} TSs connect the D_{3h} local minimum with the T-shaped C_{2v} global minima of the AtF_3 PES, while other Y-shaped C_{2v} TSs connect the T-shaped C_{2v} global minima in the XF_3 (X = Cl, Br, I) systems. Even though the relative energy between the trigonal-planar D_{3h} and T-shaped C_{2v} minima of AtF_3 is very small (~7 $kJ \cdot mol^{-1}$), we have identified that thermal and entropic contributions drop this even more, *i.e.* to ~0.3 $kJ \cdot mol^{-1}$. In contrast to what has been currently proposed in the literature, we firmly consider that an average D_{3h} AtF_3 structure would be observed in experiments, if they were possible. That is, in contrast to IF_3 in particular, At coordinates in AtF_3 in a trigonal-planar D_{3h} structure on average and not in a T-shaped C_{2v} one, with the At–F bonds being essentially ionic.

From our multiconfigurational wave-function-based calculations, we identified that the relative energy between the D_{3h} and T-shaped C_{2v} structures is primarily diminished by electron correlation and scalar relativistic effects. The former effect has been found to be dominant for the X = Cl–I cases while the latter has been found the main contributor in AtF_3. SOC has an important contribution only in the case of AtF_3 where it leads to similar energy stabilization of the individual D_{3h}, Y- and T-shaped C_{2v} structures, thus not really affecting the topology of the PES. Finally, we state that both the electron correlation and scalar relativistic effects inhibit the *pseudo* Jahn-Teller effect in AtF_3, the sum of them and the interplay between them being the cause of the emerging D_{3h} "weak" local minimum.

Bibliography:

1. D.-C. Sergentu, M. Amaouch, J. Pilmé, N. Galland, R. Maurice, *J. Chem. Phys.* Electronic structures and geometries of the XF_3 (X = Cl, Br, I, At) fluorides, **2015**, 143, 114306.
2. E. H. Appelman, E. N. Sloth, M. H. Studier, *Inorg. Chem.* Observation of astatine compounds by time-of-flight mass spectrometry, **1966**, 5, 766.
3. D. W. Magnuson, *J. Chem. Phys.* Microwave spectrum and molecular structure of bromine trifluoride, **1957**, 27, 223.
4. D. F. Smith, *J. Chem. Phys.* The microwave spectrum and structure of chlorine trifluoride, **1953**, 21, 609.
5. H. S. P. Müller, *Phys. Chem. Chem. Phys.* The rotational spectrum of chlorine trifluoride, ClF_3. Centrifugal distortion analysis, Cl nuclear magnetic shielding tensor, structure, and the harmonic force field, **2001**, 3, 1570.
6. H. Selig, H. H. Claassen, J. H. Holloway, *J. Chem. Phys.* Infrared and raman spectra of ClF_3 and BrF_3, **1970**, 52, 3517.
7. H. H. Claassen, B. Weinstock, J. G. Malm, *J. Chem. Phys.* Vibrational spectra and thermodynamic properties of ClF_3 and BrF_3, **1958**, 28, 285.
8. M. Schmeisser, D. Naumann, E. Lehmann, *J. Fluorine Chem.* Vibrational spectrum of iodine trifluoride, **1974**, 3, 441.
9. S. Hoyer, K. Seppelt, *Angew. Chem. Int. Ed.* The structure of IF_3, **2000**, 39, 1448.
10. R. J. Gillespie, *J. Chem. Educ.* The valence-shell electron-pair repulsion (VSEPR) theory of directed valency, **1963**, 40, 295.
11. R. J. Gillespie, *J. Chem. Educ.* The electron-pair repulsion model for molecular geometry, **1970**, 47, 18.
12. R. J. Gillespie, R. S. Nyholm, *Quart. Rev. Chem. Soc.* Inorganic stereochemistry, **1957**, 11, 339.
13. R. J. Gillespie, E. A. Robinson, *Angew. Chem. Int. Ed.* Electron domains and the VSEPR model of molecular geometry, **1996**, 35, 495.
14. M. Kaupp, *Angew. Chem.* "Non-VSEPR" structures and bonding in d^0 systems, **2001**, 40, 3534.
15. D.-D. Yang, F. Wang, *Phys. Chem. Chem. Phys.* Structures and stabilities of group 17 fluorides EF_3 (E= I, At, and element 117) with spin–orbit coupling, **2012**, 14, 15816.
16. P. Schwerdtfeger, *J. Phys. Chem.* Second-order Jahn-Teller distortions in group 17 fluorides EF_3 (E= Cl, Br, I, and At). Large relativistic bond angle changes in AtF_3, **1996**, 100, 2968.
17. I. B. Bersuker, *Chem. Rev. Pseudo*-Jahn-Teller effect - A two-state paradigm in formation, deformation, and transformation of molecular systems and solids, **2013**, 113, 1351.
18. H. Kim, Y. J. Choi, Y. S. Lee, *J. Phys. Chem. B.* Spin-Orbit and electron correlation effects on the structure of EF_3 (E= I, At, and element 117), **2008**, 112, 16021.
19. C. Bae, Y.-K. Han, Y. S. Lee, *J. Phys. Chem. A.* Spin-orbit and relativistic effects on structures and stabilities of group 17 fluorides EF_3 (E= I, At, and element 117): Relativity induced stability for the D_{3h} Structure of $(117)F_3$, **2003**, 107, 852.
20. T. Fleig, A. J. Sadlej, *Phys. Rev. A.* Electric dipole polarizabilities of the halogen atoms in $^2P_{1/2}$ and $^2P_{3/2}$ states: Scalar relativistic and two-component configuration-interaction calculations, **2002**, 65, 032506.

21. J. Champion, M. Seydou, A. Sabatié-Gogova, E. Renault, G. Montavon, N. Galland, *Phys. Chem. Chem. Phys.* Assessment of an effective quasirelativistic methodology designed to study astatine chemistry in aqueous solution, **2011**, 13, 14984.
22. J. Pilmé, E. Renault, T. Ayed, G. Montavon, N. Galland, *J. Chem. Theory Comput.* Introducing the ELF topological analysis in the field of quasirelativistic quantum calculations, **2012**, 8, 2985.
23. A. Hermann, R. Hoffmann, N. W. Ashcroft, *Phys. Rev. Lett.* Condensed astatine: monatomic and metallic, **2013**, 111, 116404.
24. T. Ayed, M. Seydou, F. Réal, G. Montavon, N. Galland, *J. Phys. Chem. B.* How does the solvation unveil AtO^+ reactivity?, **2013**, 117, 5206.
25. J. Pilmé, E. Renault, F. Bassal, M. Amaouch, G. Montavon, N. Galland, *J. Chem. Theory Comput.* QTAIM analysis in the context of quasirelativistic quantum calculations, **2014**, 10, 4830.
26. M. J. Frisch, G. W. Trucks, H. B. Schlegel, G. E. Scuseria, M. A. Robb, J. R. Cheeseman, G. Scalmani, V. Barone, B. Mennucci, G. A. Petersson, H. Nakatsuji, M. Caricato, X. Li, H. P. Hratchian, A. F. Izmaylov, J. Bloino, G. Zheng, J. L. Sonnenberg, M. Hada, M. Ehara, K. Toyota, R. Fukuda, J. Hasegawa, M. Ishida, T. Nakajima, Y. Honda, O. Kitao, H. Nakai, T. Vreven, J. A. Montgomery, J. E. Jr. Peralta, F. Ogliaro, M. Bearpark, J. J. Heyd, E. Brothers, K. N. Kudin, V. N. Staroverov, R. Kobayashi, J. Normand, K. Raghavachari, A. Rendell, J. C. Burant, S. S. Iyengar, J. Tomasi, M. Cossi, N. Rega, J. M. Millam, M. Klene, J. E. Knox, J. B. Cross, V. Bakken, C. Adamo, J. Jaramillo, R. Gomperts, R. E. Stratmann, O. Yazyev, A. J. Austin, R. Cammi, C. Pomelli, J. W. Ochterski, R. L. Martin, K. Morokuma, V. G. Zakrzezski, G. A. Voth, P. Salvador, J. J. Dannenberg, S. Dapprich, A. D. Daniels, Ö. Farkas, J. B. Foresman, J. V. Ortiz, J. Cioslowski, D. J. Fox, Gaussian 09, Revision A.02; Gaussian Inc.: Wallingford, CT, **2009**.
27. E. J. Bylaska, W. A. de Jong, N. Govind, K. Kowalski, T. P. Straatsma, M. Valiev, D. Wang, E. Apra, T. L. Windus, J. Hammond, P. Nichols, S. Hirata, M. T. Hackler, Y. Zhao, P.-D. Fan, R. J. Harrison, M. Dupuis, D. M. A. Smith, J. Nieplocha, V. Tipparaju, M. Krishnan, A. Vazquez-Mayagoitia, Q. Wu, T. van Voorhis, A. A. Auer, M. Nooijen, L. D. Crosby, E. Brown, G. Cisneros, G. I. Fann, H. Fruchtl, J. Garza, K. Hirao, R. Kendall, J. A. Nichols, K. Tsemekhman, K. Wolinski, J. Anchell, D. Bernholdt, P. Borowski, T. Clark, D. Clerc, H. Dachsel, M. Deegan, K. Dyall, D. Elwood, E. Glendening, M. Gutowski, A. Hess, J. Jaffe, B. Johnson, J. Ju, R. Kobayashi, R. Kutteh, Z. Lin, R. Littlefield, X. Long, B. Meng, T. Nakajima, S. Niu, L. Pollack, M. Rosing, G. Sandrone, M. Stave, H. Taylor, G. Thomas, J. van Lenthe, A. Wong, Z. Zhang, NWChem version 5.1.1: A Computational Chemistry Package for Parallel Computers. Pacific Northwest National Laboratory: Richland, **2009**.
28. K. A. Peterson, D. Figgen, E. Goll, H. Stoll, M. Dolg, *J. Chem. Phys.* Systematically convergent basis sets with relativistic pseudopotentials. II. Small-core pseudopotentials and correlation consistent basis sets for the post-d group 16–18 elements, **2003**, 119, 11113.
29. M. K. Armbruster, W. Klopper, F. Weigend, *Phys. Chem. Chem. Phys.* Basis-set extensions for two-component spin-orbit treatments of heavy elements, **2006**, 8, 4862.
30. R. A. Kendall, T. H. Dunning Jr, R. J. Harrison, *J. Chem. Phys.* Electron affinities of the first-row atoms revisited. Systematic basis sets and wave functions, **1992**, 96, 6796.
31. P. Valtazanos, K. Ruedenberg, *Theor. Chim. Acta.* Bifurcations and transition states, **1986**, 69, 281.

32. R. E. Stanton, J. W. McIver Jr, *J. Am. Chem. Soc.* Group theoretical selection rules for the transition states of chemical reactions, **1975**, 97, 3632.
33. M. Mauksch, S. P. von Ragué, *Inorg. Chem.* Effective monkey saddle points and Berry and Lever mechanisms in the topomerization of SF_4 and related tetracoordinated AX_4 species, **2001**, 40, 1756.
34. F. Neese, ORCA version 3.0.1 – An *ab initio*, density functional and semiempirical program package. Max-Planck-Institut für bioanorganische chemie, Mülheim an der Ruhr, **2013**.
35. M. Douglas, N. M. Kroll, *Ann. Phys.* Quantum electrodynamical corrections to the fine structure of helium, **1974**, 82, 89.
36. B. A. Hess, *Phys. Rev. A.* Applicability of the no-pair equation with free-particle projection operators to atomic and molecular structure calculations, **1985**, 32, 756.
37. B. A. Hess, *Phys. Rev. A.* Relativistic electronic-structure calculations employing a two-component no-pair formalism with external-field projection operators, **1986**, 33, 3742.
38. D. A. Pantazis, F. Neese, *Theor. Chem. Acc.* All-electron scalar relativistic basis sets for the 6p elements, **2012**, 131, 1.
39. D. A. Pantazis, X.-Y. Chen, C. R. Landis, F. Neese, *J. Chem. Theory Comput.* All-electron scalar relativistic basis sets for third-row transition metal atoms, **2008**, 4, 908.
40. K. A. Peterson, B. C. Shepler, D. Figgen, H. Stoll, *J. Phys. Chem. A.* On the spectroscopic and thermochemical properties of ClO, BrO, IO, and their anions, **2006**, 110, 13877.
41. D. E. Woon, T. H. Dunning Jr, *J. Chem. Phys.* Gaussian basis sets for use in correlated molecular calculations. III. The atoms aluminum through argon, **1993**, 98, 1358.
42. F. Weigend, R. Ahlrichs, *Phys. Chem. Chem. Phys.* Balanced basis sets of split valence, triple zeta valence and quadruple zeta valence quality for H to Rn: design and assessment of accuracy, **2005**, 7, 3297.
43. R. M. Minyaev, *Chem. Phys. Lett. Pseudo*-rotation in ClF_3, **1992**, 196, 203.
44. M. Reiher, A. Wolf, Relativistic quantum chemistry: the fundamental theory of molecular science. John Wiley & Sons, **2014**.

Chapter 5

Peculiarities of At Species: The Hydration-Induced Ground-State Change of AtO^+

In this chapter we focus on the environment-induced ground-state change of AtO^+, which we tackle with relativistic DFT and two-step wave-function-based approaches. Concerning this work, a manuscript has been submitted for publication in a physical chemistry journal. In the present chapter, the data is presented differently and additional information is given.

5.1 Introduction

Chemical reactions that occur with a change in the total electronic spin, when reactants are converted into products, are not uncommon.[1] Some very famous examples are the dissociation of singlet N_2O into triplet N_2 and O fragments, the dissociation of triplet CH_3O^+ into singlet H_2 and HCO^+ fragments, the addition of singlet CO to triplet $Fe(CO)_4$ that yields singlet $Fe(CO)_5$, etc.[2] At room temperature, the kinetics of such reactions may be similar to the one of chemical reactions in which the total electronic spin is conserved. Nonetheless, from a theoretical viewpoint, the reactions that occur with a change in the total electronic spin are formally called spin-forbidden reactions. Their occurrences imply that the diabatic PESs (describing pure spin-states) are brought close to or at a crossing point where hopping between them are mediated by SOC. If the SOC is strong, the chemical reaction resembles very well to a classical reaction that proceeds *via* a TS in the adiabatic representation.

In the gas phase, chemical reactions involving the AtO^+ cation and (spin-singlet) closed-shell species are expected to be spin-forbidden. Based on the SOF molecular orbital diagram of AtO^+, shown in Fig. 5.1, one may deduce that the $At^+(6p^4)$ and $O(2p^4)$ association would lead to a triplet-spin ground-state.

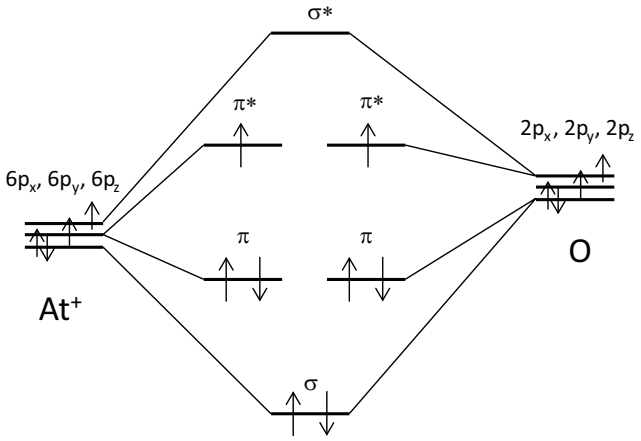

Figure 5.1 Schematic representation of the valence molecular orbital diagram of the AtO^+ cation.

Multireference 4*c*-CCSD, CASSCF and c-SOCI/NEVPT2 calculations have so far been performed in order to scrutinize and determine quantitatively the electronic structure of AtO^+.[3,4] It has been established that it has a $^3\Sigma^-$ ground SOF state, separated by ~0.6 eV from the first spin-singlet state, $^1\Delta$, and by ~1.0 eV from the second one, $^1\Sigma^+$. Hence, in analogy with O_2, AtO^+ would not readily react with closed-shell species. Nonetheless, there is indirect experimental evidence that AtO^+ readily reacts in aqueous solution with small organic and inorganic ligands like Cl^-, Br^-, SCN^- and OH^-,[5,6] suggesting that the reaction spin-forbideness is irrelevant. It is thus speculated that either (i) spin-singlet contributions to the ground SOC state of AtO^+ are sufficient to trigger the unexpected reactivities or, (ii) specific interactions with the environment are at play. Actually, SOC leads to an essentially-triplet-spin ground-state ($X\ 0^+$) which is composed mainly of the M_S=0 spin-component of the $^3\Sigma^-$ ground SOF state (~70%) and some minor contribution from $^1\Sigma^+$ (25%).[4] Also, it is worth noting that in few cases, interactions with the environment can lead to ground-state reversals. Hence, in such few cases one cannot rely anymore on the gas phase electronic structure picture to explain reactivities. Chemical species which are prone to environment-induced ground-state reversals are likely to be the ones that exhibit small energy gaps between their ground state and one or more excited states in the gas phase. Good examples of such species are the actinide-based ones, for which the close lying 5*f*, 6*d* and 7*s* orbitals of the actinide element generate plenty of low-lying and nearly-degenerate electronic states. Notably, the UO_2 and CUO species have recently been reported to undergo ground-state reversals when trapped in argon matrices.[7-11] For instance, the bare UO_2 molecule has a $^3\Phi_u$ gas phase ground-state arising from $5f^17s^1$ (U^{IV}) electronic configuration, while ~0.2 eV above it, there is a ^3H_g excited state arising from $5f^2$ (U^{IV}) configuration. In the presence of Ar atoms, the $^3\Phi_u$ state is destabilized relatively to the ^3H_g one due to repulsion between Ar and the 7*s* electron, leading this way to a ^3H_g UO_2 ground state.[7,11]

While the abovementioned reactions between AtO^+ and (spin-singlet) closed-shell species are led in aqueous solution, then one may consider that the ligand-field created by surrounding water molecules induces a ground-state change. Ayed *et al*. have investigated the role of hydration on the ground-state of AtO^+ by means of 2*c*-DFT (M06-2X) calculations.[12,13] They have found that $AtO^+(H_2O)_n$ clusters with $n \geq 4$ which adopt closed-shell ground-states become more stable than the ones adopting spin-triplet ones. They attributed the driving forces behind this change to the electrostatic interactions between AtO^+ and water molecules and to charge transfers.[13] Hence, according to these findings, the solvated AtO^+ cation would have an essentially closed-shell ground-state, and would react in a spin-allowed fashion with closed-shell ligands. However, the story has not been set aside. Gomes *et al.* have performed uc-SOCI/NEVPT2 and relativistic TD-DFT (M06-L, M06 and M06-2X) calculations in order to address the electronic structure of the essentially-triplet-spin $AtO^+(H_2O)_1$ cluster.[3] On one side, they have found that the SOCI excitation energies are only slightly lower than the ones of gas phase AtO^+. On the other side, they spotted in the TD-DFT calculations larger decreases in the excitation energies with the increasing amount of exact exchange in the used XC functional. They concluded that XC functionals that share a large percentage of exact exchange, as M06-2X, do not bode well for addressing solvation effects on AtO^+ and hence questioned the accuracy of the studies of Ayed *et. al*.[12,13] It is worth noting that we have also established in Chapter 3 that the M06-2X functional should not be used to address the properties of At species.

In this chapter we aim at resolving the observed reactivity of AtO^+ in aqueous solution with additional 2*c*-DFT and more importantly c-SOCI calculations. Our objectives are to (i) establish rigorously whether AtO^+ undergoes a hydration-induced ground-state change and (ii) identify for the first time the nature of the involved SOF and SOC many-electron states. For this purpose, we will investigate the most stable $AtO^+(H_2O)_n$ clusters (n=1−6) obtained by Ayed *et al.*,[13] and we will track down the natures of the low-lying SOF and SOC states using NEVPT2 and c-SOCI/NEVPT2 calculations, as functions of geometrical deformations.

5.2 Assessment of the computational methodology

In order to tackle our objectives, we have performed SOF and SOC calculations as detailed hereafter. The most stable $AtO^+(H_2O)_n$ clusters (n=1−6), previously optimized by Ayed *et. al* using the M06-2X density functional,[13] were re-optimized at SR- and 2*c*-DFT levels using the PBE0 functional. The scalar relativistic geometry optimizations were performed with the Gaussian 09 program package,[14] while the TURBOMOLE program package[15] was used for the 2*c* ones. For the

At center, the ECP60MDF PP was retained to mimic the role of its 60 core electrons,[16] the remaining 25 valence electrons being treated with a modified aug-cc-pVDZ-PP basis set.[5,16] For the O and H centers, the aug-cc-pVDZ basis set is used.[17,18] For convenience, the association of these basis sets will be referred hereafter as AVDZ. On the identified SR- and 2*c*-DFT most stable structures, we have performed SA-CASSCF, NEVPT2 and eventually c-SOCI/NEVPT2 single-point calculations using the MOLPRO program package.[19] In the SA-CASSCF calculations, we correlate 8 electrons in 6 MOs. This active space is explicitly shown in the MO diagram in Fig 5.1. An equal-weighted orbital averaging is performed over 6S, 9T and 2Q (quintet) spin states. Note that this active space and SA scheme have been shown to be adequate to investigate the AtO^+ free cation.[4] We have also tested that enlarging the active space with some ligand-centered orbitals does not significantly improve the description of the electronic states of interest. NEVPT2(8/6) calculations are then performed to account for the remaining part of the electron correlation. Lastly, using the SA-CASSCF(8/6) zero-order wave functions and the NEVPT2(8/6) correlated energies, c-SOCI/NEVPT2(8/6) calculations are performed in order to obtain the SOC spectra of interest. In all the wave-function-based calculations, we have retained the aforementioned ECP60MDF PP. The remaining 25 valence electrons of At are treated with the aug-cc-pVTZ-PP basis set[16] while for the O and H centers, the aug-cc-pVTZ one is used.[17,18] For the sake of simplicity, the combination of these basis sets will be referred to as AVTZ hereafter. Note that we have kept frozen the semi-core 5*s*5*p*5*d* shells of At and the 1*s* shell of O in all the NEVPT2 calculations.

Since our computational setup slightly differs from the ones used previously[3,4] to study the electronic structure of the AtO^+ cation, we start by revisiting it. We have thus performed NEVPT2(8/6)/AVTZ and c-SOCI/NEVPT2(8/6)/AVTZ single-point calculations on the 2*c*-PBE0/AVDZ equilibrium geometry of AtO^+. We have identified the $^1\Delta$ and $^1\Sigma^+$ SOF excited states lying at 0.56 and 1.00 eV, respectively, above the $^3\Sigma^-$ ground SOF state. By accounting for SOC, we found that the essentially-triplet-spin **a** 1 state and the essentially-singlet-spin **a** 2 state are located 0.42 and 0.98 eV, respectively, above the $X\ 0^+$ SOC ground state. These values are in exceptional agreement with reference ones reported in the literature (see Table 5.1). We conclude that no major basis set or a geometrical artifact is at play.

Table 5.1 Calculated SOF and SOC excitation energies (in eV) of AtO^+ at the NEVPT2(8/6)/AVTZ//2*c*-PBE0/AVDZ and c-SOCI/NEVPT2(8/6)/AVTZ//2*c*-PBE0/AVDZ levels of theory.

	Excitation	This work	NEVPT2/ANO-RCC-QZP[a]	QD-NEVPT2/AVQZ[b]	IHFSCCSD[b]
SOF	$^3\Sigma^- \rightarrow {}^1\Delta$	0.56	0.58	0.56	0.55
	$^3\Sigma^- \rightarrow {}^1\Sigma^+$	1.00	1.05	1.03	0.99
SOC	$X\ 0^+ \rightarrow$ **a** 1	0.42	0.43	0.54	0.63
	$X\ 0^+ \rightarrow$ **a** 2	0.98	0.99	0.99	1.02

[a]Taken from Ref. 4.
[b]Taken from Ref. 3.

The obtained CASSCF wave functions for the $^3\Sigma^-$, $^1\Delta$ and $^1\Sigma^+$ SOF states,

$$\begin{cases} \left|{}^3\Sigma^-\right\rangle = 88\%\left|[\ldots]\sigma^2\pi^2\pi^2\pi^{*1}\pi^{*1}\sigma^{*0}\right\rangle + \ldots \\ \left|{}^1\Delta\right\rangle^{(1)} = 42\%\left|[\ldots]\sigma^2\pi^2\pi^2\pi^{*1}\pi^{*1}\sigma^{*0}\right\rangle + 42\%\left|[\ldots]\sigma^2\pi^2\pi^2\pi^{*1}\pi^{*1}\sigma^{*0}\right\rangle + \ldots \\ \left|{}^1\Delta\right\rangle^{(2)} = 42\%\left|[\ldots]\sigma^2\pi^2\pi^2\pi^{*2}\pi^{*0}\sigma^{*0}\right\rangle + 42\%\left|[\ldots]\sigma^2\pi^2\pi^2\pi^{*0}\pi^{*2}\sigma^{*0}\right\rangle + \ldots \\ \left|{}^1\Sigma^+\right\rangle = 40\%\left|[\ldots]\sigma^2\pi^2\pi^2\pi^{*2}\pi^{*0}\sigma^{*0}\right\rangle + 40\%\left|[\ldots]\sigma^2\pi^2\pi^2\pi^{*0}\pi^{*2}\sigma^{*0}\right\rangle + \ldots \end{cases} \quad (5.1)$$

and the c-SOCI ones for the $X\ 0^+$, **a** 1 and **a** 2 states,

$$\begin{cases} \left|X\ 0^+\right\rangle = 68\%\left|{}^3\Sigma^-\right\rangle_{M_S=0} + 26\%\left|{}^1\Sigma^+\right\rangle + \ldots \\ \left|\mathrm{a}\ 1\right\rangle^{(1,2)} = 43\%\left|{}^3\Sigma^-\right\rangle_{M_S=+1} + 43\%\left|{}^3\Sigma^-\right\rangle_{M_S=-1} + \ldots \\ \left|\mathrm{a}\ 2\right\rangle^{(1)} = 83\%\left|{}^1\Delta\right\rangle^{(1)} + \ldots \\ \left|\mathrm{a}\ 2\right\rangle^{(2)} = 83\%\left|{}^1\Delta\right\rangle^{(2)} + \ldots \end{cases} \quad (5.2)$$

are as well in very close agreement with reference ones reported in the literature.[3,4] Considering that AtO^+ undergoes a solvation-induced ground-state change, from Eqs. 5.1 and 5.2 one can hypothesize that a closed-shell configuration correlating most likely with $\left|{}^1\Delta\right\rangle^{(2)}$ is strongly stabilized, becoming (or not) the ground SOF state, and most contributing to the ground SOC state. In the following sections, we will assess the validity of this hypothesis by establishing which SOF and SOC many-electron states are involved in a hypothetical ground-state change that we will question.

5.3 The $AtO^+(H_2O)_1$ system

We start by studying the $AtO^+(H_2O)_1$ cluster in order to obtain a first picture of the influence of a water molecule on the electronic structure of AtO^+, and thereafter we will investigate

the $AtO^+(H_2O)_n$ systems (n=2−6). Equilibrium geometries for the $AtO^+(H_2O)_1$ system calculated with and without SOC are shown in Fig. 5.2. In agreement with the SR-M06-2X/AVDZ results of Ayed *et al.*,[12,13] we found in SR-PBE0/AVDZ calculations that the lowest-energy structure for the unrestricted-triplet-spin cluster has the C_{2v} symmetry while the restricted-singlet-spin cluster has the C_s one. In both cases, the water molecule is in close contact with the At center of the AtO^+ unit. When these structures were relaxed in the presence of SOC (*i.e.* in 2*c*-PBE0/AVDZ calculations), the C_{2v} symmetry is maintained in an essentially-triplet-spin cluster while we failed to identify a C_s-like structure for an essentially-singlet-spin cluster. SOC appears to weaken the effect of solvation since, on one hand, it lengthens the distance between the water molecule and the AtO^+ unit in the essentially-triplet-spin cluster, and, on the other hand, it lifts the restricted-singlet-spin C_s minimum from the ground-state PES of the $AtO^+(H_2O)_1$ system.

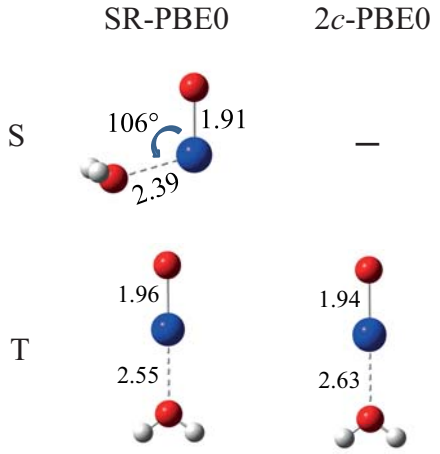

Figure 5.2 Structures of the restricted-singlet-spin and unrestricted-triplet-spin $AtO^+(H_2O)_1$ clusters obtained at the SR-PBE0/AVDZ level of theory, and structure of the essentially-triplet-spin $AtO^+(H_2O)_1$ cluster obtained at the 2*c*-PBE0/AVDZ level of theory. Interatomic distances are given in Angstroms and the $\measuredangle$OAtO in degrees. Color code: blue stands for At, red for O, and white for H.

5.3.1 The SOF electronic structure of the $AtO^+(H_2O)_1$ system

In this subsection, we track the natures of the lowest-lying SOF states in the $AtO^+(H_2O)_1$ system as function of geometrical parameters by means of CASSCF(8/6) and NEVPT2(8/6) calculations. At first, we check whether the identified SR-PBE0/AVDZ equilibrium structures correspond to minima of the NEVPT2(8/6)/AVTZ PESs. For this purpose we have performed a scan between the C_{2v} SR-PBE0/AVDZ equilibrium structure and a C_s structure in which we monitor the evolution of the low-lying SOF states. Two main coordinates are at play, in particular the $r(H_2O–AtO^+)$ distance and the $\measuredangle$OAtO angle (*i.e.* the angle between the water molecule and the AtO^+ unit). All the other parameters remain fixed at their values in the C_{2v} equilibrium structure. As can be seen in Fig. 5.3, we have obtained two minima on the ground-state PES, a C_{2v} restricted-

triplet-spin minimum, in which the water molecule interacts with the At center at ~2.54 Å, and a C_s restricted-singlet-spin minimum, in which the water molecule interacts with the At center at ~2.40 Å (in order to better evidence the C_s minimum, contour plots of the two lowest-lying singlet-spin PESs are displayed in Fig. A3.1, see Appendix 3). Since these findings are in good agreement with the SR-PBE0/AVDZ results, we further proceed by analyzing the nature of the SOF states.

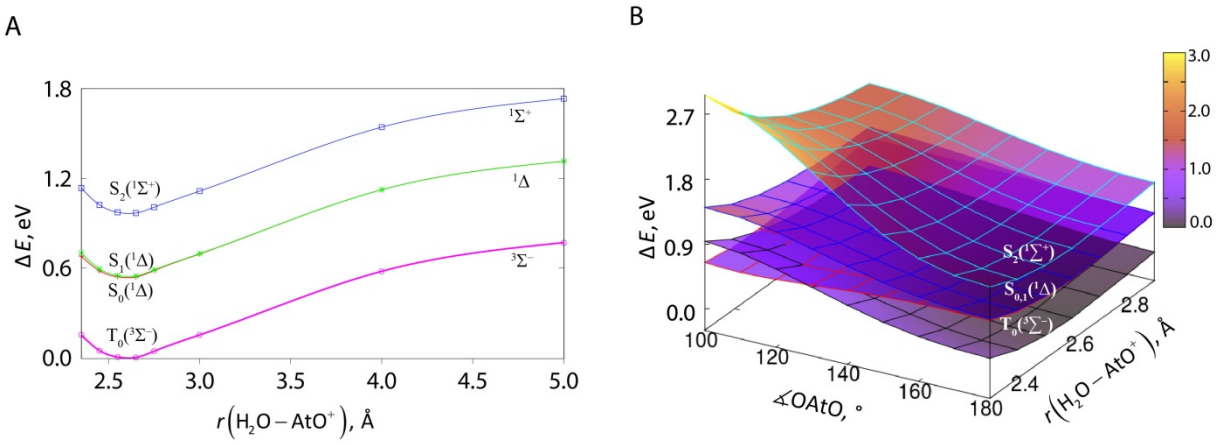

Figure 5.3 Evolution of the relative energies of the lowest-lying electronic states of the $AtO^+(H_2O)_1$ system calculated at the NEVPT2(8/6)/AVTZ level of theory as a function of the H_2O-AtO^+ distance and ∢OAtO ; A: the angle is fixed to 180° while the distance is varied; B: both the angle and the distance are varied.

Fig. 5.3A explicitly shows the evolution of the low-lying SOF states while the water molecule approaches the AtO^+ unit in a C_{2v} fashion. The nature of the states occurring at the equilibrium SR-PBE0/AVDZ unrestricted-triplet-spin cluster is pretty much clear. The ground state correlates with the $^3\Sigma^-$ one of AtO^+ while the first three excited singlet-spin states correlate with the twofold degenerate $^1\Delta$ and with the $^1\Sigma^+$ excited states of AtO^+. We denote them as $T_0(^3\Sigma^-)$, $S_0(^1\Delta)$, $S_1(^1\Delta)$ and $S_2(^1\Sigma^+)$. Fig. 5.3B further shows the evolution of these states toward the C_s structure. Firstly, it can be seen that the $S_2(^1\Sigma^+)$ state is largely destabilized. Secondly, due to the degeneracy lifting of the π^* frontier orbitals, the energy gap between the $S_0(^1\Delta)$ and $S_1(^1\Delta)$ states largely increases along the minimum energy pathway between the C_{2v} and C_s minima. The former state, $S_0(^1\Delta)$, is actually crossing the $T_0(^3\Sigma^-)$ state at ∢OAtO lower than 120° and becomes the ground state.

Table 5.2 Calculated SOF excitation energies (in eV) at the NEVPT2(8/6)/AVTZ//SR-PBE0/AVDZ level of theory. The ΔE non-adiabatic energy difference (also in eV) between the singlet-spin and triplet-spin clusters of the $AtO^+(H_2O)_1$ system is also given (a positive value means that the triplet-spin cluster is more stable).

	AtO^+	$AtO^+(H_2O)_1$, C_{2v}	$AtO^+(H_2O)_1$, C_s
$T_0(^3\Sigma^-)$	0.00	0.00	0.17
$S_0(^1\Delta)$	0.56	0.54	0.00
$S_1(^1\Delta)$	0.56	0.55	0.70
$S_2(^1\Sigma^+)$	1.00	0.97	2.08
ΔE		0.55	

In terms of energetics, the water molecule is only slightly perturbing the electronic structure of AtO^+ at the unrestricted-triplet-spin SR-PBE0/AVDZ geometry (see Table 5.2). For instance, the degeneracy between the $S_0(^1\Delta)$ and $S_1(^1\Delta)$ states is only slightly lifted, by 0.01 eV. In change, there is a reorganization of the energy levels at the restricted-singlet-spin SR-PBE0/AVDZ geometry: the $T_0(^3\Sigma^-)$ state becomes the first excited state, 0.17 eV higher in energy than the newly adopted $S_0(^1\Delta)$ ground state (see Table 5.2). At this C_s geometry, the obtained CASSCF wave functions for the different SOF states are:

$$\begin{cases} \left|S_0\left(^1\Delta\right)\right\rangle = 81\%\left|[\ldots]\sigma^2\pi^2\pi^2\pi^{*2}\pi^{*0}\sigma^{*0}\right\rangle + \ldots \\ \left|T_0\left(^3\Sigma^-\right)\right\rangle = 87\%\left|[\ldots]\sigma^2\pi^2\pi^2\pi^{*1}\pi^{*1}\sigma^{*0}\right\rangle + \ldots \\ \left|S_1\left(^1\Delta\right)\right\rangle = 41\%\left|[\ldots]\sigma^2\pi^2\pi^2\pi^{*1}\pi^{*1}\sigma^{*0}\right\rangle + 41\%\left|[\ldots]\sigma^2\pi^2\pi^2\pi^{*1}\pi^{*1}\sigma^{*0}\right\rangle + \ldots \\ \left|S_2\left(^1\Sigma^+\right)\right\rangle = 82\%\left|[\ldots]\sigma^2\pi^2\pi^2\pi^{*0}\pi^{*2}\sigma^{*0}\right\rangle + \ldots \end{cases} \quad (5.3)$$

Eq. 5.3 states notably that $S_0(^1\Delta)$ correlates with to the closed-shell component of the twofold degenerate $^1\Delta$ state of AtO^+ (*i.e.* to $^1\Delta^{(2)}$ in Eq. 5.1) whereas $S_1(^1\Delta)$ corresponds to the open-shell component (*i.e.* to $^1\Delta^{(1)}$ in Eq. 5.1). Hence, the ground state of the singlet-spin $AtO^+(H_2O)_1$ cluster is closed-shell and originates from the closed-shell $^1\Delta$ component of AtO^+.

So far, we have determined the natures of different low-lying SOF states at the SR-PBE0/AVDZ equilibrium structures of the $AtO^+(H_2O)_1$ system. Clearly, going from the unrestricted-triplet-spin cluster toward the restricted-singlet-spin one, the ground-state changes from $T_0(^3\Sigma^-)$ to $S_0(^1\Delta)$, *i.e.* between the $^3\Sigma^-$ state and the closed-shell component of $^1\Delta$ state of the free AtO^+ cation. The implication of the $S_2(^1\Sigma^+)$ state (*i.e.* of the $^1\Sigma^+$ state of AtO^+) in this process is definitely ruled out. However, at the NEVPT2(8/6)/AVTZ//SR-PBE0/AVDZ level of theory, the

triplet-spin cluster is 0.55 eV lower in energy than the singlet-spin one (see ΔE in Table 5.2). Hence, a change in the ground state of AtO^+ does not happen in the scalar relativistic limit if one considers only the one-water system.

5.3.2 The SOC electronic structure of the $AtO^+(H_2O)_1$ system

We aim now at (i) establishing the nature of the lowest-lying SOC energy levels that occur at the essentially-triplet-spin equilibrium geometry of the $AtO^+(H_2O)_1$ system (identified at the 2*c*-PBE0/AVDZ level), and (ii) determining the evolution of the SOC states identified at point (i) toward the PES region where the scalar relativistic restricted-singlet-spin equilibrium geometry was found. As the water molecule is approaching the AtO^+ unit in a C_{2v} fashion, we have monitored the evolution of the five lowest-lying SOC states of AtO^+, *i.e.* of the essentially-triplet-spin $X\ 0^+$ ground state, of the effectively twofold-degenerate and essentially-triplet-spin **a** 1 excited state, and of the effectively twofold-degenerate and essentially-singlet-spin **a** 2 excited state. We place this scan in Fig. 5.4. It can be seen that the ordering of the $X\ 0^+$, **a** 1 and **a** 2 states is maintained all along the scan. This is expected since the relative energies between the SOF components that mostly contribute to the wave functions of the SOC states in question, are basically unchanged all along the scan (*c.f.* Fig. 5.3A). Naturally, the compositions of these wave functions are also mostly unchanged. For instance, at the essentially-triplet-spin 2*c*-PBE0/AVDZ equilibrium structure, the ground SOC state is mainly composed of the M_S=0 spin-component of the $T_0(^3\Sigma^-)$ SOF state (68%), the first two essentially-triplet-spin excited SOC states are mainly composed of the |*Ms*|=1 spin-components of the $T_0(^3\Sigma^-)$ SOF state (86%), and the first two essentially-singlet-spin excited SOC states are mainly composed of the $S_0(^1\Delta)$ and $S_1(^1\Delta)$ SOF states (~82%). Hence, we label the five lowest-lying SOC states that occur at the essentially-triplet-spin 2*c*-PBE0/AVDZ equilibrium structure as $\Psi\left(X\ 0^+\right)$, $\Psi\left(\mathbf{a}\ 1\right)$ and $\Psi\left(\mathbf{a}\ 2\right)$, as shown in Fig. 5.4. We finally note that the $\Psi\left(X\ 0^+\right)\rightarrow\Psi\left(\mathbf{a}\ 1\right)$ and $\Psi\left(X\ 0^+\right)\rightarrow\Psi\left(\mathbf{a}\ 2\right)$ excitation energies (~0.40 and ~0.95 eV respectively) are very similar with their analogues in the free AtO^+ cation (*c.f.* Table 5.1), which supports again the argument that the water molecule does not perturb much the electronic structure of AtO^+ when one considers the C_{2v} geometry.

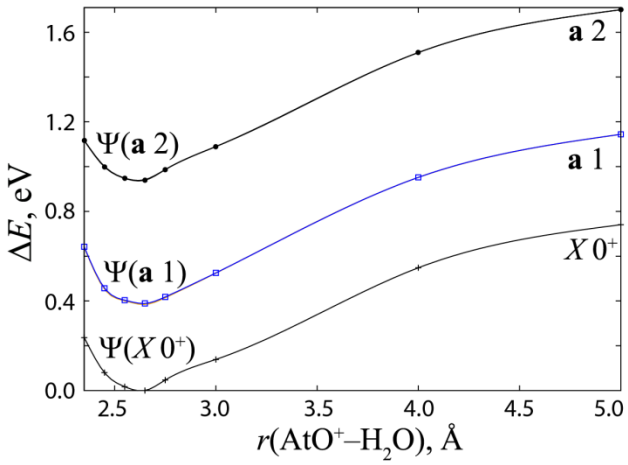

Figure 5.4 Energy profiles, calculated at the c-SOCI/NEVPT2(8/6)/AVTZ level of theory, of the lowest-lying SOC states while the water molecule approaches the AtO^+ unit in a C_{2v} symmetry.

We now continue by approaching point (ii) mentioned above. No C_s-like equilibrium geometry for an essentially-singlet-spin $AtO^+(H_2O)_1$ cluster was localized in 2*c*-PBE0/AVDZ calculations. It is of interest to clarify this issue, notably by means of c-SOCI/NEVPT2(8/6)/AVTZ calculations. We have studied the dependence of the energy of the identified $\Psi\left(X\ 0^+\right)$, $\Psi\left(\mathbf{a}\ 1\right)$ and $\Psi\left(\mathbf{a}\ 2\right)$ SOC states, and of the SOF composition of their wave functions, as a function of the $r(H_2O\text{-}AtO^+)$ and $\measuredangle OAtO$ parameters (see Fig. 5.5A). We noted that all these SOC states have minimum energy points at C_{2v} geometries and that they all rise in energy toward the PES region where the scalar relativistic restricted-singlet-spin C_s structure was localized. At first, we focus on the evolution of the SOF composition of the SOC ground state wave function, along the considered scan (see Fig. 5.5B). At the essentially-triplet-spin 2*c*-PBE0/AVDZ geometry, the SOC ground state is labeled $\Psi\left(X\ 0^+\right)$ and toward the C_s SR-PBE0/AVDZ structure, its composition in the M_S=0 $T_0(^3\Sigma^-)$ and in the $S_2(^1\Sigma^+)$ SOF spin-components is gradually diminished while the composition in the $S_0(^1\Delta)$ SOF component is increased. Indeed, the $T_0(^3\Sigma^-)$ and $S_2(^1\Sigma^+)$ SOF states are destabilized along the considered scan while the $S_0(^1\Delta)$ one is, in change, stabilized. At the SR-PBE0/AVDZ restricted-singlet-spin geometry (C_s symmetry), we find that the ground-state SOC wave function has a mixed singlet-triplet character, 45% of M_S=0 $T_0(^3\Sigma^-)$, 5% of $S_2(^1\Sigma^+)$ and 41% of $S_0(^1\Delta)$, and cannot be considered anymore as an essentially-triplet-spin ground-state. Actually, we no longer label this SOC ground state as $\Psi\left(X\ 0^+\right)$ at this geometry but simply as Ψ_0 (see Fig. 5.5A).

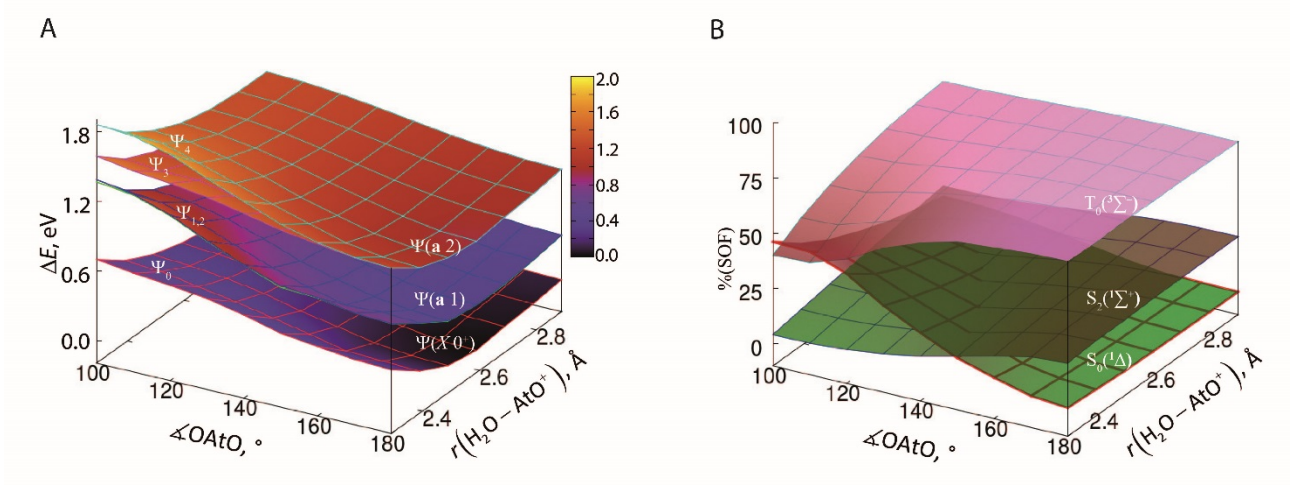

Figure 5.5 Evolution of the lowest-lying energy levels for the $AtO^+(H_2O)_1$ system calculated at the c-SOCI/NEVPT2(8/6)/AVTZ level of theory as a function of the H_2O-AtO^+ distance and of the ∢OAtO angle; A: relative energies (in eV); B: composition of Ψ_0 in terms of the M_S components of $T_0(^3\Sigma^-)$, $S_0(^1\Delta)$ and $S_2(^1\Sigma^+)$.

We now focus on the evolution of the effectively twofold-degenerate $\Psi(\mathbf{a}\,1)$ SOC state which is mainly composed of the $|M_S|$=1 spin-components of the $T_0(^3\Sigma^-)$ SOF state at the 2*c*-PBE0/AVDZ essentially-triplet-spin geometry. We noticed that its SOF composition is nearly constant all along the scan shown in Fig 5.5A. At the equilibrium SR-PBE0/AVDZ restricted-singlet-spin geometry, the degeneracy of the two $\Psi(\mathbf{a}\,1)$ components is only slightly lifted, giving rise to two SOC states that we label as Ψ_1 and Ψ_2 (see Fig. 5.5A). In terms of energy, Ψ_1 and Ψ_2 are placed at 0.67 and 0.68 eV, respectively, above the identified Ψ_0 SOC ground state. Finally, we look at the effectively twofold-degenerate $\Psi(\mathbf{a}\,2)$ SOC state. At the 2*c*-PBE0/AVDZ essentially-triplet-spin geometry, one $\Psi(\mathbf{a}\,2)$ component has a 82% contribution from the $S_0(^1\Delta)$ SOF state whereas the other one has a 83% contribution from the $S_1(^1\Delta)$ SOF state. The energy gap between the two $\Psi(\mathbf{a}\,2)$ components slightly increases toward the PES region where the scalar relativistic C_s structure has been identified (see Fig. 5.5A), giving rise to the two SOC states that we label as Ψ_3 and Ψ_4. Inspecting Ψ_3, we noticed that its $S_0(^1\Delta)$ SOF composition is diminished to only 46% at the scalar relativistic C_s structure and that the SOF contribution from the M_S=0 spin-component of $T_0(^3\Sigma^-)$, which is actually 0% at the 2*c*-PBE0/AVDZ essentially-triplet-spin geometry, is increased up to 31%. Regarding the Ψ_4 state, its composition in terms of SOF states remains almost constant all along the scan. Also, we noted that a C_s geometry does not correspond to a minimum for neither Ψ_3 nor Ψ_4 (see Fig. 5.5A), fact which is in line with our failure in localizing an essentially-singlet-spin C_s equilibrium structure at the 2*c*-PBE0/AVDZ level. In the considered

$AtO^+(H_2O)_1$ system, a fierce competition exist between SOC and solvation, the former one dominating and destabilizing the scalar relativistic restricted-singlet-spin equilibrium structure.

5.4 The $AtO^+(H_2O)_n$ systems (n=2−6)

The most stable equilibrium geometries for the $AtO^+(H_2O)_n$ systems (n=2−6) are shown in Fig. 5.6. The hydration spheres at the restricted-singlet-spin and unrestricted-triplet-spin equilibrium structures, calculated at the SR-PBE0/AVDZ level of theory, significantly differ. At the former structures, the water molecules form a network of hydrogen bonds and appear to interact with both the At and O centers of the AtO^+ unit. At the unrestricted-triplet-spin geometries, the water molecules form instead a network between them, rather far from the AtO^+ unit. One can speculate that the water molecules perturb to a lesser extent the electronic structure of AtO^+ in those unrestricted-triplet-spin clusters. Comparing properly the SR-PBE0/AVDZ and the 2*c*-PBE0/AVDZ equilibrium geometries (shown in Fig. 5.6), one can obtain the contribution of SOC to the geometry relaxations. While all distances with the close-lying water molecules are generally lengthened by SOC, mostly in the essentially-singlet-spin clusters, some of them are to a large extent shortened in the essentially-triplet-spin clusters. All these findings are in agreement with the M06-2X ones of Ayed *et al*.[12,13]

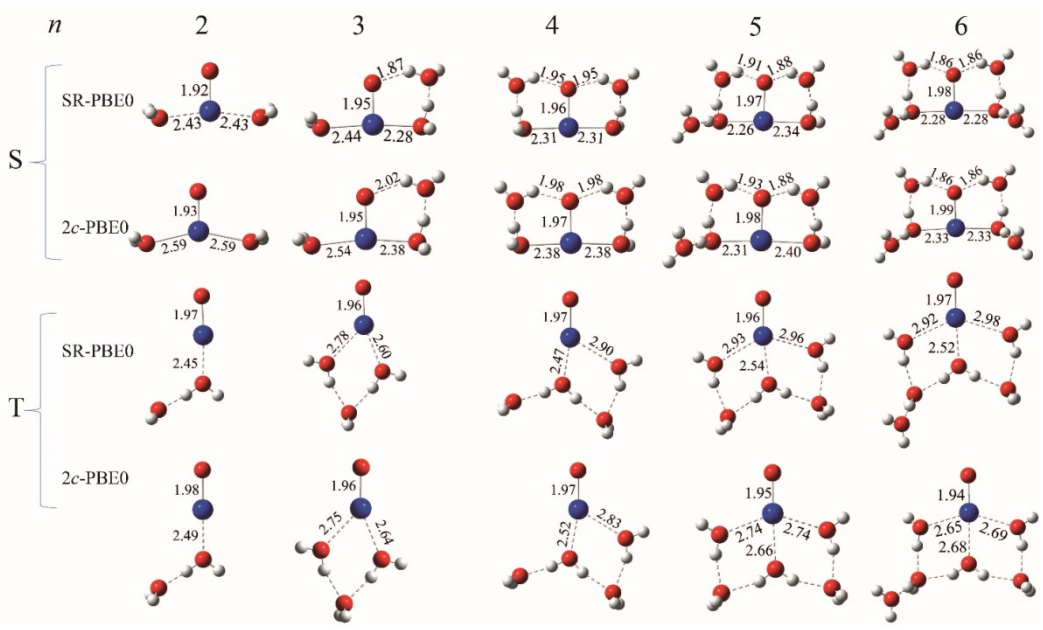

Figure 5.6 Lowest-energy structures for the restricted-singlet-spin and unrestricted-triplet-spin $AtO^+(H_2O)_n$ clusters (n=2−6) calculated at the SR-PBE0/AVDZ level of theory, and lowest-energy structures for the essentially-singlet-spin and essentially-triplet-spin clusters calculated at the 2*c*-PBE0/AVDZ level of theory. The singlet species are denoted with S while the triplet ones, with T. Color code: blue stands for At, red stands for O, and white stands for H.

5.4.1 The SOF electronic structures of the $AtO^+(H_2O)_n$ systems (n=2−6)

In this subsection, we focus on the nature of the lowest-lying SOF states at the SR-PBE0/AVDZ equilibrium structures. We are notably interested in those SOF states that correlate with the $^3\Sigma^-$, $^1\Delta$ and $^1\Sigma^+$ ones of the free AtO^+ cation. For each structure, we present in Table 5.3 the vertical excitation energies obtained at the NEVPT2(8/6)/AVTZ level of theory. At first, we discuss the energetics and natures of the CASSCF wave functions of the different SOF states obtained at the unrestricted-triplet-spin equilibrium geometries. Note that previously we have guessed that the water molecules do not perturb much the electronic structure of the AtO^+ unit. Here, we found that the ground-state CASSCF wave functions are essentially single-configurational with ~80% weights on the $[\ldots]\sigma^2\pi^2\pi^2\pi^{*1}\pi^{*1}\sigma^{*0}$ configuration, which is similar to the CASSCF wave functions of the $T_0\left(^3\Sigma^-\right)$ or $^3\Sigma^-$ SOF ground states of the unrestricted-triplet-spin $AtO^+(H_2O)_1$ cluster or of the isolated AtO^+ cation, respectively. Thus, these newly identified triplet-multiplicity electronic ground-states can safely be labeled as $T_0\left(^3\Sigma^-\right)$.

Table 5.3 Calculated SOF excitation energies (in eV) at the SR-PBE0/AVDZ geometries of the $AtO^+\left(H_2O\right)_n$ clusters (n=2−6). The ΔE non-adiabatic energy difference between the singlet-spin and triplet-spin clusters of each $AtO^+\left(H_2O\right)_n$ system is also given (a positive value means that the triplet-spin cluster is more stable).

		$AtO^+\left(H_2O\right)_2$	$AtO^+\left(H_2O\right)_3$	$AtO^+\left(H_2O\right)_4$	$AtO^+\left(H_2O\right)_5$	$AtO^+\left(H_2O\right)_6$
Unrestricted-triplet-spin clusters, SR-PBE0/AVDZ						
NEVPT2(8/6)/AVTZ	$T_0\left(^3\Sigma^-\right)$	0.00	0.00	0.00	0.00	0.00
	$S_0\left(^1\Delta\right)$	0.53	0.45	0.48	0.30	0.29
	$S_1\left(^1\Delta\right)$	0.54	0.54	0.54	0.54	0.54
	$S_2\left(^1\Sigma^+\right)$	0.96	1.09	1.02	1.24	1.25
Restricted-singlet-spin clusters, SR-PBE0/AVDZ						
NEVPT2(8/6)/AVTZ	$T_0\left(^3\Sigma^-\right)$	1.09	1.76	2.26	2.45	2.71
	$S_0\left(^1\Delta\right)$	0.00	0.00	0.00	0.00	0.00
	$S_1\left(^1\Delta\right)$	1.58	2.25	2.80	3.00	3.40
	$S_2\left(^1\Sigma^+\right)$	4.01	>4.97[a]	>5.42[a]	>5.60[a]	>5.76[a]
Energy differences						
NEVPT2(8/6)/AVTZ	ΔE	0.23 (0.26)[b]	−0.02 (−0.03)[b]	−0.26	−0.52	−0.64

[a]When $S_2\left(^1\Sigma^+\right)$ is out of the state-averaging space, we only report a lower limit for the corresponding excitation energy.

[b]The values in parenthesis are calculated at the NEVPT2(8/6)/AVTZ//SR-PBE0/AVTZ level of theory. These values show that there is no bias introduced by the use of equilibrium geometries calculated with the smaller AVDZ basis set.

We would like to point out that most of the unrestricted-triplet-spin geometries pertain to the C_1 symmetry point group. Hence the σ and π notation for the orbitals does not hold anymore from a rigorous symmetry viewpoint. Nonetheless we designate as σ or π those MOs that correlate

(according to visual inspection) with the σ and π orbitals of AtO^+. To exemplify, we show in Fig. 5.7 the natural orbitals involved in the active space of the SA-CASSCF calculation on the most stable unrestricted-triplet-spin $AtO^+(H_2O)_4$ cluster.

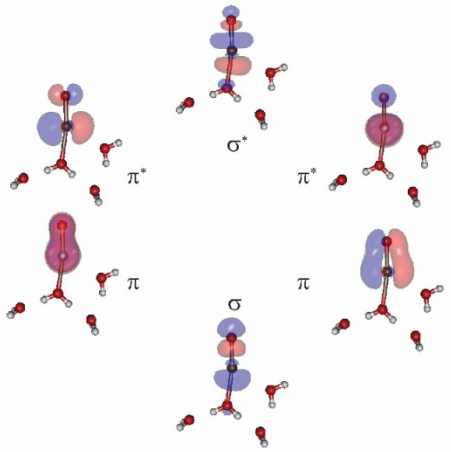

Figure 5.7 Natural orbitals of the SA-CASSCF calculation associated with the unrestricted-triplet-spin $AtO^+(H_2O)_4$ geometry.

Above the $T_0\left(^3\Sigma^-\right)$ ground state, we localized for each unrestricted-triplet-spin cluster three singlet-spin states. From Table 5.3, one can see that the first two of them are nearly degenerate at the *n*=2 geometry and that the energy gap between them increases with increasing *n* (at the *n*=6 geometry, this gap reaches 0.25 eV). Inspecting the CASSCF wave functions, we found that the lowest energy singlet-spin roots have ~82% weights on the closed shell configurations and overall exhibit more and more single-configurational character with increasing *n*, as shown in Eq. 5.4.

$$\begin{cases} n=2,\ 55\%\left|[\ldots]\sigma^2\pi^2\pi^2\pi^{*2}\pi^{*0}\sigma^{*0}\right\rangle + 28\%\left|[\ldots]\sigma^2\pi^2\pi^2\pi^{*0}\pi^{*2}\sigma^{*0}\right\rangle + \ldots \\ n=3,\ 74\%\left|[\ldots]\sigma^2\pi^2\pi^2\pi^{*2}\pi^{*0}\sigma^{*0}\right\rangle + \ 9\%\left|[\ldots]\sigma^2\pi^2\pi^2\pi^{*0}\pi^{*2}\sigma^{*0}\right\rangle + \ldots \\ n=4,\ 71\%\left|[\ldots]\sigma^2\pi^2\pi^2\pi^{*2}\pi^{*0}\sigma^{*0}\right\rangle + 12\%\left|[\ldots]\sigma^2\pi^2\pi^2\pi^{*0}\pi^{*2}\sigma^{*0}\right\rangle + \ldots \\ n=5,\ 78\%\left|[\ldots]\sigma^2\pi^2\pi^2\pi^{*2}\pi^{*0}\sigma^{*0}\right\rangle + \ 3\%\left|[\ldots]\sigma^2\pi^2\pi^2\pi^{*0}\pi^{*2}\sigma^{*0}\right\rangle + \ldots \\ n=6,\ 78\%\left|[\ldots]\sigma^2\pi^2\pi^2\pi^{*2}\pi^{*0}\sigma^{*0}\right\rangle + \ 3\%\left|[\ldots]\sigma^2\pi^2\pi^2\pi^{*0}\pi^{*2}\sigma^{*0}\right\rangle + \ldots \end{cases} \quad (5.4)$$

Concerning the CASSCF wave functions of the second singlet-spin roots, they have in all *n* cases ~80% weights on the $[\ldots]\sigma^2\pi^2\pi^2\pi^{*1}\pi^{*1}\sigma^{*0}$ configuration. It is now undoubtedly that these sets of states correlate with $^1\Delta$ of AtO^+ (*i.e.* the lowest lying one correlate with the closed-shell component of $^1\Delta$ while the second one with the open-shell component of $^1\Delta$). Thus, we labeled the first two singlet-spin states as $S_0(^1\Delta)$ and $S_1(^1\Delta)$. At this point, it is not known if the third singlet roots

actually correlate with $^1\Sigma^+$. This possibility is verified by a close inspection of the associated CASSCF wave functions which are built essentially (~80%) from the closed-shell configurations:

$$\begin{cases} n=2,\ 26\%\left|[\ldots]\sigma^2\pi^2\pi^2\pi^{*2}\pi^{*0}\sigma^{*0}\right\rangle + 53\%\left|[\ldots]\sigma^2\pi^2\pi^2\pi^{*0}\pi^{*2}\sigma^{*0}\right\rangle + \ldots \\ n=3,\ \ 8\%\left|[\ldots]\sigma^2\pi^2\pi^2\pi^{*2}\pi^{*0}\sigma^{*0}\right\rangle + 73\%\left|[\ldots]\sigma^2\pi^2\pi^2\pi^{*0}\pi^{*2}\sigma^{*0}\right\rangle + \ldots \\ n=4,\ 11\%\left|[\ldots]\sigma^2\pi^2\pi^2\pi^{*2}\pi^{*0}\sigma^{*0}\right\rangle + 70\%\left|[\ldots]\sigma^2\pi^2\pi^2\pi^{*0}\pi^{*2}\sigma^{*0}\right\rangle + \ldots \\ n=5,\ \ 3\%\left|[\ldots]\sigma^2\pi^2\pi^2\pi^{*2}\pi^{*0}\sigma^{*0}\right\rangle + 79\%\left|[\ldots]\sigma^2\pi^2\pi^2\pi^{*0}\pi^{*2}\sigma^{*0}\right\rangle + \ldots \\ n=6,\ \ 3\%\left|[\ldots]\sigma^2\pi^2\pi^2\pi^{*2}\pi^{*0}\sigma^{*0}\right\rangle + 79\%\left|[\ldots]\sigma^2\pi^2\pi^2\pi^{*0}\pi^{*2}\sigma^{*0}\right\rangle + \ldots \end{cases} \quad (5.5)$$

As the CASSCF wave function of the $S_0(^1\Delta)$ state, the one of $S_2(^1\Sigma^+)$ also becomes essentially single-configurational with increasing n (see Eq. 5.5). But $S_2(^1\Sigma^+)$ is at the same time slightly destabilized with respect to the $T_0\left(^3\Sigma^-\right)$ ground state (*c.f.* Table 5.3).

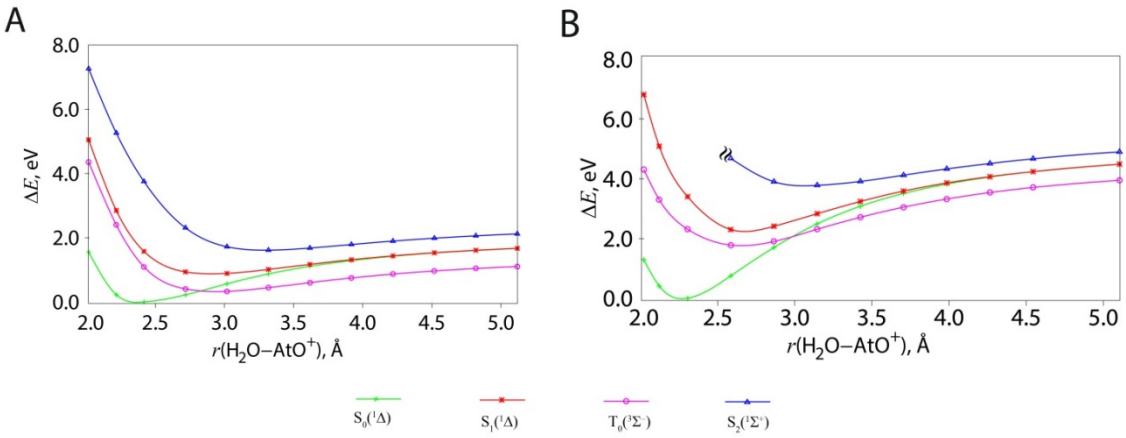

Figure 5.8 Energy of low-lying SOF electronic states as a function of the main H_2O-AtO^+ distances; A: in the restricted-singlet-spin $AtO^+(H_2O)_2$ cluster (C_{2v} symmetry); B: in the restricted-singlet-spin $AtO^+(H_2O)_6$ cluster (C_s symmetry). The SR-PBE0/AVDZ geometries are taken as references.

We now continue by discussing the energetics and the nature of the lowest-lying SOF states obtained at the restricted-singlet-spin geometries. Monitoring the evolution of $T_0\left(^3\Sigma^-\right)$, $S_0\left(^1\Delta\right)$, $S_1\left(^1\Delta\right)$ and $S_2\left(^1\Sigma^+\right)$ along a scan, in each case, becomes a tedious work since many geometrical parameters are now at play. A simpler approach would be to back-trace the lowest-lying electronic states to the isolated AtO^+ cation. We picked-up the two extremes, *i.e.* the n=2 and the n=6 restricted-singlet-spin structures, and we monitored the evolution of the states correlating with the $^3\Sigma^-$, $^1\Delta$ and $^1\Sigma^+$ ones of isolated AtO^+, while the 2(6) water molecules are approaching/moving away in C_{2v} (C_s) symmetry. We stress that in the n=6 case, two water molecules (i) are in direct contact with the At center at the $r(H_2O–AtO^+)$ equilibrium distance, and

(ii) bear each one a network of water molecules (see Fig. 5.6). While $r(H_2O{-}AtO^+)$ was increased, the two blocks of three water molecules were moving/approaching simultaneously and symmetrically with respect to the AtO^+ unit. The obtained energy profiles are displayed in Fig. 5.8. In both cases (*i.e.* restricted-singlet-spin structures of the *n*=2 and *n*=6 cases), the targeted states become attractive and evolve toward their minima placed at different equilibrium distances. Notably, the $S_0(^1\Delta)$ state (*i.e.* the state that correlates with the closed-shell component of the $^1\Delta$ state of AtO^+) crosses the $T_0(^3\Sigma^-)$ one and becomes the lowest-lying at distances somewhat lower than 2.9 Å. It is interesting to note that the resulting equilibrium distances agree well with the ones obtained in SR-PBE0/AVDZ calculations (~2.4 Å for the *n*=2 case and ~2.3 Å for the *n*=6 case, see Fig. 5.6). It is also worth noting that the $S_0(^1\Delta)$ state is much more stabilized relatively to the $T_0(^3\Sigma^-)$ one with increasing *n*; this relative stabilization amounts to ~0.5 eV for the *n*=2 case and to ~2.0 eV for the *n*=6 case (non-adiabatically). This behavior originates from the field created by the water molecules which leads to an energy gap between the originally degenerate π^* frontier orbitals of the AtO^+ unit. This gap largely increases with increasing *n*, resulting in a significant energy cost to promote an electron to the higher-lying π^* orbital than to pair two electrons in the lowest energy one (and form a closed-shell configuration characterizing the $S_0(^1\Delta)$ state). Regarding the wave function of $S_0(^1\Delta)$, it is essentially single-configurational. The weight on the leading closed-shell configuration overall slightly increases form the *n*=2 case to the *n*=6 one:

$$\begin{cases} n=2,\,80\%\left|[\ldots]\sigma^2\pi^2\pi^2\pi^{*2}\pi^{*0}\sigma^{*0}\right\rangle+\ldots \\ n=3,\,82\%\left|[\ldots]\sigma^2\pi^2\pi^2\pi^{*2}\pi^{*0}\sigma^{*0}\right\rangle+\ldots \\ n=4,\,83\%\left|[\ldots]\sigma^2\pi^2\pi^2\pi^{*2}\pi^{*0}\sigma^{*0}\right\rangle+\ldots \\ n=5,\,83\%\left|[\ldots]\sigma^2\pi^2\pi^2\pi^{*2}\pi^{*0}\sigma^{*0}\right\rangle+\ldots \\ n=6,\,84\%\left|[\ldots]\sigma^2\pi^2\pi^2\pi^{*2}\pi^{*0}\sigma^{*0}\right\rangle+\ldots \end{cases} \quad (5.6)$$

At the restricted-singlet-spin geometries of the *n*=2-6 clusters, the $T_0(^3\Sigma^-)$ states (*i.e.* the states that correlate with the $^3\Sigma^-$ one of the isolated AtO^+) are always the first excited states. Their CASSCF wave functions are mainly single-configurational with weights larger than 80% on the open shell $[\ldots]\sigma^2\pi^2\pi^2\pi^{*1}\pi^{*1}\sigma^{*0}$ configuration. From both Table 5.3 and Fig. 5.8, the $S_1(^1\Delta)$ and $S_2(^1\Sigma^+)$ states (*i.e.* the states that correlate with the open-shell component of $^1\Delta$ and with the $^1\Sigma^+$ state of the isolated AtO^+) appear largely destabilized with increasing *n*; for the *n*=6 case, $S_1(^1\Delta)$ is 3.40 eV vertically above the $S_0(^1\Delta)$ ground state (~2.5 eV non-adiabatically, see Fig. 5.8B), while $S_2(^1\Sigma^+)$ is

much higher in energy, more than 5.76 eV above $S_0(^1\Delta)$ (~4.0 eV non-adiabatically, see Fig. 5.8B). Note that the wave function of the $S_1(^1\Delta)$ state is, in each case, built from the two $[\ldots]\sigma^2\pi^2\pi^2\pi^{*1}\pi^{*1}\sigma^{*0}$ determinants, the sum of their weights being ~82%.

Finally, we look at the non-adiabatic energy difference between the equilibrium unrestricted-triplet-spin and restricted-singlet-spin $AtO^+(H_2O)_n$ structures (n=2−6). From Table 5.3 it is clear that beyond n=3 water molecules in the AtO^+ hydration shell, the singlet-spin clusters become more and more stable. For instance, the singlet-spin cluster in the n=6 case is 0.64 eV more stable than the triplet-spin one, at the NEVPT2(8/6)/AVTZ//SR-PBE0/AVDZ level of theory. At this point, we conclude that hydration induces a SOF ground state change in AtO^+ and that this ground-state change proceeds between the $T_0(^3\Sigma^-)$ and $S_0(^1\Delta)$ states of solvated AtO^+, *i.e.* between the $^3\Sigma^-$ ground state of gas phase AtO^+ and the closed-shell component of the $^1\Delta$ excited state. Thus, these findings support and complement the conclusions of Ayed *et al*.[12,13] In order to give a definite conclusion on the ground-state change in solvated AtO^+, we now investigate the occurrence and natures of the lowest-lying electronic states under the influence of SOC.

5.4.2 The SOC electronic structures of the $AtO^+(H_2O)_n$ systems (n=2−6)

In this subsection we analyze the SOC electronic structures at the 2*c*-PBE0/AVDZ equilibrium geometries corresponding to the $AtO^+(H_2O)_n$ systems (n=2−6), shown in Fig. 5.6. As pointed out previously, SOC induces some geometry relaxation which can change the ordering (or the nature) of the lowest lying SOF states. Hence, we have performed NEVPT2(8/6)/AVTZ single-point calculations at all the 2*c*-PBE0/AVDZ structures and we have looked again at the excitation energies (see Table A3.1 in Appendix 3) and CASSCF wave functions of the lowest-lying SOF states. At the essentially-singlet-spin geometries, the ordering of the SOF states is unchanged but the $S_0(^1\Delta)\rightarrow T_0(^3\Sigma^-)$, $S_0(^1\Delta)\rightarrow S_0(^1\Delta)$ and $S_0(^1\Delta)\rightarrow S_2(^1\Sigma^+)$ excitation energies are tremendously diminished. However, regarding their CASSCF wave functions, we observed no particular changes. At the essentially-triplet-spin geometries, the ordering of the SOF states and the corresponding excitation energies are mostly unaffected for $n\leq4$. For the n=5−6 cases, likely due to larger geometrical changes induced by SOC, we noticed a ground-state change: the $S_0(^1\Delta)$ states lie at lower energies than the $T_0(^3\Sigma^-)$ ones. We note that there are no particular changes in the CASSCF wave functions of the different SOF states.

We now focus on the analysis of the SOC electronic structures of the different $AtO^+(H_2O)_n$ structures (n=2−6). Vertical excitation energies from the Ψ_0 SOC ground states, computed at the c-SOCI/NEVPT2(8/6)/AVTZ level of theory, are presented in Table 5.4.

Table 5.4 Vertical excitation energies (in eV) obtained at the 2*c*-PBE0/AVDZ geometries of the $AtO^+(H_2O)_n$ clusters (n=2−6). The ΔE non-adiabatic energy differences between the essentially-singlet-spin and essentially-triplet-spin clusters are also given (a positive value means that the essentially-spin-triplet cluster is more stable). Unless indicated otherwise, all values are calculated at the c-SOCI/NEVPT2(8/6)/AVTZ level of theory.

	$AtO^+(H_2O)_2$	$AtO^+(H_2O)_3$	$AtO^+(H_2O)_4$	$AtO^+(H_2O)_5$	$AtO^+(H_2O)_6$
Essentially-triplet-spin clusters, 2*c*-PBE0/AVDZ					
Ψ_0	0.00	0.00	0.00	0.00	0.00
Ψ_1	0.37	0.43	0.44	0.62	0.71
Ψ_2	0.37	0.44	0.45	0.64	0.74
Ψ_3	0.91	0.97	0.96	1.01	1.03
Ψ_4	0.91	0.98	0.97	1.14	1.22
Essentially-singlet-spin clusters, 2*c*-PBE0/AVDZ					
Ψ_0	0.00	0.00	0.00	0.00	0.00
Ψ_1	0.89	1.44	2.04	2.21	2.31
Ψ_2	0.89	1.44	2.12	2.33	2.45
Ψ_3	1.05	1.47	2.21	2.36	2.48
Ψ_4	1.37	1.83	2.34	2.45	2.51
Energy differences					
ΔE	0.33	0.30	0.10	−0.10	−0.23
	0.32[a]	0.30[a]	-	-	-
	0.29[b]	0.28[b]	-	-	-

[a]These values are calculated at the c-SOCI/NEVTP2(8/6)/AVTZ//2c-PBE0/AVTZ level of theory. These values show that there is no bias introduced by the use of equilibrium geometries calculated with the smaller AVDZ basis set.
[b]These values are calculated at the c-SOCI/NEVPT2(8/6)/AVQZ//2c-PBE0/AVTZ level of theory. These values show that there is only trifling change introduced by the use of the larger AVQZ basis set.

We start by commenting on the essentially-triplet-spin clusters. Fig. 5.9 shows the evolutions of the SOF compositions of the five lowest-lying SOC states with increasing n. In the n=2 case, one can observe that (i) the Ψ_0 ground SOC state has a main contribution from the M_S=0 spin-component of the $T_0(^3\Sigma^-)$ state (~70%), and a secondary contribution from the spin-component of the $S_2(^1\Sigma^+)$ state (~25%), (ii) the first two excited SOC states, Ψ_1 and Ψ_2, have both large contributions from the $|M_S|$=1 spin-components of the $T_0(^3\Sigma^-)$ state (~86%), and (iii) the wave functions of the next two excited SOC states, Ψ_3 and Ψ_4 have both dominant contributions from the components of the $S_0(^1\Delta)$ and $S_1(^1\Delta)$ states (~81%), respectively. It is hence undoubtedly that these set of SOC states

correlate with $X\ 0^+$, the twofold-degenerate **a** 1 state and twofold-degenerate **a** 2 state of the isolated AtO^+ cation.

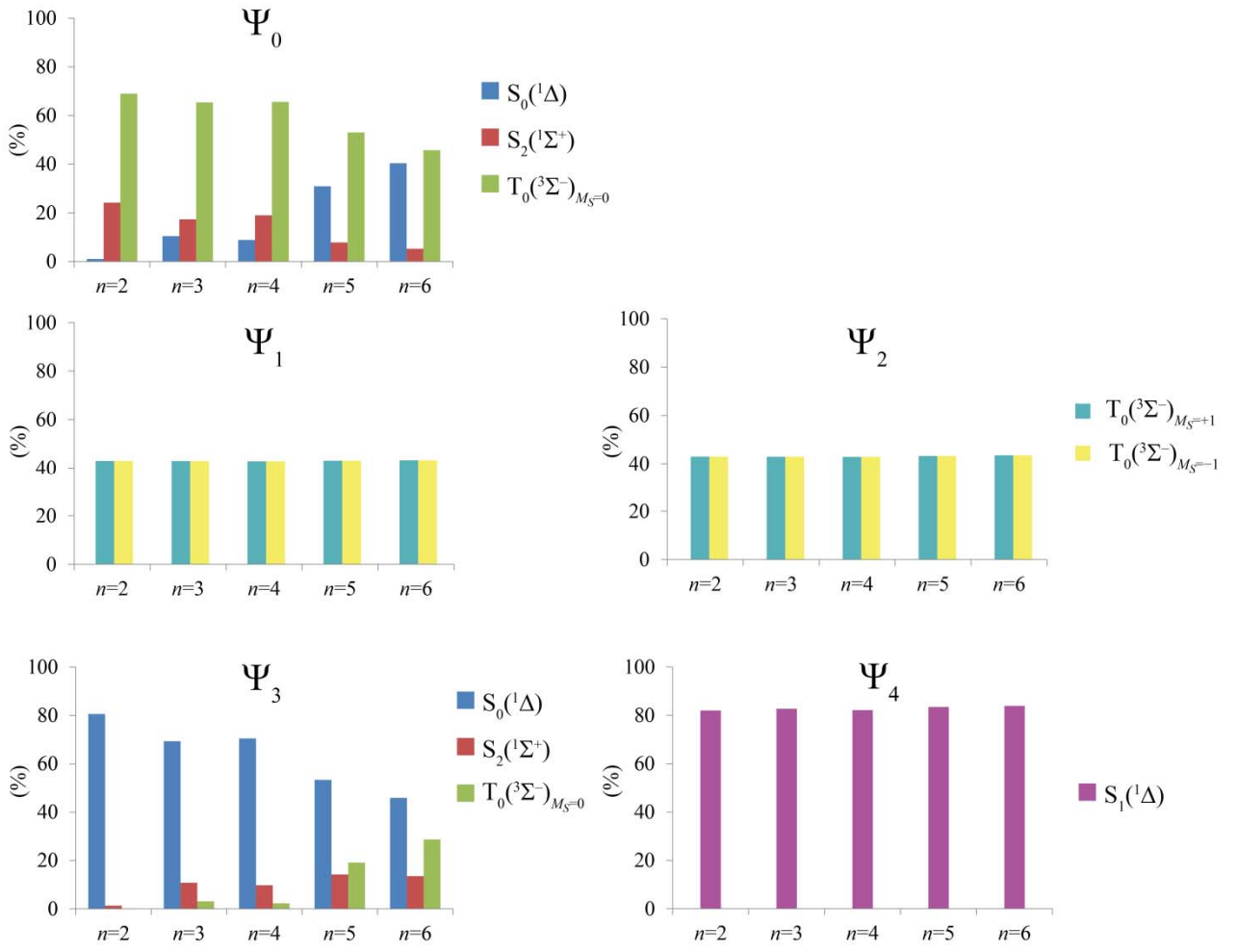

Figure 5.9 SOF compositions (in %) of the five lowest-lying SOC states that occur at the essentially-triplet-spin 2*c*-PBE0/AVDZ geometries of the $AtO^+(H_2O)_n$ systems (n=2-6).

With increasing n, the values in Table 5.4 indicate that the energy gaps between Ψ_1 and Ψ_2, and between Ψ_3 and Ψ_4, gradually increase. In fact, they are all destabilized with respect to the Ψ_0 ground states; Ψ_1 and Ψ_2 by ~0.35 eV (on average), and Ψ_3 and Ψ_4 by ~0.20 eV (on average). Fig. 5.9 shows that the wave functions of Ψ_1, Ψ_2 and Ψ_4 are mainly unchanged with increasing n while there is a concerted change in the SOF compositions of the Ψ_0 and Ψ_3 wave functions. The contribution of the M_S=0 spin-component of $T_0(^3\Sigma^-)$, as well as those of the $S_2(^1\Sigma^+)$ component, decreases in the wave function of Ψ_0 while it increases in the one of Ψ_3. Also, the contribution of the $S_0(^1\Delta)$ component is largely increased in Ψ_0 while it is largely decreased in Ψ_3. This trend was rather expected from the evolution of the SOF states that was previously discussed (see notably

Table A3.1). Reminding that Ψ_0 and Ψ_3 were established to correlate with $X\ 0^+$ and with the essentially closed-shell component of the **a** 2 SOC states of isolated AtO^+ (in the *n*=2 case), one can state that, with increasing *n*, these two SOC states of AtO^+ kind of switch between them.

We now continue by discussing the essentially-singlet-spin clusters. The evolutions of the SOF compositions of the five lowest-lying SOC state wave functions, with increasing *n*, are shown in Fig. 5.10.

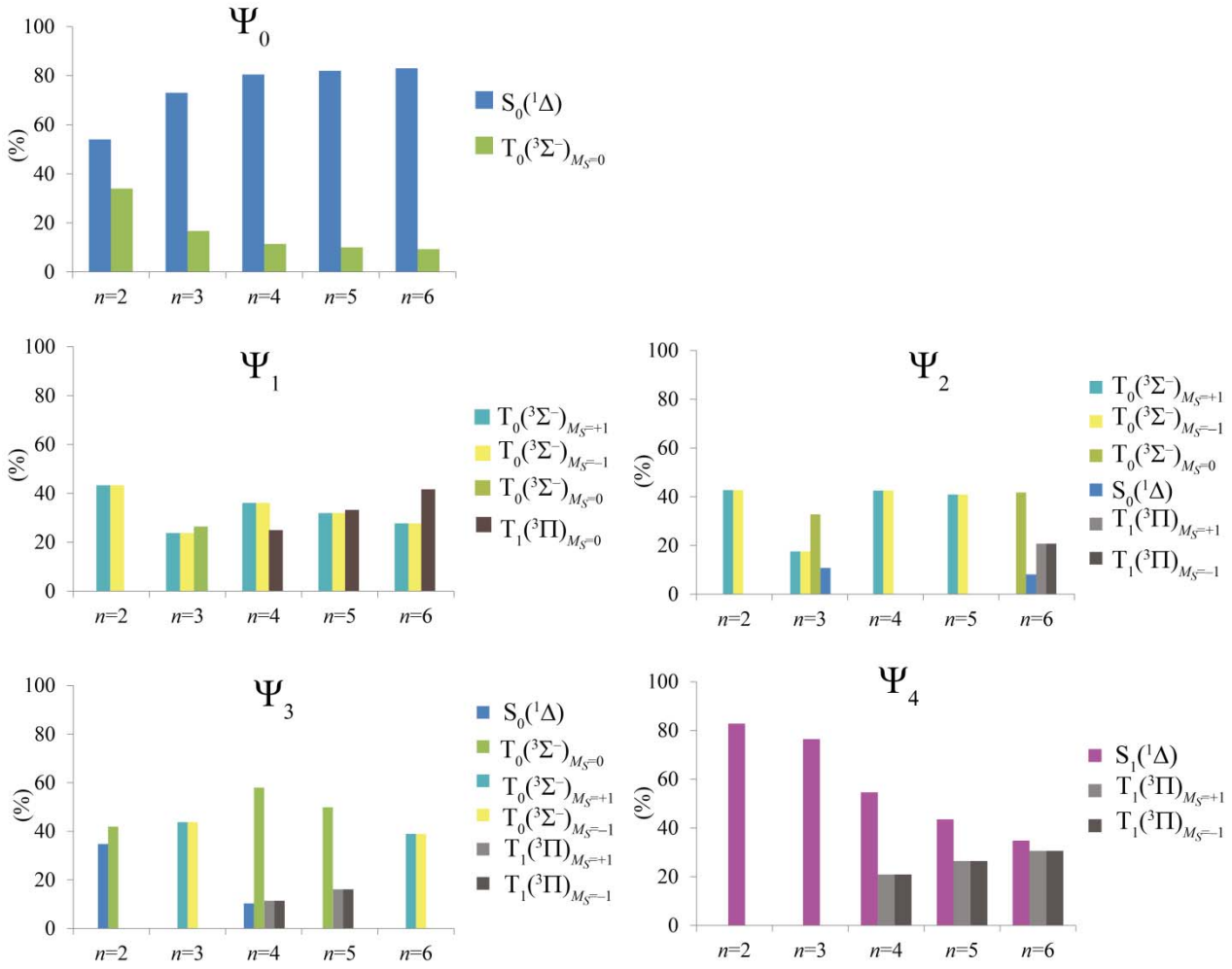

Figure 5.10 SOF composition (in %) of the five lowest-lying SOC states that occur at the essentially-singlet-spin 2*c*-PBE0/AVDZ geometries of the $AtO^+(H_2O)_n$ systems (*n*=2−6).

Regarding the *n*=2 case, the Ψ_1 and Ψ_2 states have large contributions from the $|M_S|$=1 spin-components of the $T_0(^3\Sigma^-)$ state (~86%), and thus correlate with the **a** 1 SOC state of isolated AtO^+, Ψ_4 has a dominant contribution from $S_1(^1\Delta)$ (~83%), and thus correlate with the essentially open-shell component of the **a** 2 state, and the Ψ_0 and Ψ_3 states have strong mixed singlet-triplet character, the leading SOF contribution to Ψ_0 being from the $S_0(^1\Delta)$ spin-component (~53%), and

the leading SOF contribution to Ψ_3 being from the M_S=0 spin component of the $T_0(^3\Sigma^-)$ state (~42%). Hence, we observe a concerted change in the SOF compositions of Ψ_0 and Ψ_3. As *n* increases from 2 to 6, several aspects can be observed, (i) the energy gaps between the Ψ_1 and Ψ_2 states gradually increases while they are both destabilized with respect to Ψ_0 (see Table 5.4), (ii) Ψ_1, Ψ_2 and Ψ_3 exhibit mixtures of the different M_S components of the lowest two SOF triplet-spin states ($T_0(^3\Sigma^-)$ and $T_1(^3\Pi)$), (iii) while Ψ_4 is destabilized, it has less and less contribution from the $S_1(^1\Delta)$ component while it exhibits, beyond *n*=4, contributions from the $|M_S|$=1 spin-components of the $T_1(^3\Pi)$ state (a SOF state that correlates with $^3\Pi$), and (iv) Ψ_0 exhibits more and more $S_0(^1\Delta)$ character, in line with the tremendous (relative) stabilization of this SOF state. Therefore, it is obvious that the essentially-singlet-spin $AtO^+(H_2O)_n$ clusters exhibit essentially closed-shell ground-states that correlate with the essentially closed-shell component of the **a** 2 state.

In fine, we compare the relative energies of the essentially-triplet-spin and essentially-singlet-spin $AtO^+(H_2O)_n$ clusters (*n*=2−6). Inspecting the ΔE values given in Table 5.4, we notice that beyond *n*=4, the essentially-singlet-spin clusters become more stable. As shown above, these clusters exhibit essentially-singlet-spin essentially-closed-shell ground-states. In the SOC limit, through a perturbative approach, AtO^+ undergoes a hydration-induced ground-state change to an essentially-closed-shell one, and thus can readily react in a spin-allowed fashion with closed-shell species. We hence confirm the conclusions of *Ayed et al.*[12,13] and we complement them with the involved many-electron states, $^3\Sigma^-$ and one component of $^1\Delta$ in the SOF picture, and $X\ 0^+$ and one component of **a** 2 when SOC is accounted for.

5.5 Characterizing the role of solvation on the EBO of AtO^+

The aim in this subsection is to analyze the nature of the bond in the solvated AtO^+ cation, from the viewpoint of EBO and spin-orbit-coupled EBO (SOC-EBO). Relying on a single-configurational methodology, the BO is simply calculated from the occupation numbers of a set of MOs describing the particular bond, and requires the knowledge on the MOs characters (*i.e.* bonding, anti-bonding or non-bonding). While the chemical bond is stretched toward the dissociation limit, the BO concept cannot be used anymore to probe the bond nature since, on one side the BO does not diminish gradually toward bond dissociation, and on the other side the wave function typically becomes multiconfigurational in such a context. The concept of EBO arises instead from multiconfigurational methodologies. Considering that one performs a CASSCF

calculation for instance, then the EBO is simply defined as the sum of the weighted BOs of the individual configurations that span the CASSCF wave function,[4] or by considering the populations of the natural orbitals belonging to the active space.[20] For a well-defined EBO, the choice of the active space in the CASSCF calculation must include the MOs that describe well the envisaged bond. This choice is quite trivial for diatomics but admittedly not beyond them. It may be trivial in the latter case if symmetry is retained. Having symmetry (or a near-symmetrical situation) is actually an asset since one can then classify the active space MOs according to σ, π, δ, *etc*., symmetries and divide the total EBO in EBO_σ, EBO_π, EBO_δ, *etc*. components. Nonetheless, beyond two-atom systems the active space must be converged on a set of bond-localized pairs of MOs, in order to obtain meaningful EBOs.[4]

If heavy atoms are present in the studied system, or more importantly when the studied bond involves heavy atoms, then one may account for SOC in the EBO calculation. Quite recently, the EBO concept has been extended to the framework of two-step SOC calculations as c-SOCI ones.[4,21] The derivation of the SOC-EBO from a c-SOCI calculation is readily obtained from calculated EBOs of all the SOF spin-components generated at first. Then, for a given SOC state, the SOC-EBO is nothing but the weighted sum of the EBOs corresponding to all SOF spin-components used to express the respective SOC state,[4] or it can be computed from the updated populations of the natural orbitals.[21]

5.5.1 The isolated AtO^+ cation

Both SOF-EBO and SOC-EBO concepts have recently been used to probe the nature of the bond in the lowest-lying SOF and SOC states of AtO^+.[4] Since we are actually interested in probing the bond nature in solvated AtO^+, at first, we will start by assessing the case of the gas-phase AtO^+. EBOs corresponding to the lowest-lying electronic states of isolated AtO^+, calculated using our computational setup, are presented in Table 5.5 together with values recently reported in the literature. Regarding all the envisaged states, we highlight that our calculated EBOs are in full agreement with the ones reported in the literature. We would like to point out the meaning of the ground-state EBOs. The $^3\Sigma^-$ ground state of AtO^+ has an EBO of ~1.75, value that indicates almost a formally double bond character. When SOC is accounted for, the EBO of the $X\ 0^+$ ground state of AtO^+ is only slightly diminished. This trend is due to the fact that the EBO of $^1\Sigma^+$, the second SOF spin-component that mainly contribute to the wave function of $X\ 0^+$, is just a bit lower than the one of $^3\Sigma^-$. The decreased SOC-EBO value for the $X\ 0^+$ ground state of AtO^+ actually points out the effect of SOC on this chemical bond, which is thus slightly weakened.

Table 5.5 Calculated EBOs at the NEVPT2(8/6)/AVTZ and c-SOCI/NEVPT2(8/6)/AVTZ levels of theory for the lowest-lying SOF states in AtO^+. All EBOs are obtained at the 2*c*-PBE0/AVDZ equilibrium geometry (1.928 Å).

	State	This work	Ref. 4[a]
SOF	$^3\Sigma^-$	1.75	1.76
	$^1\Delta$	1.66	1.69
	$^1\Sigma^+$	1.59	1.62
SOC	$X\ 0^+$	1.69	1.71
	a 1	1.65	1.66
	a 2	1.56	1.58

[a]The EBOs were calculated at the NEVPT2(8/6)/ANO-RCC-QZP and c-SOCI/NEVPT2(8/6)/ANO-RCC-QZP levels of theory, and at the uc-SOCI/NEVPT2(8/6)/ANO-RCC-QZP equilibrium geometry (1.893 Å).

5.5.2 The solvated AtO^+ cation

We investigate now the nature of the AtO^+ bond in the $AtO^+(H_2O)_n$ clusters (n=2−6) through the computation of the EBOs. Since the essentially-singlet-spin clusters are the ones which become the most important ones, we are thus interested in computing the EBOs of the AtO^+ bond only in those clusters. Note that we presently deal with polyatomic systems which in some cases are non-symmetric. Thus, care must be taken when EBOs are calculated. The natural orbitals of the SA-CASSCF active space, converged for the essentially-singlet-spin $AtO^+(H_2O)_n$ clusters (n=2−6), are displayed on Fig. 5.11.

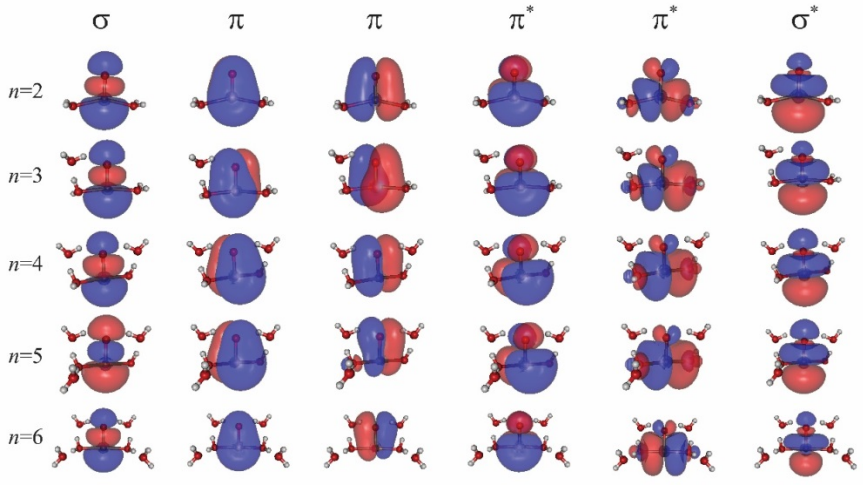

Figure 5.11 Natural orbitals of the SA-CASSCF active space calculated for the $AtO^+(H_2O)_n$ essentially-singlet-spin clusters (n=2−6).

One can see that all natural orbitals are well localized on the AtO^+ bond and, visually, have clear bonding and anti-bonding characters. Thus, we can safely derive EBOs from their natural

occupation numbers. Lastly, we note that all the MOs shown in Fig. 5.11 clearly exhibit σ or π character, and are denoted indeed to refer back to the σ and π orbitals of AtO^+.

Calculated EBOs corresponding to the ground SOF and SOC states of the essentially-singlet-spin $AtO^+(H_2O)_n$ clusters (n=2−6) are presented in Table 5.6. Also, for each n case, we print the relative energies between the σ and σ^*, and between the $\bar{\pi}$ and $\bar{\pi}^*$ (where the top bar indicates an average energy) pairs of SA-CASSCF natural orbitals.

Table 5.6 EBOs calculated at the NEVPT2(8/6)AVTZ and c-SOCI/NEVPT2(8/6)/AVTZ levels of theory for the SOF $S_0(^1\Delta)$ and SOC Ψ_0 ground states of the essentially-singlet-spin clusters. The 2*c*-PBE0/AVDZ equilibrium geometries were used.

Species	$\Delta\varepsilon(\sigma,\sigma^*)$	$\Delta\varepsilon(\bar{\pi},\bar{\pi}^*)$	State	EBO_σ	EBO_π	EBO
$AtO^+(H_2O)_2$	−0.55	−0.24	$S_0(^1\Delta)$	0.92	0.76	1.68
			Ψ_0	0.88	0.80	1.68
$AtO^+(H_2O)_3$	−0.54	−0.26	$S_0(^1\Delta)$	0.90	0.83	1.73
			Ψ_0	0.88	0.83	1.71
$AtO^+(H_2O)_4$	−0.51	−0.27	$S_0(^1\Delta)$	0.88	0.90	1.77
			Ψ_0	0.86	0.89	1.74
$AtO^+(H_2O)_5$	−0.50	−0.28	$S_0(^1\Delta)$	0.87	0.92	1.78
			Ψ_0	0.85	0.91	1.76
$AtO^+(H_2O)_6$	−0.50	−0.28	$S_0(^1\Delta)$	0.86	0.93	1.79
			Ψ_0	0.84	0.91	1.76

With increasing n, the following aspects are observed, (i) the total EBOs for both the SOF and SOC ground states are slightly increased (the change in EBO from the n=2 case to the n=6 one is ~0.1), (ii) the energy difference between the σ and σ^* natural orbitals decreases while the energy difference between the $\bar{\pi}$ and $\bar{\pi}^*$ ones increases, which implies that the bond becomes less and less σ bonding but more and more π bonding, (iii) the EBOs for the SOF and SOC ground states are quite similar and reflect the fact that the ground SOF state is by far the major contribution to the ground SOC state. The slight decreases induced by SOC are similar to the effect of SOC on the bonding in the isolated AtO^+. That is, SOC appears to excite electrons from π to the σ^* orbitals, thus reducing the total EBO. This phenomenon is illustrated in Fig. 5.12 where the occupation numbers of the CASSCF natural orbitals for the essentially-singlet-spin $AtO^+(H_2O)_6$ cluster are shown.

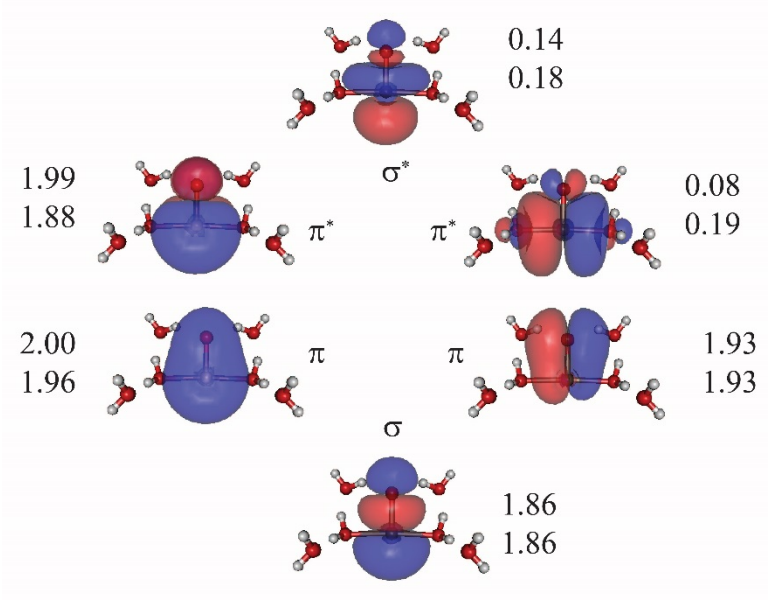

Figure 5.12 SA-CASSCF active natural orbitals for the $AtO^+(H_2O)_6$ essentially-spin-singlet cluster and their natural occupation numbers calculated from the SA-CASSCF wave function of the $S_0(^1\Delta)$ ground SOF state (first row) and from the c-SOCI wave function of the Ψ_0 ground SOC state (second row).

SOC effectively maintains the population of the σ orbital, and of one π orbital, while all the other populations change; the population of one π^* orbital decreases by 0.11 e is associated by an increase of 0.11 e on the population of the other π^* orbital. Since those orbitals are coupled *via* the SOC operator in the C_s symmetry point group, and since both population changes are opposite, we conclude that this direct coupling is responsible for the observed changes. Moreover, the population of one π orbital is decreased by 0.04 e, meanwhile the one of the σ^* orbital is increased by the same amount. Therefore, overall, the main effect of SOC on the AtO^+ bond is to promote 0.04 e from a π^* to the σ^* orbital.

Drawing a major conclusion out of this study, we would like to point out that bonding in AtO^+ is very similar in both the gas-phase and water, though they exhibit different characteristics; the bonding in bare AtO^+ is more σ than π bonding while the opposite holds in solvated AtO^+. The bond strength in solvated AtO^+ may however be slightly smaller than in gas phase since the the σ BO is decreased, which appears not to be compensated by the increase in the π one (*e.g.* the bond distance is elongated by ~0.06 Å).

5.6 Conclusion

In this chapter, the unexpected reactivity of the predominant At species in acidic and oxidizing conditions, AtO^+, with closed-shell ligands has been elucidated mainly using relativistic wave-function-based methods. In the gas phase, AtO^+ develops a $^3\Sigma^-$ ground state. When SOC is

included, the M_S=0 $^3\Sigma^-$ spin-component contributes for ~68% to the X 0^+ ground SOC state, thus rendering it of essentially-triplet-spin character. Nonetheless, a substantial closed-shell singlet-spin character is also evidenced for this SOC ground state (~26%). Even though this latter character may be sufficient to trigger non-spin-conserving reactions, we have followed the hypothesis that the reactive electronic state of AtO^+ in aqueous solution is a different one, essentially-closed-shell and of singlet-spin multiplicity. In the SOF formalism and in the presence of water molecules, we found that AtO^+ adopts a closed-shell (singlet-spin) ground-state, in agreement with the studies of Ayed *et al.*[12,13]. We have shown that this newly adopted ground state is $S_0(^1\Delta)$, a SOF state that correlates with the closed-shell component of the $^1\Delta$ state of gas phase AtO^+. That is, even though this type of phenomenon is very rare, environment induces a ground-state change in AtO^+. When SOC was accounted for alongside hydration, we have found that the most stable $AtO^+(H_2O)_n$ clusters (n≥5) adopt essentially-singlet-spin ground-states. We have shown that these SOC ground states are dominantly composed by the $S_0(^1\Delta)$ SOF components. Taking into account that the $^1\Delta$ state contributes by ~83% to the essentially-singlet-spin **a** 2 state, we conclude that the adopted SOC ground state of solvated AtO^+ actually correlates with **a** 2. More precisely, it correlates with the essentially closed-shell component of **a** 2. Thus a hydration-induced ground-state change occurs in AtO^+, the electronic state responsible for the unexpected reactivity being the essentially-singlet-spin and essentially-closed-shell **a** 2 excited state of AtO^+. We have then shown, using the EBO concept, that the bonding in AtO^+ is similar in the gas-phase and in aqueous solution, even though in the latter, solvation decreases the σ bond character and increases the π one. Pairing this with the slight bond elongation, gives hints that the bond strength in solvated AtO^+ may be slightly weaker than in the gas phase, as expected.

Finally, we would like to highlight again that the outcomes of our two-step wave-function-based studies corroborate with the 2*c*-DFT ones of Ayed *et al*, and both explain the unexpected reactivity of AtO^+ in aqueous solution. This can be considered as a further proof of the relevance of using two-step approaches to explore the electronic structures of At species.

Bibliography

1. R. Poli, J. N. Harvey, *Chem. Soc. Rev.* Spin forbidden chemical reactions of transition metal compounds. New ideas and new computational challenges, **2003**, 32, 1.
2. J. N. Harvey, *Phys. Chem. Chem. Phys.* Understanding the kinetics of spin-forbidden chemical reactions, **2007**, 9, 331.
3. A. S. P. Gomes, F. Réal, N. Galland, C. Angeli, R. Cimiraglia, V. Vallet, *Phys. Chem. Chem. Phys.* Electronic structure investigation of the evanescent AtO^+ ion, **2014**, 16, 9238.
4. R. Maurice, F. Réal, A. S. P. Gomes, V. Vallet, G. Montavon, N. Galland, *J. Chem. Phys.* Effective bond orders from two-step spin–orbit coupling approaches: The I_2, At_2, IO^+, and AtO^+ case studies, **2015**, 142, 094305.
5. J. Champion, M. Seydou, A. Sabatié-Gogova, E. Renault, G. Montavon, N. Galland, *Phys. Chem. Chem. Phys.* Assessment of an effective quasirelativistic methodology designed to study astatine chemistry in aqueous solution, **2011**, 13, 14984.
6. J. Champion, A. a. Sabatié-Gogova, F. Bassal, T. Ayed, C. Alliot, N. Galland, G. Montavon, *J. Phys. Chem. A.* Investigation of astatine (III) hydrolyzed species: Experiments and relativistic calculations, **2013**, 117, 1983.
7. J. Li, B. E. Bursten, L. Andrews, C. J. Marsden, *J. Am. Chem. Soc.* On the electronic structure of molecular UO_2 in the presence of Ar atoms: Evidence for direct U-Ar bonding, **2004**, 126, 3424.
8. J. Li, B. E. Bursten, B. Liang, L. Andrews, *Sci.* Noble gas-actinide compounds: Complexation of the CUO molecule by Ar, Kr, and Xe atoms in noble gas matrices, **2002**, 295, 2242.
9. L. Andrews, B. Liang, J. Li, B. E. Bursten, *Angew. Chem. Int. Ed. Engl.* Ground-state reversal by matrix interaction: electronic states and vibrational frequencies of CUO in solid argon and neon, **2000**, 39, 4565.
10. M. Zhou, L. Andrews, J. Li, B. E. Bursten, *J. Am. Chem. Soc.* Reaction of laser-ablated uranium atoms with CO: Infrared spectra of the CUO, CUO^-, $OUCCO$,$(\eta^2\text{-}C_2)$ UO_2, and U $(CO)_x$ (x= 1-6) molecules in solid neon, **1999**, 121, 9712.
11. I. Infante, L. Andrews, X. Wang, L. Gagliardi, *Chem. Eur. J.* Noble gas matrices may change the electronic structure of trapped molecules: the UO_2 $(Ng)_4$ [Ng= Ne, Ar] case, **2010**, 16, 12804.
12. T. Ayed, M. Seydou, F. Réal, G. Montavon, N. Galland, *J. Phys. Chem. B.* How does the solvation unveil AtO^+ reactivity?, **2013**, 117, 5206.
13. T. Ayed, F. Réal, G. Montavon, N. Galland, *J. Phys. Chem. B.* Rationalization of the solvation effects on the AtO^+ ground-state change, **2013**, 117, 10589.
14. M. J. Frisch, G. W. Trucks, H. B. Schlegel, G. E. Scuseria, M. A. Robb, J. R. Cheeseman, G. Scalmani, V. Barone, B. Mennucci, G. A. Petersson, H. Nakatsuji, M. Caricato, X. Li, H. P. Hratchian, A. F. Izmaylov, J. Bloino, G. Zheng, J. L. Sonnenberg, M. Hada, M. Ehara, K. Toyota, R. Fukuda, J. Hasegawa, M. Ishida, T. Nakajima, Y. Honda, O. Kitao, H. Nakai, T. Vreven, J. A. Montgomery, J. E. Jr. Peralta, F. Ogliaro, M. Bearpark, J. J. Heyd, E. Brothers, K. N. Kudin, V. N. Staroverov, R. Kobayashi, J. Normand, K. Raghavachari, A. Rendell, J. C. Burant, S. S. Iyengar, J. Tomasi, M. Cossi, N. Rega, J. M. Millam, M. Klene, J. E. Knox, J. B. Cross, V. Bakken, C. Adamo, J. Jaramillo, R. Gomperts, R. E. Stratmann, O. Yazyev, A. J. Austin, R. Cammi, C. Pomelli, J. W. Ochterski, R. L. Martin, K. Morokuma, V. G. Zakrzezski, G. A. Voth, P. Salvador, J. J. Dannenberg, S. Dapprich, A. D. Daniels, Ö. Farkas, J. B. Foresman, J. V. Ortiz, J. Cioslowski, D. J. Fox, Gaussian 09, revision D01; Gaussian Inc.: Wallingford, CT, **2013**.

15. R. Ahlrichs, M. K. Armbruster, R. A. Bachorz, M. Bär, H.-P. Baron, R. Bauernschmitt, F. A. Bischoff, S. Böcker, N. Crawford, P. Deglmann, Fabio Della Sala, M. Diedenhofen, M. Ehrig, K. Eichkorn, S. Elliott, D. Friese, F. Furche, A. Glöß, F. Haase, M. Häser, C. Hättig, A. Hellweg, S. Höfener, H. Horn, C. Huber, U. Huniar, M. Kattannek, W. Klopper, A. Köhn, C. Kölmel, M. Kollwitz, K. May, P. Nava, C. Ochsenfeld, H. Öhm, M. Pabst, H. Patzelt, D. Rappoport, O. Rubner, A. Schäfer, U. Schneider, M. Sierka, D. P. Tew, O. Treutler, B. Unterreiner, M. von Arnim, F. Weigend, P. Weis, H. Weiss, N. Winter, TURBOMOLE version 6.6, a development of University of Karlsruhe and Forschungszentrum Karlsruhe GmbH, TURBOMOLE GmbH, **2014**.

16. K. A. Peterson, D. Figgen, E. Goll, H. Stoll, M. Dolg, *J. Chem. Phys.* Systematically convergent basis sets with relativistic pseudopotentials. II. Small-core pseudopotentials and correlation consistent basis sets for the post-d group 16–18 elements, **2003**, 119, 11113.

17. R. A. Kendall, T. H. Dunning Jr, R. J. Harrison, *J. Chem. Phys.* Electron affinities of the first-row atoms revisited. Systematic basis sets and wave functions, **1992**, 96, 6796.

18. T. H. Dunning Jr, *J. Chem. Phys.* Gaussian basis sets for use in correlated molecular calculations. I. The atoms boron through neon and hydrogen, **1989**, 90, 1007.

19. H. J. Werner, P. J. Knowles, R. Lindh, F. R. Manby, M. Schütz, P. Celani, T. Korona, A. Mitrushenkov, G. Rauhut, T. B. Adler, R. D. Amos, A. Bernhardsson, A. Berning, D. L. Cooper, M. J. O. Deegan, A. J. Dobbyn, F. Eckert, E. Goll, C. Hampel, G. Hetzer, T. Hrenar, G. Knizia, C. Köppl, Y. Liu, A. W. Lloyd, R. A. Mata, A. J. May, S. J. McNicholas, W. Meyer, M. E. Mura, A. Nicklass, P. Palmieri, K. Pflüger, R. Pitzer, M. Reiher, U. Schumann, H. Stoll, A. J. Stone, R. Tarroni, T. Thorsteinsson, M. Wang, A. Wolf, MOLPRO version 2009.1, A package of *ab initio* programs, **2009**.

20. B. O. Roos, A. C. Borin, L. Gagliardi, *Angew.Chem. Int. Ed.* Reaching the maximum multiplicity of the covalent chemical bond, **2007**, 119, 1491.

21. F. Gendron, B. Le Guennic, J. Autschbach, *Inorg. Chem.* Magnetic properties and electronic structures of Ar_3U^{IV}–L complexes with Ar = $C_5(CH_3)_4H^-$ or $C_5H_5^-$ and L = CH_3, NO, and Cl, **2014**, 53, 13174.

Chapter 6

Reactivity of At Species: Completion of the Astatine Pourbaix Diagram

By combining outcomes of experiments and of relativistic quantum mechanical studies, we aim in the present chapter at identifying a new At species that can predominate in non-complexing media. This work is of interest to optimize or design radiolabelling protocols. It has been the subject of a publication in *Chem. Eur. J.*[1] and will be presented in a slightly different way in the present chapter since additional details will be given.

6.1 Introduction

Knowledge of the Pourbaix (*E*-pH) diagrams of chemical elements is important especially in the context of industry applications. For instance, there are the very famous examples of Fe, Ni and Cr elements whose Pourbaix diagrams play key-roles in designing anticorrosive alloys based on these metals.[2-4] Regarding the Pourbaix diagram of At, its usefulness in the context of nuclear medicine was lengthy discussed in Chapter 1. We will briefly recall only the important aspects. Gathering the currently available data, the At Pourbaix diagram that can be built is shown in Fig. 1.7. It shows that in acidic media and in the potential range of water stability ($E = -0.1$ to $+1.2$ V *vs.* NHE), four different At species can predominate: At^-, At^+, AtO^+ and AtO(OH). Less is known regarding the predominance domains of At species in basic media. In basic and reducing conditions, a negatively charged At species has been unraveled by electromobility experiments.[5] By analogy with the case of iodine, this species was assumed to be At^- (*i.e.* since the Pourbaix diagram of I shows a stable I^- species across the full pH range, see for instance Ref. 6). We do think that this species is indeed At^-,[7] and actually, the question that we would like to address is rather related to its predominance in oxidizing conditions. Indeed, for labeling purposes, knowing the predominant

species in given conditions is important since it would dictate the types of mechanistic approaches which can be used. Several authors actually do pose for the electrophilic inertness of At in some specific *in vivo* conditions.[8] Exploiting approaches that involve At^- appears interesting. However, since redox conditions may be at play, relying only on basic conditions is not sufficient. The objective in this chapter is to determine the predominant At species in basic and oxidizing conditions. Note that knowledge on this species may lead to the completion of the At Pourbaix diagram in non-complexing aqueous media (up to a given pH range).[9-11] We quote again that spectroscopic tools cannot be used to obtain structural information on At species. Hence, we combine ultra-trace radiochemical studies with outcomes of relativistic quantum mechanical calculations in order to obtain hints on the nature of the supposedly predominant At species in basic and oxidizing media.

6.1.1 Outcomes from experiments

HPIEC and competition experiments have been performed by radiochemist colleagues at the SUBATECH laboratory.[1] The radiochromatogram obtained through HPIEC revealed that, in concentrated NaOH solutions, the predominant At species is retained by the anionic exchange column. Studying the dependence of the retention factor (k) of this species as a function of NaOH concentration, it has been revealed that this species bears a single negative charge (by confronting the obtained trend to the one obtained for iodide, I^-). Furthermore, the associated peak on the radiochromatogram vanishes when lowering the pH of the media from 11 to 5.5, while a peak corresponding to the formation of the AtO(OH) species appears. The latter species was previously shown to predominate at pH~5.5.[11] SLC experiments have been thereafter performed. Briefly, the principles of SLC experiments are:[12] a resin suspension (ion exchanger) is brought to equilibrium with a bulk solution (the desired media), and the At sample is then added. After the equilibrium partition of At between the two phases is achieved, centrifugation is applied to separate them. The distribution coefficient (K_d) is calculated as:

$$K_d = \frac{A_{tot} - A_{sol}}{A_{sol}} \times \frac{V}{m} \tag{6.1}$$

where A_{tot} and A_{sol} are the total activity in the suspension (solution + resin) and the total activity in the solution, respectively, while V and m are the volume of the liquid phase and the mass of the dried resin, respectively. Varying the pH from ~4 to ~11, while maintaining oxidizing conditions, leads to a change in the K_d value above pH=6. Beyond this point, the present species exhibits a strong affinity for the anionic exchange resin. This species corresponded to the anionic one

unraveled in the HPIEC experiment. Thus, the AtO(OH) species converts into an anionic one bearing a single negative charge. Also, from the pH dependence, one can conclude that a single proton is involved in the conversion process. One can hypothesize that beyond pH~6, the AtO(OH) species (i) undergoes deprotonation leading to the candidate AtO_2^- anionic species:

$$AtO(OH)_{(aq)} \underset{}{\overset{K_a(AtO(OH))}{\rightleftharpoons}} AtO_{2(aq)}^- + H^+_{(aq)} \quad (6.2)$$

or, (ii) further hydrolyses, leading to the double hydrolysis product of AtO^+, *i.e.* to the $AtO(OH)_2^-$ anionic species:

$$AtO(OH)_{(aq)} + H_2O_{(aq)} \underset{}{\overset{K_{hyd,2}}{\rightleftharpoons}} AtO(OH)_{2(aq)}^- + H^+_{(aq)} \quad (6.3)$$

Considering both Eq. 6.2 and Eq. 6.3, the equilibrium constant (in aqueous solution) can be expressed as:

$$K = \frac{[\text{anionic species}][H^+]}{[AtO(OH)]} \quad (6.4)$$

Using the data obtained from the SLC experiments, the value of Log *K* was found to be −6.9±0.2. The missing piece from "the puzzle" is the identification of the anionic species in question, being either AtO_2^- or $AtO(OH)_2^-$, *i.e.* does the speciation change proceeds as Eq. 6.2 or Eq. 6.3? This aspect is here tackled with relativistic quantum mechanical approaches.

6.2 Computational details

According to the methodological approach presented in Chapter 3, regarding the accurate computation of thermodynamic constants, we have used thermodynamic cycles with exchange reactions that here involve At-containing species as well as Br-containing species. In order to obtain gas phase geometries, electronic energies and vibrational frequencies of the various species, we have performed quantum mechanical calculations based on DFT and 2*c*-DFT approaches. The latter one was envisaged only when calculations were performed on species containing a Br or an At atom. The B3LYP hybrid GGA density functional[13] was retained since it perform well in DFT calculations on At species (see Chapter 3), and most importantly for the computation of equilibrium constants in good agreement with experiment.[9,11] The ECP10MDF and ECP60MDF PPs[14] have been used to mimic the roles of the 10 and 60 core electrons of the Br and At centers, respectively.

For describing their remaining 25 valence electrons, we have used the aug-cc-pVDZ-PP basis set for Br[14] and the aug-cc-pVDZ-PP basis set[18] supplemented by the 2*c* extension generated by Armbruster *et al.*,[15] and improved by Champion *et al.*,[9] for At. For the H and O centers, the standard aug-cc-pVDZ basis sets have been used.[16,17] Hereafter, we will refer this combination of basis sets as AVDZ, for the sake of simplicity. We have performed (2*c*-)MP2 calculations as well on the previously obtained (2*c*-)B3LYP/AVDZ geometries. The same PPs for Br and At centers were used but in conjunction with, this time, AVTZ basis sets, *i.e.* aug-cc-pVTZ-PP for Br,[14] aug-cc-pVTZ-PP-2*c* for At,[14,15] and the standard aug-cc-pVTZ for H and O centers.[16,17] Note that in all MP2 calculations, the At 5*s*, 5*p* and 5*d* semi-core electrons, the Br 3*s*, 3*p* semi-core electrons, and the O 1*s* core electrons, were frozen according to the construction of the used basis sets and PPs. Note that the results obtained from the combination of (2*c*-)MP2/AVTZ energies and (2*c*-B3LYP/AVDZ structural and vibrational parameters will be re referred to as 2*c*-MP2//2*c*-B3LYP.

Using the aforementioned AVDZ basis sets and PPs, solvation free energies in water for the different species are calculated using the CPCM-UAHF//UAKS scheme (and associated details as presented in Chapter 3, notably regarding the construction of the solute cavities). Note that this particular combination of electronic structure methods, PPs, basis sets and solvation scheme, led to calculated equilibrium constants for eight reactions involving At species with a MUE of ~0.6 logarithmic units (see Table 3.3 and refs. 9,11). We finally note that all (2*c*-)DFT calculations were carried out using the NWChem program package,[18] the (2*c*-)MP2 ones using the TURBOMOLE program package[19] while all the solvation calculations were performed with the Gaussian one.[20]

6.3 On the potential predominance of the AtO_2^- species

In this section, we would like to assess through a quantum mechanical study if the predominant At species in basic and oxidizing conditions could be AtO_2^-. This can be done in a straightforward manner by simply (i) calculating the acidic constant of the AtO(OH) species, K_a(AtO(OH)), and (ii) confronting it to the measured equilibrium constant, *K*. The targeted K_a(AtO(OH)) can be derived from the free energy change in aqueous solution of the reaction 6.2, which in turn can be calculated simply from a thermodynamic cycle based on this reaction and by using the experimental free energy of solvation for H^+. Nonetheless, proceeding in this way we expect some accumulation of errors. Indeed, the errors that affect the description of the electron correlation/relativistic/solvation effects differ in the species occurring on the LHS and RHS of the reaction, and may add up when calculating the reaction free energy change. As we have proceeded in Chapter 3, we propose to obtain K_a(AtO(OH)) according to a scheme based on a thermodynamic

cycle rooted in a proper exchange reaction. That is, in order to profit as much as possible from an eventual cancelation of the possible abovementioned errors. We arrived at choosing a proton-exchange reaction involving the hypobromous acid (HBrO):

$$\mathrm{AtO(OH)_{(aq)} + BrO^-_{(aq)} \overset{K_{exc}}{\rightleftharpoons} AtO^-_{2(aq)} + HBrO_{(aq)}} \qquad (6.5)$$

The equilibrium constant (K_{exc}) of this exchange reaction is related to the pK_a values of AtO(OH) and HBrO, according to the following relation:

$$\mathrm{p}K_a\left(\mathrm{AtO(OH)}\right) = \mathrm{p}K_a(\mathrm{HBrO}) - \mathrm{Log}\ K_{exc} \qquad (6.6)$$

For the $\mathrm{p}K_a\left(\mathrm{HBrO}\right)$ term, one can safely use the experimental value which is accurately known (8.55).[21] Hence, in order to reach our goal, we are left with bringing a computational estimate for the $\mathrm{Log}\ K_{exc}$ term. The latter is calculated from the free energy change (ΔG^*_s) associated to reaction 6.5, which can be derived from the thermodynamic cycle shown in Scheme 6.1,

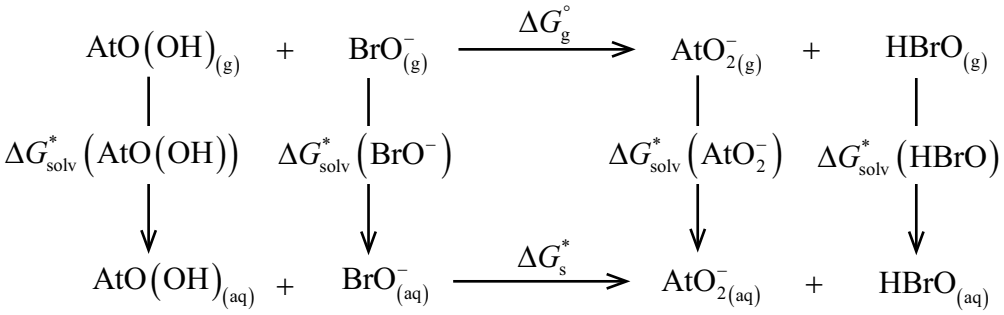

Scheme 6.1 Thermodynamic cycle used to calculate the free energy changes in aqueous solution for the reaction 6.5.

leading to the following relation:

$$\Delta G^*_s = \Delta G^\circ_g + \Delta G_{solv}\left(\mathrm{AtO_2^-}\right) + \Delta G_{solv}\left(\mathrm{HBrO}\right) - \Delta G_{solv}\left(\mathrm{AtO(OH)}\right) - \Delta G_{solv}\left(\mathrm{BrO^-}\right) \qquad (6.7)$$

where ΔG°_g is the reaction free energy change in the gas phase and the remaining terms are the free energies of solvation of the respective chemical species in water.

In Fig. 6.1, we show a schematic representation of the studied reaction where we print the equilibrium geometries of the At reactants and products as obtained at the (2*c*-)B3LYP/AVDZ level of theory.

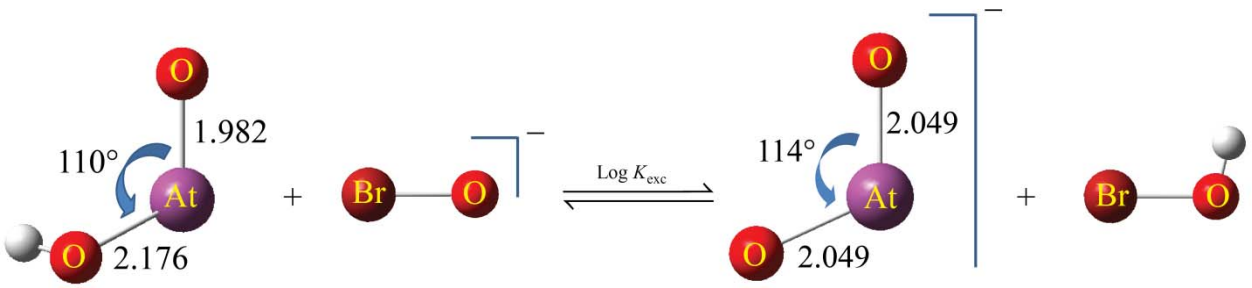

Figure 6.1 Schematic representation of the studied reaction shown in Eq. 6.5. The printed geometries for the reactants and products are the equilibrium ones obtained at the (2*c*-)B3LYP/AVDZ level of theory. For the At species, geometrical parameters are also shown (bond lengths in Å and angles in degrees).

At the 2*c*-B3LYP+CPCM-UAHF//UAKS and 2*c*-MP2//2c-B3LYP+CPCM-UAHF//UAKS levels of theory, we have obtained $\mathrm{Log}\,K_{exc}$ values of –5.6 and –3.2, respectively. Using Eq. 6.6, they lead to $\mathrm{Log}\,K_a\left(\mathrm{AtO(OH)}\right)$ values of −14.1 and −11.7, respectively. We note that these values are considerably far from the measured value, Log *K*=−6.9±0.2. One may speculate that our calculated acidic constant may improve with a better description of solvation effects. Indeed, we deal with the solvation of charged species and short-range electrostatics and hydrogen bonding for instance may bring significant energy stabilizations which cannot be accounted with implicit solvent models as CPCM. However, we note that an improvement of more than 4 logarithmic units, which could bring calculated and measured values in close agreement, is rather unlikely. For instance, calculating the equilibrium constant for a ligand-exchange reaction involving the charged AtO^+-thioacetamide complex,[22] F. Bassal found that the quantum mechanical treatment of up to three explicit water molecules in the solvation spheres of the charged species, improves it hardly by ~1 unit of Log. We hence show no interest in proceeding likewise in the present case and we conclude that the AtO_2^- species cannot be the targeted anionic species that appears above pH=6.

6.4 On the potential predominance of the $\mathrm{AtO(OH)}_2^-$ species

In this section, we would like to assess through quantum mechanical calculations if the predominant At species in basic and oxidizing conditions could be $\mathrm{AtO(OH)}_2^-$. We wish to bring a computational estimate for the equilibrium constant of the secondary hydrolysis reaction of AtO^+, $K_{hyd,2}$, and compare it to the experimentally determined *K* value. Again, we avoid computing $K_{hyd,2}$ directly from Eq. 6.3, but we use instead a proper exchange reaction involving Br-containing species. Champion *et. al* showed[11] that the first hydrolysis constant of AtO^+, $K_{hyd,1}$, can accurately be determined starting from the ligand-exchange reaction,

$$\mathrm{AtOBr_{(aq)} + HO^-_{(aq)} \overset{K_{exc}}{\rightleftharpoons} AtO(OH)_{(aq)} + Br^-_{(aq)}} \quad (6.8)$$

according to the following relation:

$$\mathrm{Log}\, K_{\mathrm{hyd,1}} = \mathrm{Log}\, K_{\mathrm{exc}} + \mathrm{Log}\, \beta_{\mathrm{Br^-}} + \mathrm{Log}\, K_{\mathrm{w}} \quad (6.9)$$

where $\beta_{\mathrm{Br^-}}$ is the complexation constant associated with the formation of the AtOBr species, which is known from experiments ($\mathrm{Log}\, \beta_{\mathrm{Br^-}} = 2.7 \pm 0.2$),[9] and K_{w} is the water self-ionization constant ($\mathrm{Log}\, K_{\mathrm{w}} = -13.995$ at T=298 K).[21] Hence, the only ingredient needed to compute $K_{\mathrm{hyd,1}}$ is K_{exc} of reaction 6.8. We now propose to obtain $K_{\mathrm{hyd,2}}$ starting from a ligand-exchange reaction similar to the one shown in Eq. 6.8:

$$\mathrm{AtOBr^-_{2\,(aq)} + 2HO^-_{(aq)} \overset{K_{2exc}}{\rightleftharpoons} AtO(OH)^-_{2(aq)} + 2Br^-_{(aq)}} \quad (6.10)$$

We get the following relation:

$$\mathrm{Log}\, K_{\mathrm{hyd,2}} = \mathrm{Log}\, K_{\mathrm{2exc}} + \mathrm{Log}\, \beta_{\mathrm{2Br^-}} + 2\mathrm{Log}\, K_{\mathrm{w}} - \mathrm{Log}\, K_{\mathrm{hyd,1}} \quad (6.11)$$

where $\beta_{\mathrm{2Br^-}}$ is the complexation constant associated with the formation of the $\mathrm{AtOBr_2^-}$ species, which is known from experiments ($\mathrm{Log}\, \beta_{\mathrm{2Br^-}} = 5.0 \pm 0.2$).[9] Using as well the determined experimental value for $\mathrm{Log}\, K_{\mathrm{hyd,1}}$, *i.e.* -1.9 ± 0.2,[11] we can obtain $\mathrm{Log}\, K_{\mathrm{hyd,2}}$ by simply bringing a computational estimate for K_{2exc} (see Eq. 6.11). This latter is calculated from the free energy change (ΔG^*_{s}) associated with reaction 6.10, which can be derived from the thermodynamic cycle shown in Scheme 6.2,

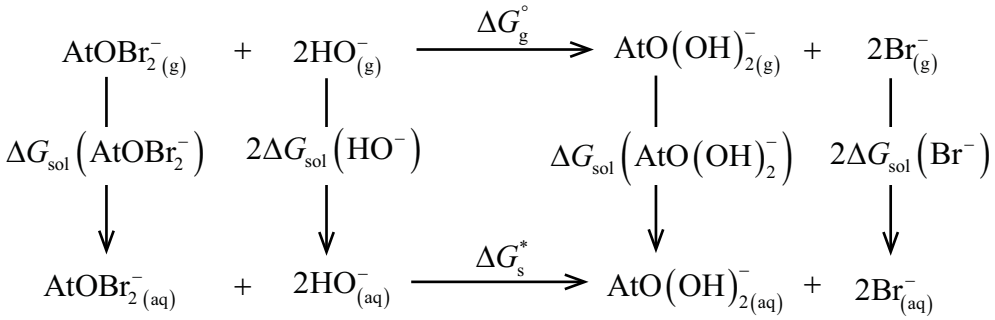

Scheme 6.2 Thermodynamic cycle used to calculate the free energy change in aqueous solution of reaction 6.10.

which leads to:

$$\Delta G_s^* = \Delta G_g^\circ + \Delta G_{sol}\left(\mathrm{AtO(OH)_2^-}\right) + 2\Delta G_{sol}\left(\mathrm{Br^-}\right) - \Delta G_{sol}\left(\mathrm{AtOBr_2^-}\right) - 2\Delta G_{sol}\left(\mathrm{HO^-}\right) \quad (6.12)$$

where ΔG_g° is the free energy change in the gas phase and the remaining terms are the free energies of solvation of the respective species in water. Note that At species of interest exhibit several stable conformers. Their free energies of solvation are thus calculated according to the Boltzmann distribution formula presented in Chapter 3 (Eq. 3.1).

In Fig. 6.2, we show a schematic representation of the studied ligand-exchange reaction with the equilibrium geometries of the reactants and products as obtained at the (2*c*-)B3LYP/AVDZ level of theory.

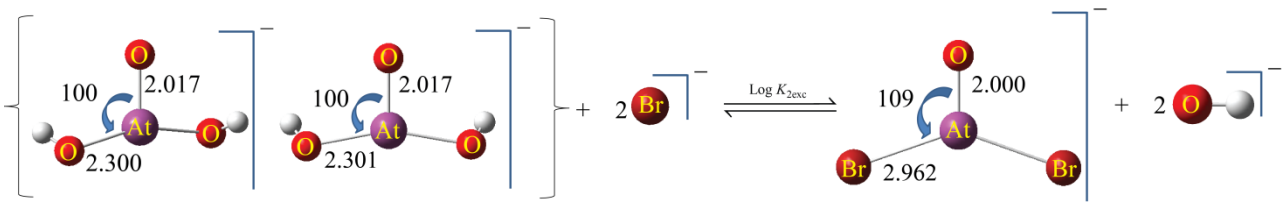

Figure 6.2 Schematic representation of the studied ligand-exchange reaction. The printed geometries for the reactants and products are the equilibrium ones obtained at the (2*c*-)B3LYP/AVDZ level of theory. For the At species, geometrical parameters are also shown (bond lengths in Å and angles in degrees).

Concerning the $\mathrm{AtO(OH)_2^-}$ species, we identified two stable conformers pertaining to the C_2 and C_s symmetry point groups. The latter conformer is the most stable one, by ~2 kJ·mol^{-1} in the gas phase and by ~4 kJ·mol^{-1} in aqueous solution. At thermal equilibrium, the populations of the stable conformers are given by the Boltzmann distribution law, and accordingly, we have for a conformer *i*:

$$p_i = \frac{\exp\left(-G_i/RT\right)}{\sum_{j=1}^{n}\exp\left(-G_j/RT\right)} \quad (6.13)$$

where G_i, G_j are free energies of the *i* conformer of interest and of all the identified *j* stable conformers, respectively. For the present $\mathrm{AtO(OH)_2^-}$ case, the Boltzmann populations of the C_2 and C_s conformers, in aqueous solution, are 20% and 80%, respectively. Definitely, the latter conformer predominates and mostly influences the reaction equilibrium constant. Comparing the equilibrium geometry of this conformer with the one of AtO(OH) (see Fig. 6.1), one can note for the present

case a slight elongation of the AtO^+ bond and longer interaction distances between the At center and the two hydroxide fragments (by more than 0.1 Å). The $AtOBr_2^-$ species exhibits a single relevant structure of C_{2v} symmetry.

At the 2*c*-B3LYP+CPCM-UAHF//UAKS and 2*c*-MP2//2c-B3LYP+CPCM-UAHF//UAKS levels of theory, we have obtained Log K_{2exc} values of 12.0 and 13.0, respectively. They lead to Log $K_{hyd,2}$ values of −9.1 and −8.1, respectively. These values appear to be consistent and, apparently, suggest that the measured value for the equilibrium constant, Log K=−6.9±0.2, can correspond to reaction 6.3. However, the 2*c*-DFT value is ~2 logarithmic units off the experimental one, preventing us to firmly conclude on the above statement. According to the reasoned discussion on the limits of the implicit solvent models, given in the previous section, we are interested for estimating the influence of microsolvation on the calculated Log $K_{hyd,2}$ value. Indeed, strong interactions primarily between the charged species and water molecules of their first hydration shells may occur, preventing us to reach the accepted ~1 logarithmic unit of accuracy when we calculate the reaction equilibrium constant using bare anionic species and an implicit solvent model.

6.4.1 Stepwise hydration study

Our aim is to calculate Log $K_{hyd,2}$ in a similar fashion as reaction 6.10, but by considering an explicit quantum mechanical treatment of water molecules in the hydration spheres of the reactants and products. Treating explicitly only molecules of the first hydration shells is admittedly sufficient, however their number is not necessary small and yet may add up to a tremendous computational cost when conformational analyses are attempted. To exemplify, a study on the aqueous solvation of the $Hg(OH)_2$ molecule revealed that up to ~24 water molecules are necessary to fully form its first hydration shell.[23] Hence, we propose to include in the quantum mechanical treatments only the water molecules involved in the strongest interactions with the solutes, while increasing their number up to when a balanced description of the interactions on the LHS and RHS of the reaction is achieved. The latter requirement arises from our methodological approach, which mostly relies on error cancelations. Note that long-range bulk effects are introduced by using the CPCM-UAHF//UAKS scheme. The Log $K_{hyd,2}$ value remains calculated from the free energy change, ΔG_s^*, of reaction 6.10, which is this time derived from the thermodynamic cycle shown in Scheme 6.3, which readily leads to:

$$\Delta G_s^* = \Delta G_g^\circ + \Delta G_{sol}^*\left(\left[\mathrm{AtO(OH)_2(H_2O)}_n\right]^-\right) + m\Delta G_{sol}^*\left(\left[\mathrm{Br(H_2O)}_1\right]^-\right) + (2-m)\Delta G_{sol}^*\left(\mathrm{Br}^-\right) - \\ - \Delta G_{sol}^*\left(\left[\mathrm{AtOBr_2(H_2O)}_n\right]^-\right) - m\Delta G_{sol}^*\left(\left[\mathrm{HO(H_2O)}_1\right]^-\right) - (2-m)\Delta G_{sol}^*\left(\mathrm{HO}^-\right) \quad 6.14$$

where *n* and *m* stand for the number of clustered water molecules with, respectively, the At-containing species and the ligands. Note that regarding Scheme 6.3 (see next page), several aspects hold true,[24] (i) the free energy changes for the formation of solvated ion clusters in liquid water are 0, (*i.e.* the $\Delta G(i)^*$ (*i*=a, b, c, d) terms), and (ii) the LHS and RHS sums of the related correction terms to the solvation free energies are equivalent and vanish in Eq. 6.14.

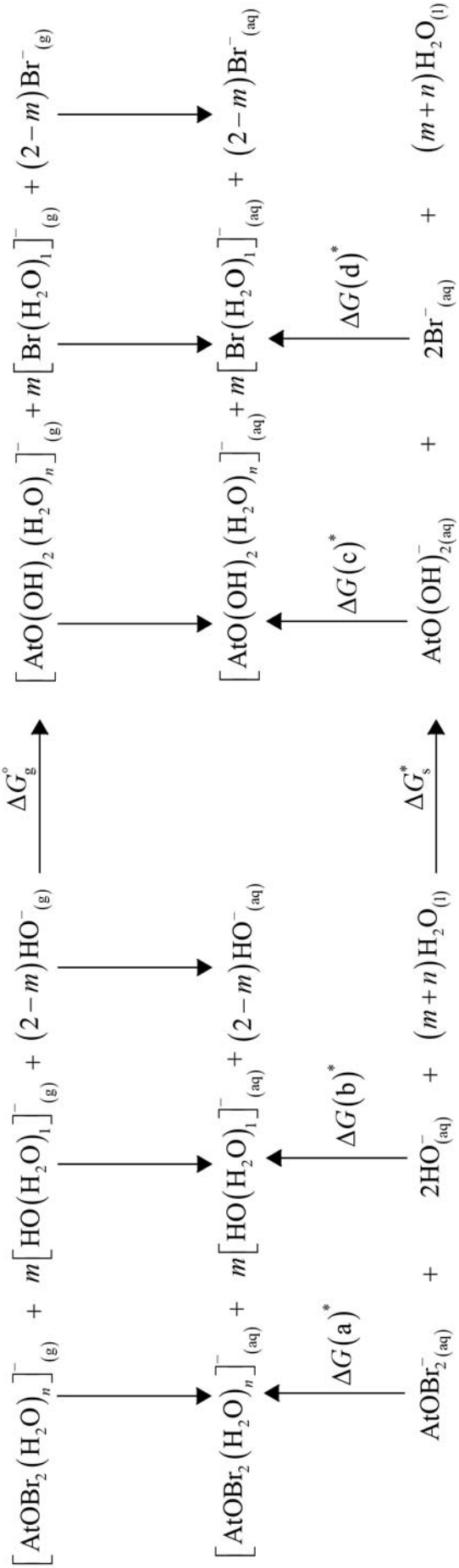

Scheme 6.3 Thermodynamic cycle used to compute the free energy change of the reaction 6.10 when solvent molecules are explicitly treated.

Calculated values for Log K_{2exc} and Log $K_{hyd,2}$ computed according to Eq. 6.14 are gathered in Table 6.1. Each particular case will be presented hereafter and the discussion will be organized in terms of *n*.

Table 6.1 Values of Log K_{2exc} and Log $K_{hyd,2}$ computed at different levels of theory. Stepwise additions of explicitly-treated water molecules are considered. These Log $K_{hyd,2}$ values should be compared to the experimental one of –6.9±0.2.

	2*c*-B3LYP+CPCM-UAHF//UAKS		2*c*-MP2//2*c*-B3LYP+CPCM-UAHF//UAKS	
	Log K_{2exc}	Log $K_{hyd,2}$	Log K_{2exc}	Log $K_{hyd,2}$
n=0, *m*=0	12.0	−9.1	13.0	−8.1
n=1, *m*=0	12.5	−8.6	12.5	−8.6
n=1, *m*=1	12.7	−8.4	13.7	−7.4
n=2, *m*=0	12.6	−8.5	13.3	−7.8
n=2, *m*=1	12.8	−8.3	14.5	−6.6
n=3, *m*=0	13.9	−7.2	13.5	−7.6
n=3, *m*=1	14.0	−7.1	14.7	−6.4
n=3, *m*=2	14.2	−6.9	15.9	−5.2
n=4, *m*=0	14.2	−7.9	12.9	−8.2
n=4, *m*=1	13.4	−7.7	14.1	−6.9
n=4, *m*=2	13.5	−7.6	15.4	−5.7

***n*=1**

Considering a single water molecule in the hydration shells of the $AtOBr_2^-$ and $AtO(OH)_2^-$ species, and only bare ligands (*i.e. m*=0), values of 12.5 and −8.6 for Log K_{2exc} and Log $K_{hyd,2}$, respectively, are obtained at the 2*c*-B3LYP+CPCM-UAHF//UAKS level of theory. Compared to the case when only bare species were considered, these values appear slightly improved. Nonetheless, there is still ~1.5 logarithmic units of disagreement between the calculated Log $K_{hyd,2}$ value and the experimental Log *K* value of –6.9±0.2. Two hypotheses can be formulated regarding this issue, (i) the explicit treatment of a single water molecule in the hydration shells of the considered anionic species is not sufficient for obtaining accurate estimates of the free energies of solvations; hence the value of *n* must be increased, and (ii) the use of the thermodynamic cycle shown in Scheme 6.3 did not allowed the computation of a more accurate Log K_{2exc} value since the interaction-by-interaction error cancelations are not sufficient enough. The equilibrium geometries of the most stable $\left[AtOBr_2(H_2O)_1\right]^-$ and $\left[AtO(OH)_2(H_2O)_1\right]^-$ conformers, obtained at the 2*c*-B3LYP/AVDZ level of theory, are shown in Fig. 6.3. On the LHS of the studied reaction, the water

molecule interacts with the sp^2 O center of the AtO^+ moiety in the most stable $\left[AtOBr_2\left(H_2O\right)_1\right]^-$ conformer.

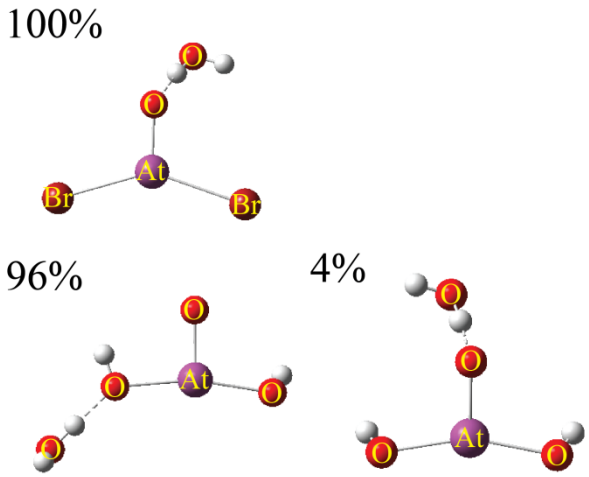

Figure 6.3 Equilibrium geometries for the most stable conformers of the $\left[AtOBr_2\left(H_2O\right)_1\right]^-$ (top) and $\left[AtO\left(OH\right)_2\left(H_2O\right)_1\right]^-$ (bottom) species obtained at the 2*c*-B3LYP/AVDZ level of theory. The printed numbers are Boltzmann populations, computed according to the solvation free energies in aqueous solution.

In contrast, on the RHS, the water molecule interacts mainly with one hydroxyde moiety in the most stable $\left[AtO\left(OH\right)_2\left(H_2O\right)_1\right]^-$ conformer. These two kinds of interactions are clearly not of the same type; they bring different energy contributions and thus unbalanced errors when their explicit treatment is attempted with approximate quantum mechanical methods. One may think of possibilities to balance the interactions occuring on the LHS and RHS of the ligand-exchange reaction. For instance, to match the water-hydroxyde interaction occuring on the RHS, one may introduce and treat explicitly one water molecule in the hydration shell of the hydroxyde ligand on the LHS (*i.e.* setting m=1). Proceeding this way, one should also introduce and treat explicitly one water molecule in the hydration sphere of the bromide ligand, on the RHS, such that the number of water molecules is itself balanced in the reaction. This newly introduced water-bromide interaction on the RHS of the reaction is however not balanced by an analogue on the LHS. Thus, we did not manage to ensure a reasonable balance of the interaction types. As it can be seen in Table 6.1, we have obtained in the n=1, m=1 case only a very slight improvement of 0.2 logarithmic units for Log $K_{hyd,2}$. It is now clear that the values of n itself must be increased in order to obtain a better description of the solvation free energies.

***n*=2**

We start the discussion by a conformational analysis. The equilibrium geometries obtained at the 2*c*-B3LYP/AVDZ level of theory for the most stable $\left[AtOBr_2\left(H_2O\right)_2\right]^-$ and $\left[AtO\left(OH\right)_2\left(H_2O\right)_2\right]^-$ conformers are shown in Fig. 6.4. In both cases there are at least two conformers which appear significantly populated. For the most populated $\left[AtOBr_2\left(H_2O\right)_2\right]^-$ conformers, the newly introduced water molecule either makes a bridge between the previous one and a bromide center, or interacts again with the sp^2 O center of the AtO^+ moiety. Some similar shapes for the water molecules arrangement hold for the most populated $\left[AtO\left(OH\right)_2\left(H_2O\right)_2\right]^-$ conformers. Either the two water molecules serve as a bridge or both interact with the sp^2 O center of the AtO^+ moiety (one water molecule furthermore interacts with a hydroxide moiety).

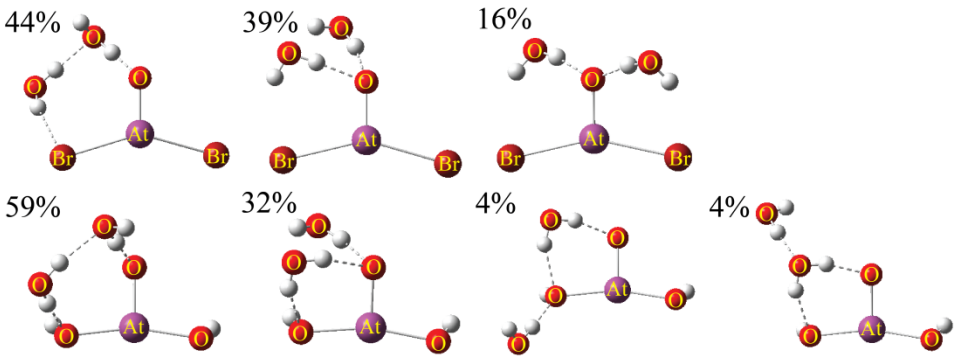

Figure 6.4 Equilibrium geometries for the most stable conformers of the $\left[AtOBr_2\left(H_2O\right)_2\right]^-$ (top) and $\left[AtO\left(OH\right)_2\left(H_2O\right)_2\right]^-$ (bottom) species obtained at the 2*c*-B3LYP/AVDZ level of theory. The printed numbers are Boltzmann populations, computed according to the solvation free energies in aqueous solution.

Labeling the water-solute interactions that can occur on the LHS and on the RHS of the reaction as:

- Type 1: interaction between one water molecule and the sp^2 O center of the AtO^+ moiety;
- Type 2: interaction between one water molecule and one hydroxide moiety/ligand;
- Type 3: interaction between one water molecule and one bromide moiety/ligand;
- Type 4: interaction between two water molecules,

allows us to conveniently summarize them and lead comparisons as in Table 6.2. Note that only the two most stable conformers, representing more than 80% of the population of the At-containing species occurring on the reaction LHS and RHS, are considered for counting the interactions.

Table 6.2 Summary of the water-solute interactions occurring on the LHS and RHS of reaction 6.10, for the microsolvation case when two water molecules are clustered with the involved At-containing species (*n*=2).

	LHS		**RHS**	
Interaction	$\left[\mathrm{AtOBr_2(H_2O)_2}\right]^- + m\left[\mathrm{(HO)(H_2O)}\right]^- + (2-m)\mathrm{H}$		$\left[\mathrm{AtO(OH)_2(H_2O)_2}\right]^- + m\mathrm{Br(H_2O)}^- + (2-m)\mathrm{Br}^-$	
	m=0	*m*=1	*m*=0	*m*=1
Type 1	3	3	3	3
Type 2	0	1	2	2
Type 3	1	1	0	1
Type 4	1	1	1	1

Considering only bare ligands, one may notice that there is an unbalance between the interactions of Type 2 and Type 3, *i.e.* interactions between water molecules and hydroxide or bromide moieties. We thus do not expect *a priori* a great improvement on Log K_{exc} and Log $K_{hyd,2}$. Introducing and treating explicitly a single water molecule in the hydration shell of the ligands (*i.e.* *n*=2, *m*=1 case) then one can fully balance the interactions of type 3 and also partly the ones of type 2. For instance, we have obtained for Log K_{exc} and Log $K_{hyd,2}$ at the 2*c*-B3LYP+CPCM-UAHF//UAKS level of theory the respective 12.8 and −8.3 values (see Table 6.1), which are a bit better than the ones obtained in the previous analogue case, *i.e.* *n*=1 and *m*=1. This improving trend gives us the motivation to proceed further by increasing *n*.

***n*=3**

We start again our analysis with the conformational study. The equilibrium geometries obtained at the 2*c*-B3LYP/AVDZ level of theory for the most stable $\left[\mathrm{AtOBr_2(H_2O)_3}\right]^-$ and $\left[\mathrm{AtO(OH)_2(H_2O)_3}\right]^-$ conformers are shown in Fig. 6.5. In each case, one very stable conformer appears to predominate the populations at thermal equilibrium. Their equilibrium geometries are closely related to their *n*=2 parents. On one side, starting from the equilibrium geometry of the most stable $\left[\mathrm{AtOBr_2(H_2O)_2}\right]^-$ conformer, the newly introduced water molecule interacts with the sp^2 O center of the AtO^+ moiety. On the other side, starting from the most stable $\left[\mathrm{AtO(OH)_2(H_2O)_2}\right]^-$ conformer, the newly added water molecule interacts with a hydroxide moiety.

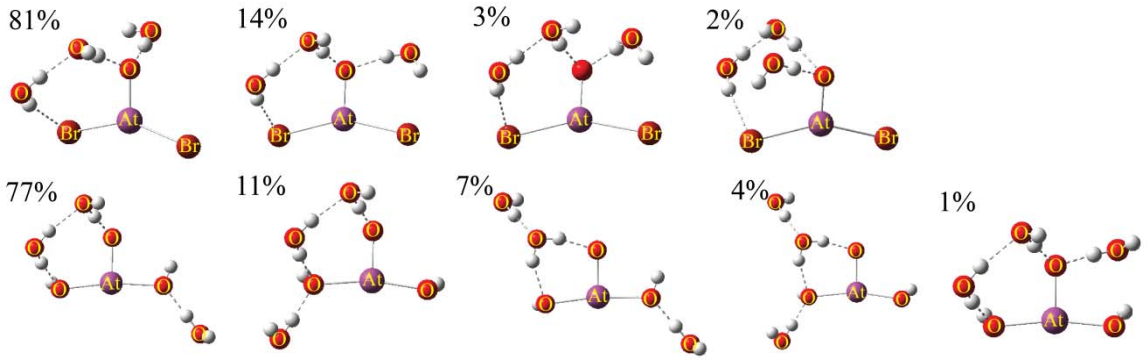

Figure 6.5 Equilibrium geometries for the most stable conformers of the $\left[AtOBr_2(H_2O)_3\right]^-$ (top) and $\left[AtO(OH)_2(H_2O)_3\right]^-$ (bottom) species obtained at the 2*c*-B3LYP/AVDZ level of theory. The printed numbers are Boltzmann populations, computed according to the solvation free energies in aqueous solution.

Using the terminology for the water-solute interaction types introduced previously, we resume the interactions occurring on the LHS and RHS of the ligand-exchange reaction in Table 6.3. Note that only the most stable conformers, representing about 80% of the population of the At-containing species occurring on the reaction LHS and RHS, are considered for counting the interactions. Considering only bare ligands, one can notice that the interaction types occurring on the LHS and on the RHS are quite unbalanced, notably regarding the Type 2 but also Type 1 and Type 3.

Table 6.3 Summary of the water-solute interactions occurring on the LHS and RHS of the studied ligand-exchange reaction 6.10, for the microsolvation case when three water molecules are clustered with the involved At-containing species (n=3).

	LHS			**RHS**		
Interaction	$\left[AtOBr_2(H_2O)_3\right]^- + m\left[(HO)(H_2O)\right]^- + (2-m)H$			$\left[AtO(OH)_2(H_2O)_3\right]^- + mBr(H_2O)^- + (2-m)Br$		
	m=0	m=1	m=2	m=0	m=1	m=2
Type 1	2	2	2	1	1	1
Type 2	0	1	2	2	2	2
Type 3	1	1	1	0	1	2
Type 4	1	1	1	1	1	1

To improve our computational estimate for Log $K_{hyd,2}$, we need to ensure as most as possible interaction-by-interaction error cancelations. Introducing and treating explicitly one water molecule in the hydration spheres of the ligands, one may note that very similar interactions types occur on both LHS and RHS of the reaction. Nevertheless, one may identify in this case, *i.e.* n=3, m=1, one more interaction of Type 1 on the LHS (*i.e.* interaction between a water molecule and the sp^2 O center of the AtO^+ moiety) while there is one more interaction of Type 2 on the RHS (*i.e.* interaction between a water molecule and a hydroxide moiety). These interactions are however not so different (hydrogen bonds between a water molecule and an O atom bonded to At). Therefore,

the results may still benefit from error cancelations associated with the treatment of these interactions. Our calculated value for Log $K_{hyd,2}$ at the 2*c*-B3LYP+CPCM-UAHF//UAKS level of theory, −7.1, so far corresponds to our best and most consistent estimate. It is worth noting that increasing the value of *m* to 2 (*i.e.* the *n*=3, *m*=2 case), the calculated Log $K_{hyd,2}$ at the same level of theory perfectly matches the experimentally determined Log *K* value of −6.9±0.2. However, inspecting the occurrence of the different interactions, there is one more interaction of Type 1 on the LHS while there is one more of Type 3 on the RHS, and they are clearly very different in nature contrary to the previous *m*=1 case. Hence, even though the calculated Log $K_{hyd,2}$ value agrees better with the experimental one, we do not consider it to be more consistent than the one calculated in the previous *n*=3, *m*=1 case, which remains yet our best estimate.

Before drawing a major conclusion, one aspect needs to be clarified related to the convergence of our calculated Log K_{2exc} and Log $K_{hyd,2}$ values at *n*=3. Indeed, if a convergence regime is not met then these two quantities will continue to increase with the further increase of *n*. We have then assessed the case of *n*=4. In Appendix 4, we place the obtained lowest energy $\left[\mathrm{AtOBr_2}\left(\mathrm{H_2O}\right)_4\right]^-$ and $\left[\mathrm{AtO}\left(\mathrm{OH}\right)_2\left(\mathrm{H_2O}\right)_4\right]^-$ conformers and the inventory of the water-solute interactions that occur, in order to keep this part clear. In Table 6.1, one can notice that the values obtained for Log $K_{hyd,2}$ range from −7.9 to −7.6 at the 2*c*-B3LYP+CPCM-UAHF//UAKS level of theory, depending on the value of *m*, and from −8.2 to −5.7 at the 2*c*-MP2//2*c*-B3LYP+CPCM-UAHF//UAKS level of theory. Hence, it is clear that a convergence regime is achieved around *n*=3 and that with the increase of *n* the calculated Log $K_{hyd,2}$ quantity will oscillate around ∼−7 depending on the efficiency of the error cancelation mechanism.

So far, we have shown that the explicit quantum mechanical treatment of *n*=3 water molecules in the hydration shells of the At-containing anionic species and *m*=1 water molecule in the hydration shells of the ligands, improves our description of the solvation free energies and leads to better computational estimate of the K_{2exc}. This latter one, allows this time the derivation of a $K_{hyd,2}$ value (−7.1 logarithmic units at the 2*c*-B3LYP+CPCM-UAHF//UAKS level of theory and −6.4 logarithmic units at the 2*c*-MP2//2*c*-B3LYP+CPCM-UAHF//UAKS level of theory) which is in excellent agreement with the *K* value measured through the experiment (−6.9±0.2 logarithmic units). This clearly supports the hypothesis that the experimentally studied reaction is the one shown in Eq. 6.3, and enables the unambiguous identification of the formed species, $\mathrm{AtO}\left(\mathrm{OH}\right)_2^-$, which predominates in basic and oxidizing aqueous solution.

6.5 Conclusion

In the present chapter, we have dealt with a complex project aiming at the identification of the predominant At species in basic and oxidizing conditions. The project has been tackled through the combination of ultra-trace experiments and relativistic quantum mechanical calculations. The information retrieved from the experimental studies suggested that the targeted At species bears a single negative charge and that, upon lowering the pH from ~11 to ~5.5, this species transforms into AtO(OH). Furthermore, the corresponding equilibrium constant has been measured. Then, two hypotheses arose, (i) either the AtO_2^- species can be formed through the deprotonation of AtO(OH), or (ii) the $AtO(OH)_2^-$ species can be formed through the hydrolysis of AtO(OH). However, which one of the two candidates is actually formed could not be discerned only from the experimental data, and quantum mechanical studies have been performed. Our strategy was to bring computational estimates for the equilibrium constants associated with the formation of the AtO_2^- and $AtO(OH)_2^-$ species, and to compare them with the experimentally determined one. In a first step, we have ruled out the possibility that the former species, *i.e.* AtO_2^-, is formed through the deprotonation reaction of AtO(OH) since our computational estimate of Log K_a(AtO(OH)), below −11, is in great disagreement with the measured constant of −6.9±0.2. We then considered the second candidate reaction, in which the $AtO(OH)_2^-$ species could be formed. Our computational estimate for the equilibrium constant associated with this latter candidate reaction, Log $K_{hyd,2}$= −7.1, is in great agreement with the experimentally determined one (−6.9±0.2). A firm identification of the formed species is thus possible.

It is now clear that the $AtO(OH)_2^-$ species is the one that predominates over At^- in basic and oxidizing conditions, and this species should be added to the Pourbaix diagram of At (see Fig. 6.6). Although the border between At^- and $AtO(OH)_2^-$ can be drawn from the available data, it cannot be further confirmed by experiment due to kinetic considerations. More importantly, it is not yet known if another species can predominate above pH=11. Therefore, we do not consider that this diagram is yet complete.

The identification of $AtO(OH)_2^-$ in basic and oxidizing conditions, and the evidence of its predominance, is particularly important for the scientific community involved in the ^{211}At-radiolabelings in aqueous media. For instance, if a radiolabeling with At^- is attempted (*via* a

nucleophilic substitution mechanism), having a basic media is a necessary but not a sufficient condition. In such a case, one needs to ensure reducing conditions as far as possible otherwise a change in the At speciation is likely to occur. Note that, with this change in speciation, a change in the oxidation number of At itself also occurs, *i.e.* from –I to +III. For example, this latter information may be important in studies aiming at coordinating ^{211}At with soft metal cations,[25-27] as done by Pruszinsky and coworkers.

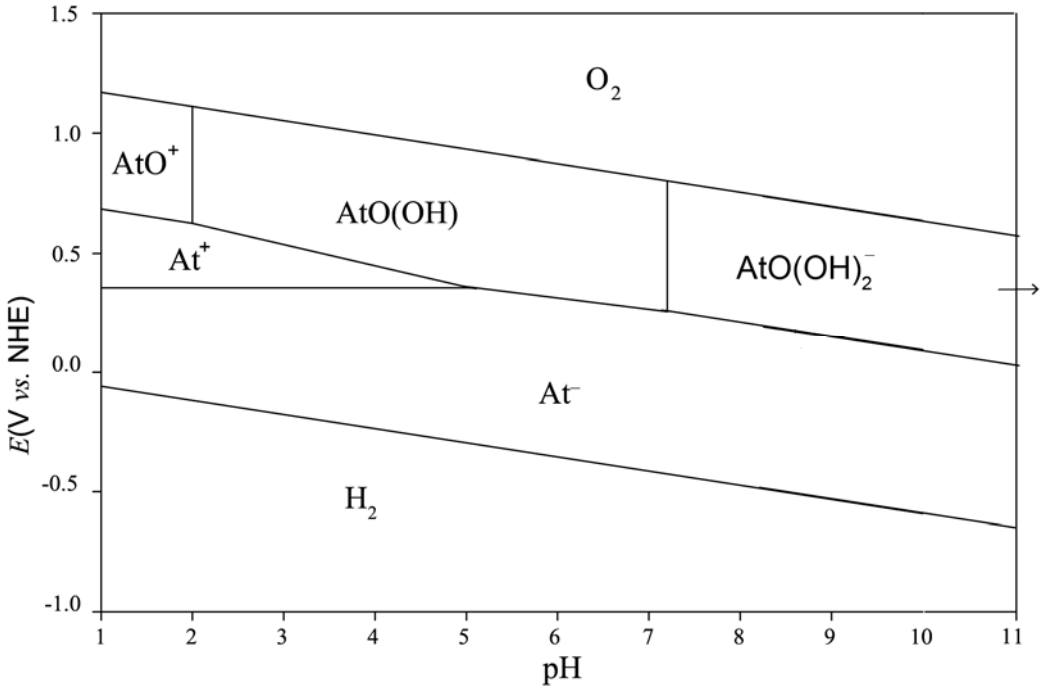

Figure 6.6 Pourbaix diagram of At in aqueous and non-complexing media.

Bibliography

1. D.-C. Sergentu, D. Teze, A. Sabatié-Gogova, C. Alliot, N. Guo, F. Bassal, I. D. Silva, D. Deniaud, R. Maurice, J. Champion, N. Galland, G. Montavon, *Chem. Eur. J.* Advances on the determination of the astatine Pourbaix diagram: Predomination of $AtO(OH)_2^-$ over At^- in basic conditions, **2016**, 22, 2964.
2. B. Beverskog, I. Puigdomenech, *Corros. Sci.* Revised Pourbaix diagrams for nickel at 25–300 °C, **1997**, 39, 969.
3. B. Beverskog, I. Puigdomenech, *Corros. Sci.* Revised pourbaix diagrams for iron at 25-300 °C, **1996**, 38, 2121.
4. B. Beverskog, I. Puigdomenech, *Corros. Sci.* Revised pourbaix diagrams for chromium at 25–300 °C, **1997**, 39, 43.
5. I. Dreyer, R. Dreyer, V. A. Chalkin, *Radiochem. Radioanal. Lett.* Studies of the migration rates of astatine compounds in an electric field, **1978**, 35, 257.
6. K. Ticknor, Y. Cho, *J. Radioanal. Nuclear Chem.* Interaction of iodide and iodate with granitic fracture-filling minerals, **1990**, 140, 75.
7. A. Sabatié-Gogova, J. Champion, S. Huclier, N. Michel, F. Pottier, N. Galland, Z. Asfari, M. Chérel, G. Montavon, *Anal. Chim. Acta.* Characterization of At^- species in simple and biological media by high performance anion exchange chromatography coupled to gamma detector, **2012**, 721, 182.
8. R. A. Milius, W. H. McLaughlin, R. M. Lambrecht, A. P. Wolf, J. J. Carroll, S. J. Adelstein, W. D. Bloomer, *Int. J. Radiat. Appl. Instrum. Part A. Appl. Radiat. Isot.* Organoastatine chemistry. Astatination via electrophilic destannylation, **1986**, 37, 799.
9. J. Champion, M. Seydou, A. Sabatié-Gogova, E. Renault, G. Montavon, N. Galland, *Phys. Chem. Chem. Phys.* Assessment of an effective quasirelativistic methodology designed to study astatine chemistry in aqueous solution, **2011**, 13, 14984.
10. J. Champion, C. Alliot, E. Renault, B. M. Mokili, M. Chérel, N. Galland, G. Montavon, *J. Phys. Chem. A.* Astatine standard redox potentials and speciation in acidic medium, **2010**, 114, 576.
11. J. Champion, A. a. Sabatié-Gogova, F. Bassal, T. Ayed, C. Alliot, N. Galland, G. Montavon, *J. Phys. Chem. A.* Investigation of astatine (III) hydrolyzed species: Experiments and relativistic calculations, **2013**, 117, 1983.
12. J. Champion, C. Alliot, S. Huclier, D. Deniaud, Z. Asfari, G. Montavon, *Inorg. Chim. Acta.* Determination of stability constants between complexing agents and At (I) and At (III) species present at ultra-trace concentrations, **2009**, 362, 2654.
13. P. J. Stephens, F. J. Devlin, C. Chabalowski, M. J. Frisch, *J. Phys. Chem.* Ab initio calculation of vibrational absorption and circular dichroism spectra using density functional force fields, **1994**, 98, 11623.
14. K. A. Peterson, D. Figgen, E. Goll, H. Stoll, M. Dolg, *J. Chem. Phys.* Systematically convergent basis sets with relativistic pseudopotentials. II. Small-core pseudopotentials and correlation consistent basis sets for the post-d group 16–18 elements, **2003**, 119, 11113.
15. M. K. Armbruster, W. Klopper, F. Weigend, *Phys. Chem. Chem. Phys.* Basis-set extensions for two-component spin-orbit treatments of heavy elements, **2006**, 8, 4862.
16. T. H. Dunning Jr, *J. Chem. Phys.* Gaussian basis sets for use in correlated molecular calculations. I. The atoms boron through neon and hydrogen, **1989**, 90, 1007.

17. R. A. Kendall, T. H. Dunning Jr, R. J. Harrison, *J. Chem. Phys.* Electron affinities of the first-row atoms revisited. Systematic basis sets and wave functions, **1992**, 96, 6796.

18. E. J. Bylaska, W. A. de Jong, N. Govind, K. Kowalski, T. P. Straatsma, M. Valiev, D. Wang, E. Apra, T. L. Windus, J. Hammond, P. Nichols, S. Hirata, M. T. Hackler, Y. Zhao, P.-D. Fan, R. J. Harrison, M. Dupuis, D. M. A. Smith, J. Nieplocha, V. Tipparaju, M. Krishnan, A. Vazquez-Mayagoitia, Q. Wu, T. van Voorhis, A. A. Auer, M. Nooijen, L. D. Crosby, E. Brown, G. Cisneros, G. I. Fann, H. Fruchtl, J. Garza, K. Hirao, R. Kendall, J. A. Nichols, K. Tsemekhman, K. Wolinski, J. Anchell, D. Bernholdt, P. Borowski, T. Clark, D. Clerc, H. Dachsel, M. Deegan, K. Dyall, D. Elwood, E. Glendening, M. Gutowski, A. Hess, J. Jaffe, B. Johnson, J. Ju, R. Kobayashi, R. Kutteh, Z. Lin, R. Littlefield, X. Long, B. Meng, T. Nakajima, S. Niu, L. Pollack, M. Rosing, G. Sandrone, M. Stave, H. Taylor, G. Thomas, J. van Lenthe, A. Wong, Z. Zhang, NWChem version 5.1.1: A computational chemistry package for parallel computers, Pacific Northwest National Laboratory: Richland, WA, **2009**.

19. R. Ahlrichs, M. K. Armbruster, R. A. Bachorz, M. Bär, H.-P. Baron, R. Bauernschmitt, F. A. Bischoff, S. Böcker, N. Crawford, P. Deglmann, F. D. Sala, M. Diedenhofen, M. Ehrig, K. Eichkorn, S. Elliott, D. Friese, F. Furche, A. Glöß, F. Haase, M. Häser, C. Hättig, A. Hellweg, S. Höfener, H. Horn, C. Huber, U. Huniar, M. Kattannek, W. Klopper, A. Köhn, C. Kölmel, M. Kollwitz, K. May, P. Nava, C. Ochsenfeld, H. Öhm, M. Pabst, H. Patzelt, D. Rappoport, O. Rubner, A. Schäfer, U. Schneider, M. Sierka, D. P. Tew, O. Treutler, B. Unterreiner, M. von Arnim, F. Weigend, P. Weis, H. Weiss, N. Winter, TURBOMOLE version 6.6, a development of University of Karlsruhe and Forschungszentrum Karlsruhe GmbH, TURBOMOLE GmbH, **2014**.

20. M. J. Frisch, G. W. Trucks, H. B. Schlegel, G. E. Scuseria, M. A. Robb, J. R. Cheeseman, J. J. A. Montgomery, T. Vreven, K. N. Kudin, J. C. Burant, J. M. Millam, S. S. Iyengar, J. Tomasi, V. Barone, B. Mennucci, M. Cossi, G. Scalmani, N. Rega, G. A. Petersson, H. Nakatsuji, M. Hada, M. Ehara, K. Toyota, R. Fukuda, J. Hasegawa, M. Ishida, T. Nakajima, Y. Honda, O. Kitao, H. Nakai, M. Klene, X. Li, J. E. Knox, H. P. Hratchian, J. B. Cross, V. Bakken, C. Adamo, J. Jaramillo, R. Gomperts, R. E. Stratmann, O. Yazyev, A. J. Austin, R. Cammi, C. Pomelli, J. W. Ochterski, P. Y. Ayala, K. Morokuma, G. A. Voth, P. Salvador, J. J. Dannenberg, V. G. Zakrzewski, S. Dapprich, A. D. Daniels, M. C. Strain, O. Farkas, D. K. Malick, A. D. Rabuck, K. Raghavachari, J. B. Foresman, J. V. Ortiz, Q. Cui, A. G. Baboul, S. Clifford, J. Cioslowski, B. B. Stefanov, G. Liu, A. Liashenko, P. Piskorz, I. Komaromi, R. L. Martin, D. J. Fox, T. Keith, M. A. Al-Laham, C. Y. Peng, A. Nanayakkara, M. Challacombe, P. M. W. Gill, B. Johnson, W. Chen, M. W. Wong, C. Gonzalez, J. A. Pople, Gaussian 03, revision E.01; Gaussian Inc.: Wallingford, CT, **2004**.

21. D. R. Lide, *CRC Press LLC: New York.* Handbook of chemistry and physics, 79th ed., **1998**.

22. F. Bassal, PhD dissertation: Exploration des propriétés métalliques de At (+III): Approche théorique, Université de Nantes, **2013**.

23. J. I. Amaro-Estrada, L. Maron, A. Ramírez-Solís, *J. Phys. Chem. A.* Aqueous solvation of $Hg(OH)_2$: Energetic and dynamical fensity functional theory studies of the $Hg(OH)_2$–$(H_2O)_n$ (n=1–24) structures, **2013**, 117, 9069.

24. V. S. Bryantsev, M. S. Diallo, W. A. Goddard Iii, *J. Phys. Chem. A.* Calculation of solvation free energies of charged solutes using mixed cluster/continuum models, **2008**, 112, 9709.

25. M. Pruszyński, A. Bilewicz, B. Wąs, B. Petelenz, *J. Radioanal. Nucl. Chem.* Formation and stability of astatide-mercury complexes, **2006**, 268, 91.

26. M. Pruszyński, A. Bilewicz, M. R. Zalutsky, *Bioconjugate Chem.* Preparation of Rh[16aneS4-diol] ^{211}At and Ir[16aneS4-diol]^{211}At complexes as potential precursors for astatine radiopharmaceuticals. Part I: Synthesis, **2008**, 19, 958.

27. M. Pruszyński, M. Łyczko, A. Bilewicz, M. R. Zalutsky, *Nucl. Med. Biol.* Stability and in vivo behavior of Rh[16aneS4-diol]^{211}At complex: A potential precursor for astatine radiopharmaceuticals, **2015**, 42, 439.

Conclusion and Perspectives

At is an “invisible” heavy main-group element which is currently thought as providing the best alpha-emission source, through its ^{211}At radionuclide, for targeted alpha-immunotherapy. While several At species have been synthesized for being connected to cancer cell targeting agents, their unknown and admittedly unintuitive physico-chemical properties currently hinder the success of At-based targeted radioimmunotherapy. Fundamental researches have been triggered to obtain information on the basic chemistry of At and its species. Computational tools play an important role in these researches and are used with a twofold aim, (i) helping in eliminating hypotheses that arise from outcomes of experiments led at ultra-trace regime, and (ii) making valuable predictions conducting future experiments toward success. Several computational studies have been carried out and presented in the present thesis. The main conclusions that arise are enumerated and briefly discussed in the following.

1. Geometries and thermodynamic properties of medium to large At species can safely be investigated with cost-effective (quasirelativistic) 2*c*-DFT approaches, providing a suitable density functional approximation and a suitable computational strategy for introducing environmental effects (*e.g.* hydration).

The degrees of freedom associated with the 2*c*-DFT approach have been addressed mainly in Chapter 3, and the obtained information has been fruitfully used through the remaining chapters. Notably, we identified the PW6B95 hybrid meta-GGA density functional to be the best choice as it allowed the computation of (i) geometries with a MUE of 1.1%, of (ii) electronic transition energies with a MUE of 0.13 eV, and of (iii) reaction equilibrium constants with a MUE of 0.9 logarithmic units, when used in conjunction with triple-zeta quality basis sets, while there is nearly no loss in accuracy when this functional is used in conjunction with smaller double-zeta quality basis sets. We furthermore established that popular and general-purpose hybrid GGA density functionals as PBE0 and B3LYP can as well be safely employed, the former one especially in computing geometries

and, the latter one, especially in computing reaction equilibrium constants. Also, we established that hybrid density functionals that have large amounts of exact exchange should be used with caution in the case of At species. At this point, it would be interesting to test the reliability of the fifth rung functionals, the so-called double hybrids, notably in predicting thermochemical properties of At species. Indeed, based on a blend including adjustable amounts of exact exchange and MP2 correlation, these latter functionals are currently considered as the most robust and accurate ones for calculating thermochemical properties of transition metal compounds.[1] Even though the double hybrids include large amounts of exact exchange (>50%), it appears interesting to know if an amount of MP2 correlation could bring a more balanced description when such functionals are applied to At systems.

2. Using a previously obtained geometry (eventually from 2*c*-DFT calculations), it appears that several properties of At systems can yet safely be explored with cost effective wave-function-based two-step approaches, in which the scalar relativistic and electron correlation problems are addressed in a first step and SOC is introduced in the second step.

Two-step approaches allowing the perturbative treatment of SOC are thought to be problematic in reproducing the correct electronic structure of heavy *p*-elements.[2] This behavior appears most likely in cases where (i) spin-orbit splittings of atomic one-electron shells start to become very large (ii) strong correlation cannot be well described with MRPT2/MRCI(-SD) schemes starting from small reference spaces, and (iii) very large state-interaction spaces are needed to maintain a good representation of the SOC operator, while truncations are either non-trivial or non-achievable, which leads in practice to large convergence artifacts. In monoatomic 6*p* systems, SOC is particularly strong in the valence 6*p* shell and, from Tl toward At, larger and larger errors are expected from two-step calculations. However, in polyatomic At species one may still successfully use such approaches in qualitative descriptions, *e.g.* SOC-EBOs, or in quantitative descriptions whenever relative quantities are sought, *e.g.* relative energies of different geometries or transition energies. Indeed, using a c-SOCI approach we have calculated (i) the relative energies between critical points of the ground state PES of AtF_3, and (ii) the lowest-lying SOC states of the AtO^+ diatomic in very good agreement with reference coupled-cluster results. Moreover, we investigated the peculiar electronic structure of AtO^+ in water using the same approach. We have obtained results that, on one hand corroborate with 2*c*-DFT ones,[3,4] and, on the other hand, are in line with indirect experimental evidences.[5-7] Precisely, we justified with the help of two-step approaches the observed reactivity of AtO^+ in aqueous solution with closed-shell species, as being primarily mediated by a hydration-induced ground-state change. As a perspective, it appears

interesting to conduct a similar study to identify whether the observed reactivity of At^+ can also be explained by a ground-state change. Indeed, At^+ has an essentially $^3P_2$ ground-state which is separated by ~3.8 eV from the first essentially-singlet-spin state, $^1D_2$, according to 4*c* multireference coupled cluster results.[8] Its reactivity with closed-shell species, while experimentally evidenced in many situations, bears thus *a priori* a degree of spin-forbideness.

3. As a consequence of relativistic effects, At can participate to unusual bonding patterns and the resulting At species can exhibit a rather different physico-chemical behavior than their I analogues.

Most radiolabelling protocols with ^{211}At are devised according to ones used with I radionuclides (*e.g.* ^{125}I) under the assumption that there is a resemblance in their chemical behavior.[9] While this is not completely untrue yet whenever issues appear, they must be understood as some peculiar behavior partly arising from the relativistic electronic structure of At and At species, and partly from the environment effects. These issues can be approached and understood currently only through theoretical calculations. In Chapter 4, we have shown that the bonding patterns in which At is involved can be quite different, even in trivially small systems, than the ones for the lower halogens, notably I. In particular, we have shown in the AtF_3 system that the trigonal-planar D_{3h} bonding pattern, not at all characteristic for the inferior halogen trifluorides, is a result of the sum and interplay between scalar relativistic effects and electron correlation. Yet, SOC brings significant energy stabilization to the individual critical points of the ground-state PES of AtF_3 but since they are overall of the same order of magnitude, the surface topology is not much affected. It triggers the signal that SOC may not be responsible of all the peculiarities that At species may exhibit. The environment can also significantly impact the bonding pattern of At. For instance, this was illustrated in Chapter 5 regarding the reactivity of AtO^+ in aqueous solution. The bond in which At is involved can be described using the EBO concept, build on top of two-step approaches,[8] and clues on the weakening or reinforcement of the bond in different contexts can be obtained. In this particular case, the EBO values were calculated for the AtO^+ bond in hydrated clusters thanks to the fact that pairs of bonding and antibonding MOs, characteristic for the AtO^+ bond, are not much delocalized on the water molecules. This may not be the case in other At systems, *i.e.* the MOs may delocalize, and one has to *a priori* perform orbital manipulations for obtaining consistent EBOs. This aspect is interesting and is part of the current perspectives that would be important to tackle in a near future. Also, interesting is to incorporate dynamic correlation in the EBO value, which currently enters only indirectly through the NEVPT2 correlated energies that dress the diagonal of the state-interaction matrix. Extracting EBO values from MRCI wave functions appears interesting.

4. Computational tools are of invaluable usefulness to supplement ultra-trace experiments in order to identify new At species that are potential precursors, or to make best "reactive" other At precursors, used in radiolabelling protocols.

The direct identification and characterization of At species through experimental techniques is non-trivial and quite often impossible since most spectroscopic tools are unsuited to the very low quantities of matter in which At is present. The outcomes of ultra-trace experiments mostly remain indirect evidences and rely on some hypotheses. Combining these outcomes with results of computational studies is the "key to success", as shown in Chapter 6. We have dealt with the identification of the predominant At species in basic and oxidizing conditions. In this particular case, ultra-trace experiments have "told" us that the species in question bears a single negative charge and that it occurs *via* a proton exchange reaction from the AtO(OH) species. Its firm identification as $AtO(OH)_2^-$ was achieved after relativistic quantum mechanical calculations relying on established 2*c*-DFT approaches, were performed. These calculations resulted in a hydrolysis constant of AtO(OH) in excellent agreement with the measured equilibrium constant when the $AtO(OH)_2^-$ species is considered. The identification of the predominance domain of this species represents an important advance regarding the completion of the astatine Pourbaix diagram, and is crucial for current radiolabeling protocols based on the At^- precursor. For instance, if its involvement is required in a nucleophilic substitution, non-reductive conditions should be avoided. As a perspective, even though it is not trivial, it is of interest to complete the Pourbaix diagram of At, and notably assess the bordering domain of $AtO(OH)_2^-$ in strong basic conditions (*i.e.* above pH=11).

Bibliography:

1. L. Goerigk, S. Grimme, *WIREs Comput. Mol. Sci.* Double-hybrid density functionals, **2014**, 4, 576.
2. M. Reiher, A. Wolf, Relativistic quantum chemistry: The fundamental theory of molecular science. Wiley-VCH, **2009**.
3. T. Ayed, M. Seydou, F. Réal, G. Montavon, N. Galland, *J. Phys. Chem. B.* How does the solvation unveil AtO^+ reactivity?, **2013**, 117, 5206.
4. T. Ayed, F. Réal, G. Montavon, N. Galland, *J. Phys. Chem. B.* Rationalization of the solvation effects on the AtO^+ ground-state change, **2013**, 117, 10589.
5. D.-C. Sergentu, D. Teze, A. Sabatié-Gogova, C. Alliot, N. Guo, F. Bassal, I. D. Silva, D. Deniaud, R. Maurice, J. Champion, *Chem. Eur. J.* Advances on the determination of the astatine Pourbaix diagram: Predomination of $AtO(OH)_2^-$ over At^- in Basic Conditions, **2016**, 22, 2964.
6. J. Champion, M. Seydou, A. Sabatié-Gogova, E. Renault, G. Montavon, N. Galland, *Phys. Chem. Chem. Phys.* Assessment of an effective quasirelativistic methodology designed to study astatine chemistry in aqueous solution, **2011**, 13, 14984.
7. J. Champion, A. a. Sabatié-Gogova, F. Bassal, T. Ayed, C. Alliot, N. Galland, G. Montavon, *J. Phys. Chem. A.* Investigation of astatine (III) hydrolyzed species: Experiments and relativistic calculations, **2013**, 117, 1983.
8. R. Maurice, F. Réal, A. S. P. Gomes, V. Vallet, G. Montavon, N. Galland, *J. Chem. Phys.* Effective bond orders from two-step spin-orbit coupling approaches: The I_2, At_2, IO^+, and AtO^+ case studies, **2015**, 142, 094305.
9. D. S. Wilbur, *Nat. Chem.* Enigmatic astatine, **2013**, 5, 246.

Appendix 1

Table A1.1 Calculated bond lengths (in Å) using several XC functionals and the AVDZ basis set, and associated MSEs, MUEs, RMSDs and MaxDs (in %).

Functional	At_2	HAt	AtF_3^{C2v}		AtF_3^{D3h}	AtO^+	MSE	MUE	RMSD	MaxD
LSDA										
SVWN[a]	3.010	1.749	-	-	2.086	1.945	1.2	1.2	1.1	2.0
GGAs										
BLYP[a]	3.155	1.764	-	-	2.136	1.983	4.5	4.5	4.7	7.5
BP86[a]	3.086	1.756	-	-	2.118	1.967	3.4	3.4	3.8	6.6
PW91[a]	3.074	1.753	-	-	2.116	1.965	2.4	2.4	2.0	3.4
PBE[a]	3.075	1.754	-	-	2.118	1.966	2.4	2.4	2.1	3.5
revPBE[a]	3.097	1.756	-	-	2.128	1.972	2.8	2.8	2.4	4.0
HCTH[a]	3.107	1.746	-	-	2.175	1.957	3.2	3.2	3.0	6.3
OLYP[a]	3.092	1.746	-	-	2.118	1.961	2.4	2.4	2.1	3.5
Meta-GGAs										
PKZB[a]	3.010	1.751	-	-	2.123	1.967	1.9	1.9	1.9	3.8
TPSS[a]	3.061	1.747	-	-	2.108	1.960	2.0	2.0	1.7	3.0
VS98	3.130	1.743	2.110	2.066	2.112	1.958	2.9	2.9	3.1	4.1
M06-L	3.137	1.750	2.107	2.068	2.104	1.946	2.8	2.8	3.1	4.3
M11-L	3.056	1.717	2.007	1.946	2.016	1.887	−1.0	1.6	1.7	2.2
Hybrid GGAs										
B3LYP	3.085	1.746	2.105	2.062	2.101	1.947	2.4	2.4	2.6	3.8
X3LYP	3.080	1.744	2.102	2.057	2.098	1.945	2.3	2.3	2.4	3.5
B3PW91	3.020	1.737	2.089	2.042	2.085	1.933	1.4	1.4	1.7	2.8
BH&HLYP	3.025	1.724	2.069	2.010	-	1.909	0.4	0.9	0.9	1.2
PBE0	3.015	1.734	2.085	2.034	2.082	1.928	1.2	1.2	1.5	2.4
B97-2	3.086	1.733	2.092	2.044	2.087	1.932	1.8	1.8	2.1	2.9
B98	3.093	1.737	2.096	2.049	2.093	1.938	2.1	2.1	2.3	3.1
Hybrid meta-GGAs										
TPSSh	3.039	1.740	2.098	2.053	2.094	1.945	1.9	1.9	2.1	3.3
MPW1B95	3.013	1.730	2.078	2.027	2.076	1.934	1.0	1.0	1.2	2.0
PW6B95	3.032	1.734	2.086	2.037	2.083	1.929	1.3	1.4	1.6	2.5
MPWB1K	2.986	1.721	2.062	2.005	-	1.905	0.0	0.8	0.9	1.3
PWB6K	2.990	1.720	2.062	2.004	-	1.904	0.0	0.7	0.8	1.3
M05[a]	3.133	1.757	2.101	2.069	2.096	1.926	2.6	2.7	3.0	4.2
M06	3.116	1.754	2.092	2.053	2.089	1.925	2.2	2.3	2.5	3.7
M05-2X	2.948	1.720	2.065	2.002	2.064	1.919	**0.0**	**0.9**	**1.0**	**1.9**
M06-2X	2.971	1.725	2.071	2.009	-	1.919	0.2	0.9	1.0	1.2
M08-HX	2.949	1.724	2.074	2.009	-	1.921	0.1	1.0	1.2	1.9
M08-SO	3.065	1.751	2.094	2.047	-	1.928	1.8	1.9	2.1	3.0
Range-separated										
CAM-B3LYP	3.021	1.733	2.084	2.033	-	1.921	1.0	1.2	1.4	2.3
LC-ωPBE	2.966	1.728	2.086	2.037	-	1.915	0.6	1.4	1.6	2.5
HSE06	3.032	1.736	2.090	2.041	2.087	1.932	1.5	1.5	1.7	2.7
BNL	3.016	1.763	2.107	2.060	-	1.939	2.0	2.0	2.4	3.6
M11	2.972	1.733	2.088	2.032	-	1.921	0.7	1.4	1.5	2.3
Ab initio										
HF[b]	3.007	1.715	2.050	1.975	-	1.877	−0.6	0.7	1.3	2.7
MP2	3.046	1.726	2.091	2.035	2.090	1.953	1.6	1.6	1.8	2.4
Reference										
	3.006[1]	1.718[2]	2.046[3]	1.987[3]	2.046[3]	1.930[4]				

[a]The C_{2v} structure of AtF_3 is not a minimum and hence it is removed from the calculation of the different errors/deviations.
[b]The D_{3h} structure of AtF_3 is not a minimum and hence it is removed from the calculation of the different errors/deviations.

Table A1.2 Calculated equilibrium constants (in Log units) using several XC functionals in conjunction with the AVDZ basis set and the CPCM-UAHF//UAKS(B3LYP) solvation scheme.

Functional	AtCl	AtSCN	AtOCl	AtOSCN	AtOOH	$AtCl_2^-$	$AtSCN_2^-$	$AtOCl_2^-$
LSDA								
SVWN	1.1	3.5	2.4	5.1	11.1	2.7	4.8	4.2
GGAs								
BLYP[a]	0.7 (0.7)	4.2 (5.1)	1.9 (1.8)	5.2 (6.0)	8.5 (8.6)	2.1 (2.0)	5.4 (7.2)	3.5 (3.3)
BP86	0.9	3.9	2.2	5.0	9.9	2.3	5.0	3.8
PW91	0.7	3.8	2.1	4.8	10.0	2.2	5.0	3.7
PBE	0.8	3.8	2.2	4.8	9.9	2.3	5.1	3.8
revPBE	0.7	3.9	2.1	5.8	9.7	2.1	5.0	3.7
HCTH	0.7	3.6	2.1	5.0	10.1	2.2	4.8	3.7
OLYP	0.7	3.7	2.1	5.8	10.0	2.2	5.0	3.7
Meta-GGAs								
PKZB	0.9	4.2	2.3	3.8	10.8	2.3	5.1	3.9
TPSS[a]	1.0 (1.0)	3.9 (4.4)	2.4 (2.4)	4.4 (4.9)	11.7 (11.7)	2.5 (2.5)	4.7 (5.9)	4.1 (4.0)
VS98	0.6	4.1	1.9	4.2	10.4	2.3	5.0	3.6
M06-L	−0.6	1.3	1.6	3.3	14.3	2.0	2.7	3.9
M11-L	3.8	6.1	5.1	7.5	23.3	5.7	6.8	7.3
Hybrid GGAs								
B3LYP[a]	0.9 (0.9)	3.9 (4.7)	2.4 (2.4)	2.6 (3.3)	11.3 (11.4)	2.5 (2.5)	5.1 (6.7)	4.2 (4.1)
X3LYP	1.0	4.0	2.5	2.4	11.6	2.7	5.2	4.3
B3PW91	1.0	3.6	2.6	2.0	12.6	2.7	5.0	4.5
BH&HLYP	1.3	4.2	3.0	6.0	15.3	3.4	5.5	5.3
PBE0	1.0 (1.0)	3.8 (4.2)	2.7 (2.7)	1.9 (2.4)	13.1 (13.1)	2.8 (2.7)	5.3 (6.2)	4.7 (4.6)
B97-2	0.8	3.6	2.5	1.9	12.4	2.5	4.7	4.3
B98	1.0	3.9	2.6	2.0	12.2	2.6	4.8	4.4
Hybrid meta-GGAs								
TPSSh[a]	1.1 (1.0)	3.8 (4.4)	2.6 (2.6)	2.8 (3.4)	12.7 (12.8)	2.7 (2.6)	4.8 (6.0)	4.4 (4.3)
MPW1B95	1.0	3.7	2.9	2.0	13.3	2.5	4.6	4.1
PW6B95	0.9	3.7	2.8	2.0	12.6	2.4	4.9	4.1
MPWB1K[a]	1.2 (1.2)	3.8 (4.2)	2.9 (2.9)	3.4 (4.1)	14.8 (14.8)	2.8 (2.8)	4.4 (5.4)	4.6 (4.5)
PWB6K	1.1	3.8	2.9	4.0	14.8	2.8	4.6	4.8
M05	0.6	1.5	2.9	3.4	12.1	2.8	3.7	4.9
M06[a]	0.3 (0.3)	1.8 (1.8)	2.4 (2.4)	2.2 (2.3)	12.6 (12.6)	2.5 (2.5)	2.8 (2.9)	4.6 (4.6)
M05-2X	2.9	5.8	4.3	10.0	15.8	4.4	6.0	6.3
M06-2X	2.1	5.0	3.6	8.5	15.5	4.1	6.2	6.0
M08-HX	2.9	5.5	4.1	10.7	15.8	4.5	5.6	6.3
M08-SO	1.1	3.4	2.6	4.3	11.2	2.7	3.6	4.6
Range-separated								
CAM-B3LYP	1.2	3.8	2.9	3.8	13.6	3.3	5.2	5.1
LC-ωPBE	1.2	3.6	3.1	2.3	13.9	3.3	4.8	5.4
HSE06	0.9	3.8	2.6	1.9	12.6	2.6	5.3	4.4
BNL	1.6	4.4	3.4	5.4	13.4	3.7	5.8	5.5
M11	1.7	4.0	3.2	8.7	13.0	3.4	4.0	5.3
Ab Initio								
HF	2.1	5.1	3.8	14.5	21.3	4.6	6.4	6.8
MP2[b]	1.2	4.3	3.2	1.7	13.1	2.7	5.9	5.0
Reference	1.9[5]	3.8[5]	2.5[5]	2.8[5]	12.1[6]	2.3[5]	5.9[5]	3.0[5]

[a]The values in parenthesis are calculated by including the Grimme's DFT-D3 dispersion correction in the gas-phase 2*c*-DFT calculations.
[b]These values are based on single-point MP2/AVTZ energies obtained on previously optimized B3LYP/AVDZ geometries.

Table A1.3 Calculated equilibrium constants (in Log units) using selected XC functionals in conjunction with the AVTZ basis set and the CPCM-UAHF//UAKS(B3LYP) solvation scheme.

Functional	AtCl	AtSCN	AtOCl	AtOSCN	AtOOH	$AtCl_2^-$	$AtSCN_2^-$	$AtOCl_2^-$
LSDA								
SVWN	1.1	2.9	2.6	2.9	11.0	2.7	3.9	4.5
GGA								
PBE	0.8	3.1	2.4	2.3	9.5	2.2	4.5	4.0
Meta-GGA								
TPSS	1.1	3.1	2.6	2.3	11.4	2.6	4.2	4.4
Hybrid GGAs								
B3LYP	1.0	3.4	2.6	1.5	11.1	2.6	4.7	4.5
X3LYP	1.0	3.4	2.6	1.4	11.3	2.7	4.7	4.5
PBE0	1.0	3.1	2.8	0.9	12.5	2.7	4.2	4.8
Hybrid meta-GGAs								
TPSSh	1.1	3.1	2.8	1.6	12.4	2.8	4.2	4.6
PW6B95	0.9	2.9	2.5	0.7	11.7	2.6	4.3	4.1
M06	0.0	1.5	2.2	2.2	10.6	1.9	2.4	4.2
M06-2X	1.6	3.3	3.3	6.1	14.3	3.6	4.2	5.6
Range-separated								
HSE06	1.0	3.1	2.7	1.1	12.0	2.6	4.3	4.6
Reference	1.9[5]	3.8[5]	2.5[5]	2.8[5]	12.1[6]	2.3[5]	5.9[5]	3.0[5]

Table A1.4 Calculated errors/deviations (in units of Log) associated with the equilibrium constants shown in Table A1.3.

Functional	MSE	MUE	RMSD	MaxD
LSDA				
SVWN	−0.3	0.9	1.1	2.0
GGA				
PBE	−0.7	0.9	1.2	2.6
Meta-GGAs				
TPSS	−0.3	0.8	0.9	1.7
Hybrid GGAs				
B3LYP	−0.4	0.8	1.0	1.5
X3LYP	−0.3	0.8	1.0	1.5
PBE0	−0.3	1.0	1.2	1.9
Hybrid meta-GGAs				
TPSSh	−0.2	0.9	1.0	1.7
PW6B95	−0.6	0.9	1.1	2.1
M06	−1.2	1.5	1.8	3.5
M06-2X	1.0	1.6	1.9	3.3
Range-separated				
HSE06	−0.4	0.9	1.1	1.7

Table A1.5 Calculated equilibrium constants (in Log units) using selected DFT functionals in conjunction with the AVDZ basis set and different solvation schemes.

Functional		AtCl	AtSCN	AtOCl	AtOSCN	AtOOH	$AtCl_2^-$	$AtSCN_2^-$	$AtOCl_2^-$
LSDA									
SVWN	UAHF	1.0	3.7	1.9	6.3	11.3	2.6	4.9	3.8
	UAKS	1.1	2.1	1.9	2.1	13.7	2.8	1.9	4.3
	UFF	2.0	2.3	1.7	15.0	23.3	4.2	1.8	5.3
	UFF[a]	1.6	3.3	1.4	14.6	21.8	3.7	3.1	4.7
GGA									
PBE	UAHF	0.8	4.0	1.7	5.5	10.2	2.2	5.1	3.4
	UAKS	0.8	2.4	1.7	1.9	12.5	2.4	2.2	3.9
	UFF	1.7	2.4	1.5	13.1	22.1	3.8	1.6	4.9
	UFF[a]	1.3	3.6	1.2	12.7	20.6	3.3	2.9	4.3
Meta-GGA									
TPSS	UAHF	0.9	4.0	1.9	5.0	11.9	2.5	4.8	3.7
	UAKS	1.0	2.4	1.9	1.5	14.3	2.7	1.9	4.2
	UFF	1.8	2.5	1.7	13.3	23.9	4.1	1.3	5.2
	UFF[a]	1.5	3.6	1.4	12.9	22.4	3.6	2.6	4.6
Hybrid GGAs									
B3LYP[a]	UAHF	0.9	4.0	1.9	3.2	11.6	2.5	5.2	3.8
	UAKS	1.0	2.5	1.9	2.5	13.9	2.5	2.9	4.3
	UFF	1.8	2.5	1.7	15.3	23.5	4.1	1.7	5.3
	UFF[a]	1.4	3.7	1.4	17.6	22.0	3.5	3.0	4.7
X3LYP	UAHF	0.9	4.1	1.9	3.1	11.8	2.6	5.3	3.9
	UAKS	1.0	2.5	2.0	3.0	14.2	2.8	2.4	4.4
	UFF	1.8	2.6	1.8	18.6	23.8	4.2	1.8	5.4
	UFF[a]	1.5	3.8	1.4	18.2	22.3	3.7	3.1	4.8
PBE0	UAHF	1.0	3.9	2.2	2.6	13.3	2.8	5.2	4.3
	UAKS	1.0	2.3	2.2	3.1	15.6	2.9	3.0	4.7
	UFF	1.9	2.4	2.0	18.7	25.2	3.5	1.8	5.8
	UFF[a]	1.5	3.6	1.7	18.3	23.8	3.8	3.1	4.8
Hybrid meta-GGAs									
TPSSh[a]	UAHF	1.0	3.9	2.1	3.4	13.0	2.7	4.8	4.0
	UAKS	1.1	2.7	2.1	0.8	15.3	2.8	2.0	4.5
	UFF	1.9	2.4	1.9	15.5	24.9	4.3	1.3	5.5
	UFF[a]	1.6	3.6	1.6	15.1	23.4	3.8	2.6	4.9
PW6B95	UAHF	0.9	3.8	2.3	2.8	12.8	2.3	4.9	3.7
	UAKS	1.0	2.2	2.3	3.4	15.2	2.5	2.6	4.2
	UFF	1.8	2.3	2.1	19.0	24.8	3.9	1.4	5.2
	UFF[a]	1.5	3.5	1.8	18.6	23.3	3.4	2.7	4.6
M06	UAHF	0.2	4.6	1.9	2.9	12.8	5.2	3.0	4.2
	UAKS	0.3	0.3	1.9	-0.5	15.2	2.6	−0.1	4.7
	UFF	1.1	0.4	1.7	13.3	24.8	4.1	0.1	5.7
	UFF[a]	0.8	3.6	1.4	13.0	23.3	5.5	1.5	5.1
M06-2X	UAHF	2.0	5.1	3.1	7.8	15.7	4.0	6.3	5.6
	UAKS	2.1	3.6	3.1	11.9	18.1	4.2	3.9	6.1
	UFF	2.9	3.6	2.9	27.4	27.7	5.6	2.7	7.1
	UFF[a]	2.6	4.8	2.6	27.1	26.2	5.1	4.0	3.5
Range-separated									
HSE06	UAHF	0.9	3.9	2.0	2.7	12.8	2.6	5.4	4.0
	UAKS	1.0	2.3	2.1	2.7	15.2	2.7	3.0	4.5
	UFF	1.8	2.4	1.9	18.2	24.8	3.3	1.8	5.5
	UFF[a]	1.5	3.6	1.5	17.9	23.3	3.6	3.1	4.9
Reference		1.9[5]	3.8[5]	2.5[5]	2.8[5]	12.1[6]	2.3[5]	5.9[5]	3.0[5]

[a]The UFF cavities are built using the 1.1 electrostatic factor for multiplying the sphere radii.

Table A1.6 Calculated errors/deviations (in units of Log) associated with the equilibrium constants shown in Table A1.5.

Functional		MSE	MUE	RMSD	MaxD
LSDA					
SVWN	UAHF	0.2	1.0	1.4	3.5
	UAKS	−0.6	1.4	1.8	4.0
	UFF	2.7	4.3	6.2	12.2
	UFF[a]	2.5	3.7	5.6	11.8
GGA					
PBE	UAHF	−0.2	1.0	1.3	2.7
	UAKS	−0.8	1.2	1.6	3.7
	UFF	2.1	3.8	5.4	10.3
	UFF[a]	2.0	3.2	4.8	9.9
Meta-GGA					
TPSS	UAHF	0.1	0.8	1.0	2.2
	UAKS	−0.6	1.5	1.8	4.0
	UFF	2.4	4.1	5.9	11.8
	UFF[a]	2.3	3.5	5.3	10.3
Hybrid GGAs					
B3LYP	UAHF	−0.2	0.6	0.6	1.0
	UAKS	−0.4	1.2	1.5	3.0
	UFF	2.7	4.3	6.3	12.5
	UFF[a]	2.9	4.0	6.4	14.8
X3LYP	UAHF	−0.1	0.5	0.6	1.0
	UAKS	−0.3	1.3	1.6	3.5
	UFF	3.2	4.7	7.2	15.8
	UFF[a]	3.1	4.1	6.7	15.4
PBE0	UAHF	0.1	0.7	0.8	1.3
	UAKS	0.1	1.5	1.8	3.5
	UFF	3.4	4.9	7.5	15.9
	UFF[a]	3.3	4.3	7.0	15.5
Hybrid meta-GGAs					
TPSSh[a]	UAHF	0.1	0.7	0.8	1.1
	UAKS	−0.4	1.7	2.1	3.9
	UFF	2.9	4.6	6.7	12.8
	UFF[a]	2.8	4.0	6.1	12.3
PW6B95	UAHF	−0.1	0.5	0.6	1.0
	UAKS	−0.1	1.4	1.8	3.3
	UFF	3.3	4.9	7.5	16.2
	UFF[a]	3.1	4.3	7.0	15.8
M06	UAHF	0.1	1.4	1.7	2.9
	UAKS	−1.2	2.5	3.1	6.0
	UFF	2.1	4.8	6.4	12.7
	UFF[a]	2.5	4.2	5.8	11.2
M06-2X	UAHF	1.9	1.9	2.5	5.0
	UAKS	2.3	2.9	4.1	9.1
	UFF	5.7	6.6	10.5	24.6
	UFF[a]	5.2	5.7	10.0	24.3
Range-separated					
HSE06	UAHF	0.0	0.5	0.6	1.0
	UAKS	−0.1	1.4	1.7	3.1
	UFF	3.2	4.7	7.3	15.4
	UFF[a]	3.1	4.2	6.8	15.1

[a]The UFF cavities are built using the 1.1 electrostatic factor for multiplying the sphere radii.

Bibliography:

1. S. Höfener, R. Ahlrichs, S. Knecht, L. Visscher, *ChemPhysChem.* Relativistic and non-relativistic electronic molecular-structure calculations for dimers of 4p-, 5p-, and 6p-block elements, **2012**, 13, 3952.
2. A. S. P. Gomes, L. Visscher, *Chem. Phys. Lett.* The influence of core correlation on the spectroscopic constants of HAt, **2004**, 399, 1.
3. D.-D. Yang, F. Wang, *Phys. Chem. Chem. Phys.* Structures and stabilities of group 17 fluorides EF_3 (E= I, At, and element 117) with spin–orbit coupling, **2012**, 14, 15816.
4. A. S. P. Gomes, F. Réal, N. Galland, C. Angeli, R. Cimiraglia, V. Vallet, *Phys. Chem. Chem. Phys.* Electronic structure investigation of the evanescent AtO^+ ion, **2014**, 16, 9238.
5. J. Champion, M. Seydou, A. Sabatié-Gogova, E. Renault, G. Montavon, N. Galland, *Phys. Chem. Chem. Phys.* Assessment of an effective quasirelativistic methodology designed to study astatine chemistry in aqueous solution, **2011**, 13, 14984.
6. J. Champion, A. a. Sabatié-Gogova, F. Bassal, T. Ayed, C. Alliot, N. Galland, G. Montavon, *J. Phys. Chem. A.* Investigation of astatine (III) hydrolyzed species: Experiments and relativistic calculations, **2013**, 117, 1983.

Appendix 2

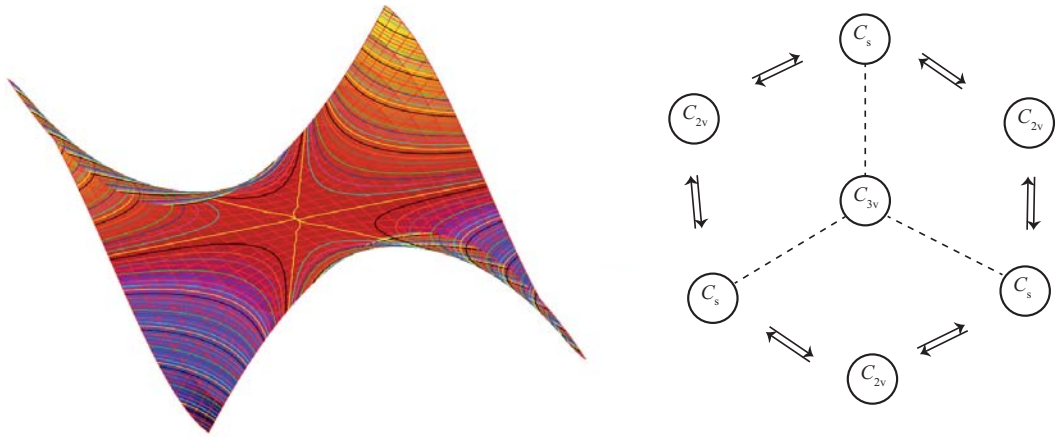

Figure A2.1 Left panel: PES ($z = x^3 - 3xy^2$) corresponding to a monkey saddle point; Right panel: schematic representation of the AtF_3 PES around the C_{3v} structure of AtF_3

Table A2.1 Dissociation energies (in $kJ \cdot mol^{-1}$) obtained at (2*c*-)PBE0 levels.

Reaction	$XF_3 \rightarrow XF + F_2$	$XF_3 \rightarrow XF_2 + F$
ClF_3	124.3	184.0
BrF_3	228.2	231.5
IF_3	349.5	274.8
AtF_3	364.0	238.8

Table A2.2 Contributions (in $kJ \cdot mol^{-1}$) to the $\Delta E^{D_{3h}-C_{2v}}$ in the XF_3 systems (X = Cl, Br, I), computed at the NEVPT2(2/3) and c-SOCI/NEVPT2(2/3) levels using the 6S3T state-averaging and state-interaction spaces.

	NEVPT2	c-SOCI/NEVPT2				(2*c*-)CCSD(T)
	$\Delta E^{D_{3h}-C_{2v}}$	$E_{SOC}^{D_{3h}}$	$E_{SOC}^{C_{2v}}$	$\Delta E_{SOC}^{D_{3h}-C_{2v}}$	$\Delta E^{D_{3h}-C_{2v}}$	$\Delta E^{D_{3h}-C_{2v}}$
ClF_3	67.2	−0.1	−0.1	−0.0	67.2	96.7[a]
BrF_3	59.6	−1.9	−1.4	−0.5	59.2	70.7[a]
IF_3	59.9	−9.3	−6.8	−2.5	57.4	67.8[1]

[a]Values calculated in the present work according to the computational details presented in chapter 4, section 4.4.

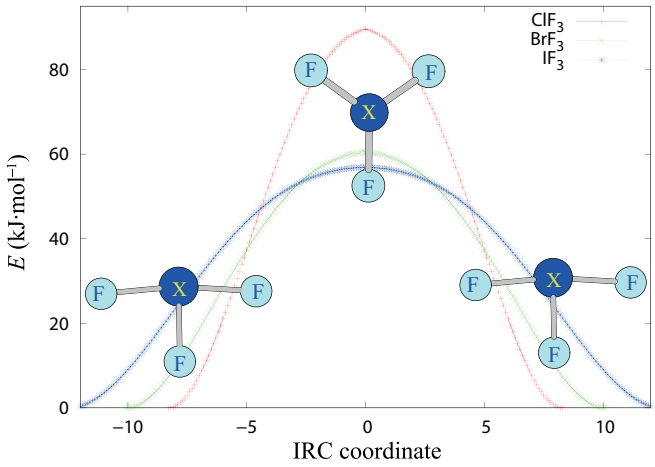

Figure A2.2 Energy along the IRC path starting from the Y-shaped *C*2v TSs, computed at the non-relativistic PBE0 level (X = Cl) or SR-PBE0 level (X = Br, I).

Bibliography

1. D.-D. Yang, F. Wang, *Phys. Chem. Chem. Phys.* Structures and stabilities of group 17 fluorides EF_3 (E= I, At, and element 117) with spin–orbit coupling, **2012**, 14, 15816.

Appendix 3

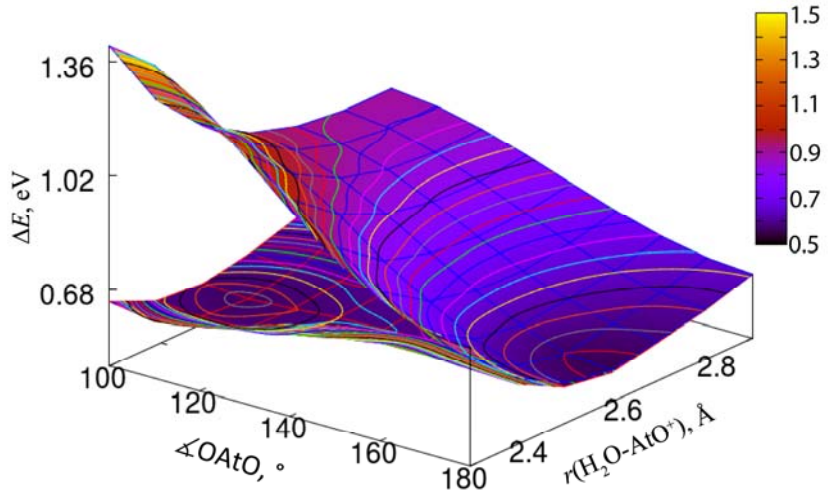

Figure A3.1 Evolution of the relative energies of the $S_0(^1\Delta)$ and $S_1(^1\Delta)$ electronic states of the $AtO^+(H_2O)_1$ system computed at the NEVPT2/AVTZ level of theory as a function of the H_2O-AtO^+ bond distance and $\measuredangle$OAtO .

Table A3.1 Calculated SOF excitation energies (in eV) for the different 2*c*-PBE0/AVDZ equilibrium structures of the $AtO^+(H_2O)_n$ clusters (*n*=2−6) shown in Fig. 5.6.

		$AtO^+(H_2O)_2$	$AtO^+(H_2O)_3$	$AtO^+(H_2O)_4$	$AtO^+(H_2O)_5$	$AtO^+(H_2O)_6$
Essentially-triplet-spin clusters, 2*c*-PBE0/AVDZ						
NEVPT2(8/6)/AVTZ	$T_0(^3\Sigma^-)$	0.00	0.00	0.00	0.01	0.21
	$S_0(^1\Delta)$	0.53	0.43	0.44	0.00	0.00
	$S_1(^1\Delta)$	0.54	0.54	0.54	0.54	0.74
	$S_2(^1\Sigma^+)$	0.95	1.10	1.06	1.63	2.08
Essentially-singlet-spin clusters, 2*c*-PBE0/AVDZ						
NEVPT2(8/6)/AVTZ	$T_0(^3\Sigma^-)$	0.50	1.14	1.80	2.08	2.28
	$S_0(^1\Delta)$	0.00	0.00	0.00	0.00	0.00
	$S_1(^1\Delta)$	1.01	1.63	2.33	2.61	2.81
	$S_2(^1\Sigma^+)$	2.74	3.94	>4.90[a]	>5.16[a]	>5.34[a]

[a]When $S_2(^1\Sigma^+)$ is out of the state-averaging space, we only report a lower limit for the corresponding excitation energy.

Appendix 4

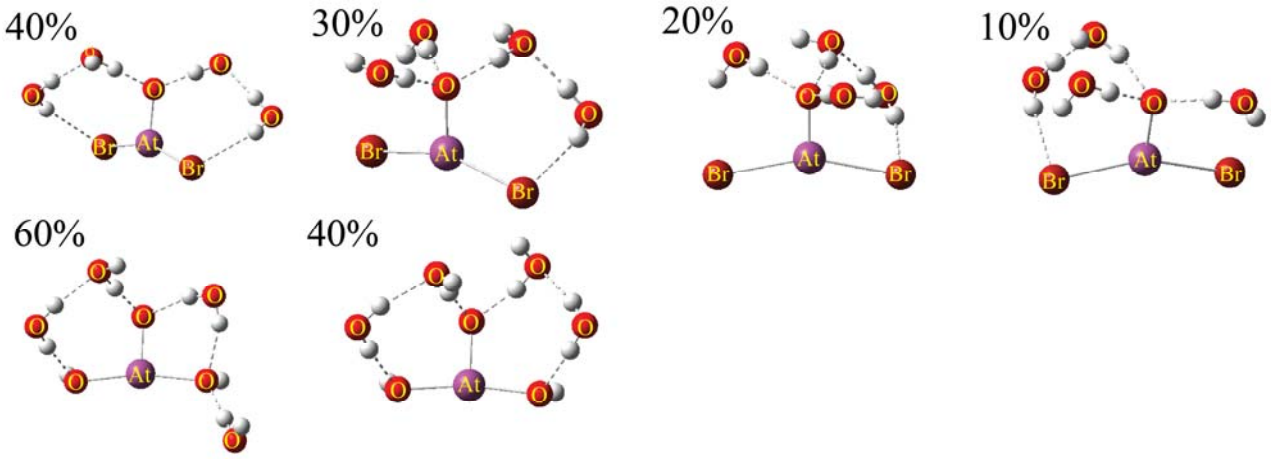

Figure A4.1 Equilibrium geometries for the most stable conformers of the $\left[\mathrm{AtOBr_2(H_2O)_4}\right]^-$ (top) and $\left[\mathrm{AtO(OH)_2(H_2O)_4}\right]^-$ (bottom) species, and their Boltzmann populations, obtained at the 2*c*-B3LYP/AVDZ level of theory.

Table A4.1 Sumary of the water-solute interactions occurring on the LHS and RHS of the studied ligand-exchange reaction 6.10, for the microsolvation case when four water molecules are clustered with the involved At-containing species (*n*=4).

Interaction	**LHS** $\left[\mathrm{AtOBr_2(H_2O)_4}\right]^- + m\left[\mathrm{(HO)(H_2O)}\right]^- + (2-m)\mathrm{H}$			**RHS** $\left[\mathrm{AtO(OH)_2(H_2O)_4}\right]^- + m\mathrm{Br(H_2O)}^- + (2-m)\mathrm{Br}^-$		
	m=0	*m*=1	*m*=2	*m*=0	*m*=1	*m*=2
Type 1	5	5	5	4	4	4
Type 2	0	1	2	5	5	5
Type 3	3	3	3	0	1	2
Type 4	3	3	3	3	3	3

UNIVERSITE BRETAGNE LOIRE

UNIVERSITÉ DE NANTES

Thèse de Doctorat

Dumitru-Claudiu SERGENTU

Geometries, electronic structures and physico-chemical properties of astatine species: An application of relativistic quantum mechanics

Géométries, structures électroniques et propriétés physico-chimiques d'espèces de l'astate : une application de la mécanique quantique relativiste

Résumé

Les tentatives menées pour détruire des cellules cancéreuses avec les agents radiothérapeutiques à base de ^{211}At qui ont été synthétisés jusqu'à présent ne sont pas encore pleinement satisfaisantes car elles sont entachées par une deastatination *in vivo*. Étant donné que ce problème est lié aux connaissances actuelles qui sont limitées concernant la chimie de base de l'astate et de ses espèces, des recherches fondamentales combinant des expériences à l'échelle des ultra-traces et des études théoriques ont été lancées. Dans cette thèse, une étude théorique de plusieurs espèces de l'astate est réalisée au moyen de méthodes relativistes basées sur la théorie de la fonctionnelle de la densité ou des méthodes à basées sur la fonction d'onde. Tout d'abord, les méthodes qui peuvent être utilisées pour faire des prédictions pertinentes sont établies. A l'aide de ces approches, nous rationaliserons les structures électroniques, géométries et propriétés physico-chimiques des différents systèmes d'intérêt théorique ou expérimental, en particulier les espèces AtF_3 et AtO^+. Finalement, nous identifierons formellement une nouvelle espèce de l'astate à l'aide de résultats expérimentaux et de calculs, ce qui non seulement complète le diagramme de Pourbaix de l'astate en milieu aqueux non complexant, mais aussi donne des informations cruciales pour identifier des conditions expérimentales pour rendre le plus « réactif » possible le précurseur At^-, qui est de nos jours impliqué dans la synthèse d'agents radiothérapeutiques innovants.

Mots clés : astate, effets relativistes, théorie de la fonctionnelle de la densité, interaction de configuration avec couplage spin-orbite

Abstract

Trials to destroy cancer cells with currently synthesized ^{211}At-based radiotherapeutic agents are not yet fully satisfactorily since they resume to *in vivo* deastatination. Since this issue is related to the limited knowledge of the basic chemistry of At and its species, fundamental researches combining ultra-trace experiments and computational studies have been initiated. In this thesis, a computational study of several At species is performed, by means of relativistic density functional theory and wave-function-based calculations. First, the quantum mechanical approaches that can safely be used to make adequate predictions are established. Using these approaches, we attempt to rationalize the electronic structures, geometries, and physico-chemical properties of various systems of theoretical and/or experimental interest, in particular the AtF_3 and AtO^+ ones. By the end, we firmly identify a new At species by combining outcomes of experiments and calculations. This new species not only completes the Pourbaix diagram of At in aqueous and non-complexing media, but also gives clues of identifying experimental conditions to make best reactive the At^- precursor, which is currently involved in the synthesis of promising radiotherapeutic agents.

Keywords: astatine, relativistic effects, density functional theory, spin-orbit configuration interaction